Solid-State Nuclear Magnetic Resonance Investigations of the Influenza M2 Protein: Structure and Dynamics Characterization of Channel Gating and Conduction

by

Jonathan K. Williams

B.A., Chemistry & Molecular Biology/Biochemistry
Goshen College, 2011

Submitted to the Department of Chemistry
in Partial Fulfillment of the Requirements for the Degree of

DOCTOR OF PHILOSOPHY
IN PHYSICAL CHEMISTRY

at the

Massachusetts Institute of Technology

September 2017

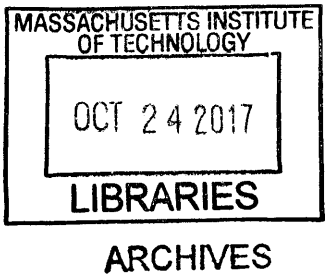

Signature redacted

Signature of Author: _____
Department of Chemistry
August 18, 2017

Signature redacted

Certified by: _____
Mei Hong
Professor of Chemistry
Thesis Supervisor

Signature redacted

Accepted by: _____
Robert W. Field
Haslam and Dewey Professor of Chemistry
Chairman, Departmental Committee on Graduate Students

This doctoral thesis has been examined by a committee of professors
from the Department of Chemistry as follows:

Professor Keith Nelson Signature redacted
Thesis Committee Chair

Professor Mei Hong Signature redacted
Thesis Supervisor

Professor Gabriela Schlau-Cohen Signature redacted
Thesis Committee Member

Solid-State Nuclear Magnetic Resonance Investigations of the Influenza M2 Protein: Structure and Dynamics Characterization of Channel Gating and Conduction

by

Jonathan K. Williams

Submitted to the Department of Chemistry
On August 18th, 2017 in Partial Fulfillment of the
Requirements for the Degree of Doctor of Philosophy in
Physical Chemistry

ABSTRACT

Solid-state nuclear magnetic resonance (ssNMR) spectroscopy is a powerful technique that can be used to probe the structure and dynamics of biomolecules that are intractable to study by other structural biology methods. In this thesis, the mechanisms of conduction and gating are investigated in the influenza AM2 and BM2 proton channels bound to native-like lipid bilayers. Using pH-dependent ^{15}N chemical shifts of the conserved Histidine residue, we have found that the proton conduction mechanism is the same in all of the M2 channels (WT AM2, S31N AM2, BM2) studied, and that the conduction cycle involves proton shuttling via hydrogen-bonding with water. For the first time, unambiguous structural restraints and sidechain dynamics were measured for the gating residue Trp41 in the AM2 channel. Trp41 was found to come into close contact with His37, close enough to undergo periodic cation-π interactions that ensure unidirectional proton flow. Water-edited ^{1}H-^{13}C correlation experiments were used to investigate the channel hydration of AM2 and BM2 tetramers, and S12 in the C-terminal BM2 channel was found to have the largest pH-dependent spin-diffusion buildup of all residues studied, indicating that the BM2 serine triplet plays an important role in conduction. New ssNMR methods were developed to probe long-range ^{13}C-^{13}C distances, and to edit and clean-up crowded spectra of peptides and proteins containing aromatic residues. The ASSET technique removes the aliphatic cross peaks of all residues except for Phe, Trp, Tyr, and His in a two-dimensional ^{13}C-^{13}C correlation experiment, while a two-dimensional ^{13}C-^{13}C correlation experiment with gated-decoupling retains only non-protonated ^{13}C resonances. The studies in this thesis have provided insight into the functionally important His and Trp residues in the M2 proton channel of the influenza virus, and provide new avenues for studying other peptides and proteins containing aromatic residues.

Thesis Supervisor: Mei Hong
Title: Professor of Chemistry

Table of Contents

0. Preface

0.1 Acknowledgements

I would like to express my gratitude to my advisor Prof. Mei Hong, who has provided an amazing opportunity to learn how to perform high-quality research. Her passion for solid-state NMR and drive for investigating interesting biological questions, coupled with the highest standards for data quality, are constant motivators.

I would also like to thank the professors who have served on my thesis committees. I am grateful to Prof. Keith Nelson and Prof. Gabriela Schlau-Cohen for their committee membership at the Massachusetts Institute of Technology. And I am also grateful to Prof. Klaus Schmidt-Rohr, Prof. Emily Smith, Prof. Yan Zhao and Prof. Robert Jernigan for their committee membership at Iowa State University.

I would like to acknowledge and thank my external scientific collaborators, who have provided unique opportunities to do interesting science throughout graduate school. Prof. Klaus Schmidt-Rohr (Brandeis U.) has provided very insightful NMR discussions and lectures, as well as the opportunity to participate in NMR experiment development. Prof. William DeGrado and Dr. Yibing Wu (UCSF), along with Prof. Jun Wang (U. Arizona) provided drug candidates and peptides for several interesting and fruitful M2 collaborations. Prof. Brad Pentelute and Peng Dai provided the opportunity to contribute my NMR knowledge to the interesting π-clamp system.

I also appreciate the collaboration and friendship of the past and present members of the Hong group. I would like to especially thank Dr. Yuan Zhang for her mentorship and training in my first year. Dr. Yongchao Su, Dr. Tuo Wang, Dr. Hongwei Yao, Dr. Yu Yang, Dr. Paul White, Dr. Daniel Tietze, Dr. Shu-Yu Liao, Dr. Keith Fritzsching, Byungsu Kwon, Myungwoon Lee, Matthew Elkins, Pyae Phyo, Marty Gelenter, Shiva Mandala, and Alex Shcherbakov have been great colleagues and I have enjoyed our many discussions and collaborations, scientific or otherwise.

And finally, I would like to thank my family for their constant love and encouragement.

0.2 Thesis Organization

This thesis is comprised of papers published during graduate school, which primarily focus on gaining a better understanding of the structure and dynamics of the influenza M2 proton channel, and in particular the aromatic residues that are essential for proton conduction and channel gating. **Chapter 1** begins with a brief introduction to solid-state NMR spectroscopy, along with the particular solid-state NMR methods and experiments used throughout my graduate research. A brief introduction to the biological system that was the focus of my research, the M2 proton channel of the influenza virus, is also presented.

Chapter 2 begins the presentation of the peer-reviewed and published manuscripts from my graduate research. This chapter shows the identification of the hydrogen-bonding partner of His37 in the influenza AM2 channel to be water, based on the ^{1}H chemical shifts of the imidazoles. A series of 2D ^{1}H-^{15}N correlation spectra were measured on AM2 samples at various pH values and temperatures, in order to determine both the binding partner and hydrogen-bond strength of the histidine residues that shuttle protons through the channel. **Chapter 3** looks at the AM2 gating residue, Trp41, which is responsible for ensuring unidirectional proton conduction through the channel. Distance measurements between the His37-Trp41 and Trp41-Trp41 sidechains enabled the determination of the equilibrium rotameric conformation of the Trp41 sidechain in both the conducting and non-conducting states of the channel. This was coupled with measurements of the Trp41 sidechain dynamics, and together provided a structural basis for understanding the M2 channels periodic cation-π interaction between His37-Trp41 and the regulation and gating of proton conduction. **Chapter 4** deals with a mutant version of the AM2 channel, S31N, which is the prevalent version of the M2 channel in current influenza seasons. In collaboration with our colleagues, we investigated the binding of novel isoxazole based drugs that target this mutant S31N channel. Using measurements of chemical shift perturbation and drug-peptide distance, we found that this new class of drugs binds within the pore of the channel, with an opposite orientation to the drugs amantadine and rimantadine that target the WT channel. We also took a look at the His37 structure and proton exchange dynamics of this mutant channel, and found the same conduction mechanism as the WT channel but with faster exchange. **Chapter 5** is a *Journal of Magnetic Resonance* perspective article, a mini-review and experimental communication, dealing with

probing the interaction of water with membrane proteins. The mechanisms of water to protein polarization transfer are briefly reviewed, along with relevant solid-state NMR techniques used to study water interactions in proteins, lipid membranes and carbohydrates. We also present an examination of the water-protein spin-diffusion build-up of the AM2 transmembrane domain, and how the water-protein interaction varies with residue position and pH.

The next two chapters present developmental work on solid-state NMR methods that focus on cleaning-up, or editing, spectra that are crowded and contain resonance overlap. **Chapter 6** discusses using a longitudinal relaxation-compensated version of the common PDSD correlation experiment, in order to reliably filter out ^{13}C-^{13}C correlations from short distances and leave behind only the correlations resulting from long-range couplings. **Chapter 7** presents two new methods for spectral editing of the aromatic region, which is plagued by severe resonance overlap when more than one aromatic residue is present in a protein. The first, dubbed gPDSD, is a simple modification of the common 2D PDSD experiment, where a period of gated ^{1}H decoupling is inserted before the acquisition of the direct dimension. This results in a spectrum where all ^{13}C resonances are encoded in the indirect dimension, but the direct dimension of the spectrum only contains the non-protonated ^{13}C resonances. In the aromatic region, this results in a significant increase in spectral resolution, since there is very little chemical shift overlap among the non-protonated carbons of the different aromatic residues. The second technique, coined ASSET, edits the spectrum by selectively filtering ^{13}C polarization from the aromatic sidechains, and then transferring to the nearby backbone $C\alpha$, $C\beta$ and CO carbons of the aromatic residues. This greatly reduces the complexity of the aliphatic region of the spectrum, which includes overlapping resonances from the other 16 amino acids.

The final chapter presents the initial work on the influenza BM2 channel, which is a functional analog of the AM2 channel but shares no sequence identity past the conserved HxxxW motif necessary for proton conduction. The BM2 channel, compared to the AM2 channel, has been neglected by structural biologists in the past but presents some unique research opportunities. In **Chapter 8**, the transmembrane domain of the BM2 protein comprising residues 1-33 is studied in a lipid membrane environment for the first time, using solid-state NMR. The pH and membrane dependent conformation and dynamics of His19, the residue responsible for shuttling protons

through the BM2 channel, are probed in this work along with the channel hydration profile. The proton exchange equilibria of His19 in the tetramer was also determined from the ratio between protonated and non-protonated ^{15}N resonances at various pH.

0.3 Copyright Permissions

Chapters 2-8 are reprints of published papers, reproduced in this thesis with permission or under licensing from their respective publishers.

Chapter 2: Reproduced with permission from the *American Chemical Society*.
Chapter 3: *Elsevier*, Open Access publication under a Creative Commons license.
Chapter 4: Reproduced with permission from the *American Chemical Society*.
Chapter 5: Reproduced with permission from *Elsevier*, under license #4105390326337.
Chapter 6: Reproduced with permission from *Springer*, under license #4105390776646.
Chapter 7: Reproduced with permission from *Elsevier*, under license #4105390931355.
Chapter 8: Reproduced with permission from the *American Chemical Society*.

1. Solid-State Nuclear Magnetic Resonance Spectroscopy and Methods

Solid-state nuclear magnetic resonance (ssNMR) spectroscopy has become an indispensable technique for studying the atomic details of many diverse and interesting systems, from organic and inorganic compounds and materials, to polymers, to complex biomolecular systems. The hallmark of ssNMR, and where the technique outshines others, is the ability to characterize those systems that are amorphous or insoluble and thus would be difficult or impossible to study by other techniques. For example, solution NMR requires molecules that undergo rapid reorientation in solution in order to achieve narrow linewidths that yield detailed atomic information. X-ray crystallography, the gold standard for obtaining atomic-resolution information, requires well-ordered crystals, which are not attainable for all compounds or biological systems. Cryo-electron microscopy, while able to study many amorphous systems under near-native conditions, has only recently begun to achieve atomic resolution and requires cryogenic temperatures, which may perturb the systems under study. In the particular case of studying membrane proteins bound to lipid membranes, which is the focus of this thesis, ssNMR provides the best opportunity to gain detailed information on the conformation and dynamics of this important class of proteins in near-native lipid bilayer environments. The remainder of this chapter aims to provide a brief introduction to the ssNMR concepts and methods used throughout my graduate studies of the influenza M2 protein.

We first start with a very brief description of the basic NMR phenomenon. When a single nucleus is placed in a static magnetic field (B_0), the nuclear spin's magnetic dipole moment will align itself parallel to the direction of the external magnetic field. If a sample containing many nuclei in random orientations is introduced to the magnetic field, under the same conditions, the individual magnetic dipole moments of the atomic nuclei will not all align themselves with the external field due to thermal fluctuations. Instead, at equilibrium, the sum of all magnetic moments in the sample will result in a net magnetic moment parallel to the external field. The magnitude of this bulk magnetic moment (M_0), also called the magnetization, is proportional to:

$$M_0 \propto \gamma(\frac{\hbar B_0}{kT})$$

This bulk magnetization vector will experience a torque by the external magnetic field, and will precess around B_0. The characteristic frequency at which the magnetization vector precesses is $\omega_0 = -\gamma B_0$, known as the Larmor frequency, and depends on the strength of the external magnetic field and the nuclei-dependent gyromagnetic ratio γ. In order to manipulate the bulk magnetization vector and obtain NMR spectra that provide information on the atomic environment in a molecule, we perturb the system by applying radio-frequency (rf) pulses of varying amplitude (B_1) close to the Larmor frequency ω_0 of the nuclei of interest, and measure the response.

The full NMR interaction Hamiltonian ($\hat{H}$) describes the contributions from all electronic and dipolar interactions between nuclear spin magnetic moments:

$$\hat{H} = \hat{H}_0 + \hat{H}_{CS} + \hat{H}_{IS} + \hat{H}_{II} + \hat{H}_J + \hat{H}_Q$$

The total Hamiltonian includes contributions from the Zeeman (H_0) interaction between the nuclear spin and the static magnetic field, the chemical shift interaction (H_{CS}), heteronuclear dipolar coupling (H_{IS}), homonuclear dipolar coupling (H_{II}), J-coupling (H_J), and quadrupolar (H_Q) interactions. The specific dependences of these Hamiltonians are summarized in **Table 1.1**.

Table 1.1 NMR Spin Interaction Hamiltonians in the Solid-State

Interaction	Hamiltonian
Zeeman	$\hat{H}_0 = \hbar\omega_0\hat{I}_z$
Chemical Shift	$\hat{H}_{CS} = \hbar\omega_0\sigma_{zz}^{LF}\hat{I}_z$
Heteronuclear Dipolar Coupling	$\hat{H}_{IS} = -\frac{\hbar\mu}{4\pi}\frac{\gamma_1\gamma_2}{r^3}\frac{1}{2}(3cos^2\theta - 1)\,2\hat{I}_z\hat{S}_z$
Homonuclear Dipolar Coupling	$\hat{H}_{II} = -\frac{\hbar\mu}{4\pi}\frac{\gamma^2}{r^3}\frac{1}{2}(3cos^2\theta - 1)\left(3\hat{I}_{1z}\hat{I}_{2z} - \hat{\vec{I}}_1 \cdot \hat{\vec{I}}_2\right)$
Quadrupolar Coupling	$\hat{H}_Q = \frac{eQ}{2I(2I-1)\hbar}\hat{\vec{I}} \cdot \hat{\vec{V}} \cdot \hat{\vec{I}}$
J (Scalar) Coupling	$\hat{H}_J = 2\pi J_{12}\hat{I}_1\hat{I}_2$

Each of these interactions can provide a large amount of information about the molecules under observation. In studying biological macromolecules, the chemical shift interaction provides a robust and clear indication of the local electronic environment of different residues in a protein, leading to information about the secondary structure.[1,2] Heteronuclear dipolar couplings provide through-space distance restraints that reveal the tertiary and quaternary structures of proteins.

Quadrupolar nuclei, such as deuterium, can be utilized to give detailed information on molecular orientations and dynamics. The scalar interaction is very important in biomolecular structure determination by solution NMR, but it is very weak in comparison to the other interactions in the solid state ($<10^2$ Hz for J-couplings, and up to 10^5 Hz for chemical shift and dipolar couplings, and even larger for quadrupolar couplings), and thus is more difficult to utilize in ssNMR.

1.1 Editing of Complex Biomolecular NMR Spectra

The static ssNMR spectra of powder samples are characterized by inherently broad lineshapes due to orientation-dependent nuclear spin interactions and frequencies. Chemical shift anisotropy (CSA), dipolar couplings, and quadrupolar couplings all lead to broad "powder patterns" under the static condition. In solution NMR, these interactions are averaged by rapid isotropic tumbling, thus giving sharp spectral lines, but in the solid state these anisotropic interactions must be actively averaged out by spinning the sample at the "magic angle" to achieve narrow spectral linewidths. The "magic angle" is $54.7° = \cos^{-1}\left(1/\sqrt{3}\right)$ between the static magnetic field (B_0) and the rotational axis of the sample rotor (**Fig. 1.1**). MAS is the basis for the work described in this thesis, to achieve chemical shift resolution that allows for assignment of complex spectra.

A large amount of information can be extracted from one dimensional (1D) ^{13}C and ^{15}N MAS spectra of peptides and proteins, including conformational information via chemical shifts and dipolar couplings, and information on molecular motion. The simplest NMR experiment to observe these nuclei involves a 90° pulse to generate transverse magnetization (a.k.a. direct polarization or direct excitation) and then detects the resulting signal oscillation under its characteristic chemical shift frequency as it decays to equilibrium (**Fig. 1.2a**). However, depending on the sample conditions, many time-consuming transients of this experiment may need to be collected to obtain a satisfactory signal-to-noise ratio, due to the low gyromagnetic ratios of ^{13}C and ^{15}N spins and the low natural abundance of ^{13}C (~1%) and ^{15}N (~0.4%).

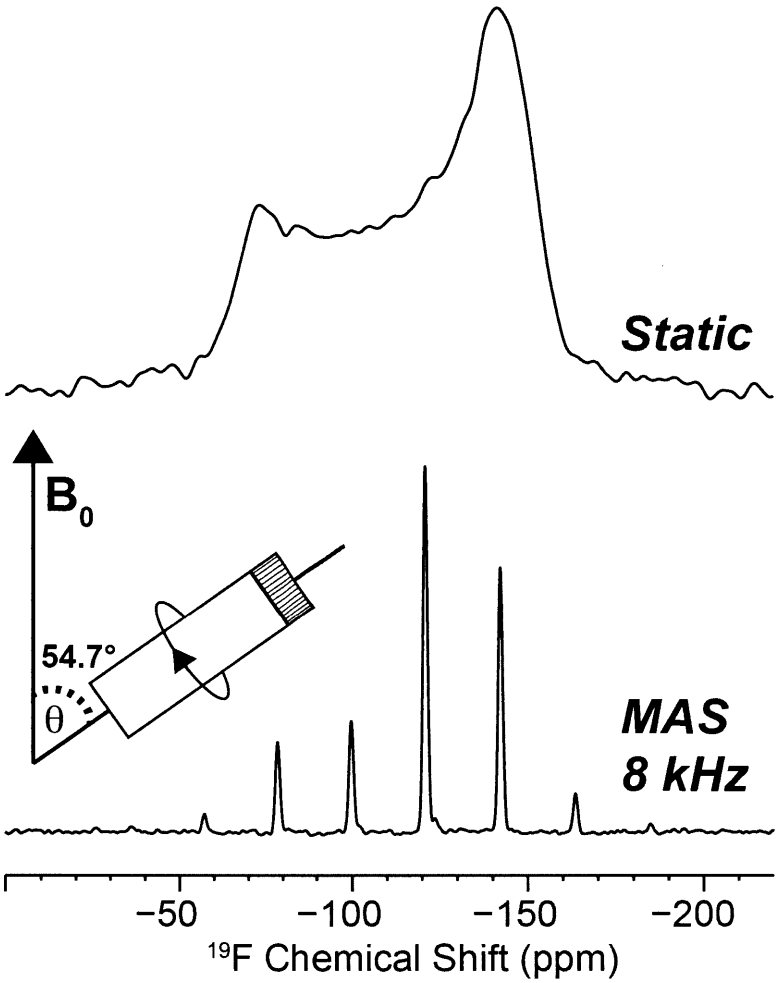

Figure 1.1 Static versus magic-angle spinning ^{19}F CP spectra of 5-^{19}F-Tryptophan. The broad powder pattern of the static spectrum reflects the ^{19}F chemical shift anisotropy, while the MAS spectrum shows the isotropic chemical shift (~ -120 ppm) flanked by spinning side-bands spaced apart by 8 kHz due to incomplete averaging out of the CSA interaction.

One method to boost spectral sensitivity relies on polarization transfer from nuclei with a large gyromagnetic ratio. This is known as cross-polarization (CP),[3-5] where the source nuclei (I) and sink nuclei (S) are mutually spin-locked in the transverse plane (**Fig. 1.2b**) with rf-amplitudes that satisfy $\omega_{1I} + \omega_{1S} = n\omega_r$.[6,7] CP is used extensively in biomolecular ssNMR to increase the polarization of low-gamma nuclei such as ^{13}C and ^{15}N by transfer from the high-gamma ^{1}H, which are abundant in biological samples. When the number of ^{1}H spins far exceeds the number of low-gamma X-spins, the polarization of the X-spin is enhanced by a factor of γ_H/γ_X, which is 4-fold for ^{13}C NMR and 10-fold for ^{15}N NMR.

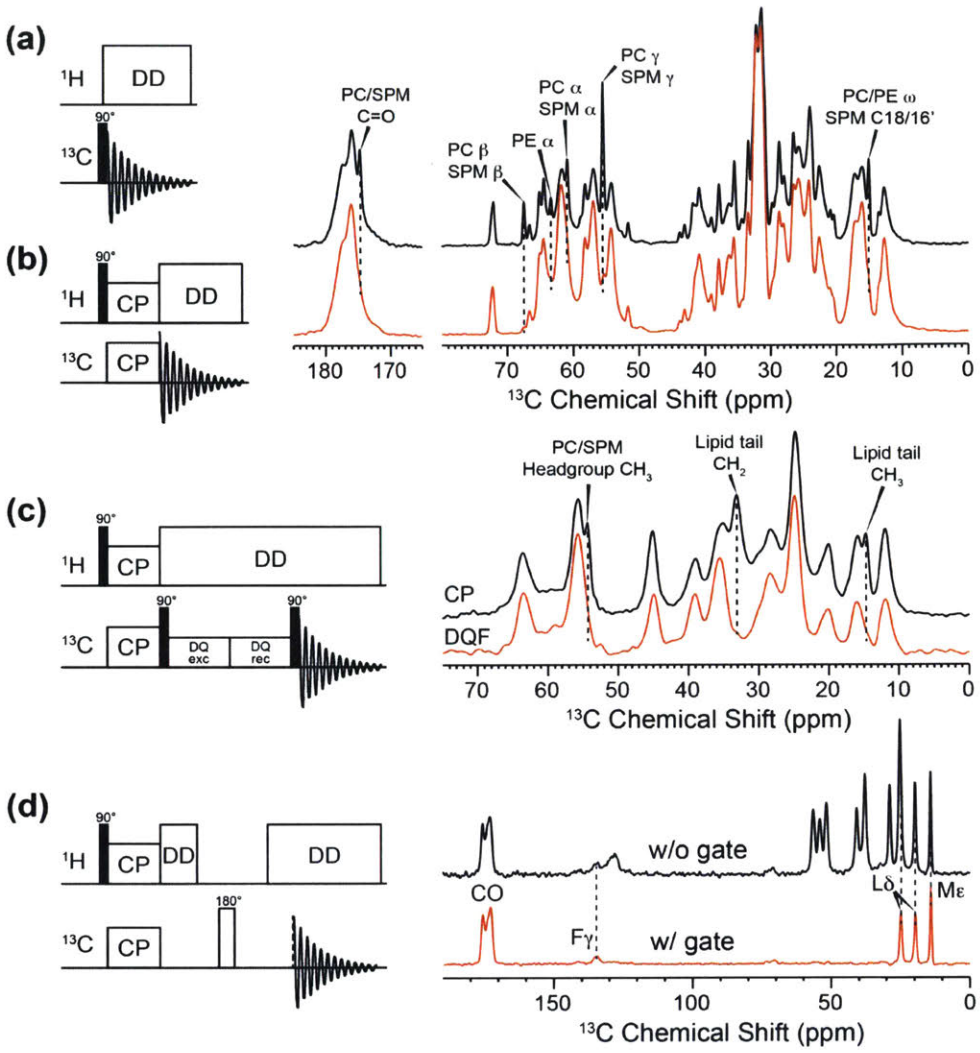

Figure 1.2 Pulse sequence diagrams and example spectra of (a) direct-polarization (DP), (b) cross-polarization (CP), (c) double-quantum filtered CP via SPC-5 (DQF), and (d) CP with gated-decoupling. (a,b) The DP (*black*) and CP (*red*) spectra show the BM2(1-33) peptide in a lipid bilayer. The mobile lipid peaks are enhanced in (a) over (b) at 303 K. (c) The DQF spectra filters out the natural abundance lipid peaks, leaving only ^{13}C-labled sites in the S31N AM2 channel. (d) The model peptide MLF shows that only the non-protonated carbonyl and Phe Cγ are retained after gating; the Leu and Met methyl groups are not fully removed because of ^{13}C-^{1}H dipolar averaging due to methyl rotation.

Isotopic enrichment of ^{13}C and ^{15}N nuclei in a sample provides a means to enhance the signal of the desired sample components (e.g. protein) while leaving other components at natural abundance (e.g. lipids). When studying peptides produced using synthetic chemistry, it is straightforward to selectively label only specific residues in the peptide.[8,9] However, synthesis

yields are only efficient for peptides or proteins up to ~50 amino acids in length. Bacterial protein expression is a robust and cost-effective way to produce isotopically enriched proteins in sufficient quantities for NMR. It becomes more difficult, however, to label specific residues when studying recombinantly expressed proteins, but strategies have been developed for amino-acid-type specific labeling and partial labeling by using selectively labeled ^{13}C-glucose, ^{13}C-pyruvate, or ^{15}N-ammonium chloride in the expression media.[10-14] With isotopic enrichment and CP, the time it takes to measure spectra of high sensitivity is greatly reduced, and many interesting experiments can be carried out to answer important biological questions.

In some cases, simple 1D CP spectra are already sufficient for assigning chemical shifts of a protein based on characteristic amino acid chemical shifts, but further spectral modification or "editing" may be needed to fully extract out the desired information when many resonances with similar chemical shifts overlap. This is often the case in ^{13}C spectra of peptides and proteins in lipid bilayers, where several amino acid residue types have similar ^{13}C chemical shifts while also overlapping with natural abundance ^{13}C resonances of lipids and cholesterol. Direct polarization (DP) and CP provide a level of spectral modification: DP preferentially detects mobile or dynamic species in a sample, while CP relies on coherent dipolar couplings for polarization transfer and therefore preferentially detects rigid species. So, in the case of the lipid-bound membrane protein, if the protein is in a more rigid state than its lipid environment, then one can enhance the protein resonances more than the lipids via CP. However, different dynamics between the protein and its surroundings is not always possible, so other spectral editing techniques are desirable.

To remove the unwanted natural abundance lipid signals from a ^{13}C spectrum of a lipid-bound membrane protein sample, a ^{13}C-^{13}C double-quantum filter (DQF) can be employed (**Fig. 1.2c**). A common DQ filter used throughout this work is based on the Supercycled Permutationally Offset-Stabilized C5 (SPC-5) recoupling sequence.[15] A first block SPC-5 sequence excites the double-quantum (DQ) coherence, and is followed by a second block of phase-shifted SPC-5 sequence to reconvert the DQ coherence back to observable single-quantum (SQ) coherence. DQ coherence forms most readily between directly bonded ^{13}C nuclei because of their strong dipolar couplings, thus the main ^{13}C signals that are selected by the DQ filter come from ^{13}C-enriched

protein. The natural abundance lipid ^{13}C signals are filtered out, since the statistical likelihood of two ^{13}C spins being directly bonded is extremely low (0.01%).

A second method of spectral editing relies on gated ^{1}H decoupling.[16] In a normal 1D DP or CP experiment, ^{1}H decoupling is applied during detection to average out the heteronuclear dipolar interaction between the detected nuclei and protons (**Fig. 1.2b**). When this decoupling is turned off for part of the detection period (**Fig. 1.2d**), the heteronuclear dipolar interaction reduces the spectral intensity of ^{13}C spins that are strongly coupled to protons. In practice, this means that only non-protonated ^{13}C spins and ^{13}C spins with motionally reduced ^{1}H-^{13}C couplings such as methyl groups survive the gated decoupling and their signals will remain in the spectrum. The gated decoupling is usually implemented with a Hahn-echo to refocus the chemical shift evolution of the observed spin. These simple spectral editing methods can be a powerful tool to simplify complex spectra. Other more advanced spectral editing techniques are reviewed and developed in the work shown in Chapter 8.

1.2 2D Homonuclear and Heteronuclear Correlation Spectroscopy

One dimensional (1D) NMR spectra can provide valuable chemical shift information, yet it is often necessary to include a second (or even third) dimension in order to better resolve resonances with similar chemical shifts. A second spectral dimension also provides information on bonding and spatial arrangement of atoms. In this thesis, several two-dimensional (2D) homonuclear and heteronuclear correlation techniques have been utilized to obtain well-resolved spectra that aid in determining the secondary structure and three-dimensional structures of biomolecules. The workhorse of these correlation techniques is the ^{13}C-^{13}C proton-driven spin-diffusion (PDSD) experiment,[17,18] and its modified version, ^{13}C-^{13}C dipolar-assisted rotational-resonance (DARR) (**Fig. 1.3**).[19] In the PDSD experiment (**Fig. 1.3a**), the ^{13}C polarization, generated by CP from ^{1}H or by DP, evolves under the chemical shift interaction during the t_1 period. A variable period of ^{13}C spin diffusion follows (t_{mix}), which transfers ^{13}C magnetization through space, and the experiment finishes with ^{13}C detection during the t_2 period. By varying the mixing time (t_{mix}), different distances between ^{13}C spins can be probed. By applying weak rf-irradiation on the ^{1}H channel during the mixing time at an amplitude equal to the spinning

frequency ($\omega_1 = \omega_r$), the DARR experiment (**Fig. 1.3b**) recouples the ^{13}C-^{1}H dipolar interaction, which broadens the ^{13}C lines, and allows for increased spectral overlap between two nearby ^{13}C spins, which speeds up ^{13}C-^{13}C polarization transfer. Short mixing times (typically <100 ms) will mostly result in intramolecular correlations, while longer mixing times (typically >100 ms) yield inter-molecular correlations.

Utilizing the symmetry-based SPC-5 sequence[15] introduced previously, the homonuclear ^{13}C-^{13}C dipolar interaction can be actively recoupled and used for polarization transfer. When the SPC-5 sequence is used in this manner, the resulting 2D ^{13}C-^{13}C correlation spectrum retains mainly one-bond correlations, and is free from natural abundance signals along the diagonal (**Fig. 1.3c**). The SPC-5 sequence requires relatively slow spinning speeds, since the rf-amplitude of the C5 symmetry block needs to be matched to 5 times the MAS rate, while ^{1}H decoupling is optimal at three-times the ^{13}C rf field. Many other homonuclear recoupling sequences have been developed for moderate to fast MAS, such as RFDR,[20] DRAMA,[21] HORROR,[22] PAR,[23] PARIS,[24] and CORD[25], which have varying matching conditions. They were not utilized in this thesis and are not discussed further.

The SPC-5 sequence can also be used to obtain 2D ^{13}C-^{13}C dipolar INADEQUATE spectra, where the indirect dimension encodes the sum chemical shift of the two carbons while the direct dimension detects the SQ ^{13}C chemical shift.[26] After a CP period to polarize the ^{13}C spins, ^{13}C magnetization is flipped along the z-direction for a period of DQ excitation using the SPC-5 sequence. This is followed by ^{13}C chemical shift evolution. The ^{13}C-^{13}C DQ coherence is then converted back to SQ coherence for detection (**Fig. 1.3d**). The resulting spectrum correlates the SQ ^{13}C chemical shift of one spin with its directly bonded neighbor at the sum of the two individual SQ ^{13}C chemical shifts. When the DQ excitation and reconversion times are kept short, this allows for the unambiguous assignment of one-bond correlations.

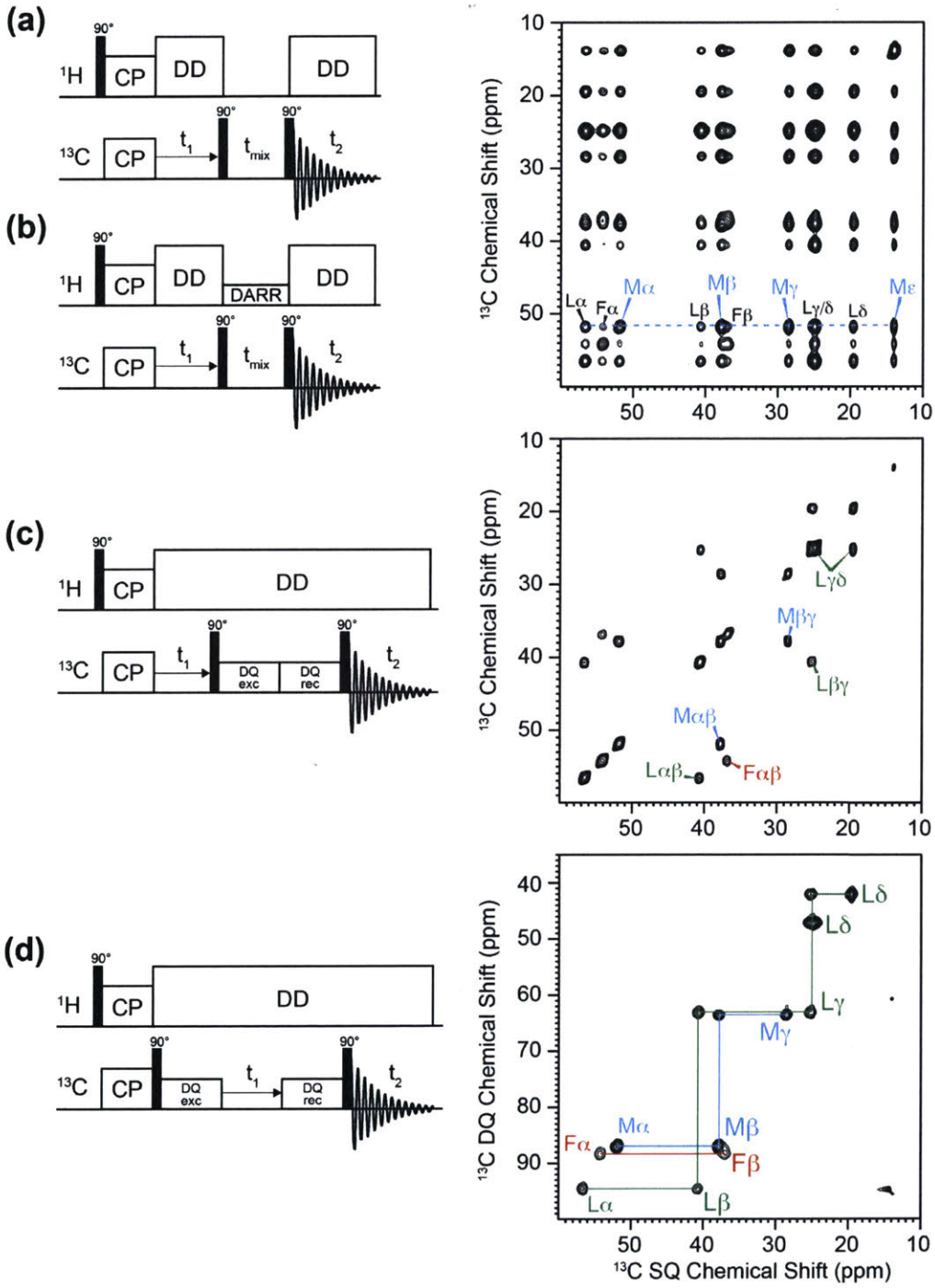

Figure 1.3 Two-dimensional ^{13}C-^{13}C correlation pulse sequences and representative spectra. (a) Proton-Driven Spin-Diffusion (PDSD) and (b) Dipolar-Assisted Rotational-Resonance (DARR) provide through space correlations via homonuclear ^{13}C spin-diffusion. (c) 2D ^{13}C-^{13}C DQ filtered correlation via SPC-5 dipolar recoupling. (d) 2D ^{13}C dipolar-INADEQUATE providing double-quantum to single-quantum chemical shift correlation. Representative spectra of the model peptide MLF show long-range inter-molecular correlations (a) and one-bond intra-molecular correlations (c) and (d).

Two-dimensional heteronuclear correlations (HETCOR) also provide important information on the conformation and topology of peptides and proteins. In this thesis, two HETCOR techniques have been heavily utilized. The first is a ^{15}N-^{13}C HETCOR experiment that utilizes a REDOR period to transfer polarization between ^{15}N and ^{13}C spins.[27] The REDOR sequence will be explored in more detail in the next section, but will be explained briefly here in the context of the HETCOR experiment. After an initial period of ^{1}H-^{13}C CP, a series of ^{15}N 180° pulses spaced every half-rotor period interrupts the refocusing of the ^{13}C-^{15}N dipolar interaction by MAS (**Fig. 1.4a**). This creates anti-phase ^{13}C magnetization, which is switched to anti-phase ^{15}N magnetization in the middle of the experiment by a pair of 90° pulses in order to encode the ^{15}N chemical shift. After encoding, the magnetization is switched back to anti-phase ^{13}C, and a second REDOR period is used to convert the ^{13}C coherence to in-phase SQ coherence for detection. A more straightforward way of obtaining the same ^{15}N-^{13}C HETCOR spectra involves a ^{15}N-^{13}C CP period, but puts a significant amount of strain on the probe due to the long spin-lock times needed for ^{15}N-^{13}C CP.

The second correlation technique is the versatile ^{1}H-^{13}C HETCOR experiment,[28-30] used in this thesis to probe water-protein interactions in various influenza M2 proton channels. This experiment starts out with a ^{1}H T_2 filter (**Fig. 1.4b**), in order to differentiate ^{1}H magnetization between water, peptide, and lipids in a hydrated membrane sample. By cooling the sample slightly below the membrane phase-transition temperature, the peptide and lipids are rigid with short ^{1}H T_2 relaxation times, while water remains mobile with much longer ^{1}H T_2 relaxation times. The total T_2 filter time is chosen to be longer than the peptide ^{1}H T_2, so that it relaxes back to equilibrium and is not observed. The T_2 filter is followed by ^{1}H chemical shift evolution, and then the ^{1}H magnetization is allowed to spin diffuse to nearby protons. A short ^{1}H-^{13}C CP period transfers magnetization to nearby ^{13}C spins for detection. When carried out in this 2D manner, the ^{1}H-^{13}C HETCOR experiment provides information on the peptide proximity to water and lipids, separated by their characteristic ^{1}H chemical shifts, and is able to probe the time-dependent spin-diffusion buildup of ^{1}H magnetization.

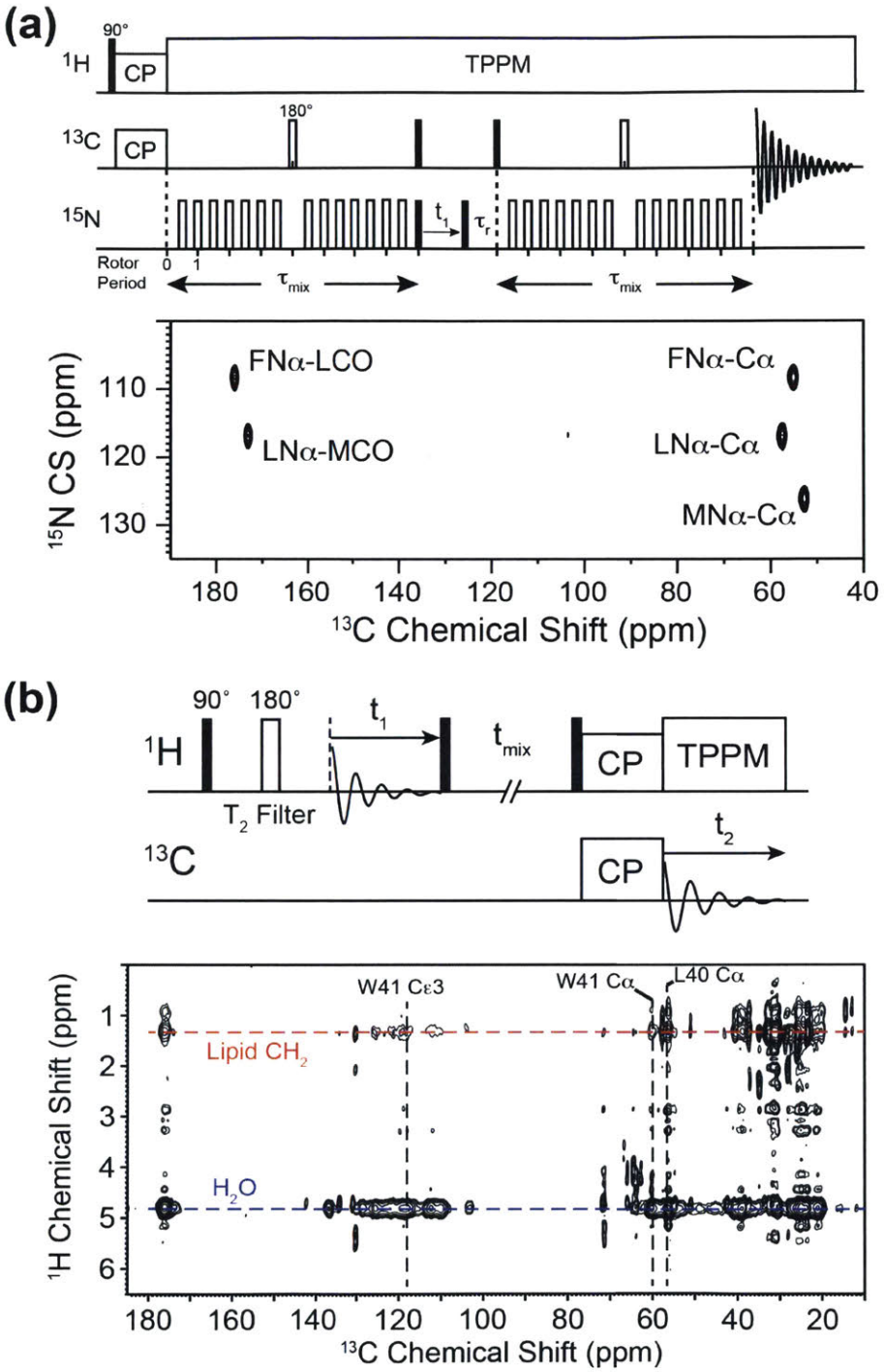

Figure 1.4 Two-dimensional heteronuclear correlation techniques. (a) ^{15}N-^{13}C HETCOR via a REDOR based sequence (*top*) and spectrum of MLF (*bottom*). (b) ^{1}H-^{13}C T_2-filtered HETCOR (*top*) and spectrum of the membrane bound AM2 proton channel (*bottom*), showing correlations between the peptide and lipids (*red*) or water (*blue*).

1.3 Distance Determination Using REDOR and CODEX

Up to this point, the ssNMR methods described have primarily been used to provide detailed chemical shift information, which gives insight into the local structure and conformation of proteins. This is very useful in determining protein backbone conformation, i.e. α-helix, β-sheet, or random coil propensities, but is limited in its ability to provide tertiary structure and quaternary oligomerization information. Two techniques fill this gap: the REDOR experiment[31] provides long-range heteronuclear distance information, while the CODEX experiment[32] provides homonuclear distance information. In this thesis work, these two methods have been used with site-specific ^{19}F labeling, taking advantage of its high gyromagnetic ratio, to provide targeted long-range distance constraints to determine sidechain conformations of functionally important residues in Chapter 3. REDOR has also been utilized in a more qualitative manner to assess the binding site of ^{2}H-labeled drug molecules in the M2 proton channel in Chapter 4.

1.3.1 Rotational-Echo Double-Resonance

Rotational-Echo Double-Resonance (REDOR) was developed by Schaffer and Gullion to recouple the heteronuclear dipolar couplings that are spun out by MAS, and to quantify that coupling.[31,33] As shown in **Table 1.1**, the truncated heteronuclear dipolar coupling Hamiltonian is of the form $\widehat{H}_{IS} = \omega_{IS} 2\hat{I}_z\hat{S}_z$, where ω_{IS} contains the spatial information, including the magnitude of the dipolar coupling between two spins, which is proportional to the nuclear gyromagnetic ratios and the internuclear distance. Under MAS, this Hamiltonian becomes time dependent, with $\widehat{H}_{IS}(t) = \omega_{IS}(t) 2\hat{I}_z\hat{S}_z$, and

$$\omega_{IS}(t) = -\frac{\hbar\mu}{4\pi}\frac{\gamma_1\gamma_2}{r^3}\frac{1}{2}\left(\sin^2\beta\cos 2(\alpha+\omega_r t) - \sqrt{2}\sin 2\beta\cos(\alpha+\omega_r t)\right).$$

The α and β in this equation refer to the azimuthal and polar angles, respectively, between the internuclear vector and the rotational axis, while ω_r is the MAS frequency. Under a control REDOR experiment (S_0, no pulses on the non-observed spin), the heteronuclear coupling Hamiltonian will average to zero over one rotor period:

$$\int_0^{t_r} \widehat{H}_{IS}(t)\,dt = \int_0^{t_r/2} \widehat{H}_{IS}(t)\,dt + \int_{t_r/2}^{t_r} \widehat{H}_{IS}(t)\,dt = 0.$$

Rewritten in another way, we can define the phase accumulation for each half rotor period as $\phi = \int_0^{t_r/2} \omega_{IS}(t)\,dt$, and then $\phi_{0\to t_r/2} = -\phi_{t_r/2\to t_r}$, such that the total magnitude of the accumulated phase vanishes for the S_0 experiment.[33]

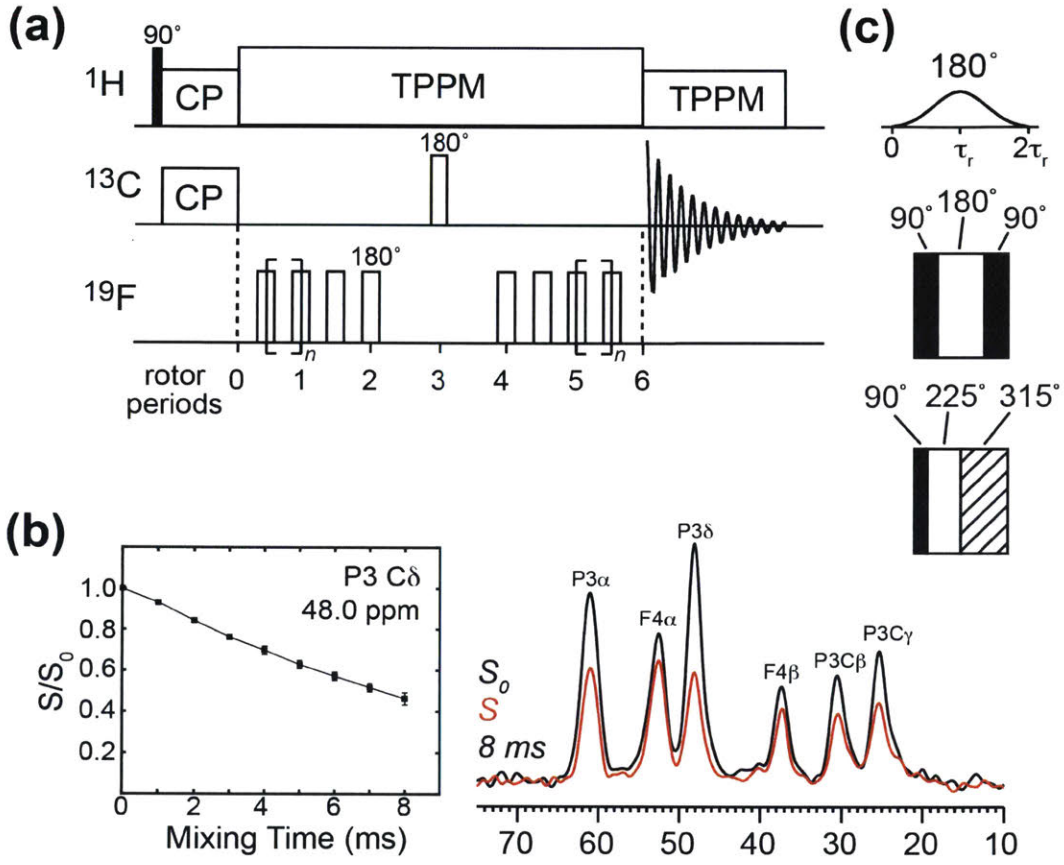

Figure 1.5 ^{13}C-^{19}F heteronuclear distance measurement using the Rotational-Echo Double-Resonance (REDOR) experiment. (a) REDOR pulse sequence, showing the π-pulse train on the non-observe ^{19}F channel used to recouple the ^{19}F-^{13}C dipolar interaction in the *S* experiment. The S_0 experiment omits these π-pulses. (b) Time-dependent S/S_0 intensity decay (*left*), extracted from the ratio of intensities of a control (*black*) and dephased (*red*) spectrum. (c) A soft Gaussian refocusing pulse can be used in place of the hard-180° pulse on the ^{13}C channel to remove ^{13}C-^{13}C J-coupling effects (*top*); two different composite π-pulses have been used on the ^{19}F channel.

Now if the averaging of the heteronuclear coupling interaction is interrupted by a 180° pulse on every half-rotor period (S, **Fig. 1.5a**), the relative sign of the phase accumulation ϕ in the second half of a rotor period can be flipped, and no longer averages to zero, with the total phase accumulation after one rotor period expressed as $\phi = \frac{\lambda}{\pi}\sqrt{2}\sin 2\beta \sin\alpha$. This non-zero phase accumulation causes incomplete refocusing of the magnetization, resulting in a time-dependent reduction of the spectral intensity that is proportional to the heteronuclear dipolar coupling. REDOR experiments are carried out in pairs, with a control S_0 experiment without dephasing pulses and a S experiment with dephasing pulses, in order to remove contributions to spectral dephasing that arise from T_2 relaxation during the experiment. A series of these paired S and S_0 experiments are run, each with a different dipolar recoupling period, and the normalized intensity (S/S_0) is plotted as a function of the recoupling time (**Fig. 1.5b**). The time-dependent S/S_0 intensity can be described by a universal REDOR curve, which is dependent on the unitless parameter $\lambda = Nt_rD$, where N is the number of rotor periods during the recoupling period, t_r is the rotor period, and D is the dipolar coupling. Taking into account all possible internuclear orientations in a solid-sample, with ϕ, α, and β defined above, the powder-averaged S/S_0 result is expressed as:[33]

$$S/S_0 = \frac{1}{2\pi}\int_0^{\pi}\int_0^{\pi}\cos(\phi)\sin\beta\, d\alpha\, d\beta.$$

Several factors can influence the successful recoupling of the dipolar interaction, and different modifications of the basic REDOR experiment help to compensate for these influences. Imperfections in the π-pulses of the dephasing spins, such as B_1 inhomogeneity or narrowband inversion, can lead to incomplete dephasing of the REDOR intensity and under-estimation of the dipolar coupling. These pulse imperfections can be compensated by using composite-pulse schemes[34] such as 90°-180°-90°,[35] or 90°-225°-315°,[36] to achieve B_1 homogeneity or broadband inversion, respectively (**Fig. 1.5c**). In uniformly ^{13}C labeled systems, ^{13}C-^{13}C scalar couplings can also modulate the spectral intensity and cause ambiguity in quantifying dipolar couplings. This J-couplings can be removed by utilizing a soft-Gaussian pulse in place of the short rectangular ^{13}C recoupling pulse in the middle of the experiment (**Fig. 1.5c**).[37,38]

While extraction of the dipolar coupling information can in principle be accomplished by fitting experimentally determined S/S_0 values to the analytical expression for the universal REDOR

curve, this expression inherently assumes the simple situation of two coupled spins free from any other interactions. As is often the case, there may be many dephasing spins coupled to a single spin under observation, leading to faster S/S_0 intensity decay and therefore a stronger apparent dipolar coupling. Computational packages for simulating ssNMR experiments have been developed, and can calculate REDOR dephasing in multi-spin systems and take into account other interactions that may affect the dephasing. In this thesis, two computational packages have been utilized at various points to simulate multi-spin REDOR curves of various systems: SIMPSON[39] and SPINEVOLUTION.[40] SIMPSON can handle REDOR calculations up to ~6 spins in a reasonable amount of time, and was sufficient for much of the needs of my research. SPINEVOLUTION provides both an improvement in computation time and ease-of use over SIMPSON, but was not further utilized due to monetization.

1.3.2 Centerband-Only Detection of Exchange

The Centerband-Only Detection of Exchange (CODEX) experiment was developed by Schmidt-Rohr and coworkers to probe slow reorientational motions in polymers through CSA recoupling.[32] Following a period of ^{1}H-X cross-polarization (where X is commonly ^{13}C or ^{19}F), a series of π-pulses spaced every half-rotor period is applied to the X-channel (**Fig. 1.6a**), in the same fashion as the REDOR π-pulse train, in order to recouple the CSA interaction. Afterwards, a variable spin-diffusion delay (t_{SD}) allows magnetization to exchange with chemically-equivalent but orientationally different spins. This is followed by a second π-pulse train, a second period of spin-diffusion called a "z-filter" (t_z), and finally detection. The CODEX experiments are also run in pairs, with a control (S_0) and dephased (S) experiments, to compensate for T_1 relaxation effects. Unlike the REDOR experiments, however, the π-pulse trains are present in both experiments. Instead, the lengths of the spin-diffusion and z-filter delays define the S_0 and S experiments. For S_0, the length of t_{SD} is kept short while t_z is long. In the S experiment the delay times are switched, with t_{SD} long and t_z short. The total time that the magnetization spends along the z-direction is kept constant between the two experiments (i.e. $t_{total} = t_{SD} + t_z$).

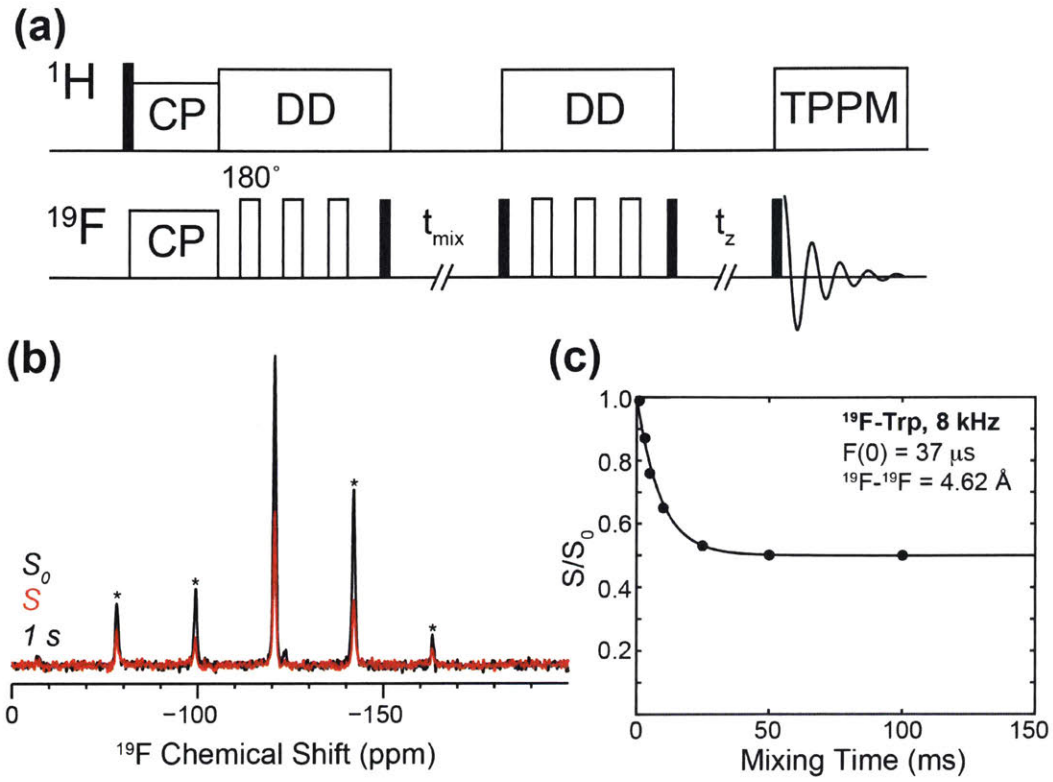

Figure 1.6 ^{19}F-^{19}F homonuclear distance determination using the Centerband-Only Detection of Exchange (CODEX) experiment. (a) CODEX pulse diagram. The total time magnetization is stored along the z-axis ($t_{total} = t_{mix} + t_z$) is kept constant between a control (S_0) and dephased (S) experiment. (b) Representative S_0 and S spectra of 5-^{19}F-Tryptophan at a mixing time of 1 s. (c) Time-dependent S/S_0 dephasing of 5-^{19}F-Tryptophan. The dephasing reaches an equilibrium value of ~0.5, reflecting that this model compound is a two-spin system.

The analysis of the CODEX recoupling periods follows the same outline as for REDOR dipolar recoupling, but focuses on the CSA interaction.[41,42] The chemical shift frequency under MAS can be expressed as:

$$\omega_{CS}(t) = \omega_{iso} + \frac{1}{2}\delta(3\cos^2\theta_r - 1 - \eta\sin^2\theta_r\cos 2\omega_r t)$$

where ω_{iso} is the isotropic chemical shift frequency, θ_r is the angle between B_0 and the rotor axis, and ω_r is the rotor spinning frequency. The chemical shift anisotropy parameter (δ) and asymmetry parameter (η) describe the shape of the chemical shift tensor (i.e. the electronic environment), and are defined as:

$$\delta \equiv \sigma_{zz}^{PAS} - \sigma_{iso}$$

$$\eta \equiv \frac{\sigma_{yy}^{PAS} - \sigma_{xx}^{PAS}}{\sigma_{zz}^{PAS} - \sigma_{iso}}.$$

Under MAS, the total phase accumulation during the CSA recoupling periods can be derived in an analogous fashion to that presented in the REDOR section, where the phase accumulations for the first and second CSA recoupling periods are equal but opposite in sign. So, in the CODEX control experiment (S_0), the magnetization is refocused and no loss of spectral intensity is observed (**Fig. 1.6b**). But, when spin-diffusion is allowed to occur between the two recoupling periods, magnetization exchanges with spins having a different CSA orientation relative to B_0. The CS frequency is now different during the second recoupling period and the magnetization is not fully refocused, resulting in a reduction of spectral intensity (S experiment).

While the original experiment was designed to probe slow motions, we instead focus on the rate of spin-diffusion as a probe of homonuclear distances, using a rate exchange matrix formalism.[43] The sample is frozen down to temperatures of ~235 K to remove molecular motions, so the observation of reduced spectral intensity comes only from spin-diffusion among like spins. The rate constant of spin-diffusion among some X-nuclei in the presence of ^{1}H can be approximated as:[18,43,44]

$$k_{ij} = \frac{\pi}{2}\omega_{ij}^2 F_{ij}(0)$$

where ω_{ij} is the spatial part of the homonuclear dipolar Hamiltonian. $F_{ij}(0)$ is the overlap integral that describes the probability of single-quantum transitions occurring at the same frequency for spins i and j. The value of F(0) depends on the single-quantum line shape, and will vary depending on nuclear spin (^{13}C or ^{19}F) and MAS frequency. Therefore it is necessary to determine F(0) experimentally using model compounds whose chemical structure is well defined. For ^{19}F we typically use 5-^{19}F-Tryptophan, whose crystal structure shows a nearest neighbor ^{19}F-^{19}F distance of 4.62 Å.[43,45] A series of CODEX experiments is collected, with an increasing spin-diffusion mixing time in different pairs of S and S_0 experiments. The normalized intensities S/S_0 are plotted as a function of mixing time, which decays to a value of 1/N, where N is the number of spins sharing the equilibrated magnetization (**Fig. 1.6c**). Given the labeling scheme of a sample, this

provides information on the oligomeric state of the system. To extract distance information, the time dependent S/S_0 decay is fit to calculations of the time-evolution of the magnetization during spin-diffusion:[43]

$$\frac{d\vec{M}(t)}{dt} = -\hat{K}\vec{M}(t)$$

where $\hat{K}$ is the exchange matrix, containing the rate constants k_{ij}, that describes the spin system. A more detailed description of the analysis of this time-evolution has been provided previously by our group, and a MATLAB based script is used for fitting CODEX data to extract distance information.[45]

1.4 Influenza M2 Proton Channels and Lipid Membrane Environments

The influenza virus is a negative-sense, single stranded RNA virus[46] that is responsible for seasonal epidemics, as well as global pandemics, which can lead to severe respiratory distress and even death.[47] Three strains of influenza exist (A, B, and C), however only A and B are responsible for infecting humans during flu seasons, with Influenza A being more prevalent than B (**Fig. 1.7**) (data publicly available from CDC FluView, www.cdc.gov/flu/weekly/). Out of the 11 proteins encoded by the influenza genome, the M2 protein is the lone ion channel in the virus. Matrix 2 (M2) is a ~100 amino acid (97 aa AM2, 109 aa BM2) protein, which assembles to form a tetrameric channel that selectively conducts protons into the virus interior. After a viral particle attaches to sialic acid receptors on the exterior of a host cell via its hemagglutinin (HA) proteins, the virus enters the cell through endocytosis (**Fig. 1.8**).[46] The pH of the endosome is acidic (~5), which activates the M2 channel and acidifies the interior of the virus. This acidification of the virus causes the viral membrane to fuse with the endosomal membrane, and the viral ribonucleoproteins to be released into the host cell. Besides proton conduction, the M2 protein plays a role the budding and membrane scission of new viral particles.[48] The small molecule drugs amantadine and rimantadine are known to act as antivirals against influenza infection, and target the AM2 protein but not the BM2 protein.[49] At the heart of all M2 proton channels are two residues: a His and a Trp spaced in a conserved HxxxW motif. Mutation of His abolishes the proton conduction of the channel,[50,51] while mutation of the Trp abolishes the channels ability to conduct protons uni-directionally.[52]

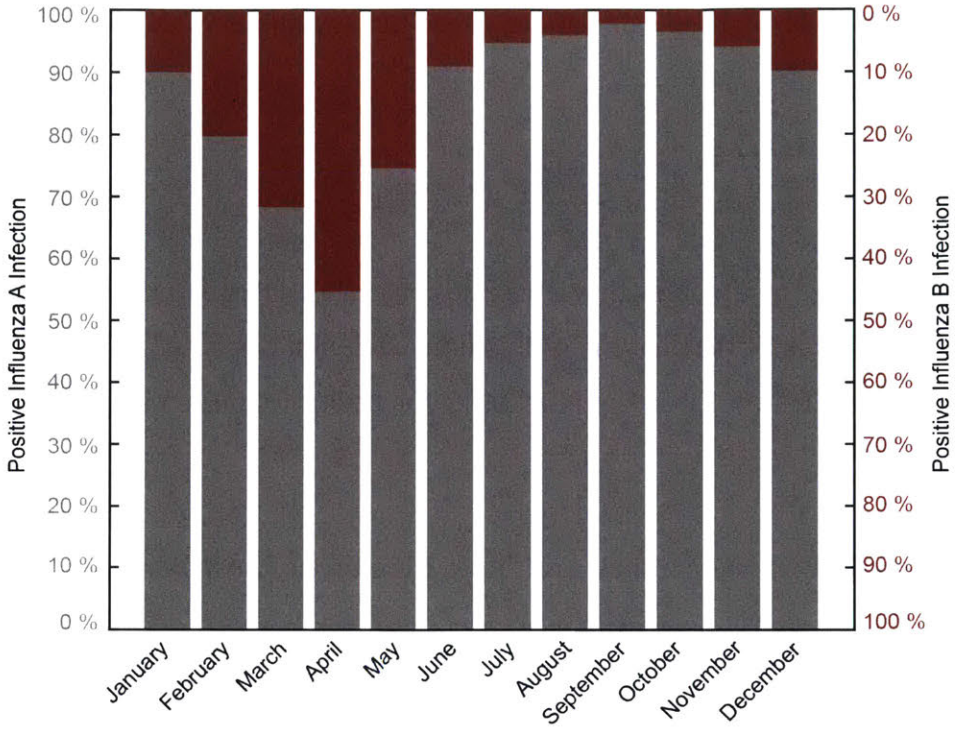

Figure 1.7 Average monthly incidences of positive type A (*gray*) or B (*red*) influenza infection in the USA, from the period of October 1997 to January 2015, as reported to the CDC-NREVSS (data publicly available from CDC FluView website). Influenza A is responsible for a majority of infections, but influenza B on average becomes more prevalent in the spring months.

Since the M2 proton channel is a transmembrane protein, solid-state NMR is well suited to study its conformation, dynamics, and underlying proton conduction mechanism in a native-like environment. Previous work in the Hong group has probed the conduction mechanism and membrane-bound conformation of the wild-type AM2 protein.[43,53-58] The work presented in this thesis has found that the underlying proton conduction mechanism is conserved amongst wild-type AM2, drug-resistant S31N AM2, and wild-type BM2 channels (see Chapter 2, 4, 8) and determined the gating mechanism of Trp in wild-type AM2 (Chapter 3), as well as water's interaction with the AM2 and BM2 channels (Chapter 5, 8).

The environment in which the M2 channel is reconstituted and studied plays an important role the observed conformation and dynamics,[59,60] and there are significant differences in the published structures of M2 determined in lipid-cubic phases (X-ray),[61] detergents (X-ray),[62,63]

detergent micelles (solution NMR),[64-66] and lipids (ssNMR).[57,67-69] The composition of eukaryotic cell membranes has been found to be comprised of ~64% glycophospholipids (PA/PC/PE/PG/PI/PS), ~28% sterols, and ~8% sphingolipids, while influenza viral particles were found to be enriched in sterols (~52%) and sphingolipids (~19%).[70,71]

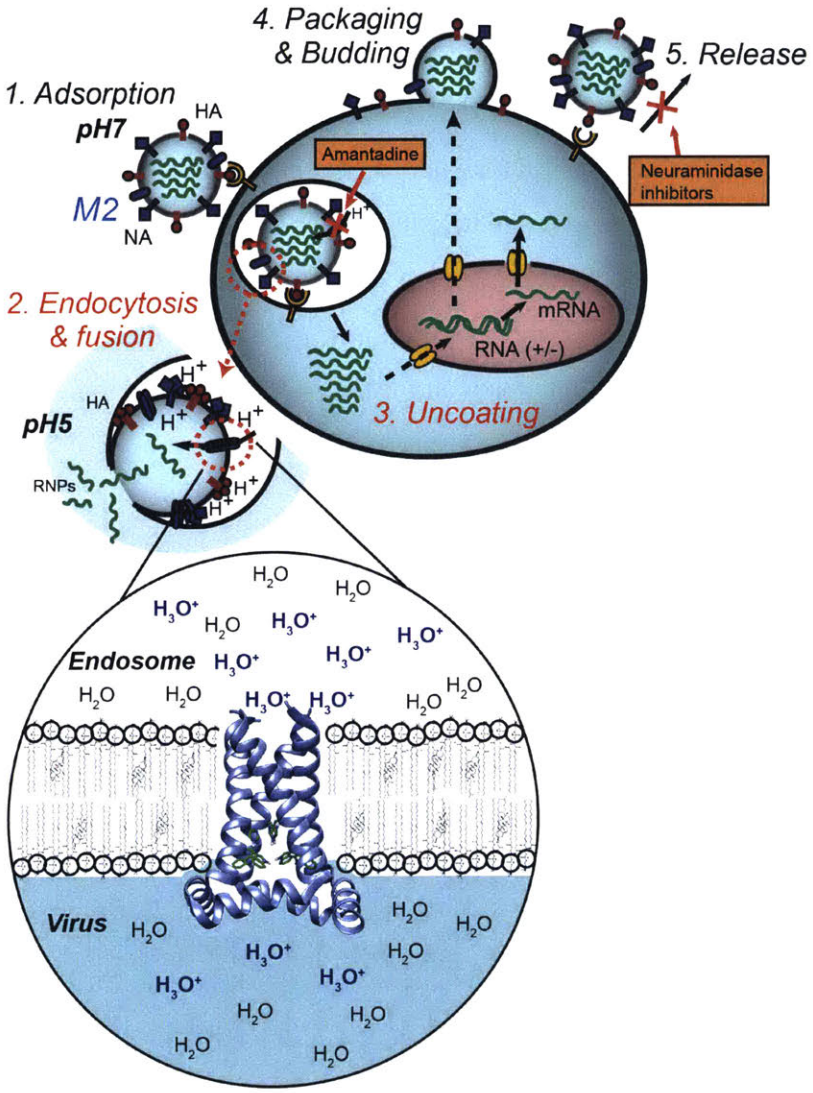

Figure 1.8 The influenza virus lifecycle. (*1*) The virus hemagglutinin attaches to a host cell via sialic acid receptors. (*2*) During endocytosis, the low pH environment triggers the M2 protein to shuttle protons into the virus interior, acidifying and causing the viral particle to release its ribonucleoproteins (vRNPs) into the host cell. (*3*) The vRNPs are transported further into the host cell, where the host machinery is used to produce new viral proteins. (*4*) The viral proteins and RNA are packaged into new particles at the host cell membrane, where the viral particle budding is partially mediated by the M2 protein. (*5*) Finally, the new viral particles are released from the host cell membrane.

With this in mind, our group has consistently studied the M2 channel in a lipid mixture that resembles these environments, and two membrane mimetics were developed.[72,73] The first, VM, is comprised of DPPC (1,2-dipalmitoyl-*sn*-glycero-3-phosphocholine), DPPE (1,2-dipalmitoyl-*sn*-glycero-3-phosphoethanolamine), SM (egg sphingomyelin), and Chol (cholesterol) at a molar ratio of 21:21:28:30%. This mixture uses lipids with a high average transition temperature (T_m ~50°C), and the presence of cholesterol broadens out this transition. The second, VM+, is comprised of POPC (1-palmitoyl-2-oleoyl-*sn*-glycero-3-phosphocholine), POPE (1-palmitoyl-2-oleoyl-*sn*-glycero-3-phosphoethanolamine), SM, and Chol at a molar ratio of 25.6 : 25.6 : 25.6 : 23%. The lipids in this mixture have a lower average transition temperature (T_m ~20°C) than VM, due to the unsaturated oleyol chains. Both lipid mixtures serve as approximate mimics of the eukaryotic and viral membranes, include the important sphingolipids and sterols that are present in the native membrane environments of the M2 channel, and were used throughout this thesis.

1.5 References

[1] C. Ye, R. Fu, J. Hu, L. Hou and S. Ding. "Carbon-13 Chemical Shift Anisotropies of Solid Amino Acids." *Magn. Reson. Chem.* **1993**, 31, 699–704.

[2] Y. Wang. "Secondary Structural Effects on Protein NMR Chemical Shifts." *J. Biomol. NMR* **2004**, 30, 233–244.

[3] S. R. Hartmann and E. L. Hahn. "Nuclear Double Resonance in the Rotating Frame." *Phys. Rev.* **1962**, 128, 2042–2053.

[4] A. Pines, M. G. Gibby and J. S. Waugh. "Proton-Enhanced NMR of Dilute Spins in Solids." *J. Chem. Phys.* **1973**, 59, 569–590.

[5] E. O. Stejskal, J. Schaefer and J. S. Waugh. "Magic-Angle Spinning and Polarization Transfer in Proton-Enhanced NMR." *J. Magn. Reson.* **1977**, 28, 105–112.

[6] M. Sardashti and G. E. Maciel. "Effects of Sample Spinning on Cross Polarization." *J. Magn. Reson.* **1987**, 72, 467–474.

[7] B. H. Meier. "Cross Polarization Under Fast Magic Angle Spinning: Thermodynamical Considerations." *Chem. Phys. Lett.* **1992**, 188, 201–207.

[8] R. B. Merrifield. "Solid Phase Peptide Synthesis. I. The Synthesis of a Tetrapeptide." *J. Am. Chem. Soc.* **1963**, 85, 2149–2154.

[9] G. B. Fields and R. L. Noble. "Solid Phase Peptide Synthesis Utilizing 9-fluorenylmethoxycarbonyl Amino Acids." *Int. J. Pept. Protein Res.* **1990**, 35, 161–214.

[10] M. Hong and K. Jakes. "Selective and Extensive ^{13}C Labeling of a Membrane Protein for Solid-State NMR Investigation." *J. Biomol. NMR* **1999**, 14, 71–74.

[11] P. Lundström, K. Teilum, T. Carstensen, I. Bezsonova, S. Wiesner, D. F. Hansen, T. L. Religa, M. Akke and L. E. Kay. "Fractional ^{13}C Enrichment of Isolated Carbons using [1-^{13}C]- or [2-^{13}C]-Glucose Facilitates the Accurate Measurement of Dynamics at Backbone Cα and Side-Chain Methyl Positions in Proteins." *J. Biomol. NMR* **2007**, 38, 199–212.

[12] A. L. Lee, J. L. Urbauer and A. J. Wand. "Improved Labeling Strategy for ^{13}C Relaxation Measurements of Methyl Groups in Proteins." *J. Biomol. NMR* **1997**, 9, 437–440.

[13] F. Castellani, B. van Rossum, A. Diehl, M. Schubert, K. Rehbein and H. Oschkinat. "Structure of a Protein Determined by Solid-State Magic-Angle-Spinning NMR Spectroscopy." *Nature* **2002**, 420, 98–102.

[14] V. A. Higman, J. Flinders, M. Hiller, S. Jehle, S. Markovic, S. Fiedler, B. J. van Rossum and H. Oschkinat. "Assigning Large Proteins in the Solid State: A MAS NMR Resonance Assignment Strategy Using Selectively and Extensively ^{13}C-Labelled Proteins." *J. Biomol. NMR* **2009**, 44, 245–260.

[15] M. Hohwy, C. M. Rienstra, C. P. Jaroniec and R. G. Griffin. "Fivefold Symmetric Homonuclear Dipolar Recoupling in Rotating Solids: Application to Double-Quantum Spectroscopy." *J. Chem. Phys.* **1999**, 110, 7983–7992.

[16] S. J. Opella and M. H. Frey. "Selection of Non-Protonated Carbon Resonances in Solid-State Nuclear Magnetic Resonance." *J. Am. Chem. Soc.* **1979**, 101, 5854–5856.

[17] N. M. Szeverenyi, M. J. Sullivan and G. E. Maciel. "Observation of Spin Exchange by Two-Dimensional Fourier Transform ^{13}C Cross Polarization-Magic-Angle Spinning." *J. Magn. Reson.* **1982**, 47, 462–475.

[18] B. H. Meier. "Polarization Transfer and Spin Diffusion in Solid-State NMR." *Adv. Magn. Opt. Reson.* **1994**, 18, 1–116.

[19] K. Takegoshi, S. Nakamura and T. Terao. "^{13}C–^{1}H Dipolar-Assisted Rotational Resonance in Magic-Angle Spinning NMR." *Chem. Phys. Lett.* **2001**, 344, 631–637.

[20] A. E. Bennett, R. G. Griffin, J. H. Ok and S. Vega. "Chemical Shift Correlation Spectroscopy in Rotating Solids: Radio Frequency-Driven Dipolar Recoupling and Longitudinal Exchange." *J. Chem. Phys.* **1992**, 96, 8624-8627.

[21] R. Tycko and G. Dabbagh. "Measurement of Nuclear Magnetic Dipole-Dipole Couplings in Magic Angle Spinning NMR." *Chem. Phys. Lett.* **1990**, 173, 461–465.

[22] N. C. Nielsen, H. Bildsoe, H. J. Jakobsen and M. H. Levitt. "Double-Quantum Homonuclear Rotary Resonance: Efficient Dipolar Recovery in Magic-Angle Spinning Nuclear Magnetic Resonance." *J. Chem. Phys.* **1994**, 101, 1805–1812.

[23] J. R. Lewandowski, G. De Paëpe, M. T. Eddy, J. Struppe, W. Maas and R. G. Griffin. "Proton Assisted Recoupling at High Spinning Frequencies." *J. Phys. Chem. B.* **2009**, 113, 9062–9069.

[24] M. Weingarth, D. E. Demco, G. Bodenhausen and P. Tekely. "Improved Magnetization Transfer in Solid-State NMR with Fast Magic Angle Spinning." *Chem. Phys. Lett.* **2009**, 469, 342–348.

[25] G. Hou, S. Yan, J. Trébosc, J. P. Amoureux and T. Polenova. "Broadband Homonuclear Correlation Spectroscopy Driven by Combined Sequences Under Fast Magic Angle Spinning for NMR Structural Analysis of Organic and Biological Solids." *J. Magn. Reson.* **2013**, 232, 18–30.

[26] M. Hong. "Solid-State Dipolar INADEQUATE NMR Spectroscopy with a Large Double-Quantum Spectral Width." *J. Magn. Reson.* **1999**, 136, 86–91.

[27] M. Hong and R. G. Griffin. "Resonance Assignments for Solid Peptides by Dipolar-Mediated $^{13}C/^{15}N$ Correlation Solid-State NMR." *J. Am. Chem. Soc.* **1998**, 120, 7113–7114.

[28] K. K. Kumashiro, K. Schmidt-Rohr, O. J. Murphy, K. L. Ouellette, W. A. Cramer and L. K. Thompson. "A Novel Tool for Probing Membrane Protein Structure: Solid-State NMR with Proton Spin Diffusion and X-Nucleus Detection." *J. Am. Chem. Soc.* **1998**, 120, 5043–5051.

[29] D. Huster, X. Yao and M. Hong. "Membrane Protein Topology Probed by ^{1}H Spin Diffusion from Lipids Using Solid-State NMR Spectroscopy." *J. Am. Chem. Soc.* **2002**, 124, 874–883.

[30] X. L. Yao and M. Hong. "Dipolar Filtered ^{1}H-^{13}C Heteronuclear Correlation Spectroscopy for Resonance Assignment of Proteins." *J. Biomol. NMR* **2001**, 20, 263–274.

[31] T. Gullion and J. Schaefer. "Rotational Echo Double Resonance NMR." *J. Magn. Reson.* **1989**, 81, 196–200.

[32] E. R. deAzevedo, W. G. Hu, T. J. Bonagamba and K. Schmidt-Rohr. "Centerband-Only Detection of Exchange: Efficient Analysis of Dynamics in Solids by NMR." *J. Am. Chem. Soc.* **1999**, 121, 8411–8412.

[33] T. Gullion. "Introduction to Rotational-Echo, Double-Resonance NMR." *Concepts Magn. Reson.* **1998**, 10, 277–289.

[34] M. H. Levitt. "Composite Pulses." *Prog. Nucl. Magn. Reson. Spectrosc.* **1986**, 18, 61–122.

[35] M. H. Levitt and R. Freeman. "NMR Population Inversion Using a Composite Pulse." *J. Magn. Reson.* **1979**, 33, 473–476.

[36] Z. Starcuk and V. Sklenar. "Composite Pulse Sequences with Variable Performance." *J. Magn. Reson.* **1985**, 62, 113–122.

[37] C. P. Jaroniec, B. A. Tounge, C. M. Rienstra, J. Herzfeld and R. G. Griffin. "Measurement of ^{13}C-^{15}N Distances in Uniformly ^{13}C Labeled Biomolecules: J-Decoupled REDOR." *J. Am. Chem. Soc.* **1999**, 121, 10237–10238.

[38] C. P. Jaroniec, B. A. Tounge, J. Herzfeld and R. G. Griffin. "Frequency Selective Heteronuclear Dipolar Recoupling in Rotating Solids: Accurate ^{13}C-^{15}N Distance Measurements in Uniformly ^{13}C,^{15}N-Labeled Peptides." *J. Am. Chem. Soc.* **2001**, 123, 3507–3519.

[39] M. Bak, J. T. Rasmussen and N. C. Nielsen. "SIMPSON: A General Simulation Program for Solid-State NMR Spectroscopy." *J. Magn. Reson.* **2000**, 147, 296–330.

[40] M. Veshtort and R. G. Griffin. "SPINEVOLUTION: A Powerful Tool for the Simulation of Solid and Liquid State NMR Experiments." *J. Magn. Reson.* **2006**, 178, 248–282.

[41] E. R. deAzevedo, W. G. Hu, T. J. Bonagamba and K. Schmidt-Rohr. "Principles of Centerband-Only Detection of Exchange in Solid-State Nuclear Magnetic Resonance, and Extension to Four-Time Centerband-Only Detection of Exchange." *J. Chem. Phys.* **2000**, 112, 8988-9001.

[42] K. Schmidt-Rohr, E. R. deAzevedo and T. J. Bonagamba. "Centerband-Only Detection of Exchange (CODEX): Efficient NMR Analysis of Slow Motions in Solids." *eMagRes* **2007**.

[43] W. Luo and M. Hong. "Determination of the Oligomeric Number and Intermolecular Distances of Membrane Protein Assemblies by Anisotropic ^{1}H-Driven Spin Diffusion NMR Spectroscopy." *J. Am. Chem. Soc.* **2006**, 128, 7242–7251.

[44] D. L. VanderHart. "Natural-Abundance ^{13}C-^{13}C Spin Exchange in Rigid Crystalline Organic Solids." *J. Magn. Reson.* **1987**, 72, 13–47.

[45] W. Luo. "Spin Diffusion and Dynamics Studies of the Channel Forming Membrane Proteins by Solid-State Nuclear Magnetic Resonance." *PhD Thesis* **2010**.

[46] T. Samji. "Influenza A: Understanding the Viral Life Cycle." *Yale J. Biol. Med.* **2009**, 82, 153-159.

[47] J. H. Beigel. "Concise Definitive Review: Influenza." *Crit. Care Med.* **2008**, 36, 2660–2666.

[48] J. S. Rossman, X. Jing, G. P. Leser and R. A. Lamb. "Influenza Virus M2 Protein Mediates ESCRT-Independent Membrane Scission." *Cell* **2010**, 142, 902–913.

[49] M. Koutsakos, T. H. Nguyen, W. S. Barclay and K. Kedzierska. "Knowns and Unknowns of Influenza B Viruses." *Future Microbiol.* **2016**, 11, 119–135.

[50] C. Wang, R. A. Lamb and L. H. Pinto. "Activation of the M2 Ion Channel of Influenza Virus: A Role for the Transmembrane Domain Histidine Residue." *Biophys. J.* **1995**, 69, 1363–1371.

[51] P. Venkataraman, R. A. Lamb and L. H. Pinto. "Chemical Rescue of Histidine Selectivity Filter Mutants of the M2 Ion Channel of Influenza A Virus." *J. Biol. Chem.* **2005**, 280, 21463–21472.

[52] Y. Tang, F. Zaitseva, R. A. Lamb and L. H. Pinto. "The Gate of the Influenza Virus M2 Proton Channel is Formed by a Single Tryptophan Residue." *J. Biol. Chem.* **2002**, 277, 39880–39886.

[53] S. D. Cady, C. Goodman, C. D. Tatko, W. F. DeGrado and M. Hong. "Determining the Orientation of Uniaxially Rotating Membrane Proteins Using Unoriented Samples: A ^{2}H, ^{13}C, and ^{15}N Solid-State NMR Investigation of the Dynamics and Orientation of a Transmembrane Helical Bundle." *J. Am. Chem. Soc.* **2007**, 129, 5719–5729.

[54] S. D. Cady and M. Hong. "Amantadine-Induced Conformational and Dynamical Changes of the Influenza M2 Transmembrane Proton Channel." *Proc. Natl. Acad. Sci. U.S.A.* **2008**, 105, 1483–1488.

[55] F. Hu, W. Luo and M. Hong. "Mechanisms of Proton Conduction and Gating in Influenza M2 Proton Channels from Solid-State NMR." *Science* **2010**, 330, 505–508.

[56] W. Luo and M. Hong. "Conformational Changes of an Ion Channel Detected Through Water-Protein Interactions Using Solid-State NMR Spectroscopy." *J. Am. Chem. Soc.* **2010**, 132, 2378–2384.

[57] S. D. Cady, K. Schmidt-Rohr, J. Wang, C. S. Soto, W. F. DeGrado and M. Hong. "Structure of the Amantadine Binding Site of Influenza M2 Proton Channels in Lipid Bilayers." *Nature* **2010**, 463, 689–692.

[58] F. Hu, K. Schmidt-Rohr and M. Hong. "NMR Detection of pH-Dependent Histidine-Water Proton Exchange Reveals the Conduction Mechanism of a Transmembrane Proton Channel." *J. Am. Chem. Soc.* **2012**, 134, 3703–3713.

[59] H. X. Zhou and T. A. Cross. "Influences of Membrane Mimetic Environments on Membrane Protein Structures." *Annu. Rev. Biophys.* **2013**, 42, 361–392.

[60] E. V. Ekanayake, R. Fu and T. A. Cross. "Structural Influences: Cholesterol, Drug, and Proton Binding to Full-Length Influenza A M2 Protein." *Biophys. J.* **2016**, 110, 1391–1399.

[61] J. L. Thomaston, M. Alfonso-Prieto, R. A. Woldeyes, J. S. Fraser, M. L. Klein, G. Fiorin and W. F. DeGrado. "High-Resolution Structures of the M2 Channel from Influenza A Virus Reveal Dynamic Pathways for Proton Stabilization and Transduction." *Proc. Natl. Acad. Sci. U.S.A.* **2015**, 112, 14260-14265.

[62] A. L. Stouffer, R. Acharya, D. Salom, A. S. Levine, L. Di Costanzo, C. S. Soto, V. Tereshko, V. Nanda, S. Stayrook and W. F. DeGrado. "Structural Basis for the Function and Inhibition of an Influenza Virus Proton Channel." *Nature* **2008**, 451, 596–599.

[63] A. Acharya, V. Carnevale, G. Fiorin, B. G. Levine, A. Polishchuk, V. Balannick, I. Samish, R. A. Lamb, L. H. Pinto, W. F. DeGrado and M. L. Klein. "Structural Mechanism of Proton Transport Through the Influenza A M2 Protein." *Proc. Natl. Acad. Sci. U.S.A.* **2010**, 107, 15075–15080.

[64] J. R. Schnell and J. J. Chou. 2008. "Structure and Mechanism of the M2 Proton Channel of Influenza A Virus." *Nature* **2008**, 451, 591–595.

[65] R. M. Pielak, K. Oxenoid and J. J. Chou. "Structural Investigation of Rimantadine Inhibition of the AM2-BM2 Chimera Channel of Influenza Viruses." *Structure* **2011**, 19, 1655–1663.

[66] R. M. Pielak, J. R. Schnell and J. J. Chou. "Mechanism of Drug Inhibition and Drug Resistance of Influenza A M2 Channel." *Proc. Natl. Acad. Sci. U.S.A.* **2009**, 106, 7379–7384.

[67] M. Sharma, M. Yi, H. Dong, H. Qin, E. Peterson, D. D. Busath, H. X. Zhou and T. A. Cross. "Insight into the Mechanism of the Influenza A Proton Channel from a Structure in a Lipid Bilayer." *Science* **2010**, 330, 509–512.

[68] J. Hu, T. Asbury, S. Achuthan, C. Li, R. Bertram, J. R. Quine, R. Fu and T. A. Cross. "Backbone Structure of the Amantadine-Blocked Trans-Membrane Domain M2 Proton Channel from Influenza A Virus." *Biophys. J.* **2007**, 92, 4335–4343.

[69] S. D. Cady, T. V. Mishanina and M. Hong. "Structure of Amantadine-Bound M2 Transmembrane Peptide of Influenza A in Lipid Bilayers from Magic-Angle-Spinning Solid-State NMR: The Role of Ser31 in Amantadine Binding." *J. Mol. Biol.* **2009**, 385, 1127–1141.

[70] H. D. Klenk, R. Rott and H. Becht. "On the Structure of the Influenza Virus Envelope." *Virology* **1972**, 47, 579–591.

[71] M. J. Gerl, J. L. Sampaio, S. Urban, L. Kalvodova, J. M. Verbavatz, B. Binnington, D. Lindemann, C. A. Lingwood, A. Shevchenko, C. Schroeder and K. Simons. "Quantitative Analysis of the Lipidomes of the Influenza Virus Envelope and MDCK Cell Apical Membrane." *J. Cell Biol.* **2012**, 196, 213–221.

[72] S. D. Cady, T. Wang and M. Hong. "Membrane-Dependent Effects of a Cytoplasmic Helix on the Structure and Drug Binding of the Influenza Virus M2 Protein." *J. Am. Chem. Soc.* **2011**, 133, 11572–11579.

[73] W. Luo, S. D. Cady and M. Hong. "Immobilization of the Influenza A M2 Transmembrane Peptide in Virus Envelope-Mimetic Lipid Membranes: A Solid-State NMR Investigation." *Biochemistry* **2009**, 48, 6361–6368.

2. Hydrogen-Bonding Partner of the Proton-Conducting Histidine in the Influenza M2 Proton Channel Revealed From ^{1}H Chemical Shifts

Mei Hong, Keith J. Fritzsching*, Jonathan K. Williams*
*equal contribution

Department of Chemistry, Iowa State University, Ames, IA

Journal of the American Chemical Society, **2012**, vol. 134, pp. 14753-14755.
DOI: 10.1021/ja307453v

2.1 Abstract

The influenza M2 protein conducts protons through a critical histidine (His) residue, His37. Whether His37 only interacts with water to relay protons into the virion or whether a low-barrier hydrogen bond (LBHB) also exists between the histidines to stabilize charges before proton conduction is actively debated. To address this question, we have measured the imidazole $^{1}H^{N}$ chemical shifts of His37 at different temperatures and pH using 2D ^{15}N-^{1}H correlation solid-state NMR. At low temperature, the H^{N} chemical shifts are 8–15 ppm at all pH values, indicating that the His37 sidechain forms conventional hydrogen bonds (H-bonds) instead of LBHBs. At ambient temperature, the dynamically averaged H^{N} chemical shifts are 4.8 ppm, indicating that the H-bonding partner of the imidazole is water instead of another histidine in the tetrameric channel. These data show that His37 forms H-bonds only to water, with regular strength, thus supporting the His-water proton exchange model and ruling out the low-barrier H-bonded dimer model.

2.2 Communication

The influenza M2 protein forms a tetrameric proton channel important for the virus lifecycle.[1-3] Activated by the low pH environment of the endosome, the channel opens to acidify the virion, which causes viral uncoating. The mechanism of proton conduction through M2 has long been debated. Early computational studies and functional data diverged on whether proton conduction occurs by Grotthuss hopping along a water wire[4,5] or requires conformational changes of the only titratable residue in the transmembrane (TM) domain, His37[6] (**Fig. 2.1a**). Recent data

have ruled out the water wire model and converged on the active participation of His37 in proton relay. Evidence for proton shuttling by His37 came from magic angle spinning (MAS) ^{15}N NMR spectra showing chemical exchange of the imidazole nitrogens between the protonated (NH) and unprotonated (N) states at the physiological pH of the endosome.[7] This exchange is accompanied by low-pH specific imidazolium reorientation on the microsecond time scale with an energy barrier comparable to the proton conduction barrier.[8]

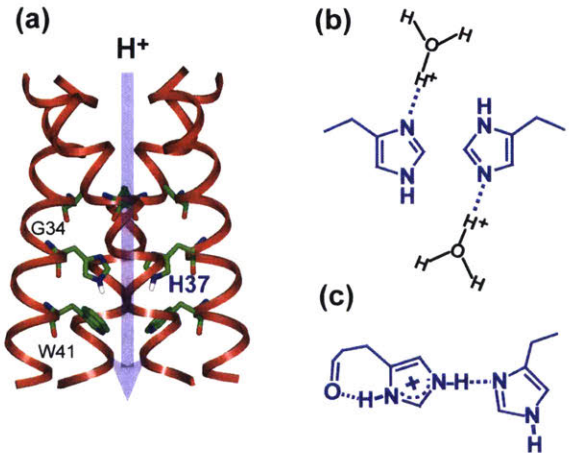

Figure 2.1 Two proton conduction models for the influenza M2 channel. (a) Structure of M2TM at pH 6.5 (PDB: 3LBW), showing the location of the key His37 and Trp41. (b) His37-water proton exchange model. (c) His-His low-barrier H-bonded dimer model. The dimer of dimer state is proposed to exist stably in the +2 tetrad to stabilize charge before proton transfer to water.

Despite the general consensus that His37 shuttles protons, the mechanism by which charge is stabilized in the His37 tetrad is still actively debated. The ^{15}N chemical exchange and imidazolium reorientation led to the proposal that His37-water H-bonding and proton exchange are sufficient for proton conduction (**Fig. 2.1b**)[7] and that excess protons are stabilized by delocalization over the His37 tetrad and the surrounding water molecules.[9] In contrast, an alternative model posits a LBHB between a neutral and a cationic histidine in the +2 state of the channel (**Fig. 2.1c**),[10] which stabilizes the charges before channel activation. This model was motivated by the observation of a very high pK_a of 8.2 for the first two protonation steps in DMPC/DMPG bilayer-bound M2 TM peptide (M2TM),[10] and by computational modeling of the His37 side-chain structure.[11] The latter yielded His37 (χ_1, χ_2) torsion angles of (180°, 90°) to establish the putative Nε2-H···Nδ1 H-bond. Recently reported chemical shift multiplicity of some

of the TM residues,[12,13] although observed at neutral pH, was also interpreted as supporting the LBHB model.

Equilibrium conformation of His37 measured by solid-state NMR[8] and X-ray crystallography[9,14] at acidic pH have so far shown no direct His-His H-bonding: the His37 χ_1 and χ_2 angles were measured to be ~180° in both lipid bilayers and detergents, which points the Nε2-H and Nδ1 toward the interior and exterior of the channel rather than toward each other. ^{13}C-^{13}C 2D correlation spectra of the +2 charged channel displayed no imidazole-imidazolium cross peaks,[7] also challenging the LBHB model. However, the ^{15}N NMR spectra showing N-NH chemical exchange, can, in principle, be due to either His-water proton transfer or His-His H-bonding. Thus, we sought more definitive evidence for the H-bonding partner of His37 as well as the strength of the His37 H-bond. The strength of H-bonds can be discerned through the ^1H chemical shift: a proton in a low-barrier or strong H-bond should have a large chemical shift of greater than 16 ppm,[15-18] whereas a proton in a regular unequal-well H-bond should have a smaller chemical shift of 8-15 ppm.[19,20] The identity of the H-bonding partner for membrane proteins in hydrated lipid bilayers can be determined through the temperature dependence of the ^1H chemical shift. Between -30 °C and +30 °C, the diffusion rates of water in the channel change significantly;[21,22] thus, a regular N-H···O H-bond should involve only one or a few water molecules at low temperature but should undergo rapid exchange with many water molecules at physiological temperature. This should result in a ^1H chemical shift close to the imidazole H^N value at low temperature but a population-weighted value near the water ^1H chemical shift at high temperature. In contrast, for a pK_a-matched N-H···N LBHB,[23,24] the central proton has a much higher activation energy for exchange with water;[25] moreover proton transfer dynamics between the two nitrogens is ultrafast. Thus, the ^1H chemical shift will be insensitive to temperature at this range and remain large. Thus, the low-temperature ^1H chemical shift reveals the H-bond strength, whereas the high-temperature chemical shift indicates the identity of the H-bonding partner.

We measured the ^1H chemical shift using the 2D ^{15}N-^1H heteronuclear correlation (HETCOR) experiment. To detect only cross peaks due to direct N-H dipolar coupling without relayed transfer, we suppressed ^1H spin diffusion using ^1H homonuclear decoupling during the

evolution period and the ^{1}H-^{15}N cross-polarization period.[26] His37-labeled M2TM bound to a virus-mimetic lipid membrane were measured at pH 6.0, 4.5, and 8.5.[8] Since all initial experiments that led to the LBHB model were conducted on M2TM, we used the same construct to avoid potential ambiguities in interpretation. Previous measurement of His37 pK_a's in this virus-mimetic membrane indicated that the channel was 80% in the +2 state at pH 6, in a mixed +3 and +4 state at pH 4.5, and about 90% neutral at pH 8.5.[7] Thus, the pH 6.0 sample is the closest to the putative LBHB state. The 2D HETCOR spectra were measured at 245 K to determine the H-bond strength and 296 K to determine the H-bonding partner.

Figure 2a shows the 2D HETCOR spectra of the pH 6.0 sample. At 245 K, the imidazole Nε2 (τ tautomer) and Nδ1 (π tautomer) peaks at 160-180 ppm exhibit ^{1}H chemical shifts of 8-12 ppm, similar to the backbone amide ^{1}H chemical shift range. Thus, imidazole H^N lies in a regular H-bond. For comparison, histidine hydrochloride (**Fig. 2.S1**, Supporting Information [SI]) shows a large Hδ1 chemical shift of 16.8 ppm due to a strong intermolecular H-bond to a C=O with an N···O distance of 2.63 Å.[27] Both ^{15}N and ^{1}H shifts reflect the strength of the H-bond: small ^{15}N and ^{1}H shifts indicate a stronger covalent N-H bond, while large shifts indicate a more deprotonated nitrogen or a stronger H-bond.[17,18] The correlation gives a slope of ~3 between the ^{15}N and ^{1}H chemical shifts (**Fig. 2a**). The ^{1}H shift distribution (**Fig. 2.S2**, SI), detected for both backbone and imidazole nitrogens, indicates a distribution of H-bond strengths. The backbone distribution is likely due to varying degrees of helix ideality in an ensemble with mixed protonation states, while the imidazole H^N shift distribution can be attributed to the presence of multiple N-H species, including Nε2H(τ), Nδ1H(π), and the Nε2H and Nδ1H of cationic imidazolium (**Fig. 2.S3**, SI).

When the temperature increased to 296 K, the imidazole ^{1}H chemical shifts decreased uniformly to 4.8 ppm, indicating definitively that the H-bonding partner of His37 is water instead of another His. Since ^{1}H homonuclear decoupling was applied in the experiment, both rigid and mobile protons were equally detected; thus, the observed ^{1}H chemical shift near the unperturbed water frequency indicates a large number of water molecules in exchange with the imidazole nitrogens. For comparison, the backbone H^N chemical shift is unaffected by temperature, as expected for the persistence of N-H···O=C H-bonds at these temperatures.

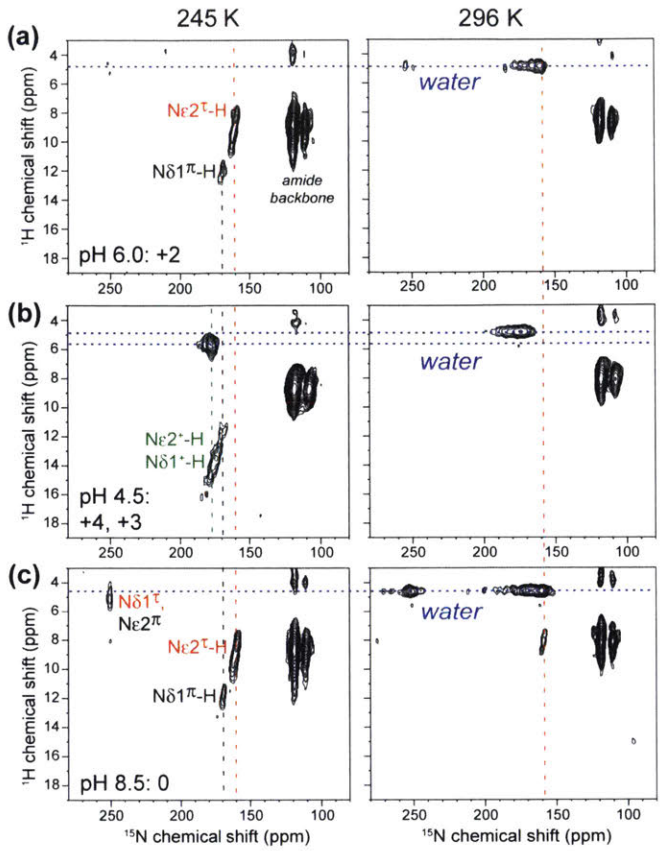

Figure 2.2 Two-dimensional ^{15}N-^{1}H HETCOR spectra of membrane-bound His37-labeled M2TM at (a) pH 6.0, (b) pH 4.5, and (c) pH 8.5 at 245 K (left) and 296 K (right). The main charged states of the M2TM channel at each pH are indicated. The ^{1}H dimension of the spectrum was measure with ^{1}H homonuclear decoupling to eliminate spin diffusion effects. Assignments are shown in red for the neutral τ tautomer, black for the neutral π tautomer, and green for cationic His37.

The 2D spectra of the pH 4.5 sample (**Fig. 2.2b**) further support the His37-water interaction model.[7,9] Even at low temperature, the 178 ppm ^{15}N peak already shows a water ^{1}H cross peak (5.7 ppm) in addition to the Hε2/Hδ1 signal (12-15 ppm), consistent with previous data showing a more hydrated channel at this low pH.[28] The Hε2/Hδ1 chemical shift is larger than at pH 6, indicating stronger N-H bond elongation at this pH.[8] The ^{15}N/^{1}H chemical shift slope is the same as at pH 6.0 (**Fig. 2.S2**, SI), as expected for the intrinsic correlation between ^{15}N protonation and N-H···O H-bond strength. Again, the identity of the H-bonding partner is determined by the high-temperature spectrum, which shows a ^{1}H chemical shift at the water position of 4.8 ppm, indicating that His37 H-bonds only to water.

At pH 8.5, the high-temperature spectrum retained the dominant water cross peak, but a weak signal at ~8 ppm was also detected and can be assigned to Hε2. Although the channel does not conduct protons at this pH, some water molecules are still present, for example between His37 and Trp41,[8,9,29] thus allowing polarization transfer to ^{15}N. At low temperature, the unprotonated nitrogen, mainly Nδ1, exhibits a ^{1}H cross peak at ~5 ppm due to Hε1, as verified by the spectrum of amino acid histidine (**Fig. 2.S1**, SI).[27]

These low-temperature ^{1}H chemical shifts are smaller than expected for an LBHB or a strong H-bond, while the high-temperature ^{1}H chemical shifts reveal the H-bonding partner to be water. Thus, the data support the direct His37-water interaction model and rule out the His-His LBHB-dimer model. The 1.65 Å crystal structure at pH 6.5[9] detected tightly clustered water molecules near the His37 tetrad, with N···O distances as short as 2.8 Å, also supporting direct His37-water interactions. On the other hand, all experimental data so far, including the initial ^{15}N NMR spectra from which the dimer model was proposed,[10] show an *absence* of imidazole-imidazolium H-bond. An LBHB entails either a single ^{15}N peak at the averaged chemical shift between N and NH for equal-well potentials or two ^{15}N peaks centered around the averaged frequency for unequal-well potentials. Instead, the ^{15}N spectra showed a single peak away from the averaged chemical shift, without the partner peak. Molecular modeling of the HxxxW structure[11] was questionable because it used the putative LBHB as a starting distance restraint to enforce the expected geometry during MD simulations. Finally, the LBHB model implies a hydrophobic environment for the donor and acceptor with a very small pK_a difference,[30] which contradicts the observed different proton affinities of Nε2 and Nδ1 in His37 and the high hydration of this residue.

In conclusion, temperature-dependent ^{1}H chemical shifts of the His37 side chain indicate that His37-water H-bonding and proton exchange dominate the equilibrium structure of the His37 tetrad throughout the whole pH range. His-His interactions are indirectly mediated by water. If a direct His-His H-bond is too transient to be detectable by NMR, then it cannot be an LBHB and cannot provide stabilization for the dimer state. We propose that charges are stabilized by water-mediated interactions[7,9] and by cation-π interaction between His37 and Trp41.[5]

This temperature-dependent ^{1}H chemical shift approach avoids the difficulty of measuring N···N and N···O distances across a H-bond by NMR; moreover, it directly reveals the structure of the most essential player in a proton relay chain. It is applicable to both biological and synthetic proton conductors to understand the nature of the H-bond in proton transport.

2.3 Acknowledgements

We thank Professor Schmidt-Rohr for useful discussions. This work is supported by NIH Grant GM088204.

2.4 References

[1] L. H. Pinto and R. A. Lamb. "The M2 Proton Channels of Influenza A and B Viruses." *J. Biol. Chem.* **2006**, 281, 8997-9000.

[2] S. D. Cady, W. B. Luo, F. Hu and M. Hong. "Structure and Function of the Influenza A M2 Proton Channel." *Biochemistry* **2009**, 48, 7356-7364.

[3] J. Wang, J. X. Qiu, C. Soto and W. F. DeGrado. "Structural and Dynamic Mechanisms for the Function and Inhibition of the M2 Proton Channel from Influenza A Virus." *Curr. Opin. Struct. Biol.* **2011**, 21, 68-80.

[4] M. S. P. Sansom, I. D. Kerr, G. R. Smith and H. S. Son. "The Influenza A Virus M2 Channel: A Molecular Modeling and Simulation Study." *Virology* **1997**, 233, 163-173.

[5] A. Okada, T. Miura and H. Takeuchi. "Protonation of Histidine and Histidine-Tryptophan Interaction in the Activation of the M2 Ion Channel from Influenza A Virus." *Biochemistry* **2001**, 40, 6053-6060.

[6] L. H. Pinto, G. R. Dieckmann, C. S. Gandhi, C. G. Papworth, J. Braman, M. A. Shaughnessy, J. D. Lear, R. A. Lamb and W. F. DeGrado. "A Functionally Defined Model for the M2 Proton Channel of Influenza A Virus Suggests a Mechanism for Its Ion Selectivity." *Proc. Natl. Acad. Sci. U.S.A.* **1997**, 94, 11301-11306.

[7] F. Hu, K. Schmidt-Rohr and M. Hong. "NMR Detection of pH-Dependent Histidine-Water Proton Exchange Reveals the Conduction Mechanism of a Transmembrane Proton Channel." *J. Am. Chem. Soc.* **2012**, 134, 3703-3713.

[8] F. Hu, W. Luo and M. Hong. "Mechanisms of Proton Conduction and Gating in Influenza M2 Proton Channels from Solid-State NMR." *Science* **2010**, 330, 505-508.

[9] R. Acharya, V. Carnevale, G. Fiorin, B. G. Levine, A. Polishchuk, V. Balannick, I. Samish, R. A. Lamb, L. H. Pinto, W. F. DeGrado and M. L. Klein. "Structure and Mechanism of Proton Transport Through the Transmembrane Tetrameric M2 Protein Bundle of the Influenza A Virus." *Proc. Natl. Acad. Sci. U.S.A.* **2010**, 107, 15075-15080.

[10] J. Hu, R. Fu, K. Mishimura, L. Zhang, H. X. Zhou, D. D. Busath, V. Vijayvergiya and T. A. Cross. "Histidines, Heart of the Hydrogen Ion Channel from Influenza A Virus: Toward and Understanding of Conductance and Proton Selectivity." *Proc. Natl. Acad. Sci. U.S.A.* **2006**, 1003, 6865-6870.

[11] M. Sharma, M. Yi, H. Dong, H. Qin, E. Peterson, D. D. Busath, H. X. Zhou and T. A. Cross. "Insight into the Mechanism of the Influenza A Proton Channel from a Structure in a Lipid Bilayer." *Science* **2010**, 330, 509-512.

[12] L. B. Andreas, M. T. Eddy, J. J Chou and R. G. Griffin. "Magic-Angle-Spinning NMR of the Drug Resistant S31N M2 Proton Transporter from Influenza A." *J. Am. Chem. Soc.* **2012**, 134, 7215-7218.

[13] T. V. Can, M. Sharma, I. Hung, P. L. Gor'kov, W. W. Brey and T. A. Cross. "Magic Angle Spinning and Oriented Sample Solid-State NMR Structural Restraints Combine for Influenza A M2 Protein Functional Insights." *J. Am. Chem. Soc.* **2012**, 134, 9022- 9025.

[14] A. L. Stouffer, R. Acharya, D. Salom, A. S. Levine, L. Di Costanzo, C. S. Soto, V. Tereshko, V. Nanda, S. Stayrook and W. F. DeGrado. "Structural Basis for the Function and Inhibition of an Influenza Virus Proton Channel." *Nature* **2008**, 451, 596-599.

[15] S. P. Brown. "Applications of High-Resolution 1H Solid-State NMR." *Solid State Nucl. Magn. Reson.* **2012**, 41, 1-27.

[16] P. Gilli, B. Bertolasi, V. Ferretti and G. Gilli. "Evidence for Intramolecular N-H···O Resonance-Assisted Hydrogen Bonding in β-Enaminones and Related Heterodienes. A Combined Crystal-Structure, IR and NMR Spectroscopic, and Quantum-Mechanical Investigation." *J. Am. Chem. Soc.* **2000**, 122, 10405-10417.

[17] P. Lorente, I. G. Shenderovich, N. S. Golubev, G. S. Denisov, G. Buntkowsky and H.-H. Limbach. "$^{1}H/^{15}N$ NMR Chemical Shielding, Dipolar $^{15}N/^{2}H$ Coupling and Hydrogen Bond Geometry Correlations in a Novel Series of Hydrogen-Bonded Acid-Base Complexes of Collidine with Carboxylic Acids." *Magn. Reson. Chem.* **2001**, 39, S18-S29.

[18] S. Sharif, D. Schagen, M. D. Toney and H.-H. Limbach. "Coupling of Functional Hydrogen Bonds in Pyridoxal-5'-Phosphate-Enzyme Model Systems Observed by Solid-State NMR Spectroscopy." *J. Am. Chem. Soc.* **2007**, 129, 4440-4455.

[19] B. Berglund and R. W. Vaughan. "Correlations Between Proton Chemical Shift Tensors, Deuterium Quadrupole Couplings, and Bond Distances for Hydrogen Bonds in Solids." *J. Chem. Phys.* **1980**, 73, 2037-2043.

[20] M. Barfield. "Structural Dependencies of Interresidue Scalar Coupling $^{h3}J_{NC'}$ and Donor ^{1}H Chemical Shifts in the Hydrogen Bonding Regions of Proteins." *J. Am. Chem. Soc.* **2002**, 124, 4158-4168.

[21] I. Nicoterra, L. Coppola, C. O. Rossi, M. Youssry and G. A. Ranieri. "NMR Investigation of the Dynamics of Confined Water in Nafion-Based Electrolyte Membranes at Subfreezing Temperatures." *J. Phys. Chem. B* **2009**, 113, 13935-13941.

[22] S. Takahara, M. Makano, S. Kittaka, Y. Kuroda, T. Mori, H. Hamano and T. Yamaguchi. "Neutron Scattering Study on Dynamics of Water Molecules in MCM-41." *J. Phys. Chem. B* **1999**, 103, 5814-5819.

[23] X. J. Song and A. E. McDermott. "Proton Transfer Dynamics and N-H Bond Lengthening in N-H···N Model Systems: A Solid-State NMR Study." *Magn. Reson. Chem.* **2001**, 39, S37-S43.

[24] B. Wehrle, H. Zimmermann and H.-H. Limbach. "A Solid-State ^{15}N CPMAS NMR Study of Dye Tautomerism in Glassy Polystyrene: Site Dependence of Double Minimum Potentials and Their Motional Averaging." *J. Am. Chem. Soc.* **1988**, 110, 7014-7024.

[25] J. Lin, W. M. Westler, W. W. Cleland, J. L. Markley and P. A. Frey. "Fractionation Factors and Activation Energies for Exchange of the Low Barrier Hydrogen Bonding Proton in Peptidyl Trifluoromethyl Ketone Complexes of Chymotrypsin." *Proc. Natl. Acad. Sci. U.S.A.* **1998**, 95, 14664-14668.

[26] M. Hong, X. L. Yao, K. Jakes and D. Huster. "Investigation of Molecular Motions by Lee-Goldburg Cross-Polarization NMR Spectroscopy." *J. Phys. Chem. B* **2002**, 106, 7355-7364.

[27] S. Li and M. Hong. "Protonation, Tautomerization, and Rotameric Structure of Histidine: A Comprehensive Study by Magic-Angle-Spinning Solid-State NMR." *J. Am. Chem. Soc.* **2011**, 133, 1534-1544.

[28] W. Luo and M. Hong. "Conformational Changes of an Ion Channel Detected Through Water-Protein Interactions Using Solid-State NMR Spectroscopy." *J. Am. Chem. Soc.* **2010**, 132, 2378-2384.

[29] Y. Su, F. Hu and M. Hong. "Paramagnetic Cu(II) for Probing Membrane Protein Structure and Function: Inhibition Mechanism of the Influenza M2 Proton Channel." *J. Am. Chem. Soc.* **2012**, 134, 8693-8702.

[30] C. N. Schutz and A. Warshel. "The Low Barrier Hydrogen Bond (LBHB) Proposal Revisited: The Case of the Asp···His Pair in Serine Proteases." *Proteins* **2004**, 55, 711-723.

2.5 Supporting Information

2.5.1 NMR Samples

The M2TM membrane samples were prepared as described before.[1,2] Briefly, Gly34, His37 and Ile39 or Ile42 labeled M2(22-46) were synthesized and purified using Fmoc solid-phase protocols by PrimmBiotech, and incorporated into a virus-mimetic membrane using detergent dialysis. The membrane consists of DPPC:DPPE:sphingomyeling:cholesterol (21:21:28:30 mole ratio). The detergent octyl-β-D-glucoside was used for solubilizing and reconstituting the peptide into the lipid membrane. The peptide:lipid molar ratio was 1:15. Hydrated membrane pellets were obtained by ultracentrifugation and packed into 4 mm MAS rotos for solid-state NMR experiments. Three M2TM samples at pH 6.0, 4.5 and 8.5 were measured, and histidine amino acid recrystallized at the same pH values served as control samples.[3]

2.5.2 Solid-State NMR Experiments

Solid-state NMR experiments were carried out on a Bruker AVANCE 600 MHz (14.1 Tesla) spectrometer using a 4 mm MAS probe. Typical radiofrequency (rf) field strengths were 40 kHz for ^{15}N and 80 kHz for ^{1}H. ^{15}N chemical shifts were referenced to the N-aceytl-valine signal at 122.0 ppm on the liquid ammonia scale. ^{1}H chemical shifts were calibrated indirectly to those of formyl-Met-Leu-Phe[4] and verified with the published ^{1}H chemical shifts of amino acid histidine at various pH.[3] 2D ^{15}N-^{1}H HETCOR spectra were measured at 245 K and 296 K under 10 kHz MAS. Lee-Goldburg (LG) cross polarization (CP) was used to remove ^{1}H spin diffusion during CP. The ^{1}H and ^{15}N power levels for LG-CP were optimized similarly to the histidine amino acids to ensure proper detection of the unprotonated ^{15}N signal. The LG-CP contact time ranged from 0.5 ms to 2 ms and the ^{1}H effective spin-lock field strength was 50 kHz. Longer contact time was avoided to minimize long-range ^{1}H-^{15}N correlation signals. During the ^{1}H evolution period (t_1), the FSLG[5] pulses for ^{1}H homonuclear decoupling used a transverse field strength of 80 kHz and a corresponding frequency jump of ±56.6 kHz. The FSLG-scaled effective t_1 dwell time was 47.15 μs, and the typical number of t_1 slices was 80 or 88, resulting in a maximum t_1 evolution time of ~2 ms. Several experiments were co-added for each final spectrum, and the total number of scans ranged from 512 to 1956 per spectrum.

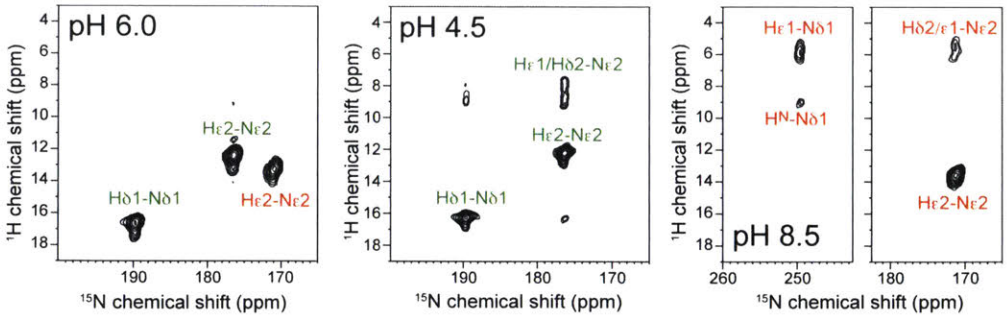

Figure 2.S1 2D ^{15}N-^{1}H HETCOR spectra of amino acid histidine at pH 6.0, 4.5 and 8.5. Assignments were made based on previous work.[3] These spectra were measured under the same FSLG and LG-CP conditions as the membrane-bound M2TM samples and served as controls for the ^{1}H chemical shifts. Note the downfield Hδ1 chemical shift of 17 ppm for cationic histidine (assigned in green) in the pH 4.5 and 6.0 spectra, which results from an intermolecular hydrogen bond with a backbone C=O with an R_{NO} of 2.63 Å.[3] Assignments for the neutral τ tautomer are given in red.

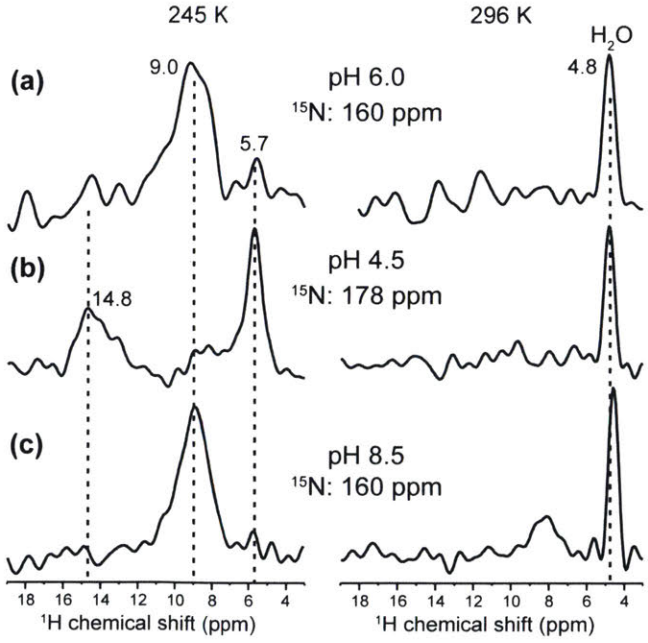

Figure 2.S2 Representative ^{1}H cross sections from the 2D HETCOR spectra of membrane-bound M2TM at (a) pH 6.0, (b) pH 4.5, and (c) pH 8.5. Left and right columns are cross sections extracted from the 245 K and 296 K spectra, respectively.

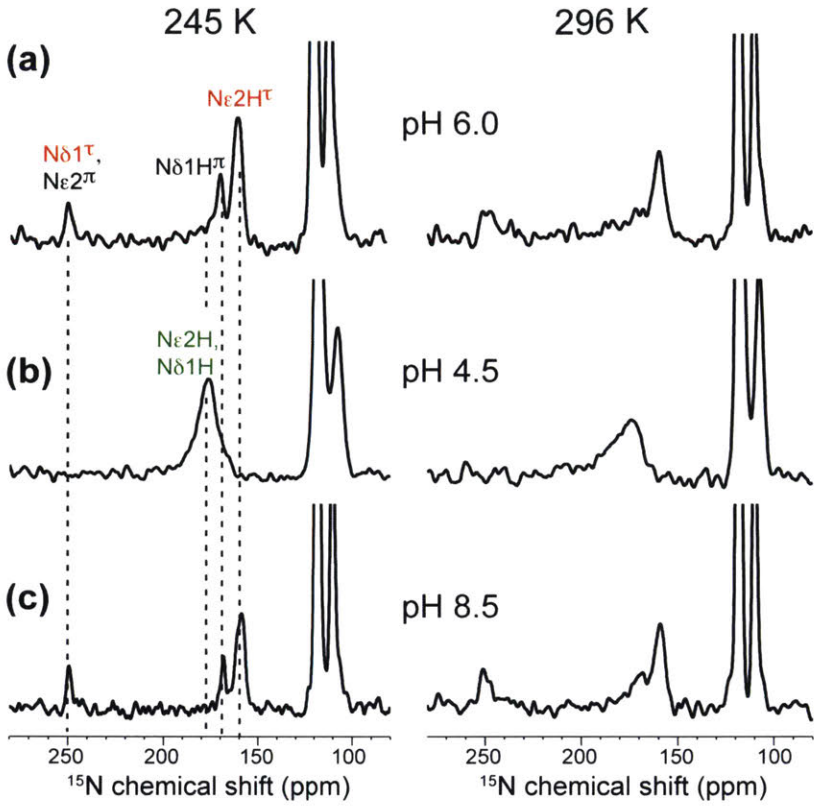

Figure 2.S3 ^{15}N LG-CP spectra of membrane-bound M2TM at 245 K (left column) and 296 K (right column) at pH 6.0 (a), pH 4.5 (b), and pH 8.5 (c). The spectra were measured immediately before and after the 2D HETCOR spectra under the same LG-CP conditions. ^{15}N assignments were based on previously reported 2D correlation spectra.[1] LG-CP contact time varied from 0.5 to 2 ms, which were shorter than necessary to reach equilibrium intensities for the unprotonated ^{15}N signal at 250 ppm, thus the spectral intensities shown here are not quantitative. Previous quantification of the ^{15}N CP-MAS spectra[2] showed that the relative intensity of the 250-ppm peak was about 2-fold higher at pH 8.5 than at pH 6 at 243 K.

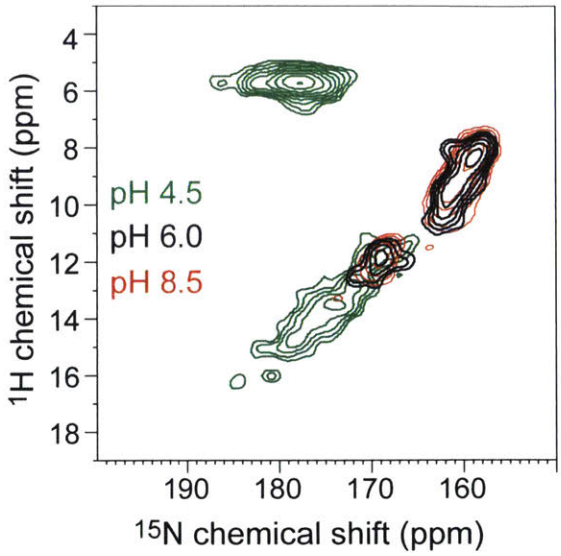

Figure 2.S4 Superposition of the protonated imidazole ^{15}N region of the 245 K HETCOR spectra of membrane-bound M2TM at three pH values. The pH 4.5 sample shows larger ^{15}N and ^{1}H chemical shifts than the pH 6.0 and pH 8.5 samples due to stronger imidazolium-water H-bonding. In addition, a water cross peak is observed at pH 4.5 even at low temperature, consistent with the fact that the lowest-pH channel has the most hydrated pore.[6] The water ^{1}H chemical shift (~6 ppm) is larger at low temperature than at ambient temperature (~5 ppm) due to stronger H-bonding.

2.5.3 Supporting Information References

[1] F. Hu, W. Luo and M. Hong. "Mechanisms of Proton Conduction and Gating in Influenza M2 Proton Channels from Solid-State NMR." *Science* **2010**, 330 (6003), 505-508.

[2] F. Hu, K. Schmidt-Rohr and M. Hong. "NMR Detection of pH-Dependent Histidine-Water Proton Exchange Reveals the Conduction Mechanism of a Transmembrane Proton Channel." *J. Am. Chem. Soc.* **2012**, 134 (8), 3703-3713.

[3] S. Li and M. Hong. "Protonation, Tautomerization, and Rotameric Structure of Histidine: A Comprehensive Study by Magic-Angle-Spinning Solid-State NMR." *J. Am. Chem. Soc.* **2011**, 133 (5), 1534-1544.

[4] C. M. Rienstra, L. Tucker-Kellogg, C. P. Jaroniec, M. Hohwy, B. Reif, M. T. McMahon, B. Tidor, T. Lozano-Perez and R. G. Griffin. "De Novo Determination of Peptide Structure with Solid-State Magic-Angle Spinning NMR Spectroscopy." *Proc. Natl. Acad. Sci. U.S.A.* **2002**, 99 (16), 10260-10265.

[5] A. Bielecki, A. C. Kolbert and M. H. Levitt. "Frequency-Switched Pulse Sequences: Homonuclear Decoupling and Dilute Spin NMR in Solids." *Chem. Phys. Lett.* **1989**, 155 (4-5), 341-346.

[6] W. Luo and M. Hong. "Conformational Changes of an Ion Channel Detected Through Water-Protein Interactions Using Solid-State NMR Spectroscopy." *J. Am. Chem. Soc.* **2010**, 132 (7), 2378-2384.

3. pH-Dependent Conformation, Dynamics, and Aromatic Interaction of the Gating Tryptophan Residue of the Influenza M2 Proton Channel from Solid-State NMR

Jonathan K. Williams, Yuan Zhang, Klaus Schmidt-Rohr, Mei Hong

Department of Chemistry, Iowa State University, Ames, IA

Biophysical Journal, **2013**, vol. 104, pp. 1698-1708.
DOI: 10.1016/j.bpj.2013.02.054

3.1 Abstract

The M2 protein of the influenza virus conducts protons into the virion under external acidic pH. The proton selectivity of the tetrameric channel is controlled by a single histidine (His37), whereas channel gating is accomplished by a single tryptophan (Trp41) in the transmembrane domain of the protein. Aromatic interaction between these two functional residues has been previously observed in Raman spectra, but atomic-resolution evidence for this interaction remains scarce. Here we use high-resolution solid-state NMR spectroscopy to determine the side-chain conformation and dynamics of Trp41 in the M2 transmembrane peptide by measuring the Trp chemical shifts, His37-Trp41 distances, and indole dynamics at high and low pH. The interatomic distances constrain the Trp41 side-chain conformation to *trans* for χ_1 and 120-135° for χ_2. This *t*90 rotamer points the Nε1-Cε2-Cζ2 side of the indole toward the aqueous pore. The precise χ_1 and χ_2 angles differ by ~20° between high and low pH. These differences, together with the known changes in the helix tilt angle between high and low pH, push the imidazole and indole rings closer together at low pH. Moreover, the measured order parameters indicate that the indole rings undergo simultaneous χ_1 and χ_2 torsional fluctuations at acidic pH, but only restricted χ_1 fluctuations at high pH. As a result, the Trp41 side chain periodically experiences strong cation-π interactions with His37 at low pH as the indole sweeps through its trajectory, whereas at high pH the indole ring is further away from the imidazole. These results provide the structural basis for understanding how the His37-water proton exchange rate measured by NMR is reduced to the small proton flux measured in biochemical experiments. The indole dynamics, together with the known motion of

the imidazolium, indicate that this compact ion channel uses economical side-chain dynamics to regulate proton conduction and gating.

3.2 Introduction

The influenza A M2 protein forms a homo-tetrameric proton channel that acidifies the virus after endocytosis[1-3] and maintains the high pH of the Golgi network for proper hemagglutinin function.[4] M2 also mediates virus budding from the host cell by causing membrane scission.[5] The proton channel is activated by low pH of the external environment, which is presented by the endosome during endocytosis. A conserved HxxxW motif is responsible for unidirectional proton conduction from the exterior into the virion. In this HxxxW motif, His37 is now known from solid-state NMR data to exchange protons with water molecules at a rate of 10^5 s^{-1}, facilitated by small-angle ring reorientations on the same time scale.[6,7] The histidine sidechain adopts the *trans-trans* conformation for the χ_1 and χ_2 torsion angles, such that Nδ1 and Nε2 point towards the N- and C-termini of the channel, respectively, primed to accept and release protons. The single-channel proton conductivity is the highest when three out of four histidines of the tetramer are protonated, which occur with a pK_a of 4.9 in cholesterol-rich virus-mimetic lipid membranes.[7] The water-His37 proton transfer is facilitated by an extensive network of imidazole-water hydrogen bonds at acidic pH,[6,8] but the hydrogen-bonding network is incomplete at high pH, when the channel is closed.

Whereas His37 is the proton-selective residue, Trp41 is the gating residue, blocking diffusion of protons from inside the virus but not from the outside.[9] Electrophysiology data show that when pH_{out} is lower than pH_{in}, there is robust inward proton flux, which is much larger than the outward current when the situation is reversed. This asymmetry is lost when Trp41 is replaced by other amino-acid residues except Tyr, which also has an electron-rich aromatic ring capable of forming cation-π interactions with His37. These results suggest that when the Trp41 gate is closed, protons cannot rapidly access His37 from inside the virus, thus outward flux is slow under low pH_{in} and high pH_{out}.

Table 3.1 Trp41 rotamers in various structures of the influenza M2 peptides, solved at different pH, in different membrane-mimetic solvents, using different protein constructs and biophysical methods.

PDB ID	pH	Lipid/detergent	Method	Construct	Trp41 (χ_1, χ_2)
1NYJ	7.0	DMPC	SSNMR	22-46	180°, -105°
2H95	8.8	DMPC	SSNMR	22-46	-100°, 110°
2L0J	7.5	DOPC/DOPE	MD, SSNMR	22-62	180°, -70°
2KAD	7.5	DLPC	SSNMR	22-46	180°, 90°
2KQT	7.5	DMPC	SSNMR	22-46	180°, 90°
3C9J	5.3	Octylglucoside	X-ray	22-46, G34A	180°, 90°
3LBW	6.5	Octylglucoside	X-ray	22-46, G34A	180°, 90°
2RLF	7.5	DHPC	Solution NMR	18-60	160°, -120°
2KWX	7.5	DHPC	Solution NMR	18-60, V27A	180°, -90°
2KIH	7.5	DHPC	Solution NMR	18-60, S31N	180°, -115°

DHPC, dihexanoylphosphatidylcholine.

Despite these functional data on the role of Trp41 in the channel activity, high-resolution structural information about pH-dependent His37-Trp41 aromatic interaction is still scarce, and the Trp41 side-chain conformation is still unresolved. Various high-resolution structures of M2 domains showed divergent Trp41 rotamers that placed the indole ring at varying positions relative to the pore (**Table 3.1**). Most structural models found the χ_1 angle to be *trans* (*t*) but differed on whether the χ_2 angle is positive or negative 100°. ^{19}F spin diffusion NMR experiments of 5-^{19}F (Hζ3)-labeled Trp41 in the M2 transmembrane peptide (M2TM)[10] found nearest-neighbor ^{19}F-^{19}F distances of ~11 Å at both high and low pH, suggesting a *t*90 rotamer, which points the five-membered nitrogen-containing pyrrole ring toward the channel pore (**Fig. 3.1a**). Crystal structures of M2TM at pH 6.5 and pH 5.3 also concluded the *t*90 rotamer.[11,12] In comparison, an earlier solid-state NMR measurement of the His37 Nε2-Trp41 Cγ distance in M2TM found a distance upper limit of 3.9 Å, which was interpreted to constrain the Trp rotamer to *t*-105 (χ_1 = 180°, χ_2 = -105°)[13] (**Fig. 3.1b**). The negative χ_2 angle points the six-membered benzene ring toward the center of the channel, occluding the pore. Solution NMR structures of a combined transmembrane (TM) and cytoplasmic helix domain of wild-type and mutant M2 proteins also concluded the Trp41 rotamer to be *t*-105 based on the side-chain J-couplings, residual dipolar couplings, and nuclear Overhauser effects.[14,15] Finally, a ^{19}F NMR study of the lineshapes of 6-^{19}F (Hη2) Trp41 in M2TM[16] found a

nearest-neighbor ^{19}F-^{19}F distance of ~8.0 Å at low pH and ~3.2 Å at high pH, which led to the proposal of a positive χ_2 of +100°, but a negative χ_1 of -100° and -50° for the high- and low-pH states, respectively (**Fig. 3.1c**).

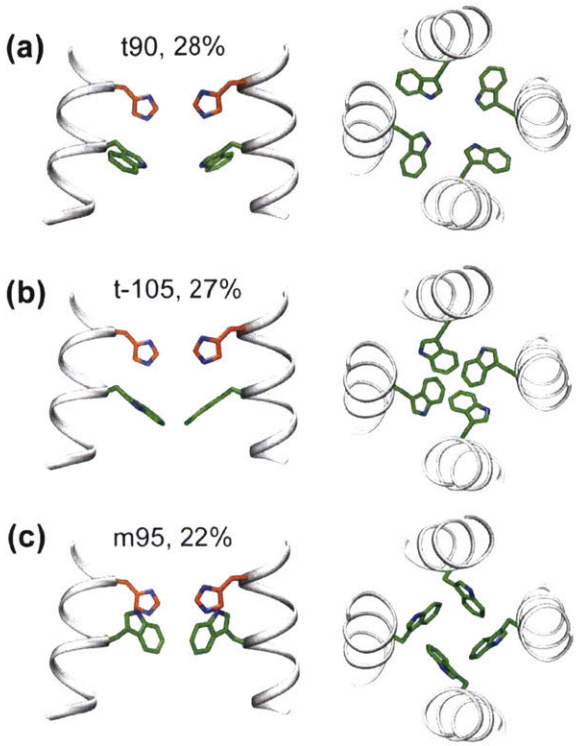

Figure 3.1 Several Trp41 rotamers that have been proposed in the literature using various experimental techniques (Table 1). Population percentages for α-helices from the Penultimate Rotamer Library are shown.[42] (*Left* column) Side view of two of the four helices; both His37 and Trp41 side chains are depicted. Note the shortest distances between these two residues are between two adjacent helices rather than from the same helix. (*Right column*) Top view of the four helices and the Trp41 sidechains. (a) *t*90 rotamer (χ_1 = 180°, χ_2 = +90°). (b) *t*-105 rotamer (χ_1 = 180°, χ_2 = -105°). (c) *m*95 rotamer (χ_1 = -60°, χ_2 = +95°).

Direct experimental evidence of His37-Trp41 aromatic interactions so far mainly comes from ultraviolet resonance Raman spectra, which showed Trp41 intensity changes at certain wavenumbers at low pH.[17] These changes were attributed to cation-π interactions between the imidazolium and the indole rings, whereas environmental hydrophobicity and indole hydrogen bonding were ruled out. A recent molecular dynamics simulation that modeled the HxxxW segment led to the proposal that cation-π interactions at low pH disrupted a low-barrier hydrogen bond between a cationic and neutral histidine,[18] thus activating the channel. However, measured

chemical shifts of the protons bonded to the imidazole nitrogens indicate regular His-water hydrogen bonds[8] rather than direct His-His hydrogen-bonds.

In this work, we investigate the conformation and dynamics of Trp41 in M2TM by measuring the Trp41 chemical shifts, His37-Trp41 distances, and indole dynamics as a function of pH. We show that Trp41 adopts the *t*90 conformation at both high and low pH, but the exact χ_1 and χ_2 angles differ by ~20°. These torsion angle differences, together with the known increase in the helix tilt angle at low pH, push the imidazole of one helix towards the indole of the neighboring helix at low pH. Moreover, measured order parameters indicate that the indole ring undergoes Gaussian fluctuations around both the χ_1 and χ_2 bonds at low pH, which further promote His-Trp interaction. These results give fresh insight into the coordinated motion between His37 and Trp41 that regulates proton conduction and channel gating.

3.3 Materials and Methods

3.3.1 Membrane Peptide Samples

The TM segment (residues 22-46: SSDPLVVAASII GILHLILWILDRL) of the Udorn strain of the influenza A M2 protein was synthesized by PrimmBiotech (Cambridge, MA). Two isotopically labeled M2TM peptides were synthesized, one containing uniformly ^{13}C-, ^{15}N-labeled Leu40 and Trp41 (LW-M2TM) and the other containing ^{13}C-, ^{15}N-labeled Gly34, His37, and 5-^{19}F-labeled Trp41 (GHW-M2TM).

Two virus-mimetic lipid membranes were used to reconstitute the peptides.[19,20] The VM membrane consists of DPPC (1,2-dipalmitoyl-*sn*-glycero-3-phosphocholine), DPPE (1,2-dipalmitoyl-*sn*-glycero-3-phosphoethanolamine), SM (egg sphingomyelin), and Chol (cholesterol) at a molar ratio of 21:21:28:30%, whereas the VM+ membrane consists of POPC (1-palmitoyl-2-oleoyl-*sn*-glycero-3-phosphocholine), POPE (1-palmitoyl-2-oleoyl-*sn*-glycero-3-phosphoethanolamine), SM, and Chol at a molar ratio of 25.6:25.6:25.6: 23%. The VM+ membrane is more dynamic than the VM membrane due to the use of chain-unsaturated phospholipids. For both membranes the lipids and cholesterol were dissolved in chloroform, SM

was dissolved in chloroform/methanol solution, and all components were combined at the desired molar ratios. The lipid mixture was dried under a stream of nitrogen gas, redissolved in cyclohexane, and lyophilized overnight. The resulting dry lipid powder was resuspended in the appropriate buffer, vortexed, and subject to 8-10 cycles of freeze-thawing to produce uniform vesicles. Lipid solutions were prepared at two different pH: the pH 8.5 sample used a 10 mM Tris buffer (10 mM Tris, 1 mM EDTA, 0.1 mM NaN_3) whereas the pH 4.5 sample used a 10 mM citric acid buffer (10 mM citric acid/sodium citrate, 1 mM EDTA, and 0.1 mM NaN_3).

M2TM was reconstituted into the lipid membrane by detergent dialysis. The peptide was dissolved in an octyl-β-D-glucoside (OG) solution that is well above the critical micelle concentration. The peptide/OG solution was then added to the lipid vesicle solution, at which point the OG concentration drops below the critical micelle concentration of 7.3 mg/mL at room temperature.[21] The mixed solution was shaken for 2 h and dialyzed for three days at room temperature with six buffer changes to remove the detergent. The LW-M2TM sample was reconstituted in the VM+ membrane, whereas the GHW-M2TM sample was reconstituted in the VM membrane. The peptide/lipid molar ratio was 1:15 for all samples. The dialyzed proteoliposomes solutions were centrifuged at 55,000 rpm at 5°C for 4 h to obtain homogeneous membrane pellets, which were spun into 4 mm MAS rotors for solid-state NMR experiments.

3.3.2 Solid-State NMR Experiments

All solid-state NMR (SSNMR) experiments were performed on a Bruker DSX-400 MHz (9.4 T) spectrometer (Bruker Biospin Billerica, MA) using two 4-mm MAS probes tuned to $^{1}H/^{13}C/^{15}N$ and $^{1}H/^{19}F$ frequencies. Typical radio frequency field strengths were 50 kHz for ^{13}C, 42 kHz for ^{15}N, 50 kHz for ^{19}F, and 62-83 kHz for ^{1}H. ^{13}C chemical shifts were referenced to the α-Gly carbonyl at 176.465 ppm on the tetramethylsilane scale, whereas ^{15}N chemical shifts were referenced to the ^{15}N signal of N-acetylvaline at 122.0 ppm on the liquid ammonia scale. ^{19}F chemical shifts were referenced to the ^{19}F signal of Teflon at -122.0 ppm.

One-dimensional (1D) ^{13}C cross-polarization spectra were measured under 7 kHz MAS between 243 K and 303 K. One-dimensional ^{13}C double-quantum-filtered (DQF) spectra were

measured at 303 K under 7 kHz MAS. Two-dimensional (2D) DQF ^{13}C-^{13}C correlation spectra were measured at 273 K under 7 kHz MAS. To determine motional order parameters, we measured ^{13}C-^{1}H dipolar couplings using the dipolar chemical-shift correlation experiment (DIPSHIFT) under 4.4 kHz MAS at 303 K. ^{1}H homonuclear decoupling was achieved using the MREV-8 sequence with a 90° pulse length of 3.5 μs. An MREV-8 scaling factor of 0.47 and a rigid-limit coupling of 22.7 kHz were used to calculate the Trp41 order parameters. Cε1-Nε1 and Cδ1-Nε1 dipolar couplings were measured using the rotational-echo double-resonance (REDOR) experiment[22] under 7 kHz MAS at 303 K. To calculate the C-N dipolar order parameter, a rigid-limit coupling of 1.15 kHz was used, which was verified on amino acid tryptophan.

A ^{13}C-^{19}F REDOR experiment was used to measure ^{13}C-^{19}F distances between ^{13}C-labeled His37 and 5-^{19}F-Trp41 in the GHW-M2TM samples at pH 8.5 and 4.5. The REDOR pulse sequence utilized composite 90°225°315° ^{19}F pulses to achieve broadband inversion of the ^{19}F polarization.[23] A soft Gaussian ^{13}C 180° pulse was applied in the middle of the REDOR period to refocus the ^{13}C chemical shift and the ^{13}C-^{13}C scalar coupling in the uniformly ^{13}C-labeled His37.[24,25] For the low-pH sample, MAS frequencies of 3.0, 3.3 and 6.6 kHz were used to detect the aromatic ^{13}C signals of His37 without overlap from the CO sidebands. For the high-pH sample, the REDOR experiment was conducted under 3.3 and 5.0 kHz MAS. All ^{13}C-^{19}F REDOR spectra were measured at 243 K and the mixing times varied from 1.2 to 9.6 ms, with 20,000-70,000 scans of signal averaging per spectrum.

The centerband-only-detection of exchange (CODEX) experiment[26,27] was used to measure interhelical Trp41-Trp41 distances. The experiments were conducted under 8 kHz MAS at ~230 K. Two rotor periods of ^{19}F π-pulses spaced at every half a rotor period was applied before and after a longitudinal mixing time to recouple the ^{19}F chemical shift anisotropy. After the second π-pulse train, a second longitudinal mixing time was applied to factor out ^{19}F T_1 relaxation. Analogous to the REDOR experiments, the CODEX experiments were conducted in a pairwise fashion, with a control (S_0) and dephasing (S) experiment, and normalized intensity (S_0/S) is fit to obtain distances. CODEX mixing times of 1 ms to 2 s were used.

3.3.3 Data Analysis and Simulation

The error bars for the ^{13}C-^{19}F REDOR data points were propagated from the experimental signal/noise ratios. The ^{13}C-^{19}F REDOR S/S_0 values as a function of mixing time were first simulated using the program SIMPSON,[28] assuming two-spin geometry. Best-fit distances were obtained by minimizing the root-mean-square deviations (RMSDs) between the simulated and experimental intensities. After the Trp41 (χ_1, χ_2) rotamers were determined, we used the SPINEVOLUTION program[29] to conduct model-dependent five-spin (one ^{13}C and four ^{19}F spins) simulations for each possible rotamer. PDB files were generated for each Trp41 rotamer, then the coordinates for each Trp41 ^{13}C and ^{19}F sites were provided to the SPINEVOLUTION program for use in the five-spin simulations.

The ^{19}F CODEX exchange data were fit using a MATLAB program (The MathWorks, Natick, MA) that employs the exchange-matrix formalism to treat spin diffusion in the four-spin system. The 4 x 4 exchange matrix contains rate constants that are proportional to an overlap integral and the square of the internuclear dipolar couplings. Based on previous model compound results, the overlap integral value is 37 μs[10,30] under our experimental conditions. Best-fit distances were obtained by minimizing the RMSD between the calculated and experimental CODEX intensities.

DIPSHIFT curves are simulated using a FORTRAN program. A phenomenological T_2 relaxation time was applied to the best-fit simulated curves to reproduce the observed asymmetry in the time signal.

3.3.4 Analysis of Trp41 Rotameric Conformation

To model the sidechain conformation of Trp41 from the measured His-Trp and Trp-Trp distances, we first considered the choice of the backbone structure. For the high-pH data, we used the distance-constrained solid-state NMR structure (PDB:2KQT) and the 1.65-Å crystal structure (PDB:3LBW) as backbone structural models, because they have similar helix tilt angles. For the low-pH data, we used the pH 5.3 crystal structure (PDB:3C9J) and the DLPC

(dilauroylphosphatidylcholine)-based solid-state NMR structural model (PDB:2KAD).[31,32] These two backbone structures resemble each other in having a helix tilt angle of 35-38°, which is consistent with the helix orientation measured using oriented-membrane solid-state NMR experiments.[13,33] The DLPC-based solid-state NMR structure has C4 symmetry, which simplifies the rotamer analysis, whereas the low-pH crystal structure (PDB:3C9J) has significant asymmetry.

In all distance analyses, the His37 sidechain was fixed to the *tt* rotamer ($\chi_1 = \chi_2 = 180°$) determined by SSNMR and crystallography.[6,11] The Trp41 χ_1 and χ_2 angles were varied and the His-Trp ^{13}C-^{19}F distances and Trp-Trp intermolecular ^{19}F-^{19}F distances were measured and compared to the experimental data. In a first round of analysis, the Trp41 χ_1 and χ_2 angles were manually varied in 30° steps in CHIMERA[34] to obtain a coarse-grained map of the possible Trp41 rotamers that agree with the experimental data. These results were then refined in a second round of analysis, where the software YASARA[35] was used to tabulate the ^{13}C-^{19}F and ^{19}F-^{19}F distances in 5° steps of χ_1 and χ_2. The best fit was determined by calculating the RMSDs between the model-free two-spin best-fit distances for the experimental data and the model-dependent distances. For the latter, out of four possible values for each type of distance, only the shortest distance was used to compare with the experimental result in order to simplify the analysis. For the high-pH sample, the RMSD was the sum of the Cα-F, Cγ-F, Cε1-F, and F-F distance RMSDs. For the low-pH sample, the Cδ2-F distance was also included in the RMSD analysis. The rotamers with the minimum RMSD were then checked in CHIMERA for obvious steric clashes. For the best-fit Trp41 rotamers without steric conflict, we extracted the shortest ^{13}C-^{19}F distances for two-spin SIMPSON simulations of the data, and all four distances for five-spin SPINEVOLUTION simulations. These model-specific simulations were compared with the experimental REDOR and CODEX data to check for agreement.

3.3.5 Calculation of Motionally Averaged Dipolar Couplings in the Trp41 Side Chain

The motional amplitudes around the Cα-Cβ and Cβ-Cγ bonds of Trp41 were reflected in the motionally averaged C-H and C-N dipolar couplings, i.e., order parameters. To constrain the motional geometry, we calculated the order parameters of the indole ring using a Gaussian biaxial

fluctuation model,[36] where the indole is rotated around the Cα-Cβ and Cβ-Cγ bonds by ϕ_1 and ϕ_2, respectively. The distribution of ϕ_1 and ϕ_2 was a normalized Gaussian function g_1 and g_2 with a standard deviation of σ_1 and σ_2, with a cutoff at $2\sigma_n$. The most probable rotation angle ϕ_n, which corresponds to the center of the Gaussian, was the equilibrium torsion angle χ_n determined from the ^{13}C-^{19}F and ^{19}F-^{19}F distance measurements. The two torsional rotations were assumed to be independent, and all covalent bond angles were held fixed.

The Cβ-Cγ axis was rotated by a certain angle $\phi_{1,n}$, around the Cα-Cβ bond, then the C-H dipolar tensor in the indole ring was rotated around the Cβ-Cγ axis by $\phi_{2,k}$. The motionally averaged dipolar tensor $\overleftrightarrow{D}(\phi_{1,n}, \phi_{2,k})$ was calculated as the weighted average of the individual rotated tensors (3 x 3 matrices) for systematically varied $\phi_{1,n}$ and $\phi_{2,n}$ values, where the weighting function is the product of the normalized Gaussian distributions:

$$\overline{\overleftrightarrow{D}}(\sigma_1, \sigma_2) = \sum_k \sum_n \overleftrightarrow{D}(\phi_{1,n}, \phi_{2,k})\, g_1(\phi_{1,n}, \sigma_1) g_2(\phi_{2,k}, \sigma_2).$$

The principal values $\overline{D}_x, \overline{D}_y, \overline{D}_z$ of the traceless average tensor $\overline{\overleftrightarrow{D}}$, ordered such that $\overline{D}_z$ has the largest magnitude and $\overline{D}_y$ the smallest, give the motionally averaged dipolar coupling constant $\overline{\delta} = \overline{D}_z$. The asymmetry parameter of the averaged coupling tensor is $\overline{\eta} = (\overline{D}_y - \overline{D}_x)/\overline{D}_z$. The calculated $\overline{\delta}$ was converted to the order parameter as $S_{CH} = \overline{\delta}/\delta$, and then compared with the measured S_{CH} from the DIPSHIFT experiments. To determine the values of σ_1 and σ_2 that are compatible with all measured order parameters, S_{CH} as a function of σ_1 and σ_2 for several indole bonds were superimposed, and the regions consistent with the experimental values were highlighted.

3.4 Results and Discussion

3.4.1 Conformation of Trp41

To determine the side-chain conformation of Trp41 and its dependence on pH, we measured the Trp41 ^{13}C and ^{15}N chemical shifts using 2D ^{13}C-^{13}C and ^{15}N-^{13}C correlation

experiments. **Fig. 3.2** shows representative 1D and 2D spectra of LW-M2TM. The 1D ^{13}C spectra of M2TM show similar ^{13}C intensity patterns at high and low pH. No significant intensity changes were observed between 303 and 243 K, consistent with the previously reported immobilization of M2TM by the cholesterol-rich virus-mimetic membranes.[19,20] The Cα and Cβ chemical shifts of L40 and W41 are generally consistent with the α-helical secondary structure, as expected for this four-helix bundle. However, the L40 Cα and Cβ chemical shifts change to more ideal α-helical values at low pH (larger Cα and smaller Cβ chemical shifts), consistent with previous reports that the helix becomes straighter and more tilted at low pH due to charge repulsion at His37.[32]

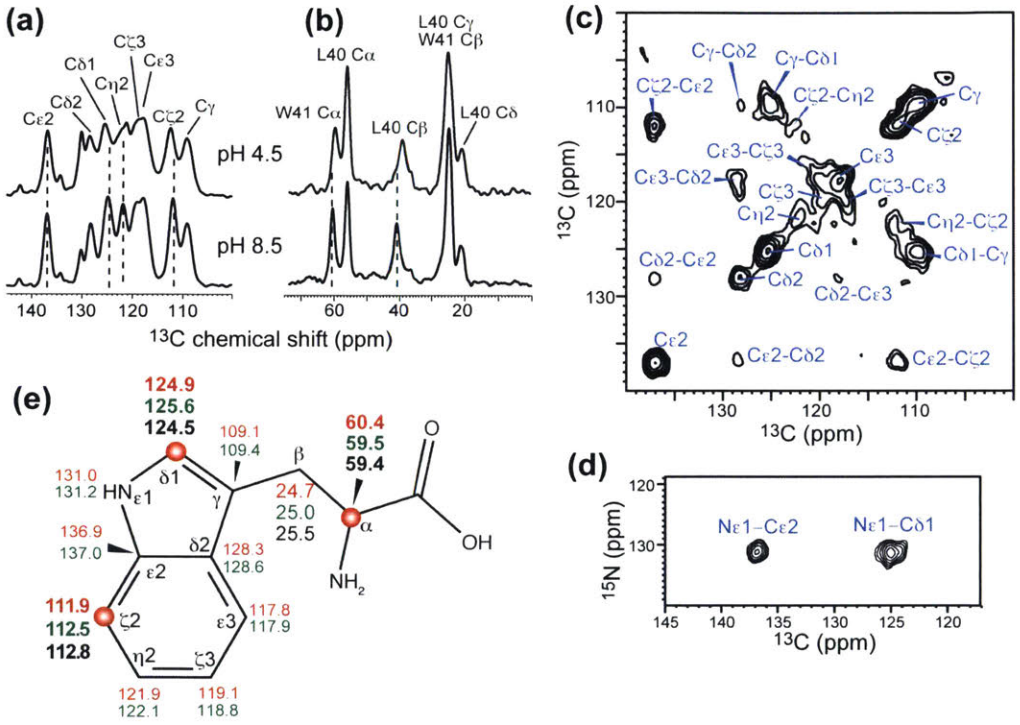

Figure 3.2 Trp41 chemical shifts at pH 4.5 and 8.5 in LW-M2TM bound to the VM+ membrane. (a) Aromatic region of the 1D ^{13}C cross-polarization spectra at pH 4.5 and 8.5. (b) Aliphatic region of the 1D ^{13}C DQF spectra at the two pH conditions. The lipid peaks were suppressed by the double-quantum filter. Note the chemical shift changes of Trp41 and Leu40 Cα and Cβ peaks, indicating pH-induced small conformation changes of the helix backbone. (c) 2D ^{13}C-^{13}C DQF spectrum of LW-M2TM at pH 8.5. (d) 2D ^{15}N-^{13}C correlation spectrum of the peptide at high pH. (e) Summary of Trp41 ^{13}C and ^{15}N chemical shifts at high pH (red) and low pH (green). (*Black*) High-pH chemical shifts of M2(22-62) in DOPC/DOPE bilayers[38] for sites that have > 0.5 ppm chemical shift difference from the M2TM values. (*Bold*) Chemical shifts that differ by > 0.5 ppm between high and low pH. All ^{13}C chemical shifts are reported on the tetramethylsilane scale.

Full assignment of the indole ^{13}C and ^{15}N chemical shifts were obtained from 2D ^{13}C-^{13}C DQF correlation spectra and ^{15}N-^{13}C correlation spectra (**Fig. 3.2c,d**). In these spectra, only a single chemical shift was observed for each site, with an average ^{13}C line-width of 1.8 ppm. This contrasts with the peak doubling reported for the longer M2 construct that contains both the TM and cytoplasmic helices,[37,38] for which chemical shift differences as large as 2.7 ppm were detected, which is larger than the resolution limit of our spectra. The chemical shift difference for the peak-doubled longer M2 construct is the largest at backbone Cα (about 2 ppm), which strongly suggests that the cytoplasmic helix affects the backbone conformation of the TM domain.[37,38] This effect is consistent with the recent report that the cytoplasmic helix has the ability to cause the formation of high-curvature membrane domains, which shifts the conformational equilibrium of the TM segment to a form that is incompetent for binding the antiviral drug amantadine.[19,39] The absence of such peak doubling for the TM construct used here indicates that the TM segment adopts a single conformation in the absence of the cytoplasmic helix. Based on all available experimental evidence so far,[6,19,32] this conformation is sensitive to both pH and drug and is thus functionally relevant.

Further information about the local environment of Trp41 can be gleaned by comparing the ^{13}C and ^{15}N chemical shifts between pH 8.5 and pH 4.5 and between the short and long M2 constructs at high pH (**Fig. 3.2e**). For the TM construct, most side-chain atoms exhibit similar (< 0.5 ppm) chemical shifts at high and low pH, with the exception of Cδ1 and Cζ2, which also show nonnegligible chemical shift differences between the short and long M2 constructs (**Fig. 3.2e**). For Cα and Cβ chemical shifts, which are sensitive to the backbone conformation, the long-peptide chemical shifts are closer to the short peptide's low-pH chemical shifts. This phenomenon can be understood. The presence of the cytoplasmic helix is known to moderately increase proton conduction,[40] which implies that the channel may adopt the acid-activated conformation more readily in the presence of the cytoplasmic helix. The M2(22-62) chemical shifts were also measured at slightly lower pH (pH 7.5) than the high-pH sample here, thus a higher percentage of tetramers should exist in the partially charged states for proton conduction. Finally, the longer M2 construct was studied in the more fluid membranes of DOPC/DOPE (dioleoylphosphatidyl-choline / dioleoylphosphatidyl-ethanolamine) in one case[38] and DPhPC (diphytanoylphosphatidylcholine)

membrane in another,[37] which should facilitate the conformational motion that is necessary for the TM helix to adopt the low-pH conformation.

3.4.2 His37-Trp41 and Trp41-Trp41 Distances

His37-Trp41 aromatic interactions have been implicated in channel gating at low pH based on resonance Raman data.[17] Here we directly measured the distances between these two residues using ^{13}C-labeled His37 and 5-^{19}F-labeled Trp41 (**Fig. 3.3a**). The latter corresponds to the Hζ3 position of the indole ring. The high gyromagnetic ratio of the ^{19}F spin allows ^{13}C-^{19}F distances to be measured up to ~8 Å (~55 Hz).[23,41] We measured the ^{13}C-^{19}F distances using a variant of the REDOR experiment, where a selective ^{13}C π-pulse was applied in the middle of the REDOR period to suppress one-bond ^{13}C-^{13}C J-coupling and lengthen the effective ^{13}C T_2.[24,25] **Fig. 3.3b,c** shows representative REDOR spectra, where the His37 Cγ, Cε1, and Cδ2 signals, which are sensitive to pH, are assigned according to published 2D spectra.[6] Several MAS frequencies were used in these experiments to avoid resonance overlap between the carbonyl sidebands and the aromatic carbons of interest. The largest intensity differences between the control (S_0) and dephased (S) REDOR spectra were observed for Cγ and Cδ2 of the low-pH sample, which showed S/S_0 values as low as 0.3 by ~8 ms. The high-pH peptide shows comparatively less REDOR dephasing, indicating longer distances between His37 and Trp41. The difference is the largest for Cγ (**Fig. 3.3d**), whose dephasing corresponds to a two-spin Cγ-F distance of 8.4 Å at pH 8.5 but 6.2 Å at pH 4.5. For Cδ2, only low-pH data could be obtained with sufficient sensitivity, and the REDOR dephasing was fast, corresponding to a short two-spin distance of 6.0 Å.

Complementing the His37-Trp41 ^{13}C-^{19}F distances, we also measured the ^{19}F-^{19}F distances using the ^{19}F CODEX experiment (see **Fig. 3.S1** in the Supporting Material). We have previously measured these distances in DMPC (dimyristoylphosphatidylcholine)-bound M2TM, where the peptide was reconstituted into the membrane using a different protocol.[10] Under those conditions, the nearest-neighbor distance between the ^{19}F spins was 11 ± 1 Å at both high and low pH. For the virus-mimetic membrane samples prepared by detergent dialysis, the CODEX dephasing curves show detectable differences between high and low pH: the best-fit nearest-neighbor distance is

11.3 Å at high pH and 12.4 Å at low pH, indicating that the inter-Trp separation is enlarged at low pH. This is consistent with most available experimental evidence showing that the C-terminal region of the four-helix bundle is expanded at low pH.[12]

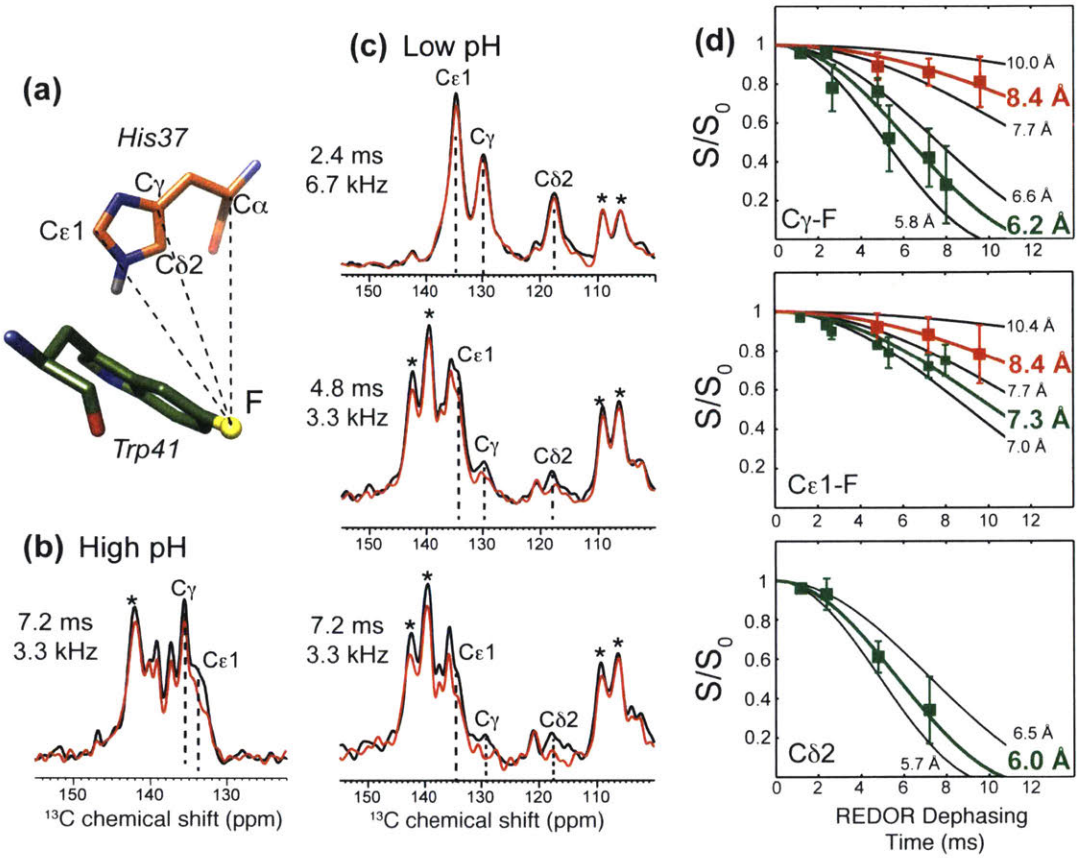

Figure 3.3 ^{13}C-^{19}F REDOR distance measurements of ^{13}C-labeled His37 and 5-^{19}F-labeled Trp41 in VM bound M2TM. (a) Approximate spatial arrangement of His37 of one helix and Trp41 of the neighboring helix. (b) Representative ^{13}C-detected ^{19}F-dephased REDOR control (S_0, *black*) and dephased (S, *red*) spectra of the peptide at pH 8.5. The spectra were measured at 243 K under 3.3 kHz MAS. (c) Representative REDOR spectra of the peptide at pH 4.5. The spectra were measured under 3.0, 3.3 and 6.7 kHz MAS in order to detect all His37 aromatic ^{13}C signals without overlap from the carbonyl sidebands (*asterisks*). (d) ^{13}C-^{19}F REDOR S/S_0 intensity as a function of mixing time for the high-pH (*red*) and low-pH (*green*) peptides. De novo two-spin simulations are shown. Best-fit distances are highlighted for the high-pH data (*red*) and the low-pH data (*green*).

3.4.3 pH-Dependent Trp41 Rotameric Structure and His37-Trp41 Contact

These ^{13}C-^{19}F and ^{19}F-^{19}F distances, together with the known backbone structure of M2TM[42] and the known His37 side-chain conformation,[6] allowed us to constrain the Trp41 side-chain conformation. Two PDB structures were used for each pH condition to assess the influence of the backbone conformation on the Trp41 rotamer determination. Interresidue distances were extracted as a function of Trp41 χ_1 and χ_2 angles to compare with the measured ^{13}C-^{19}F and ^{19}F-^{19}F distances. The two high-pH models (PDB:2KQT and PDB:3LBW) yielded a consistent best-fit rotamer of (-175°, +120°) (**Fig. 3.4**), indicating that the rotamer is ~*t*90. In contrast, the two low-pH structures did not give a single consensus rotamer. The solid-state NMR backbone structure (PDB:2KAD) gave a best-fit Trp41 rotamer of (-155°, 135°) whereas the low-pH crystal structure (PDB:3C9J) gave two possible Trp41 rotamers: (-115°, 45°) and (-145°, -125°) when solutions with steric clashes were ruled out. Because the PDB:3C9J backbone shows considerable asymmetry, and it is energetically more costly for Trp41 to undergo a large-angle conformational change than a small-angle change between high and low pH, we favor the (-155°, 135°) rotamer as the low-pH Trp41 conformation. The overall similarity of the χ_2 angle at high and low pH is consistent with the Raman data,[17] while the *trans*-χ_1 angle is consistent with the previously measured His37 Nε2-Trp41 Cγ distance.[13] Other rotamer minima seen in **Fig. 3.4** can be ruled out based on steric conflicts. For example, multiple rotamer minima in PDB:3C9J have steric clashes with either the helix backbone or other sidechains in the HxxxW segment (see **Fig. 3.S2a,b**). The (-90°, 180°) rotamer in PDB:3LBW and PDB:2KAD causes steric clashes among the four Trp side chains (see **Fig. 3.S2c**). The (95°, -125°) rotamer in PDB:3LBW and PDB:2KQT is rarely populated in the protein database[43] and is therefore not considered further (see **Fig. 3.S2d**).

Fig. 3.5a,b shows model-dependent fits of the ^{13}C-^{19}F REDOR and ^{19}F-^{19}F CODEX data at high and low pH for the best-fit Trp41 rotamers. For the ^{13}C-^{19}F REDOR data, the five-spin and two-spin simulations both show good agreement with the measured data within experimental uncertainty, indicating that the shortest interhelical distance accounts for the majority of the observed REDOR dephasing.

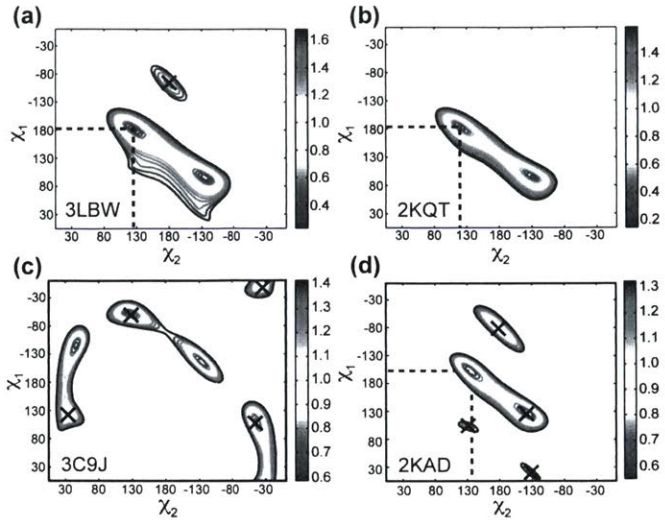

Figure 3.4 Total RMSD between the measured and modeled Cα-F, Cγ-F, Cε1-F, Cδ2-F, ^{19}F-^{19}F distances as a function of Trp41 (χ_1, χ_2) torsion angles. Different backbone structure models for M2TM at high (a, b) and low (c, d) pH are used for structural modeling. Only the shortest of the four possible distances in the tetramer for each two-spin combination is used to compare with the experimental data. (a) PDB:3LBW backbone structure. (b) PDB:2KQT backbone structure. (c) PDB:3C9J backbone structure. (d) PDB:2KAD backbone structure. Between the two high-pH backbone structures, consensus (χ_1, χ_2) results were found at (-175°, 120°). For the low-pH state, the best-fit Trp41 rotamer depends on the backbone structure. For the PDB:2KAD structure (d), the best-fit solution is (χ_1, χ_2) = (-155°, 135°), whereas the PDB:3C9J structure (c) shows two rotamer minima without steric conflict. (*Crosses*) Rotamers with steric clashes, which are not considered further (see **Fig. 3.S2**).

The high- and low-pH His-Trp side chains are compared in **Fig. 3.5c,d**. At both pH conditions, the Trp41 side chain broadly adopts the *t*90 rotamer, which is consistent with the observed pH sensitivity of the Cδ1 and Cζ2 chemical shifts, because these two carbons of the indole ring face the aqueous pore. In contrast, the *t*-105 rotamer would point Cδ1 to the lipid (**Fig. 3.1**), inconsistent with the pH sensitivity of its chemical shift. Under this broad similarity of the Trp41 rotamer, His37 and Trp41 establish closer contact at low pH, due to a downward movement of the imidazole rings as a result of the larger helix tilt angle. The 15-20° Trp41 χ_1 and χ_2 angle differences between the two pH have a more subtle effect on the aromatic packing: the χ_1 change (from -175° at high pH to -155° at low pH) pushes the indole ring toward the center of the channel, while the χ_2 change (from 120° at high pH to 135° at low pH) moves the Cη2/Cζ3 end of the indole towards the C-terminus. These counterdirectional χ_1 and χ_2 changes may serve to avoid

steric clashes with the side chains of Leu38 and Ile42 while still allowing the indole face to be exposed to His37. The closer contact between the imidazole and indole rings of two neighboring helices at low pH creates stronger aromatic interactions, consistent with the Raman spectral changes.[17]

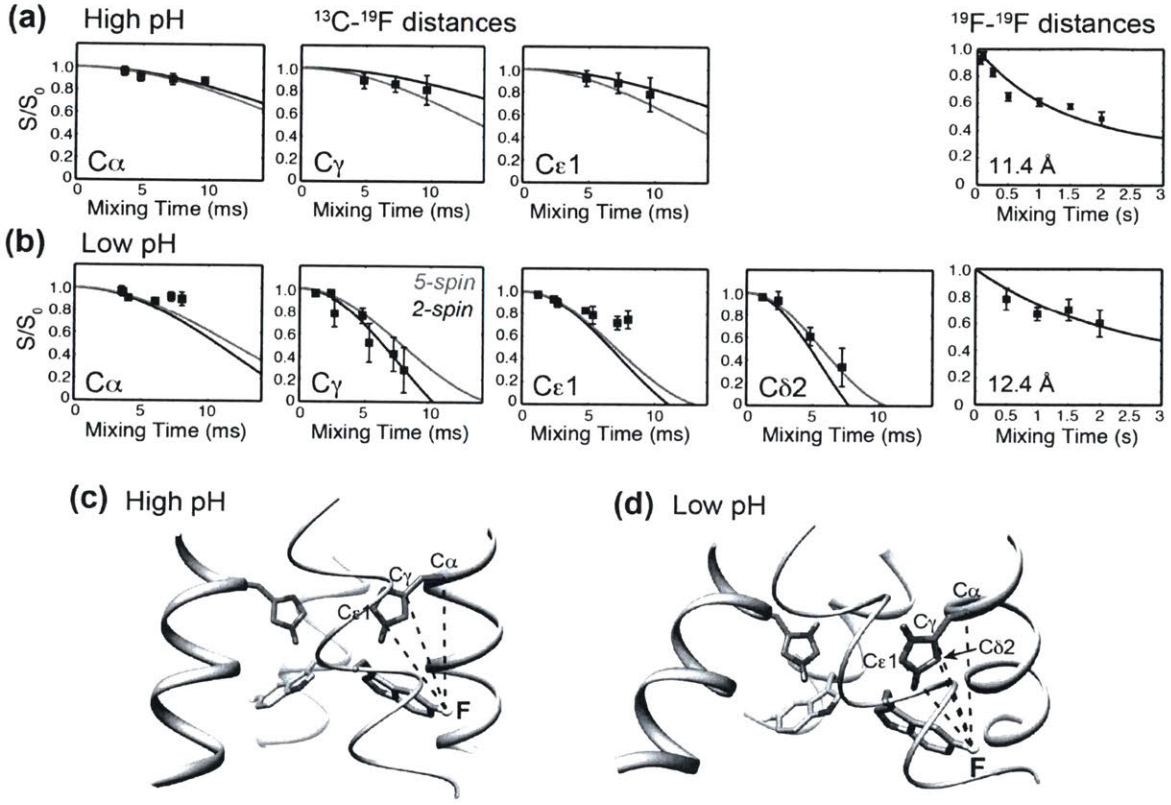

Figure 3.5 His37-Trp41 contacts and Trp41 side-chain conformation at high and low pH. (a) Best fits of the ^{13}C-^{19}F REDOR and ^{19}F-^{19}F CODEX data at high pH, using PDB:2KQT for the backbone structure and a Trp41 rotamer of $\chi_1 = -175°$ and $\chi_2 = +120°$. (*Red* and *black curves*) Model-dependent five-spin and two-spin best-fit simulations. (b) Best fits of the ^{13}C-^{19}F REDOR and ^{19}F-^{19}F CODEX data at low pH, using PDB:2KAD as the backbone structure and a Trp41 rotamer of $\chi_1 = -155°$ and $\chi_2 = +135°$. (c) His-Trp region of the high-pH structure (PDB:2KQT), with Trp41 (χ_1, χ_2) angles of (-175°, 120°). (d) His-Trp region of the low-pH structure (PDB:2KAD), where the Trp41 rotamer is (-155°, 135°). (*Dashed* lines) Relevant His-Trp ^{13}C-^{19}F distances. At low pH, the imidazole and indole rings approach each other more closely, due to the combined effect of the helix backbone orientation change and Trp41 (χ_1, χ_2) changes.

3.4.4 Dynamics of the Trp41 Side Chain

To investigate whether the Trp41 side chain is dynamic to affect proton gating and interaction with His37, we measured the order parameters of several indole ^{13}C-^{1}H and ^{13}C-^{15}N bonds at high temperature. **Fig. 3.6** shows representative ^{13}C-^{1}H and ^{13}C-^{15}N dipolar coupling data obtained at 303 K. The ^{13}C-^{1}H dipolar couplings were measured using the 2D DIPSHIFT experiment whereas the ^{13}C-^{15}N dipolar couplings were measured using REDOR. We found order parameters of 0.7-0.9 for the indole bonds (with uncertainty of 0.05), with the lowest bond order parameters along the Cζ2-Cε3 axis. pH change caused the largest difference in the order parameters of the Cδ1-H and Cζ3-H bonds, with the low-pH sample showing smaller S_{CH} values or larger-amplitude dynamics.

Qualitatively, the relatively large order parameters (> 0.7) indicate that the motional amplitude of the indole ring is small at both pH conditions. To determine the motional geometry, we first considered simple two-site jump motions around either the Cβ-Cγ bond (χ_2) or the Cα-Cβ bond (χ_1). The indole bonds have fixed orientations from the Cβ-Cγ axis but variable angles from the Cα-Cβ axis depending on the χ_2 angle. The equilibrium (χ_1, χ_2) angles are known from the above His-Trp distance measurements: (-175°, 120°) at high pH and (-155°, 135°) at low pH. Thus, the indole bond orientations relative to the Cα-Cβ and Cβ-Cγ axes are determined by the equilibrium conformation and the jump angle. We calculated the average dipolar couplings as a function of jump angle for the various indole bonds, as shown before for His37,[6] and did not find any jump angle that simultaneously satisfied all the measured order parameters. This indicates that the indole ring does not undergo a simple two-site jump motion.

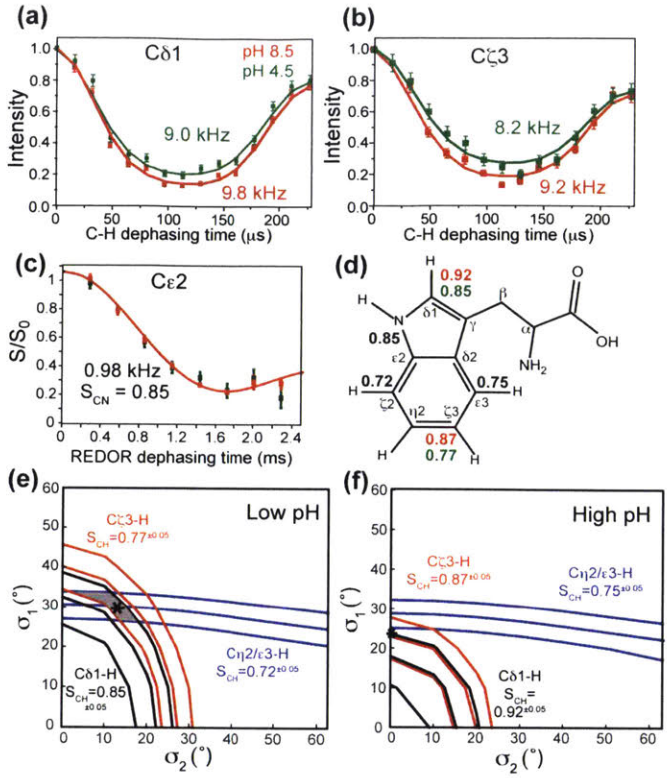

Figure 3.6 Trp41 side-chain dynamics at high pH (*red*) and low pH (*green*) in VM+ membranes at 303 K. (a,b) Representative ^{13}C-^{1}H DIPSHIFT curves for (a) Cδ1-H and (b) Cζ3-H couplings. (c) Cε2-Nε1 REDOR dephasing curve. (d) Summary of all dipolar order parameters of the indole ring at high and low pH. Cδ1-H and Cζ3-H bonds show different order parameters between high (*red*) and low (*green*) pH. Most order parameters have an experimental uncertainty of ± 0.05. (e) Calculated order parameters as a function of the standard deviations (σ) of the Gaussian fluctuations around the Cα-Cβ and Cβ-Cγ bonds. Only values that agree with the measured low-pH S_{CH} are shown. Small-amplitude Gaussian fluctuations with $\sigma_1 \approx 30°$ and $\sigma_2 \approx 15°$ (*shaded area*) agree with all measured order parameters. (f) Calculated order parameters that agree with the high-pH S_{CH} values. Only torsional motion around the χ_1 axis is compatible with the experimental data, with $\sigma_1 \approx 25°$ (indicated by a *star*).

This prompted us to consider a more general motional model, which is Gaussian fluctuation of the indole ring around both the Cα-Cβ and Cβ-Cγ bonds with Gaussian widths σ_1 and σ_2. Successive rotations around the Cα-Cβ and Cβ-Cγ bonds change the orientations of the indole bonds and the associated dipolar couplings. The average dipolar coupling tensors were obtained as a function of the standard deviation, σ_1 and σ_2, of the Gaussian functions. The principal values of the average tensor yielded the order parameter and average asymmetry parameter. **Fig. 3.6e,f**

shows the (χ_1, χ_2) values for the calculated Cδ1-Hδ1, Cζ2-Hζ2, Cε3-Hε3 and Cζ3-Hζ3 order parameters that agree with the measured S_{CH} values within experimental uncertainty. For the low-pH data, the Gaussian widths that agree with all measured S_{CH} values are approximately $\sigma_1 = 30°$ and $\sigma_2 = 15°$, indicating that the indole undergoes small-angle fluctuations around both the χ_1 and χ_2 bonds. In contrast, at high pH, the larger S_{CH} for Cδ1-H and Cζ3-H bonds indicate a clear change in the motional geometry, with negligible χ_2 changes. The remaining χ_1 torsional motion has a σ_1 of 25°. At both pH, the calculations show that the motionally averaged asymmetry parameters do not deviate significantly from uniaxiality (see **Fig. 3.S3**), thus validating the uniaxial approximation in the order parameter extraction from the experimental data.

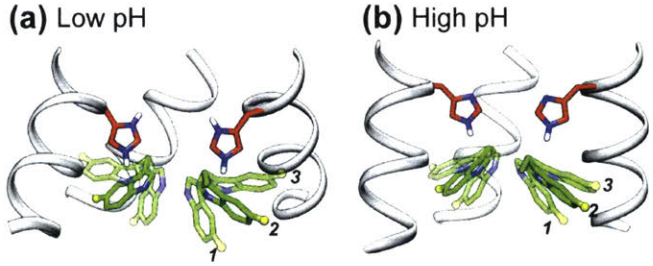

Figure 3.7. Trp41 conformational dynamics and aromatic interaction with His37. (a) Low-pH scenario. The measured equilibrium (χ_1, χ_2) rotamer of (-155°, 135°) is shown as position 2, together with two limiting rotamers based on the measured order parameters. The (-125°, 150°) rotamer (position 3) is closer to His37 whereas the (175°, 120°) rotamer (position 1) is further away from His37. These angles were chosen to be one standard deviation (30° for σ_1 and 15° for σ_2) from the average angle. (b) High-pH scenario. The equilibrium rotamer is (-175°, 120°) (position 2), and the limiting rotamers are (-150°,120°) (position 1) and (160°, 120°) (position 3), based on a σ_1 of 25° and no χ_2 fluctuation.

Figure 3.7 depicts the equilibrium Trp41 rotameric conformation at high and low pH as well as their dynamic changes. To indicate the range of excursion of the indole ring, we show two limiting rotamers that are one standard deviation (σ) away from the equilibrium χ_1 and χ_2 angles. It can be seen that at acidic pH, not only is the average position of the indole ring closer to the imidazolium compared to high pH, but the χ_1 and χ_2 motions further appose the indole to His37. As a result, at low pH, the indole alternates between very strong and very weak cation-π interactions with the imidazolium during its reorientational motion.[44] To give a quantitative estimate of the His37-Trp41 proximity, we calculated the distances of His37 Nε2 to the center of

the six-membered benzene ring and the center of the five-membered pyrrole ring. For the equilibrium low-pH Trp41 rotamer of (-155°, 135°), Nε2 is 4.3 Å from the center of the benzene ring and 3.0 Å from the pyrrole ring (**Table 3.2**). Due to the torsional fluctuation, the closest approach of indole to the imidazolium has distances of 3.5 Å and 2.5 Å, whereas the remote position of the indole shows a Nε2-benzene distance of 5.3 Å and an Nε2-pyrrole distance of 3.6 Å. For comparison, at high pH, the His-Trp distances for the equilibrium Trp41 conformation are longer, 5.4 Å and 3.7 Å, respectively, comparable to the largest separation at low pH, and the Trp41 motional range is too small to make a significant difference (**Table 3.2**).

Table 3.2 Trp41-His37 distances as a function of pH and rotameric dynamics.

pH	Indole position	Trp41 (χ_1, χ_2)	Nε2-benzene (Å)	Nε2-pyrrole (Å)
Low	Position 3	(-125°, 150°)	3.5	2.5
	Equilibrium	(-155°, 135°)	4.3	3.0
	Position 1	(175°, 120°)	5.3	3.6
High	Position 3	(160°, 120°)	5.3	3.6
	Equilibrium	(-175°, 120°)	5.4	3.7
	Position 1	(-150°, 120°)	5.5	3.8

His37 Nε2 distances to the center of the six-membered benzene ring and to the midpoint of the Nε1-Cγ vector of the pyrrole ring are listed. Positions 3 and 1 correspond to those shown in Fig. 7.

3.4.5 Implication of the Trp41 Structure and Dynamics to Channel Gating

The above results provide direct experimental evidence for the closer contact between His37 and Trp41 at acidic pH and the existence of the cation-π interaction. The closest approach between His37 Nε2 and the indole face is 2.5 Å, which is shorter than the reported distance range of 3.5-4.0 Å between cationic amino-acid side chains such as Arg and aromatic rings[44] in proteins. This close proximity is achieved by the combined actions of the increased helix tilt angle and the Trp41 side-chain conformational dynamics. At low pH, the equilibrium conformation of Trp41 is roughly perpendicular to the His37 side chain (**Fig. 3.7**), suggesting that the His-Trp interaction has a significant hydrogen-bonding component.[44] At high pH, the equilibrium position of the indole ring is similar to the furthest position of the indole from the imidazolium at low pH, and the

motional amplitude is insufficient to bring the indole closer to His37. Therefore, the aromatic interaction is significantly weaker.

We propose that this close contact between His37 and Trp41 at low pH is an important reason for the low proton flux of the M2 channel compared to the measured His37-water proton-exchange rate. ^{15}N NMR lineshapes indicated a water-His37 proton exchange rate of 4.5 x 10^5 s^{-1} between pH 5 and 6.[7] This is at least two orders of magnitude faster than the proton flux of 10-10^3 per second estimated from whole-cell currents and liposome assays.[45-47] Therefore, at most only 1% of His-exchanged protons successfully reach the virion. The dynamically fluctuating His-Trp separation at low pH obtained from our experiments suggest that, when the indole approaches the imidazolium ring, the cation-π interaction should prevent proton dissociation from His37 to water, while as the indole moves away from the imidaolium, the protons can be released to water. This concept has been recently proposed based on molecular modeling of the His-Trp dyad.[18] Our results provide the first concrete experimental evidence for this dynamic gating model.

In addition to Trp41-mediated regulation of the proton flux, other mechanisms can exist to affect the number of protons released to the C-terminus: these include futile exchange between multiple histidines through intervening water molecules[8] and occasional proton release to the N-terminus, although the latter should be less frequent than proton release to the C-terminus due to the inherent pH gradient in the channel.[48]

In a channel with a reverse proton gradient, where the virus interior is acidic but the exterior is neutral, the lack of reverse current has been attributed to the gating function of Trp41.[9] Although NMR experiments, similar to most other biophysical techniques, cannot easily mimic the pH gradient used in functional assays, our data provide some insight into this inward rectification. The distance-based structural modeling here indicates that the key first event that reduces the His-Trp separation is the backbone orientational change due to His-His charge repulsion. Thus, as long as the protons from the virus interior cannot pass Trp41 to reach His37, no imidazole protonation and charge repulsion can occur, and the helix tilt angle will remain relatively small, corresponding to the situation in **Fig. 3.7b**.

3.5 Conclusion

The His-Trp distances, Trp41 chemical shifts and dynamics measured here provide detailed insights into the aromatic interaction between these two functional residues of the M2 proton channel. Our results indicate that the two aromatic side chains are able to approach each other at low pH due to the increased tilt angle of the helix and the microsecond (χ_1, χ_2) torsional fluctuations of the indole ring at low pH. The low-pH side-chain motion periodically enhances and weakens the His37-Trp41 cation-π interaction as the indole moves through its trajectory, thus blocking and releasing protons. In contrast, at high pH only χ_1 motion is present and the average position of the indole is further from the imidazole due to small (χ_1, χ_2) differences. The pH-dependent Trp41 side-chain dynamics, with amplitudes of 15-30°, are reminiscent of the small-angle (45°) χ_2 change of His37 that shuttles protons.[6,7] Nature seems to have designed the compact functional heart of this ion channel by relying on economical small-angle side-chain conformational dynamics, coupled with backbone orientational changes, to regulate proton conduction and channel gating.

3.6 Acknowledgement

This work is supported by National Institutes of Health grant No. GM088204.

3.7 References

[1] L. H. Pinto and R. A. Lamb. "The M2 Proton Channels of Influenza A and B Viruses." *J. Biol. Chem.* **2006**, 281, 8997-9000.

[2] S. D. Cady, W. B. Luo, F. Hu and M. Hong. "Structure and Function of the Influenza A M2 Proton Channel." *Biochemistry* **2009**, 48, 7356-7364.

[3] M. Hong and W. F. DeGrado "Structural Basis for Proton Conduction and Inhibition by the Influenza M2 Protein." *Protein Sci.* **2012**, 21, 1620-1633.

[4] F. Ciampor, D. Cmarko, J. Cmarkova and E. Zadvodska. "Influenza Virus M2 Protein and Heamagglutanin Conformation Changes During Intracellular Transport." *Acta Virol.* **1995**, 39, 171-181.

[5] J. S. Rossman, X. Jing, G. P. Leser and R. A. Lamb. "Influenza Virus M2 Protein Mediates ESCRT-Independent Membrane Scission." *Cell* **2010**, 142, 902-913.

[6] F. Hu, W. Luo and M. Hong. "Mechanisms of Proton Conduction and Gating by Influenza M2 Proton Channels from Solid-State NMR." *Science* **2010**, 330, 505-508.

[7] F. Hu, K. Schmidt-Rohr and M. Hong. "NMR Detection of pH-Dependent Histidine-Water Proton Exchange Reveals the Conduction Mechanism of a Transmembrane Proton Channel." *J. Am. Chem. Soc.* **2012**, 134, 3703-3713.

[8] M. Hong, K. J. Fritzsching and J. K.Williams "Hydrogen-Bonding Partner of the Proton-Conducting Histidine in the Influenza M2 Proton Channel Revealed from ^{1}H Chemical Shifts." *J. Am. Chem. Soc.* **2012**, 134, 14753-14755.

[9] Y. Tang, F. Zaitseva, R. A. Lamb and L. H. Pinto. "The Gate of the Influenza Virus M2 Proton Channel is Formed by a Single Tryptophan Residue." *J. Biol. Chem.* **2002**, 277, 39880-39886.

[10] W. Luo, R. Mani and M. Hong. "Sidechain Conformation and Gating of the M2 Transmembrane Peptide Proton Channel of Influenza A Virus from Solid-State NMR." *J. Phys. Chem.* **2007**, 111, 10825-10832.

[11] A. Acharya, V. Carnevale, G. Fiorin, B. G. Levine, A. Polishchuk, V. Balannick, I. Samish, R. A. Lamb, L. H. Pinto, W. F. DeGrado and M. L. Klein. "Structural Mechanism of Proton Transport Through the Influenza A M2 Protein." *Proc. Natl. Acad. Sci. U.S.A.* **2010**, 107, 15075-15080.

[12] A. L. Stouffer, R. Acharya, D. Salom, A. S. Levine, L. Di Costanzo, C. S. Soto, V. Tereshko, V. Nanda, S. Stayrook and W. F. DeGrado. "Structural Basis for the Function and Inhibition of an Influenza Virus Proton Channel." *Nature* **2008**, 451, 596-599.

[13] K. Nishimura, S. Kim, L. Zhang and T. A. Cross. "The Closed State of a H+ Channel Helical Bundle Combining Precise Orientational and Distance Restraints from Solid State NMR." *Biochemistry* **2002**, 41, 13170-13177.

[14] J. R. Schnell and J. J. Chou. "Structure and Mechanism of the M2 Proton Channel of Influenza A Virus." *Nature* **2008**, 451, 591-595.

[15] R. M. Pielak, J. R. Schnell and J. J. Chou. "Mechanism of Drug Inhibition and Drug Resistance of Influenza A M2 Channel." *Proc. Natl. Acad. Sci. U.S.A.* **2009**, 106, 7379-7384.

[16] R. Witter, F. Nozirov, U. Sternberg, T. A. Cross, A. S. Ulrich and R. Fu. "Solid-State ^{19}F NMR Spectroscopy Reveals that Trp41 Participates in the Gating Mechanism of the M2 Proton Channel of Influenza A Virus." *J. Am. Chem. Soc.* **2008**, 130, 918-924.

[17] A. Okada, T. Miura and H. Takeuchi. "Protonation of Histidine and Histidine-Tryptophan Interaction in the Activation of the M2 Ion Channel from Influenza A Virus." *Biochemistry* **2001**, 40, 6053-6060.

[18] M. Sharma, M. Yi, H. Dong, H. Qin, E. Peterson, D. Busath, H. X. Zhou and T. A. Cross. "Insight Into the Mechanism of the Influenza A Proton Channel from a Structure in a Lipid Bilayer." *Science* **2010**, 330, 509-512.

[19] S. D. Cady, T. Wang and M. Hong. "Membrane-Dependent Effects of a Cytoplasmic Helix on the Structure and Drug Binding of the Influenza Virus M2 Protein." *J. Am. Chem. Soc.* **2011**, 133, 11572-11579.

[20] W. Luo, S. D. Cady and M. Hong. "Immobilization of the Influenza A M2 Transmembrane Peptide in Virus-Envelope Mimetic Lipid Membranes: A Solid-State NMR Investigation." *Biochemistry* **2009**, 48, 6361-6368.

[21] M. da Graca Miguel, O. Eidelman, M. Ollivon and A. Walter. "Temperature Dependence of the Vesicle-Micelle Transition of Egg Phophatidylcholine and Octyl Glucoside." *Biochemistry* **1989**, 28, 8921-8928.

[22] T. Gullion and J. Schaefer. "Rotational Echo Double Resonance NMR." *J. Magn. Reson.* **1989**, 81, 196-200.

[23] S. Wi, N. Sinha and M. Hong. "Long Range ^{1}H-^{19}F Distance Measurement in Peptides by Solid-State NMR." *J. Am. Chem. Soc.* **2004**, 126, 12754-12755.

[24] C. P. Jaroniec, B. A. Tounge, J. Herzfeld and R. G. Griffin. "Frequency Selective Heteronuclear Dipolar Recoupling in Rotating Solids: Accurate ^{13}C-^{15}N Distance Measurements in Uniformly ^{13}C,^{15}N-Labeled Peptides." *J. Am. Chem. Soc.* **2001**, 123, 3507-3519.

[25] C. P. Jaroniec, B. A. Tounge, C. M. Rienstra, J. Herzfeld and R. G. Griffin. "Measurement of ^{13}C-^{15}N Distances in Uniformly ^{13}C Labeled Biomolecules: J-Decoupled REDOR." *J. Am. Chem. Soc.* **1999**, 121, 10237-10238.

[26] E. R. deAzevedo, T. J. Bonagamba, W. Hu and K. Schmidt-Rohr. "Centerband-Only Detection of Exchange: Efficient Analysis of Dynamics in Solids by NMR." *J. Am. Chem. Soc.* **1999**, 121, 8411-8412.

[27] E. R. deAzevedo, S. B. Kennedy and M. Hong. "Determining Slow Motions in Extensively Labeled Proteins by ^{13}C-Detected ^{15}N Exchange NMR." *Chem. Phys. Lett.* **2000**, 321, 43-48.

[28] M. Bak, T. Rasmussen and N. C. Nielsen. "SIMPSON: A General Simulation Program for Solid-State NMR Spectroscopy." *J. Magn. Reson.* **2000**, 147, 296-330.

[29] M. Veshtort and R. G. Griffin. "SPINEVOLUTION: A Powerful Tool for the Simulation of Solid and Liquid State NMR Experiments." *J. Magn. Reson.* **2006**, 178, 248-282.

[30] W. Luo and M. Hong. "Determination of the Oligomeric Number and Intermolecular Distances of Membrane Protein Assemblies by Anisotropic ^{1}H-Driven Spin Diffusion NMR Spectroscopy." *J. Am. Chem. Soc.* **2006**, 128, 7242-7251.

[31] S. D. Cady, T. V. Mishanina and M. Hong. "Structure of Amantadine-Bound M2 Transmembrane Peptide of Influenza A in Lipid Bilayers from Magic-Angle-Spinning Solid-State NMR: The Role of Ser31 in Amantadine Binding." *J. Mol. Biol.* **2009**, 385, 1127-1141.

[32] F. Hu, W. Luo, S. D. Cady and M. Hong. "Conformational Plasticity of the Influenza A M2 Transmembrane Peptide in Lipid Bilayers Under Varying pH, Drug Binding and Membrane Thickness." *Biochim. Biophys. Acta* **2011**, 1808, 415-423.

[33] J. Wang, S. Kim, F. Kovacs and T. A. Cross. "Structure of the Transmembrane Region of the M2 Protein H^+ Channel." *Protein Sci.* **2001**, 10, 2241-2250.

[34] E. F. Pettersen, T. D. Goddard, C. C. Huang, G. S. Couch, D. M. Greenblatt, E. C. Meng and Ferrin, T.E. "UCSF Chimera-A Visualization System for Exploratory Research and Analysis." *J. Compu. Chem.* **2004**, 25, 1605-1612.

[35] E. Krieger, G. Koraimann and G. Vriend. "Increasing the Precision of Comparative Models with YASARA NOVA-A Self-parameterizing Force Field." *Proteins: Struct., Funct., Genet.* **2002**, 47, 393-402.

[36] T. Bremi and R. Bruschweiler. "Locally Anisotropic Internal Polypeptide Backbone Dynamics by NMR Relaxation." *J. Am. Chem. Soc.* **1997**, 28, 6672-6673.

[37] L. B. Andreas, M. T. Eddy, J. J. Chou and R. G. Griffin. "Magic-Angle-Spinning NMR of the Drug Resistant S31N M2 Proton Transporter from Influenza A." *J. Am. Chem. Soc.* **2012**, 134, 7215-7218.

[38] T. V. Can, M. Sharma, I. Hung, P. L. Gor'kov, W. W. Brey and T. A. Cross. "Magic Angle Spinning and Oriented Sample Solid-State NMR Structural Restraints Combine for Influenza A M2 Protein Functional Insights." *J. Am. Chem. Soc.* **2012**, 134, 9022–9025.

[39] T. Wang, S. D. Cady and M. Hong. "NMR Determination of Protein Partitioning into Membrane Domains with Different Curvatures and Application to the Influenza M2 Peptide." *Biophys. J.* **2012**, 102, 787-794.

[40] C. Ma, A. L. Polishchuk, Y. Ohigashi, A. L. Stouffer, A. Schön, E. Magavern, X. Jing, J. D. Lear, E. Freire, R. A. Lamb, W. F. DeGrado and L. H. Pinto. "Identification of the Functional Core of the Influenza A Virus A/M2 Proton-Selective Ion Channel." *Proc. Natl. Acad. Sci. U.S.A.* **2009**, 106, 12283-12288.

[41] R. Mani, M. Tang, X. Wu, J. J. Buffy, A. J. Waring, M. A. Sherman and M. Hong. "Membrane-Bound Dimer Structure of a β-Hairpin Antimicrobial Peptide from Rotational-Echo Double-Resonance Solid-State NMR." *Biochemistry* **2006**, 45, 8341-8349.

[42] S. D. Cady, K. Schmidt-Rohr, J. Wang, C. S. Soto, W. F. DeGrado and M. Hong. "Structure of the Amantadine Binding Site of Influenza M2 Proton Channels in Lipid Bilayers." *Nature* **2010**, 463, 689-692.

[43] S. C. Lovell, J. M. Word, J. S. Richardson and D. C. Richardson. "The Penultimate Rotamer Library." *Proteins: Struct., Funct., Genet.* **2000**, 40, 389-408.

[44] J. C. Ma and D. A. Dougherty. "The Cation-π Interaction." *Chem Rev.* **1997**, 97, 1303-1324.

[45] T. I. Lin and C. Schroeder. "Definitive Assignment of Proton Selectivity and Attoampere Unitary Current to the M2 Ion Channel Protein of Influenza A Virus." *J. Virol.* **2001**, 75, 3647-3656.

[46] J. A. Mould, J. E. Drury, S. M. Frings, U. B. Kaupp, A. Pekosz, R. A. Lamb and L. H. Pinto. "Permeation and Activation of the M2 Ion Channel of Influenza A Virus." *J. Biol. Chem.* **2000**, 275, 31038-31050.

[47] J. A. Mould, H. C. Li, C. S. Dudlak, J. D. Lear, A. Pekosz, R. A. Lamb and L. H. Pinto. "Mechanism for Proton Conduction of the M2 Ion Channel of Influenza A Virus." *J. Biol. Chem.* **2000**, 275, 8592-8599.

[48] M. Yi, T. A. Cross and H. X. Zhou. "Conformational Heterogeneity of the M2 Proton Channel and a Structural Model for Channel Activation." *Proc. Natl. Acad. Sci. U.S.A.* **2009**, 106:13311-13316.

3.8 Supporting Information

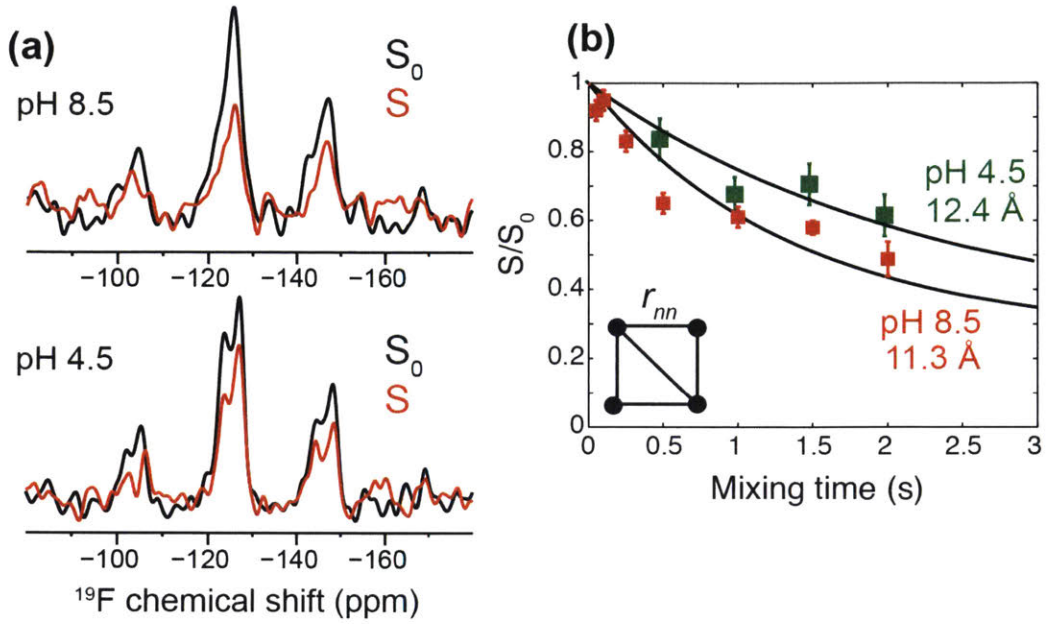

Figure 3.S1 ^{19}F CODEX spin diffusion data of 5-^{19}F-labeled Trp41 in VM-bound M2TM. (a) Representative CODEX control (S_0) and dephased (S) spectra of the pH 8.5 and pH 4.5 samples under 8 kHz MAS at 230 - 235 K. (b) Normalized S/S_0 intensity as a function of mixing time. The high-pH sample shows faster decay than the low-pH sample, indicating shorter ^{19}F-^{19}F intermolecular distances. Best fits assuming a symmetric tetramer gave a nearest-neighbor distance of 11.3 Å for the high-pH sample and 12.4 Å for the low-pH sample.

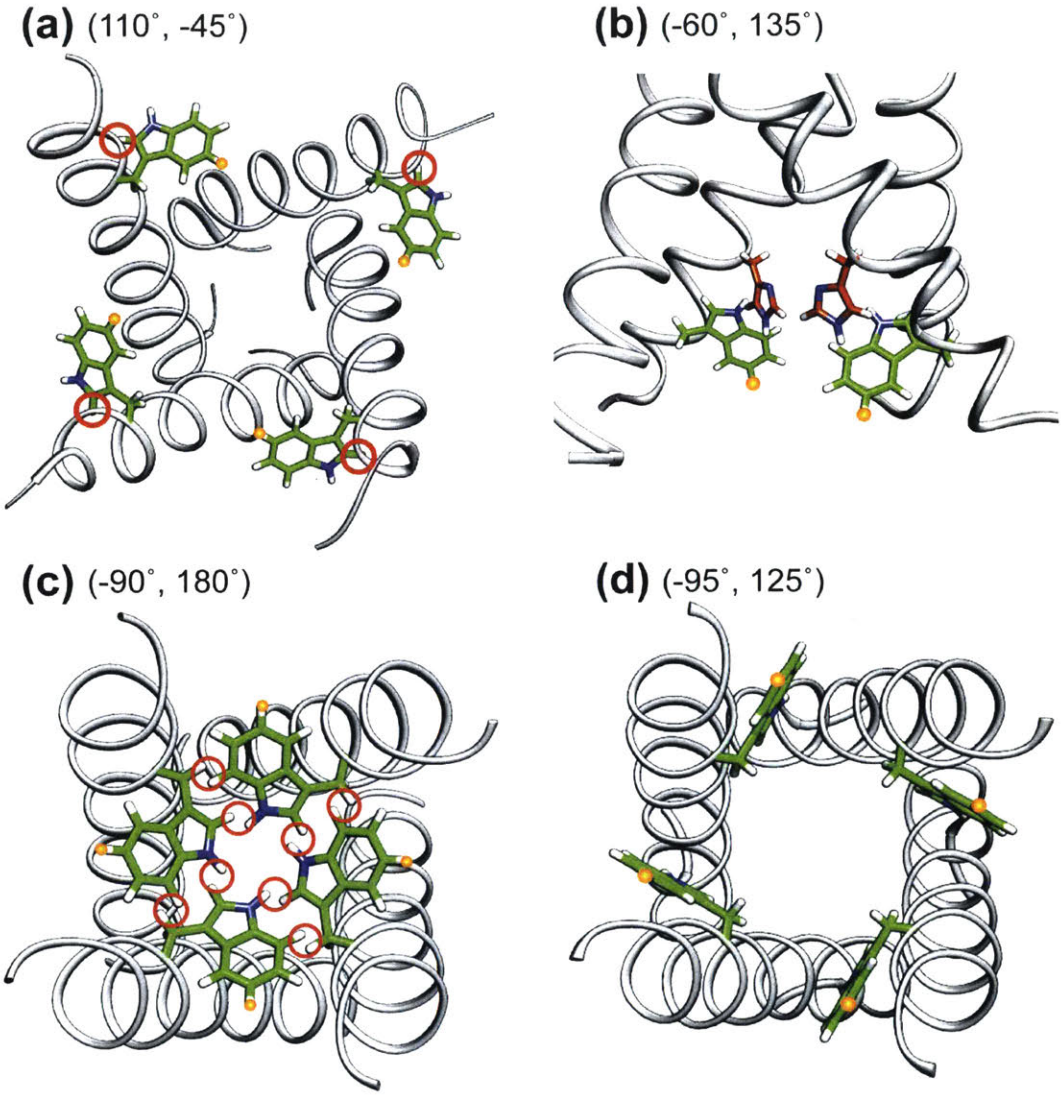

Figure 3.S2 Examples of Trp41 (χ_1, χ_2) rotamers that are ruled out because of steric clash or low statistical probability. The 5-^{19}F position (Hζ3) is highlighted in orange. (a) PDB:3C9J backbone with a Trp rotamer of (110°, -45°) has steric clash between the Trp41 Cδ1 and the helix backbone (red circles). (b) PDB:3C9J backbone with a Trp rotamer of (-60°,135°) has intrahelical steric clashes between the His37 Nε2-H, Cδ2-H bonds and the Trp 41 Cζ2-H, Nε1-H bonds. For clarity only two of the four rings are shown for each residue. (c) PDB:3LBW backbone with a Trp41 rotamer of (-90°, 180°) shows Trp-Trp clashes between Nε1 and Cδ1, and between Cβ and Cζ2 of adjacent indole rings (red circles). (d) PDB:2KQT backbone with a Trp rotamer (95°,-125°). This is rarely populated in α-helices (~2%).[43]

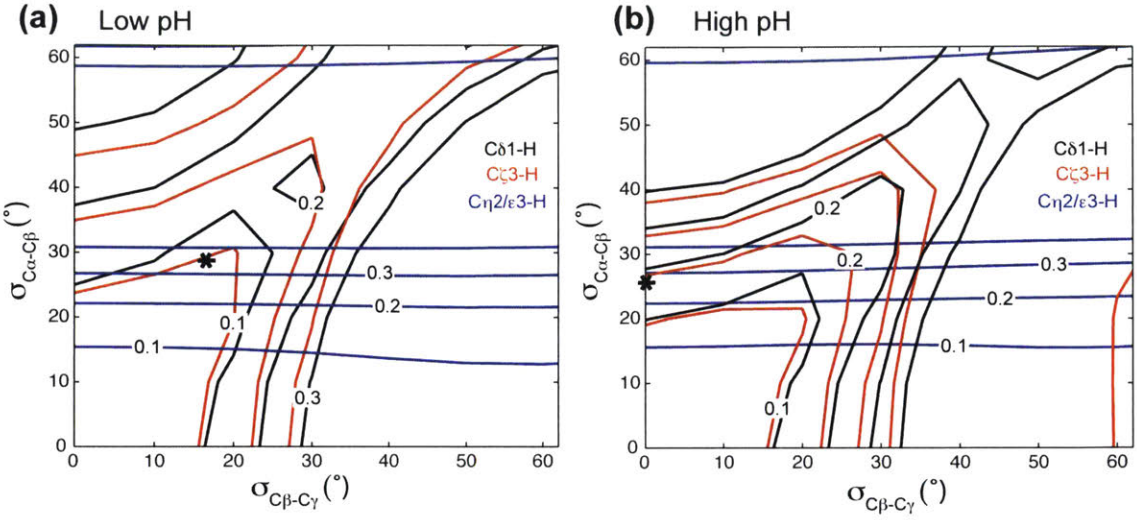

Figure 3.S3 Motionally averaged asymmetry parameters $\overline{\eta}$ as a function of the standard deviations of the Gaussian fluctuations around the Cα-Cβ and Cβ-Cγ axes. Only asymmetry parameters between 0.1 and 0.4 are indicated for simplicity. (a) Low pH data, calculated using $\chi_2 = +135°$. (b) High pH data, calculated using $\chi_2 = +120°$. The position of the best-fit motional amplitudes at each pH is indicated with a cross. With these motional amplitudes, the averaged asymmetry parameters do not deviate significantly from 1. The Cδ1-H and Cζ3-H couplings have an $\overline{\eta}$ of less than 0.1 at low pH and about 0.2 at high pH. The Cη2/Cε3-H couplings have a modestly larger $\overline{\eta}$ of 0.3. Within experimental uncertainty, these small $\overline{\eta}$ values are not detected in the C-H dipolar dephasing curves, and the uniaxial approximation is reasonable for estimating the order parameters from the experimental data.

4. Drug-Induced Conformational and Dynamical Changes of the S31N Mutant of the Influenza M2 Proton Channel Investigated by Solid-State NMR

Jonathan K. Williams[1], Daniel Tietze[1], Jun Wang[2], Yibing Wu[2], William F. DeGrado[2], Mei Hong[1]

[1]Department of Chemistry, Iowa State University, Ames, IA
[2]Department of Pharmaceutical Chemistry, University of California San Francisco, San Francisco, CA

Journal of the American Chemical Society. **2013**, vol. 135, pp. 9885-9897.
DOI: 10.1021/ja4041412

4.1 Abstract

The M2 protein of influenza A viruses forms a tetrameric proton channel that is targeted by the amantadine class of antiviral drugs. A S31N mutation in the transmembrane (TM) domain of the protein has caused widespread amantadine resistance in most of the currently circulating flu viruses. Recently, a new family of compounds based on amantadine- and aryl-substituted isoxazole were discovered to inhibit the S31N channel activity and reduce replication of S31N-harboring viruses. We now use solid-state NMR spectroscopy to investigate the effects of one of these isoxazole compounds, WJ352, on the conformation of the S31N TM segment and the dynamics of the proton-selective residue, His37. Chemical shift perturbations show that WJ352 changes the conformational equilibrium of multiple TM residues, with the maximal perturbation occurring at the crucial Asn31. ^{13}C-^{2}H distance measurements and ^{1}H-^{1}H NOE cross peaks indicate that the adamantane moiety of the drug is bound in the spacious pore between Asn31 and Gly34 while the phenyl tail is located near Val27. Thus, the polar amine points to the channel exterior rather than to His37, in contrast to amantadine and rimantadine in the wild-type channel, suggesting that the drug is significantly stabilized by hydrophobic interactions between the adamantane and the TM peptide. ^{15}N and ^{13}C chemical shifts indicate that at low pH, His37 undergoes fast exchange among the τ tautomer, the π tautomer, and the cationic state due to proton transfer with water. The exchange rate is higher than the wild-type channel, consistent with the larger single-channel

conductance of the mutant. Drug binding at acidic pH largely suppresses this exchange, reverting the histidines to a similar charge distribution as that of the high-pH closed state.

4.2 Introduction

The M2 protein of influenza A viruses spans the viral envelope and forms a tetrameric channel that conducts protons across the membrane when the external environment is acidic. This proton channel activity is important for virus uncoating[1,2] and in some viruses, also for maintaining the high pH of the trans-Golgi network to prevent premature conformational changes of hemagglutinin.[3] A single histidine residue, His37, in the transmembrane (TM) domain of the protein is responsible for pH activation and proton selectivity of the channel.[4] Detailed information about how His37 mediates proton conduction has been obtained from solid-state NMR studies of phospholipid-bound M2 TM peptides (M2TM).[5] At acidic pH, the imidazolium rings undergo small-amplitude reorientations[6] and exchange protons with water molecules at a rate of 10^5 s^{-1}.[7,8] The energy barrier of the ring motion, found to be at least 60 kJ/mol, is consistent with the proton-conduction energy barrier of ~100 kJ/mol measured in liposome assays.[9] ^{15}N NMR chemical shifts allowed determination of the four pK_a values of the His37 tetrad.[8,10] In virus-mimetic lipid bilayers, the His37 tetrad protonates with pK_a values of 7.6, 6.8, 4.9 and 4.2. When compared with pH-dependent proton currents, these pK_a values indicate that the +3 channels conduct the majority of the proton current at the physiological pH of the endosome.[8] A 1.65-Å X-ray crystal structure showed that the four histidines form an extensive hydrogen-bonding network with a cluster of water molecules,[11] suggesting proton delocalization. One helical turn away from His37, Trp41 is responsible for inward rectification of the channel.[12] Cation-π interaction between His37 and Trp41 was observed in resonance Raman spectra[13] and suggested by molecular dynamics (MD) simulations.[14] Recent solid-state NMR distance and dynamics data showed that at low pH Trp41 moved closer to His37 and underwent microsecond side chain reorientations.[15] The resulting periodic cation-π interactions with the cationic His37 may restrict proton release from His37, thus explaining the low proton flux compared to the water-His proton exchange rate.

The M2 proton channel is inhibited by the amantadine class of antiviral drugs, which blocks the N-terminal region of the channel pore near residue Ser31.[16-19] Bound at this site, amantadine

(**Fig. 4.1**) dehydrates the aqueous pore,[20] which prevents protonation of the His37 sidechains,[8,21] in turn stopping conformational changes of the helix backbone and the imidazole rings that are important for proton conduction.[8] However, in the past decade, several amantadine-resistant TM mutations have become widespread in the M2 proteins of circulating flu viruses.[22] The most prevalent drug-resistant mutant, S31N, dominates in H1N1, H5N1, and H3N2 strains isolated from humans, birds, and swine.[23-25] The replacement of the hydroxyl group by the bulkier carboxamide at residue 31 not only abolished amantadine binding,[26,27] but also gave rise to a moderately better proton channel, with ~20% higher single-channel conductance than the wild-type (WT) protein.[28]

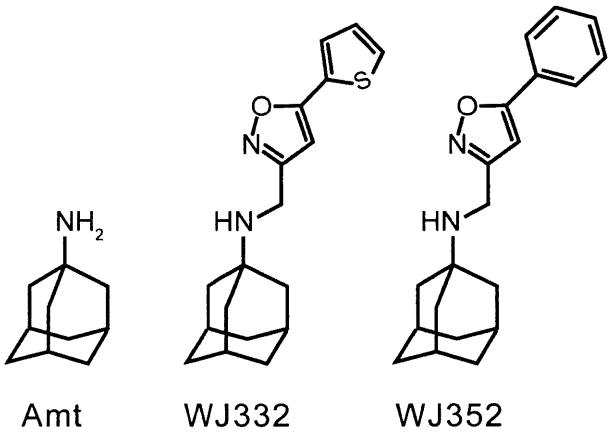

Figure 4.1 Chemical structures of adamantyl-based drugs against influenza M2 proton channels: amantadine (Amt) against the WT protein, and WJ332 and WJ352 against the S31N mutant.

To inhibit the S31N-M2 channel, Wang *et al.* recently designed a family of isoxazole compounds.[29] By functionalizing the heterocyclic isoxazole with amantadine and aryl substituents, they identified molecules that selectively inhibit S31N-M2 with a potency greater than that of amantadine against the WT channel. Solution NMR structures of the S31N M2(19-49) peptide in DPC micelles[29] bound with one such compound, 5-(thiophen-2-yl)-3-(*N*-adamantyl-methylamine)-1,2-isoxazole (WJ332), showed both similarities and major differences to the structure of amantadine-complexed WT peptide.[18] This drug is a derivative of amantadine, in which the basic amine group is linked to a biheteroaryl group via a methylene group (**Fig. 4.1**), which retains the basicity of the amine. In the solution NMR structure of the S31N-WJ332 complex, the adamantane group is located in approximately the same region of the channel as amantadine in the WT, but it is flipped by 180° so that the pendant amino group projects upward

toward the outside of the channel rather than downward toward His37, in contrast to the direction of amantadine and rimantadine in WT M2.[19] MD simulations based on the structure indicate that the N31 backbone carbonyl group helps solvate the ammonium group of WJ332 via water-mediated interactions, and the isoxazole group of the drug additionally interacts with N31.

Given the reversed direction of the isoxazole drug in micelle-bound S31N-M2, the predicted small energy difference between the amine-up and amine-down orientations, and the possibility of detergent micelles affecting drug binding, we wish to verify the binding mode of the isoxazole drug in phospholipid-bilayer-bound S31N-M2 using solid-state NMR spectroscopy. To facilitate isotopic labeling of the drug, we chose WJ352, a potent analogue of WJ332 in which the terminal thiophene is replaced by a phenyl group (**Fig. 4.1**). Solid-state NMR also allows us to answer important questions about the charge state of the tetramer recognized by the drug. Amantadine binds with greater affinity to the neutral form of the channel than to the low-pH forms.[30] The neutral form may be stabilized by amantadine in part because the charged ammonium destabilizes the cationic form of His37 and in part because the neutral form of the channel has a conformation that is more complementary to the shape of the drug.[18] However, the ammonium group of the reverse oriented isoxazole is more distant from His37, so it was not clear whether the isoxazole would bind exclusively to the neutral state of the channel, or whether it might also associate with partially charged channels. Finally, studies in phospholipid bilayers allow us to examine the conformational and proton exchange dynamics of S31N-M2, since the mutant appeared more mobile than the WT peptide in detergent micelles.[26,29]

Using magic-angle-spinning (MAS) solid-state NMR spectroscopy, we have now measured the effects of WJ352 on the chemical shifts of key TM residues in S31N and on the proton exchange dynamics of His37. Chemical shift perturbation and drug-peptide distance measurements show that the adamantyl group is located between N31 and G34 while the phenyl tail points to the N-terminus. ^{15}N and ^{13}C chemical shifts of His37 show that S31N-M2 undergoes faster proton exchange with water than the WT. This exchange causes rapid interconversion among three states of His, which is observed for the first time. Drug binding suppressed most of the chemical exchange, providing direct evidence of the mechanism of inhibition of this mutant proton channel.

4.3 Materials and Methods

4.3.1 Isotopically Labeled Peptides and Drugs

Two peptide constructs were used in this study, one spanning residues 19-49 and the other spanning residues 22-46 of the S31N mutant of the Udorn strain of M2. The amino acid sequence of residues 19-49 is SNDSSPLVVAANIIGILHLILWILDRLFFK. Three isotopically labeled peptides were synthesized using an optimized protocol as described previously.[19] After cleavage from the resin, the crude peptide was precipitated in cold ether and purified via HPLC (Vydac, C4 column). The first peptide contained ^{13}C, ^{15}N-labeled residues at G34, I35, H37, and L38 ($GIHL_{22\text{-}46,S31N}$). The second sample contained ^{13}C, ^{15}N-labeled V27, A30, N31, I33, and G34 ($VANIG_{19\text{-}49,S31N}$). The third sample contained ^{13}C, ^{15}N-labeled V28, G34, I35, H37, and L38 ($VGIHL_{19\text{-}49,S31N}$).

5-phenyl-3-(*N*-adamantyl-methylamine)-1,2-isoxazole (WJ352) was synthesized using a modified procedure from that described previously[29] to incorporate deuterium labels. The synthesis protocol is provided in the Supporting Information. Two compounds were synthesized, one with deuterated benzene (d_5-WJ352) and the other with perdeuterated adamantane (d_{15}-WJ352) (**Fig. 4.S1**). The purified drugs were verified by ^1H solution NMR and electrospray ionization mass spectrometry to have the correct chemical structures.

4.3.2 Membrane Sample Preparation

The isotopically labeled peptides were reconstituted in two types of lipid membranes. The first membrane is 1,2-dimyristoyl-*sn*-glycero-3-phophocholine (DMPC), and the second is a virus-mimetic lipid mixture (VM+) containing 1-palmitoyl-2-oleoyl-*sn*-glycero-3-phophocholine (POPC), 1-palmitoyl-2-oleoyl-*sn*-glycero-3-phosphoethanolamine (POPE), egg sphingomyelin (SM), and cholesterol (Chol) at molar ratios of 25.6%:25.6%:25.6%:23%. DMPC lipid vesicles were prepared by eight to ten freeze-thaw cycles. The VM+ lipids were first mixed and dissolved in chloroform/methanol 1:1 (v:v). The bulk of the organic solvents were removed with nitrogen gas, then the lipids were dissolved in cyclohexane and lyophilized overnight. The resulting homogeneous dry powder was suspended in buffer, vortexed, and subjected to eight freeze-thaw

cycles to create uniform vesicles. The M2 peptide was solubilized in octyl-β-D-glucoside (OG) solution and mixed with the lipid vesicle solution. The peptide-lipid mixture was vortexed for 2 hours, then dialyzed at room temperature against 1 L of buffer for 3 days with 6 buffer changes. The dialyzed proteoliposomes were spun down at 55,000 rpm at 5°C for 4 h to yield homogenous membrane pellets, which were spun into 4 mm MAS rotors for solid-state NMR measurements. The peptide-to-lipid molar ratio was 1:15 for all the samples and the hydration level was 40-50% (by mass).

In total, nine membrane samples were used in this study. Three $GIHL_{22\text{-}46,S31N}$ samples were reconstituted into the DMPC membrane at pH 7.5 with a Tris buffer (10 mM Tris base, 1mM EDTA, 0.1mM NaN_3). The first sample contained no drug (apo), the second contained d_5-WJ352 at a drug:tetramer molar ratio of 1:1, and the third contained d_5-WJ352 at a drug:tetramer ratio of 8:1. Three $VANIG_{19\text{-}49,S31N}$ samples were reconstituted into DMPC bilayers at pH 6.5 with a phosphate buffer (10 mM NaH_2PO_4/Na_2HPO_4, 1 mM EDTA, 0.1 mM NaN_3). The first sample contained no drug, the second sample contained d_{15}-WJ352 at a drug:tetramer ratio of 1:1, and the third sample contained d_{15}-WJ352 at a drug:tetramer ratio of 10:1. Three $VGIHL_{19\text{-}49,S31N}$ samples were prepared in the VM+ membrane to investigate His37 structure and dynamics. Two of these samples were prepared at pH 5.4 with use of a citrate buffer (10 mM citric acid/sodium citrate, 1 mM EDTA, 0.1 mM NaN_3), one without drug and the other with protonated WJ352 at a drug:tetramer ratio of 10:1. The third sample was prepared at pH 7.5 with a phosphate buffer without drug.

For drug-bound samples, the desired aliquot of a stock ethanol solution containing the drug was dried down and redissolved in 20-30 μL of ethanol. This concentrated solution was titrated into the membrane pellets from ultracentrifugation and mixed thoroughly to ensure homogenous distribution of the drug. The membranes were then dried to remove ethanol and rehydrated before being spun into the MAS rotors for solid-state NMR measurements.

4.3.3 Solid-State NMR Experiments

All MAS NMR experiments were carried out on Bruker DSX-400 MHz (9.4 T) and AVANCE 600 MHz (14.1 T) spectrometers (Karlsruhe, Germany), using 4 mm triple resonance MAS probes tuned to $^{1}H/^{13}C/^{15}N$ and $^{1}H/^{13}C/^{2}H$ frequencies. Typical radiofrequency (rf) field strengths were 50-63 kHz for ^{13}C, 42 kHz for ^{15}N, 50 kHz for ^{2}H, and 62-83 kHz for ^{1}H. ^{13}C chemical shifts were referenced to the methylene signal of adamantane at 38.48 ppm on the tetramethylsilane scale and ^{15}N chemical shifts were referenced to the ^{15}N signal of N-acetylvaline at 122.0 ppm on the liquid ammonia scale. Sample temperature was controlled using a FTS Systems XR401 Air-Jet cooler, with an additional liquid nitrogen heat exchanger placed in series for temperatures below 240 K.

One-dimensional (1D) ^{13}C and ^{15}N MAS spectra were recorded using a cross-polarization (CP) sequence under 7 kHz MAS. Spectra were measured at 308 K to detect conformational motion and proton exchange, and between 190 and 243 K to determine the rigid-limit conformation of the peptide and the protonation state and tautomeric structure of His37. 1D ^{13}C-^{13}C double-quantum (DQ) filtered spectra were measured at 200 K or 230 K under 7 kHz MAS using the SPC5 sequence[31] to suppress the natural abundance ^{13}C signals of lipids. ^{15}N-^{13}C dipolar filtered 1D ^{13}C spectra were measured at 7 kHz with use of a REDOR-based pulse sequence.[32] Two-dimensional (2D) ^{13}C-^{13}C ^{1}H-driven spin diffusion (PDSD) experiments were conducted under 7 kHz MAS with a 30 ms mixing time between 230 and 308 K. 2D ^{15}N-^{13}C correlation spectra were measured at 230 and 308 K under 10 kHz MAS for the $VGIHL_{19\text{-}49,S31N}$ samples, and at 243 K under 7 kHz MAS for the $VANIG_{19\text{-}49,S31N}$ samples. A ^{13}C-^{15}N REDOR period of 0.8 ms was used to obtain one-bond ^{15}N-^{13}C correlation peaks. Under 10 kHz MAS, the Cγ resonance of His37 was suppressed by rotational resonance with the directly bonded Cβ,[33] thus allowing the distinction between the Nδ1 and Nε2 signals in the 2D spectra.

^{13}C-^{2}H REDOR experiments for determining peptide-drug spatial contact were conducted with and without ^{13}C-^{13}C DQ filtering.[18,34,35] The former was used to remove the lipid natural abundance signals in case of severe overlap with the peptide ^{13}C signals. Both types of REDOR experiments include a selective ^{13}C Gaussian pulse to suppress ^{13}C-^{13}C J coupling.[36] The DQ

filtered REDOR experiments were carried out on the $VANIG_{19\text{-}49,S31N}$ sample under 5 kHz MAS, while the regular selective REDOR experiments were carried out on the $GIHL_{19\text{-}49,S31N}$ sample under 4.5 kHz MAS. In all REDOR experiments, a control (S_0) experiment without ^2H pulses and a dephasing (S) experiment with ^2H pulses were conducted back to back. ^{13}C sites close to the ^2H spins have lower intensities in the S spectrum than the S_0 spectrum. The ratio S/S_0 thus reflects ^2H-^{13}C distances: the shorter the distances, the lower the S/S_0 value. All REDOR spectra were measured at 243 K with 20,000-80,000 scans of signal averaging.

4.3.4 Solution NMR Experiments

Peptide and drug were added to deuterated dodecylphosphocholine (DPC) (Cambridge Isotope Laboratory) powder from their ethanol stocks at the desired molar ratios. Ethanol was removed by nitrogen purging, followed by overnight lyophilization. A phosphate buffer (10% D_2O, 50 mM sodium phosphate, pH 6.8) was added to the dried mixture to make a 2 mM (monomer) S31N M2(19-49) sample with 20 mM WJ332 or WJ352 in 100 mM deuterated DPC.

Two 2D ^{13}C-(^1H)-^1H NOESY spectra were measured on selectively labeled $VANIG_{19\text{-}49,S31N}$, using a Bruker 900 MHz Avance II spectrometer equipped with a cryogenic probe. The experiments were conducted at 313 K with a mixing time of 150 ms, $t_{1,max}$ of 7 ms, and $t_{2,max}$ of 71 ms, and 128 scans per t_1 slice. The ^1H carrier frequency was set to the water signal. The ^1H chemical shift was referenced to the residual water peak at 4.63 ppm relative to *DSS* while the ^{13}C chemical shift was referenced indirectly via the gyromagnetic ratio. The spectra were processed and analyzed using the NMRPipe program.[37] The first three time points of the indirect ^{13}C dimension were extended by linear prediction. Time domain data were multiplied by sine square bell window functions shifted by 90° and zero-filled once before Fourier transformation.

4.3.5 Calculation of Chemical Shift Perturbation

To examine drug-induced conformational change, we calculated the average chemical shift perturbation (CSP) of each residue between the apo and drug-bound states using the following empirical relation:[38]

$$\Delta\delta_{av} = \left\{\frac{1}{n}\left[\sum_{i=1}^{n-1}(\Delta\delta_{C,i})^2 + \left(\frac{\Delta\delta_N}{2.5}\right)^2\right]\right\}^{1/2}$$

where n is the total number of chemical shifts measured in each residue and $\Delta\delta$ is the individual-site's chemical shift difference between the apo and drug-bound states. We used chemical shifts obtained from the DMPC-bound membrane samples, with the exception of V28, which was only labeled in the $VGIHL_{19\text{-}49,S31N}$ sample bound to the VM+ membrane. For residues N31, I33, and G34, drug binding did not create new chemical shifts but changed the equilibrium between two sets of chemical shifts. We used the difference between these two sets of chemical shifts to represent drug perturbation of the conformation of these residues. For His37, a single set of backbone chemical shifts was observed for the apo peptide, and drug binding created a second set, so the average difference between these two sets of chemical shifts was calculated. Only the Nα, CO, Cα, and Cβ chemical shifts were used in the His37 calculation, because imidazole chemical shifts are sensitive to chemical structure factors not directly related to conformational changes.

4.4 Results

4.4.1 Drug-Induced Chemical Shift Changes of S31N-M2

We first investigated the effects of the isoxazole drug on S31N-M2 structure by analyzing the chemical shifts of the TM residues. **Figures 4.2 and 4.3** show representative 2D ^{13}C-^{13}C and ^{15}N-^{13}C correlation spectra of DMPC-bound S31N-M2 at pH 6.5. Among the five labeled N-terminal residues (V27, A30, N31, I33, and G34), the isoxazole drug either selected one of the conformations or changed the equilibrium between multiple conformations. For example, N31 exhibits two sets of Cα and Cβ chemical shifts whereas G34 exhibits two CO chemical shifts. Drug binding largely removed the signals of the more α-helical chemical shifts of N31, retaining the smaller Cα and CO chemical shifts (**Table 4.S1**). Similarly, the less α-helical (smaller) CO chemical shift of G34 is a minor component in the apo peptide but is equally populated as the more helical (larger) CO chemical shift in the drug-bound state (**Fig. 4.2e**). The less helical G34 chemical shift also shows cross peaks with I33 at long ^{13}C spin diffusion mixing times (**Fig. 4.2c,**

d). For A30, conformational heterogeneity was less pronounced in the apo state, but drug binding also changed the Cα, Cβ and CO chemical shifts to less helical values (**Fig. 4.3**).

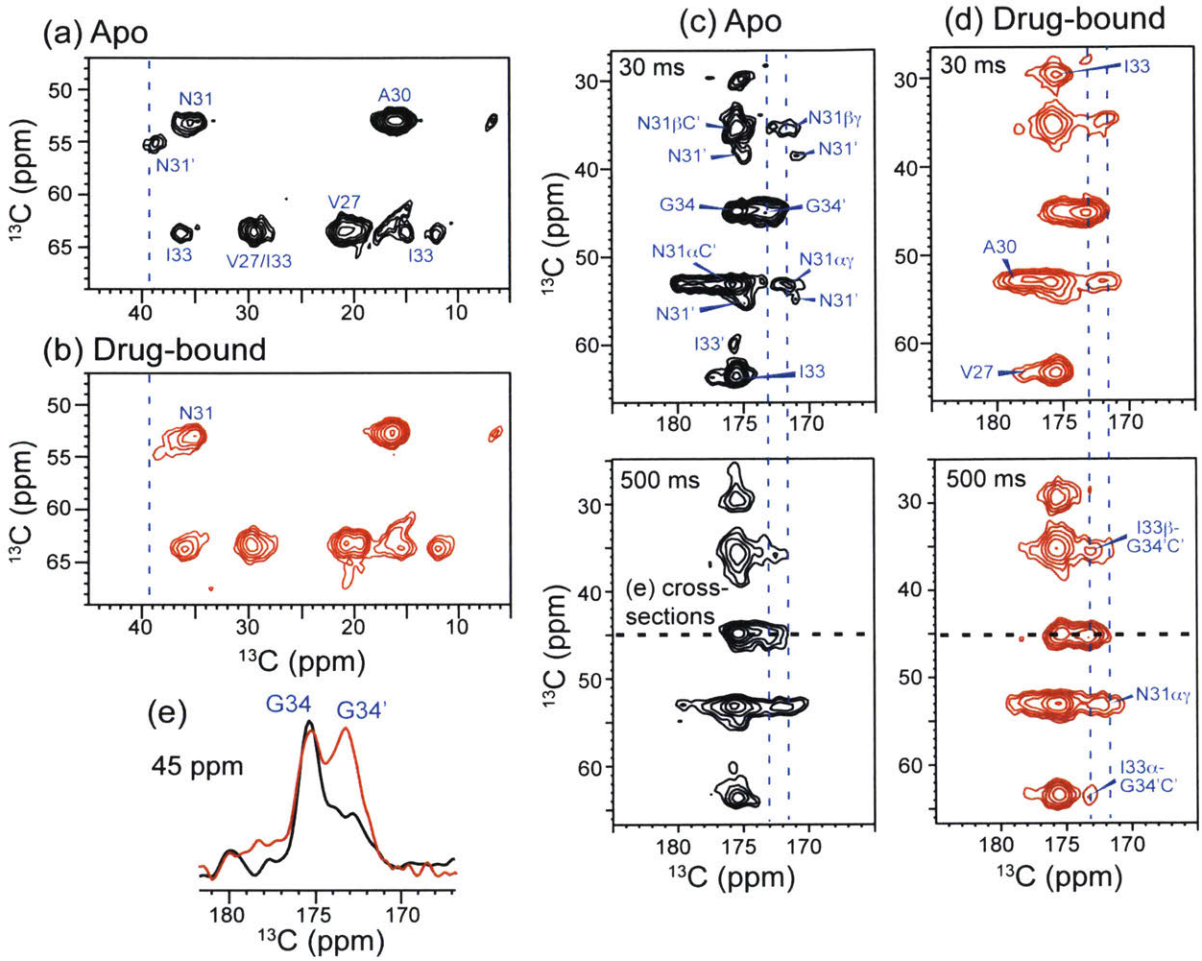

Figure 4.2 2D ^{13}C-^{13}C correlation spectra of $VANIG_{19\text{-}49,S31N}$ in DMPC bilayers without and with WJ352 at pH 6.5. (a, b) Aliphatic region of the 30 ms spectra of the apo peptide (a) and drug-bound peptide (b). Drug binding changed the conformational equilibrium of the N31 Cα-Cβ peaks. (c, d) Carbonyl region of the 30 ms (top) and 500 ms (bottom) spectra of the (c) apo and (d) drug-bound peptide. N31, I33, and G34 exhibit two sets of chemical shifts. (e) The 45-ppm cross section of the apo (black) and drug-bound (red) peptide, showing the G34 Cα-CO cross peak. All spectra were measured at 243 K under 7 kHz MAS.

Figure 4.4 shows the aliphatic region of the 2D ^{13}C PDSD spectra of $VGIHL_{19\text{-}49,S31N}$ in the VM+ membrane. Three samples with different pH and drug-binding states are compared. The chemical shifts show complex dependences on pH, drug binding, and temperature. At low

temperature, the low-pH apo peptide exhibited a single set of Cα and Cβ chemical shifts for I35, H37 and L38, but upon drug binding and pH increase, these residues showed two sets of Cα and Cβ chemical shifts, indicating two distinct backbone conformations. Drug binding at low pH gave rise to the same two chemical shifts as those of the high-pH apo peptide, indicating that drug binding created the same conformational distribution as the closed state of the channel. The presence of two backbone conformations of H37 in the drug-bound state is qualitatively reproduced in the DMPC membrane (not shown). Thus, the conformation of the functionally essential His37 is largely dictated by pH and drug binding and is not sensitive to the membrane environment.

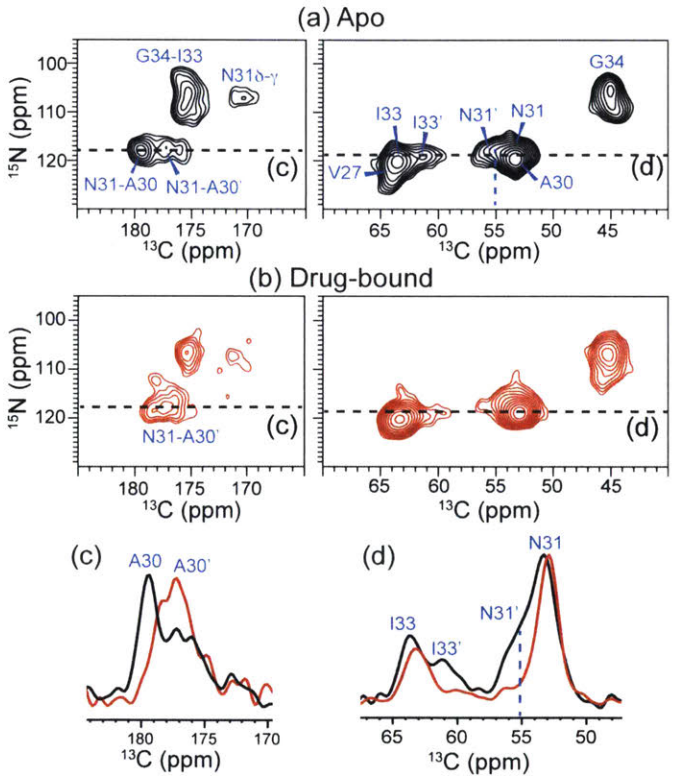

Figure 4.3 2D ^{15}N-^{13}C correlation spectra of VANIG$_{19\text{-}49,S31N}$ in DMPC bilayers at pH 6.5: (a) without drug (black) and (b) with drug (red) at the 10:1 drug:tetramer ratio. (c) A30 CO cross section at the ^{15}N chemical shift of 117.6 ppm. Drug binding changed the intensity distribution of two A30 CO peaks. (d) I33 and N31 Cα cross section at 119.1 ppm ^{15}N chemical shift. Drug binding selected one of the two peaks of I33 and N31. The spectra were measured at 243 K under 7 kHz MAS.

I35 and L38 exhibit a single set of side chain chemical shifts in the low-pH apo peptide at low temperature, but at high temperature, both side chains show two sets of chemical shifts (**Fig. 4.S2**), which are similar to those of the high-pH and drug-bound samples. These observations indicate that the energetic balance between the two side chain conformations of these interfacial residues changes between the open state and the closed or inhibited state of the channel. The minor conformation is less stable in the open state and thus not populated at low temperature, but it is stabilized in the closed and inhibited states.

To compare the magnitudes of the chemical shift changes of the various residues by the drug, we calculated the CSP. **Figure 4.5** shows that N31 has the largest chemical shift perturbation, followed by H37 and G34. This trend is very similar to the effect of amantadine on the WT peptide, where S31 was the site of maximum chemical shift perturbation, followed by G34 and V28.[39] H37 was not included in the WT chemical shift perturbation study.

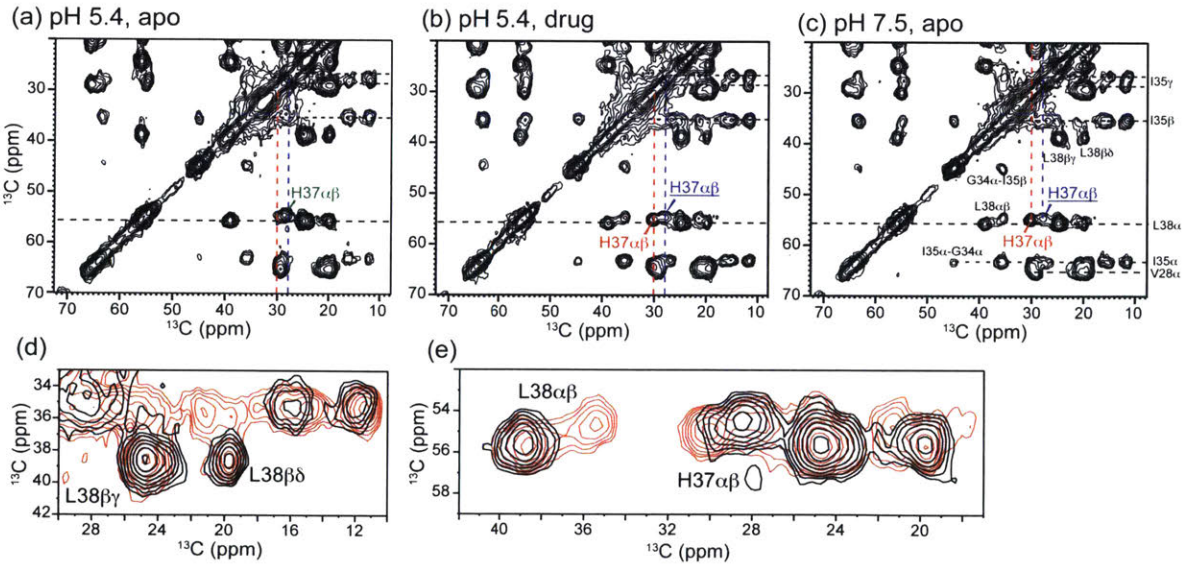

Figure 4.4 Aliphatic region of the 2D ^{13}C-^{13}C correlation spectra of VM+ membrane bound $VGIHL_{19\text{-}49,S31N}$. The spectra were measured at 243 K under 7 kHz MAS: (a) apo peptide at pH 5.4; (b) drug-bound peptide at pH 5.4; and (c) apo peptide at pH 7.5. The signals of τ, π, and cationic His37 are annotated in red, blue underline, and green, respectively. (d) Amplified L38 and I35 side chain region of the apo (black) and drug-bound (red) spectra at low pH. (e) Amplified H37 and L38 Cα-Cβ region of the apo and drug-bound spectra at low pH. The low-pH drug-bound spectrum resembles the high-pH spectrum, indicating that WJ352 shifts the backbone conformation of S31N to that of the closed channel state.

Interestingly, while N31 exhibited the largest chemical shift perturbation, the Asn sidechain Cγ chemical shift is relatively unaffected by the drug. This is seen in the 2D spectra in **Fig. 4.2c,d** and **Fig. 4.3**, and further verified in ^{15}N-^{13}C filtered 1D ^{13}C specta measured between 190 and 270 K (**Fig. 4.S3**). Below 240 K, the Cγ intensities are consistently 7-10% of the full spectral intensity, indicating full detection of this signal and ruling out the possibility of an invisible dynamic population. The absence of Cγ chemical shift change indicates that the average N31 rotameric conformation is little affected by the drug. However, at 270 K, the Cγ intensity in the drug-bound sample appears lower than in the apo sample (**Fig. 4.S3**), suggesting the onset of rotameric exchange, whose detail will require further experiments to elucidate.

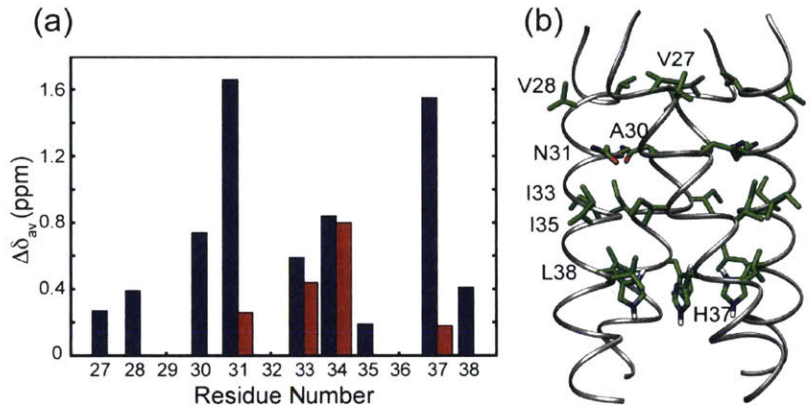

Figure 4.5 (a) Residue-specific average chemical shift change in S31N M2TM induced by the drug WJ352. Residues with a single set of chemical shifts in both the apo and drug-bound states have a single blue bar for the average CSP, while residues with two sets of chemical shifts in the apo state but only one set in the drug-bound state have two CSP values. (b) Solution NMR structure of S31N M2TM (PDB:2LY0), showing the positions of most residues whose CSPs were measured.

4.4.2 WJ352 Binding Site in the S31N-M2 Channel

The ability of WJ352 and its derivatives to inhibit the S31N-M2 channel[29] is somewhat surprising given the larger size of the isoxazoles compared to amantadine and rimantadine and the more constricted channel due to the replacement of Ser by Asn. To investigate how exactly the bulky isoxazole fits into the S31N channel, we selectively deuterated WJ352 either at the

adamantane head (d_{15}) or at the phenyl tail (d_5). Using the versatile REDOR experiment, we measured the location and orientation of deuterated WJ352 bound to ^{13}C-labeled S31N-M2.

For d_5-WJ352 complexed $GIHL_{22\text{-}46,S31N}$, we did not observe ^{13}C-^{2}H REDOR intensity differences between the control (S_0) and dephased (S) spectra at drug:tetramer ratios of either 1:1 or 8:1. In particular, the well-resolved G34 Cα signal had no intensity change (**Fig. 4.6a**), indicating that the phenyl tail is far from this segment. Under excess drug, the lipid headgroup Cγ showed moderate intensity reduction in the S spectrum, indicating that excess WJ352 partitions to the membrane-water interface, analogous to amantadine and rimantadine.[40,41] In comparison, d_{15}-WJ352 complexed $VANIG_{19\text{-}49,S31N}$ showed clearly lower S intensities than the S_0 intensities for most labeled sites both at the stoichiometric drug concentration (**Fig. 4.6b**) and under excess drug (data not shown). At a REDOR mixing time of 9.6 ms, the I33/V27 Cα peak exhibits an S/S_0 value of 0.81 ± 0.07, the A30/N31 Cα peak has an S/S_0 value of 0.88 ± 0.03, while G34 Cα has S/S_0 = 0.86 ± 0.05. These REDOR spectra were measured under ^{13}C DQ filtering to suppress the lipid ^{13}C signals, thus the low sensitivity prohibits the use of longer mixing times to quantify the distances. Although the V27 and I33 Cα peaks overlap, I33 likely contributes to the majority of the measured REDOR dephasing at 64 ppm because of the proximity of I33 to G34, whose Cα signal also shows significant REDOR dephasing. Taken together, these spectra indicate that WJ352 binds to the channel lumen with the adamantane head spanning the segment from A30 to G34, while the phenyl tail is directed toward the N-terminus. Solution-state ^{13}C-^{1}H NOESY spectra of $VANIG_{19\text{-}49,S31N}$ in DPC micelles further confirm this result: the adamantane H6, H7, and H8 protons show clear cross peaks with I33 side chains while the phenyl H1-H4 protons exhibit cross peaks with V27 side chains (**Fig. 4.6c,d**). Thus, the solution and solid-state NMR spectra indicate that in both lipid bilayers and DPC micelles, the isoxazole drug binds to the S31N channel pore with the amine pointing to the exterior (**Fig. 4.6e**).

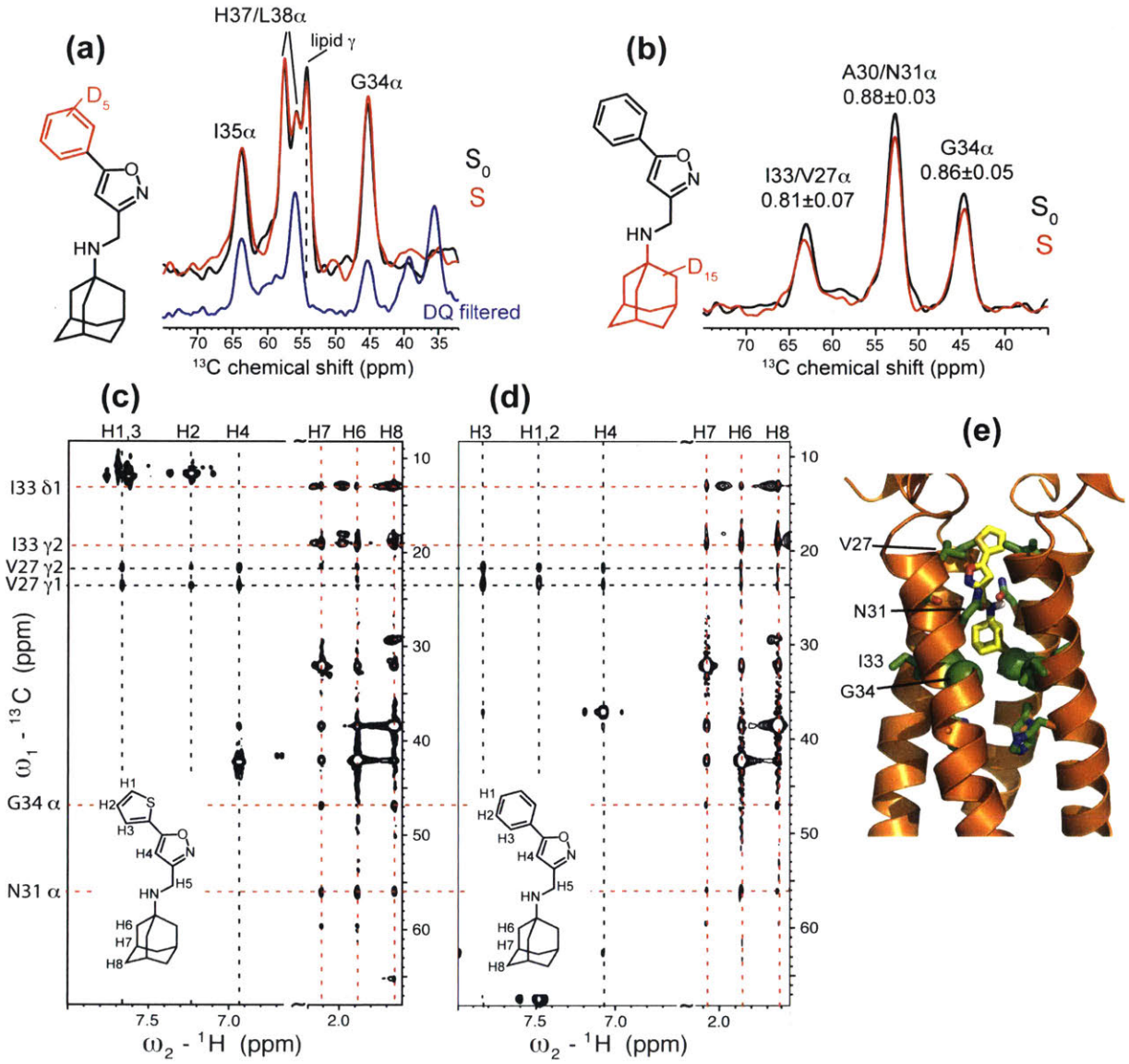

Figure 4.6 Binding site and orientation of WJ352 in S31N bound to DMPC bilayers (a, b) and DPC micelles (c, d). (a) ^{13}C-^{2}H REDOR S_0 (black) and S (red) spectra of d_5-WJ352 complexed $GIHL_{22\text{-}46,S31N}$ in DMPC bilayers. The mixing time was 14.2 ms and the drug:tetramer ratio was 8:1. The deuterated phenyl group did not dephase any peptide ^{13}C signals, especially G34. The REDOR spectra were measured without DQ filtering, thus showing a lipid headgroup Cγ peak at 54 ppm. This is verified by the absence of the peak in a ^{13}C DQ filtered spectrum (blue). (b) ^{13}C-^{2}H DQ filtered REDOR spectra of d_{15}-WJ352 bound $VANIG_{19\text{-}49,S31N}$ in DMPC bilayers. The mixing time was 9.6 ms and the drug:tetramer ratio was 1:1. The deuterated adamantane dephased multiple ^{13}C signals. (c, d) 2D ^{13}C-(^{1}H)-^{1}H NOESY (150 ms) spectra of $VANIG_{19\text{-}49,S31N}$ in DPC micelles with bound WJ332 (c) or with bound WJ352 (d). Drug-peptide cross peaks are observed and consistent with the amine-up orientation. (e) Solution NMR structure of S31N-M2 with bound WJ332 (PDB:2LY0).[29]

4.4.3 Effects of Isoxazole Drug on His37 Structure and Dynamics

To investigate how S31N conducts protons and how drug binding interferes with this conduction, we measured the His37 ^{15}N and ^{13}C chemical shifts, which are highly sensitive to the protonation state and tautomeric structure of the His sidechain.[42-45] **Figure 4.7** and **Fig. 4.9** show 1D ^{15}N and ^{13}C spectra of $VGIHL_{19\text{-}49,S31N}$ at high temperature (308 K) where dynamic processes are active and at low temperature where rigid-limit chemical shifts allow quantification of the various species of histidine present under a certain condition. The ^{15}N and ^{13}C chemical shifts were assigned based on the 2D spectra in **Fig. 4.8** and **Fig. 4.S4** and by comparison with the WT data.[6,8]

For the high-pH apo peptide, the ^{15}N spectra (**Fig. 4.7c**) show the Nε2H peak of the τ tautomer (159 ppm) and the Nδ1H peak of the π tautomer (170 ppm), similar to WT M2TM.[6] The unprotonated ^{15}N peak at 251 ppm has high intensity, indicating that neutral histidines dominate at this pH. Since the multiple protonated nitrogens are not well resolved between neutral and cationic His, the presence of cationic His is better ascertained from the ^{13}C spectra (**Fig. 4.9c**). The Cδ2 chemical shift is an excellent indicator of the τ tautomer, π tautomer, and cationic His.[46] At pH 7.5 all three species were detected: the τ tautomer (Cδ2 at 114 ppm) dominates, followed by the π tautomer (Cδ2 at 124 ppm), while a weak cationic Cδ2 peak at 117 ppm is also detected in the DQ filtered and ^{15}N-^{13}C filtered ^{13}C spectra. Thus, cationic His indeed exists at a low percentage at this neutral pH, similar to the WT channel.[8]

In the low-pH apo peptide, the low-temperature ^{15}N spectrum shows a strong and broad peak at ~170 ppm (**Fig. 4.7a**). The large width of this peak distinguishes it from the π tautomer Nδ1H peak at high pH and identifies it as cationic Nδ1H, as verified by 2D correlation spectra (**Fig. 4.8a** and **Fig. 4.S4a**). The unprotonated ^{15}N signal (251 ppm) is weak, further indicating that the percentage of neutral His is much lower than at pH 7.5. Increasing the temperature to 308 K dramatically changed the ^{15}N spectra: two dominant signals appear at intermediate ^{15}N chemical shifts of 213 and 185 ppm, indicating fast interconversion of various His species. Both peaks were also observed in the WT ^{15}N spectra, but with much larger linewidths.[8] In addition to these two

peaks, a significant intensity band between 160 and 180 ppm was also detected and constitutes about 30% of the total aromatic intensity.

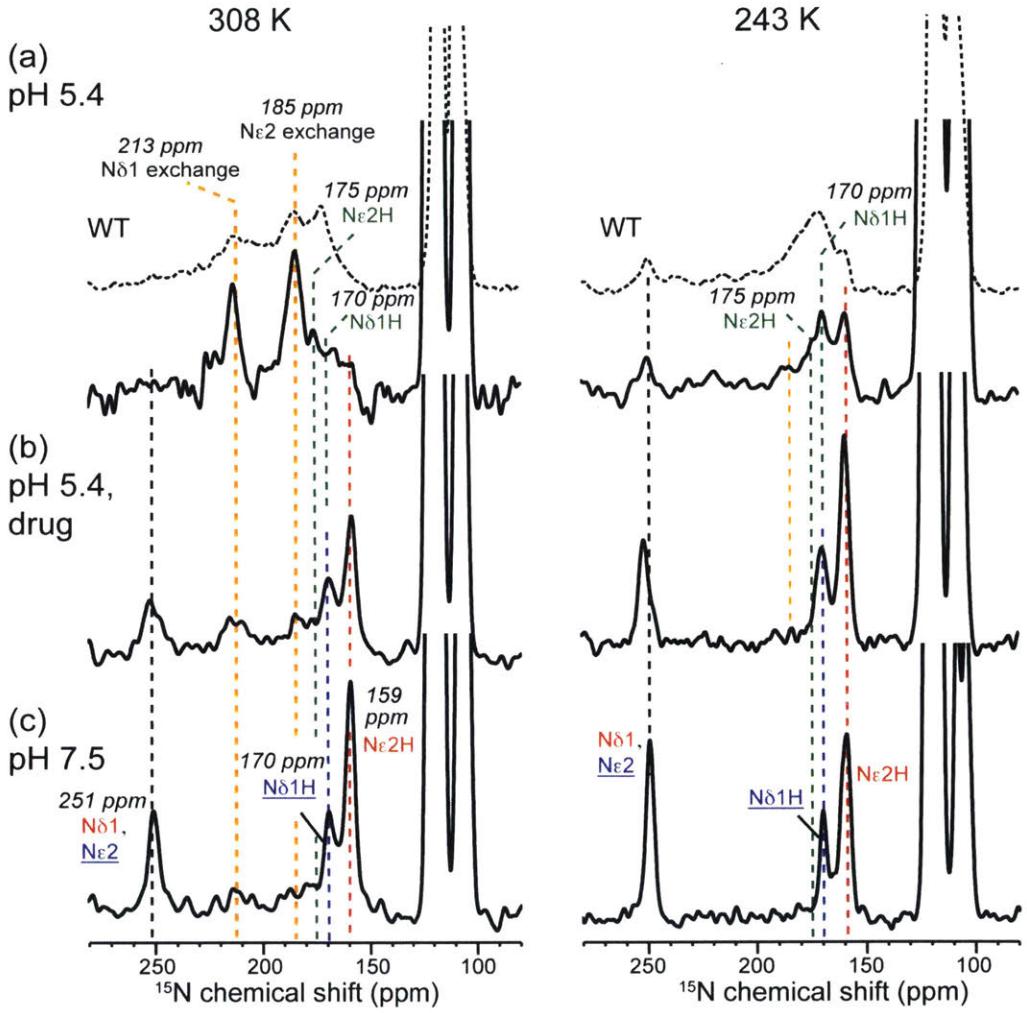

Figure 4.7 1D ^{15}N CP-MAS spectra of His37 in VM+ membrane bound $VGIHL_{19\text{-}49,S31N}$ at 308 (left) and 243 K (right). The spectra were scaled to show roughly equal integrated intensities for the imidazole nitrogens: (a) apo peptide at pH 5.4; (b) drug-bound peptide at pH 5.4; (c) apo peptide at pH 7.5. Assignments shown here and in subsequent figures are annotated in red for the τ tautomer, blue underline for the π tautomer, and green for cationic His. For comparison, the pH 5.2 spectra of WT His37 are shown (dotted line) above the S31N spectra in part (a). At low pH and high temperature, S31N-M2 exhibited sharp ^{15}N exchange peaks. WJ352 binding largely suppressed these peaks.

Drug binding to the low-pH channel largely reverted the ^{15}N spectra to those of the high-pH apo state (**Fig. 4.7b**): at low temperature, the broad cationic ^{15}N signals between 170 and 180

ppm sharpened to become the signature of the π tautomer Nδ1H peak, while the 251-ppm peak greatly increased its intensity. The spectrum resembles the high-pH spectrum at low temperature. Increasing the temperature gave rise to residual exchange intensities at 213 and 185 ppm, but the spectrum remains dominated (~70%) by the sharp signals at the frequencies of neutral His. Thus, isoxazole binding at low pH converted most of the cationic His's to the neutral, non-conducting conformation.

To elucidate the origin of the 213- and 185-ppm peaks, we measured 2D ^{15}N-^{13}C correlation spectra (**Fig. 4.8**), supplemented with 2D ^{13}C-^{13}C correlation spectra (**Fig. 4.S4**). The 185-ppm ^{15}N peak is correlated to two ^{13}C signals (134 and 118 ppm) while the 213-ppm peak is correlated only to a 134-ppm peak (**Fig. 4.8a**). These 2D ^{15}N-^{13}C correlation spectra were measured under 10 kHz MAS, near the rotational-resonance condition[33] between Cβ and Cγ of His37, which broadened the Cγ signal. As a result, Nδ1 has only one correlation peak (to Cε1) while Nε2 has two correlation signals (to Cε1 and Cδ2). Thus, the 213-ppm signal must be assigned to Nδ1 while the 185-ppm peak must be assigned to Nε2. Similarly, at high pH (**Fig. 4.8c**), the 170-ppm ^{15}N peak can be assigned to Nδ1 while the 159-ppm peak was confirmed to result from Nε2. The 2D ^{15}N-^{13}C correlation spectrum of the drug-bound sample (**Fig. 4.8b**) confirms the 1D observation that the sample is a mixture of a small fraction of unbound channels with exchange peaks and bound channels in which His37 adopts the high-pH apo structure.

The low-temperature 1D ^{13}C spectra (**Fig. 4.9**) allow us to quantify the concentrations of the three His species in each sample based on the distinct Cδ2 chemical shifts.[46] At pH 7.5, the concentration ratios are 65%:25%:10% (±5%) for τ:π:cationic His, indicating the predominance of neutral His. For the apo pH 5.4 sample, the ratios are 36%:12%:52% (±5%), indicating that half of the His are cationic. The drug-bound sample showed concentration ratios of 60%:28%:12% (±10%) for τ:π:cationic His, quantitatively indicating that isoxazole converted most His to the neutral form at this low pH.

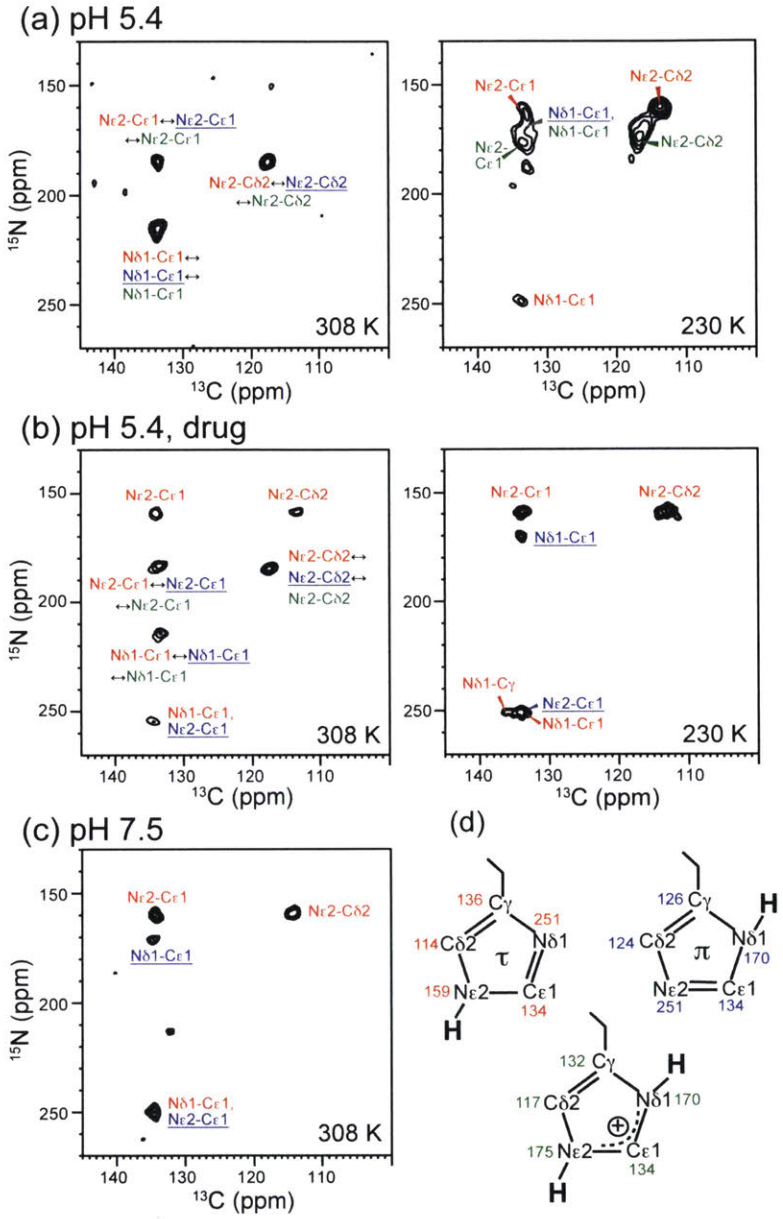

Figure 4.8 2D ^{15}N-^{13}C correlation spectra of VM+ bound VGIHL$_{19\text{-}49,S31N}$ at 308 and 230 K under 10 kHz MAS: (a) apo peptide at pH 5.4; (b) drug-bound peptide at pH 5.4; (c) apo peptide at pH 7.5. The Cγ signal was not detected due to rotational resonance with Cβ, thus allowing the distinction between Nδ1 and Nε2 signals. (d) Imidazole chemical shifts for the τ tautomer, π tautomer, and cationic His.

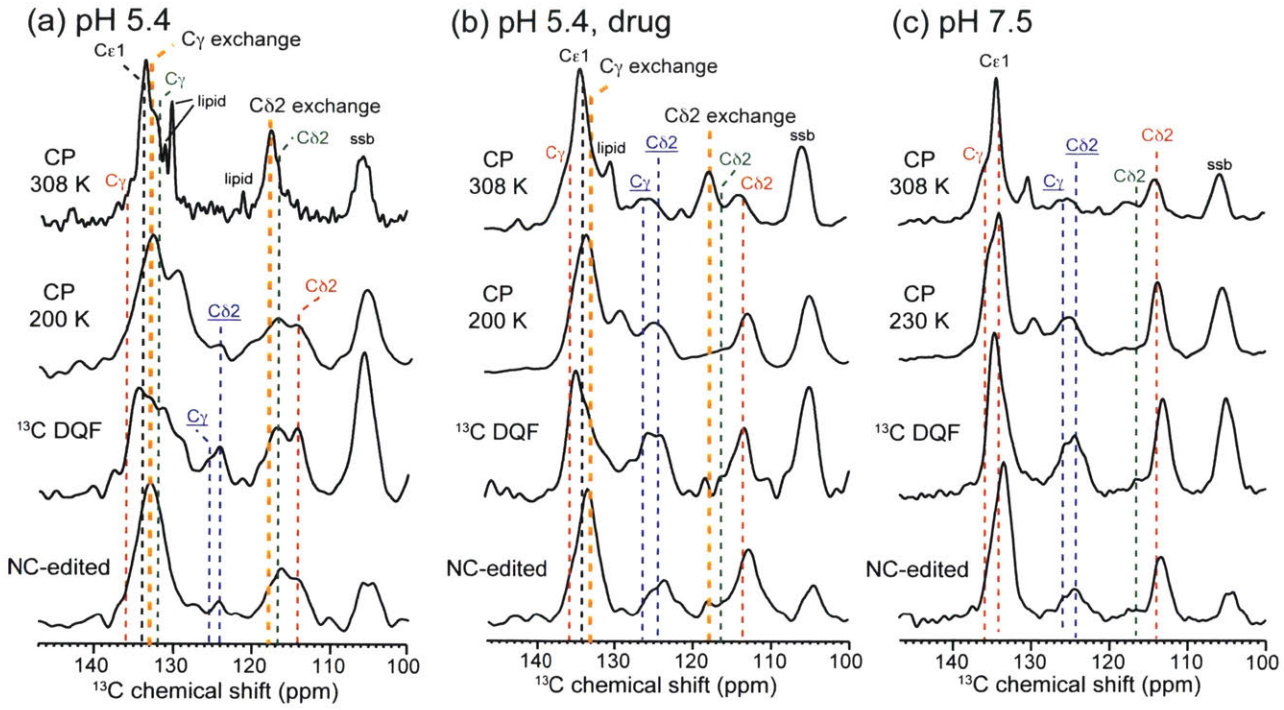

Figure 4.9 Aromatic region of the 1D ^{13}C MAS spectra of His37 in VM+ bound $VGIHL_{19\text{-}49,S31N}$. From top to bottom are the 308 K ^{13}C CP-MAS spectra, the low-temperature CP-MAS (200 or 230 K) spectra, the low-temperature ^{13}C-^{13}C DQ filtered (DQF) spectra, and the low-temperature ^{15}N-^{13}C filtered spectra: (a) apo peptide at pH 5.4; (b) drug-bound peptide at pH 5.4; (c) apo peptide at pH 7.5. Spinning sidebands are denoted as ssb. All spectra were measured under 7 kHz MAS.

4.5 Discussion

4.5.1 Isoxazole Binding Site and the Effects of Drug on S31N-M2 Conformation

The observed ^{13}C and ^{15}N chemical shifts indicate that the isoxazole drug perturbed the conformation of S31N in a similar fashion as amantadine to wild-type M2TM. Most importantly, the drug significantly changed the Cα and Cβ chemical shifts of residue 31, thus achieving the design purpose of targeting this amantadine-resistant mutation site. Both amantadine and isoxazole perturbed the chemical shifts of G34, whose conformation is known to be sensitive to the environment.[39,47,48] However, a major difference exists in the way that the two drugs are oriented in the pore. While amantadine and rimantadine are oriented with the polar amine pointing down to H37,[19] the biaryl isoxazoles are flipped by 180° and point the polar amine up to the exterior, as

evidenced by ^{13}C-^{2}H REDOR data and NOE cross peaks (**Fig. 4.6**). This opposite orientation suggests that both amantadine and isoxazole drugs are significantly stabilized by hydrophobic interactions of the adamantane with the peptide, mainly at the segment between N31 and G34 (**Fig. 4.6e**).[18] In addition to the hydrophobic interaction, MD simulations show the presence of multiple hydrogen bonds between the amine and the Asn side chains and between the isoxazole nitrogen and the Asn side chains, which should further stabilize the amine-up orientation.[29]

Isoxazole binding shifted the conformational equilibrium of various residues, selecting one of two conformations at N31, I33, and G34 while creating two conformations at H37. The nature of the two conformations in apo S31N-M2 is not yet fully understood. A longer construct of the protein, S31N M2(18-60), was also reported to show peak doubling, which was found for most residues.[27] The current data on the TM construct suggest that one possible cause of the two conformations is tautomerism of His37, since the two His37 Cβ chemical shifts are individually correlated to the τ and π resonances (**Fig. 4.S4**). This hypothesis is supported by the observation that the two Cα-Cβ peaks of Leu38 have similar intensity ratios as the His37 Cα-Cβ peak intensity ratios in the high-pH sample (**Fig. 4.4b,c**).

Interestingly, while the drug selected one of the two backbone conformations of N31, the carboxamide Cγ chemical shift is largely unaffected by the drug at low temperature (**Fig. 4.S3**), indicating that the average rotameric conformation of N31 is unperturbed by the drug. On the other hand, the N31 side chain chemical shifts of DMPC-bound S31N M2(19-49) measured here differ significantly from the N31 chemical shifts of S31N M2(18-60) bound to the diphytanoylphosphocholine membrane:[27] the Cγ and Nδ chemical shifts are about 173 (DSS scale) and 106 ppm in the current study (**Table 4.S1**) but 175-178 and 113-115 ppm, respectively, in the previous study. These differences indicate that the rotameric structures of N31 may be sensitive to the lipid membrane and/or the peptide construct length.

An increasing number of membrane proteins have been found to adopt multiple conformations under different conditions and undergo slow exchange among these conformations.[49] For example, the structures of phospholamban,[40] the G-protein coupled receptor β_2-adrenoreceptor,[35] wild-type influenza M2 transmembrane peptide,[47,50] and viral fusion

peptides[51-53] are all significantly influenced by the membrane composition, and other factors such as temperature[54] and pH[55] can also modulate membrane protein structure. Such conformational plasticity is usually associated with function, such as ion channel opening, closing, and inactivation;[41,56,57] enzyme catalysis;[58] and protein-protein interactions.[40] The fact that drug binding to S31N-M2TM did not simply cause a conformational change but selected a subset of conformations that pre-existed in the apo peptide[59] suggests that the energy landscape of the M2 transmembrane domain, even in the lipid bilayer instead of detergent micelles,[60] is rough, and this roughness may be relevant for the multiple functions of M2, including proton conduction,[2] membrane scission,[61] and virus assembly,[62] in addition to drug binding.[5]

4.5.2 Proton-Exchange Dynamics of His37 in S31N-M2

The conformation and dynamics of His37 in S31N reveal the proton conduction mechanism of the M2 channels. Similar to the WT channel, S31N shows His37 exchange dynamics at low pH, as manifested by the 213- and 185-ppm ^{15}N chemical shifts and the associated ^{13}C exchange peaks.[8] Also similar to the WT channel, these exchange peaks are highly sensitive to temperature (**Fig. 4.7a**), indicating significant energy barriers, which support the assignment of these peaks to His-water proton transfer[5,7] rather than strong His-His hydrogen bonding,[14] which would be essentially barrier-less.[63] The rate of this His-water proton transfer is discernibly faster for S31N than for WT M2, as evidenced by the narrower line widths of the ^{15}N exchange peaks. This difference is qualitatively consistent with the higher proton conductance of S31N than the WT channel.[28] On the other hand, the conductance difference is only about 20%, while the His-water proton transfer rate difference appears much larger. We recently calculated an exchange rate of $\sim 10^5$ s^{-1} for WT M2[8] based on its exchange line widths. This rate is already more than 2 orders of magnitude larger than the proton flux per second.[9] We attribute the smaller proton flux partly to the interaction of His37 with the gating residue, Trp41.[12] Recent solid-state NMR data of WT M2TM indicate that at low pH, Trp41 moves closer to His37 by ~2 Å and undergoes larger-amplitude side chain reorientation.[15] The resulting periodic cation-π interactions with His37 should reduce the number of protons released from His37 to water. Similar Trp41-His37 interactions should be present in S31N as well, which would reduce the number of protons transported into the virion.

Further insight into the mechanism of His-mediated proton transfer is obtained by determining the nature and populations of the molecular species that give rise to the ^{15}N exchange peaks. The similar line widths of the two ^{15}N exchange peaks (**Fig. 4.7a** and **4.8a**) suggest that they originate from the same exchange process. Since protonated nitrogens have ^{15}N chemical shifts below ~185 ppm, the 213-ppm ^{15}N exchange peak is only possible when unprotonated nitrogens constitute roughly 50% of the interconverting His species.[8] Since both τ and π tautomers contain unprotonated nitrogens, all three His species can in principle participate in exchange. Using the rigid-limit ^{15}N chemical shifts (**Table 4.1**), we solve for three simultaneous linear equations,

$$213 \text{ ppm} = 251 \text{ ppm} \cdot f_\tau + 170 \text{ ppm} \cdot f_\pi + 170 \text{ ppm} \cdot f_+$$
$$185 \text{ ppm} = 159 \text{ ppm} \cdot f_\tau + 251 \text{ ppm} \cdot f_\pi + 175 \text{ ppm} \cdot f_+$$
$$1 = f_\tau + f_\pi + f_+$$

which gives molar fractions of $f_\tau = 53\%, f_\pi = 24\%$, and $f_+ = 23\%$ for τ, π, and cationic His.

Table 4.1 ^{15}N and ^{13}C chemical shifts (ppm) of individual His37 in S31N-M2 bound to the virus-mimetic membrane.

site	τ tautomer	π tautomer	cation	obsd τ:π:cation 53:24:23 exchange
Cα	55.4	54.8	54.8	55.1[a]
Cβ	30.1	27.9	28.4	29.2
Cγ	136	126	132	133
Nδ1	251	170	170	213
Cε1	134	134	134	134[a]
Nε2	159	251	175	185
Cδ2	114	124	117	118

[a]These are predicted exchange-averaged chemical shifts, which cannot be resolved from unexchange peaks.

This three-site exchange model is confirmd by the high-temperature ^{13}C spectrum of the apo peptide (**Fig. 4.9a**), where the main Cδ2 signal at 118 ppm can be distinguished from the cationic Cδ2 peak (117 ppm) as well as the neutral Cδ2 peaks (124 ppm for π and 114 ppm for τ) at low temperature. This 118-ppm peak is consistent with the weighted average of the three rigid-limit Cδ2 chemical shifts, but inconsistent with any two-site exchange models such as τ-cationic

or τ-π exchange. For example, a τ-cationic exchange model that agrees with the 213-ppm ^{15}N peak would require a 1:1 ratio, which would lead to an average Cδ2 chemical shift of less than 117 ppm, in contradiction with the measured Cδ2 chemical shift. The three-site exchange with the above ratios predicts an average Cγ chemical shift of 133 ppm, which is also detected in the high-temperature spectrum. Cε1 is insensitive to exchange because all three states of His have the same rigid-limit Cε1 chemical shift of 134 ppm. Taken together, the high-temperature ^{13}C spectra and the clear identification of the 185-ppm ^{15}N peak as an exchange peak revise our previous understanding of the interconverting His species during His-water proton transfer, by including the π-tautomer in the exchange.

The τ:π:cationic ratio of 53%:24%:23% obtained from the exchange-averaged ^{15}N chemical shifts is noteworthy, because the cationic fraction is much lower than expected, and lower than the low-temperature ^{13}C spectra derived cationic His concentration of ~52% (**Fig. 4.9a**). This apparent discrepancy is resolved by the fact that the observed exchange peaks mainly result from tetramers with low charge states of +1 and +2, where only one or two His residues are cationic. Higher-charged, +3 and +4, tetramers, which are also populated at pH 5.4 based on the measured pK_a values of the WT channel,[8] do not contribute to these specific ^{15}N exchange peaks because they give average ^{15}N chemical shifts in the 160-190 ppm range, which cannot be easily distinguished from non-exchange protonated nitrogen signals. Indeed, the 160-180 ppm band in the low-pH high-temperature ^{15}N spectrum (**Fig. 4.7a**) constitutes ~30% of the total aromatic intensity, and is consistent with the presence of exchange signals from higher charged tetramers. In other words, exchange within low-charged tetramers is more detectable due to a high population of unprotonated nitrogens, which shifts the average ^{15}N frequencies downfield, away from the protonated ^{15}N signals. If we combine the 30% cationic His intensity from the 160-180 band with the cationic His fraction from the exchange peaks, which is ~23% of the remaining 70% aromatic intensity (~70% x 23% = 16%), then we indeed obtain a higher cationic fraction of close to 50%, in good agrement with the low-temperature ^{13}C intensities.

In addition to charge-conserved interconversion of the four histidines within a tetramer, the charge state of a tetramer can also change due to net His-water proton transfer, which may be

considered as intertetramer exchange. More definitive information about the second process will require further experiments. What is clear from the current data is that high pH suppresses both intratetramer fast exchange and any possible intertetramer exchange, even though a small fraction (10%) of cationic His remains.

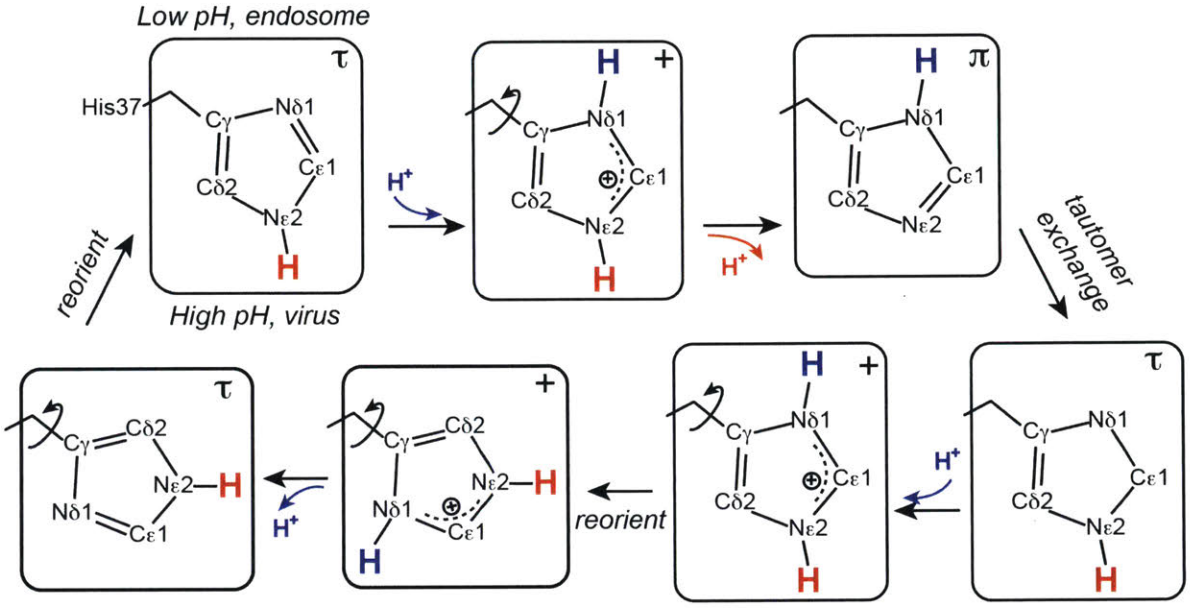

Figure 4.10 Proposed mechanism of His37-water proton exchange for S31N and WT M2 channels. His37 residues undergo rapid interconversion among τ, π, and cationic states during proton transfer with water. Ring reorientations facilitate this proton shuttling by pointing the unprotonated nitrogen towards the low-pH exterior.

The fast τ-π-cationic His interconversion at low pH refines our model of the His37-mediated proton transfer in M2 channels (**Fig. 4.10**).[6] In this model, in addition to proton acquisition by a neutral His to convert to the cationic state and proton release by the cation to a neutral His, τ and π tautomers can exchange rapidly by coupled release of a proton on one nitrogen (e.g., Nδ1) and acquisition of a proton on the other nitrogen (e.g., Nε2). Such prototropic tautomerism of heterocycles has been studied extensively,[64,65] and is known to involve much lower energy barriers when it is mediated by solvent molecules instead of proceeding purely by an intramolecular mechanism. Thus, His37 interaction with water molecules on both sides of the ring is most likely required for this tautomerism to occur. Indeed, exchange-averaged ^{1}H chemical shifts associated with the His37 nitrogens were recently measured for WT M2 and were shown to be

close to the water ^{1}H chemical shift at high temperature,[7] indicating that the proton-transfer partner of all three His species is water. Ring motion remains important in the model, to orient the imidazolium with water molecules to achieve proton transfer.

Although the model in **Fig. 4.10** depicts only the dynamic transformations of a single His residue, in reality the process should reflect the ensemble average of all His's in each tetramer, since protons relayed from one His can be transferred via water to a neighboring His. This model is applicable to both S31N and WT channels, based on the fundamental similarity of the observed exchange frequencies.

4.5.3 Effects of the Isoxazole Drug on His37-Water Proton Exchange

Binding of the isoxazole drug, although only as deep as G34, largely suppressed the His-water proton exchange, and changed the His37 chemical shifts to a form similar to the high-pH closed state. These are fully consistent with the observed Cα and Cβ chemical shifts, which also indicate a reversion of the peptide conformation to that of the closed state. Thus, isoxazole binding dehydrates the S31N channel, and interrupts the water wire that leads to His37,[5] which inhibits proton shuttling by His37.

Although we did not directly measure the pK_a values of the His37 tetrad in S31N-M2, the similar pH-dependence of the ^{15}N spectra between the S31N and WT peptides[8] suggests similar thermodynamic parameters for protonation and deprotonation. This implies that the pH 5.4 apo S31N in the VM+ membrane should contain significant amounts of +2 and +3 tetramers. We showed recently that the +3 channel has the highest specific conductance for the WT peptide, and in this state the imidazole undergoes ring reorientation and proton exchange.[6,8] Any effective drug must therefore inhibit the +3 charged channels. In general, the drug affinity to the channel is pH dependent: for example, titration of WJ352 to DPC-bound S31N showed an optimal pH of 6.8 for drug binding,[29] which is close to the third pK_a of S31N-M2 in DPC micelles. But the effective pK_a values are sensitive to the membrane environment: a more dynamic membrane causes higher pK_a values. In the chain-saturated virus-mimetic membrane the WT M2 has a third pK_a of 4.9. The more dynamic, unsaturated, VM+ membrane[66] used here is expected to increase the His pK_a values

moderately, so the third pK_a should shift to between pH 5 and 6. Thus, S31N in the VM+ membranes at pH 5.4 may have a similar charge distribution as S31N in DPC micelles at pH 6.8: both should be dominated by +2 and +3 channels, and both are inhibited by the isoxazole drugs based on the NMR spectra. Therefore, both micelle and bilayer data suggest that the isoxazole drugs significantly inhibit the activated channel at acidic pH. This may result from the reduced sensitivity of the amine-up drug to the charge state of His37 and from the bulky size of the drug, whose larger contact area with the peptide makes it less sensitive to small shape differences between the low-pH and high-pH channel pores.

4.6 Conclusion

In conclusion, we found that the isoxazole drug WJ352 perturbed the conformational equilibrium of S31N-M2, shifting the TM segment to a less ideal helical conformation. N31 exhibits the largest chemical shift perturbation, similar to S31 of the WT protein in complex with amantadine. In the low-pH S31N channel, the four His37 residues of the tetramer undergo proton transfer with water more rapidly than the WT channel, causing fast interconversion among τ, π, and cationic His. This exchange is more easily detected for tetramers with low charge states but is also present for the high-charge states. Drug binding at low pH suppressed most of the chemical exchange process, reverting the His37 residues to a similar charge distribution as that of the high-pH closed state. The conformation of other TM residues also reverts to the closed state structure. Therefore, the isoxazole drug, while bound more than one helical turn away from His37, potently arrests the atomic processes that shuttle protons in this channel.

4.7 Acknowledgement

This work is funded by NIH grants GM088204 to M.H. and AI074571 to W.F.D.

4.8 References

[1] R. A. Lamb, K. J. Holsinger and L. H. Pinto. "The Influenza A Virus M2 Ion Channel Protein and Its Role in the Influenza Virus Life Cycle." E. Wemmer, Ed. *Cellular Receptors of Animal Viruses*. Cold Spring Harbor Lab Press: Plainview, NY, **1994**, 303-321.

[2] L. H. Pinto and R. A. Lamb. "The M2 Proton Channels of Influenza A and B Viruses." *J. Biol. Chem.* **2006**, 281, 8997-9000.

[3] R. J. Sugrue, G. Bahadur, M. C. Zambon, M. Hall-Smith, A. R. Douglas and A. J. Hay. "Specific Structural Alteration of Influenza Haemagglutinin by Amantadine." *EMBO J.* **1990**, 9, 3469-3476.

[4] C. Wang, R. A. Lamb and L. H. Pinto. "Activation of the M2 Ion Channel of Influenza Virus: A Role for the Transmebrane Domain Histidine Residue." *Biophys. J.* **1995**, 69, 1363-1371.

[5] M. Hong and W. F. Degrado. "Structural Basis for Proton Conduction and Inhibition by the Influenza M2 Protein." *Protein Sci.* **2012**, 21, 1620-1633.

[6] F. Hu, W. Luo and Hong, M. "Mechanisms of Proton Conduction and Gating in Influenza M2 Proton Channels from Solid-State NMR." *Science* **2010**, 330, 505-508.

[7] M. Hong, K. J. Fritzsching and J. K. Williams. "Hydrogen-Bonding Partner of the Proton-Conducting Histidine in the Influenza M2 Proton Channel Revealed from ^{1}H Chemical Shifts." *J. Am. Chem. Soc.* **2012**, 134, 14753-14755.

[8] F. Hu, K. Schmidt-Rohr and M. Hong. "NMR Detection of pH-Dependent Histidine-Water Proton Exchange Reveals the Conduction Mechanism of a Transmembrane Proton Channel." *J. Am. Chem. Soc.* **2012**, 134, 3703-3713.

[9] T. I. Lin and C. Schroeder. "Definitive Assignment of Proton Selectivity and Attoampere Unitary Current to the M2 Ion Channel Protein of Influenza A Virus." *J. Virol.* **2001**, 75, 3647-3656.

[10] J. Hu, R. Fu, K. Nishimura, L. Zhang, H. X. Zhou, D. D. Busath, V. Vijayvergiya and T. A. Cross. "Histidines, Heart of the Hydrogen Ion Channel from Influenza A Virus: Toward and Understanding of Conductance and Proton Selectivity." *Proc. Natl. Acad. Sci. U.S.A.* **2006**, 103, 6865-6870.

[11] A. Acharya, V. Carnevale, G. Fiorin, B. G. Levine, A. Polishchuk, V. Balannick, I. Samish, R. A. Lamb, L. H. Pinto, W. F. DeGrado and M. L. Klein. "Structure and Mechanism of Proton Transport Through the Transmembrane Tetrameric M2 Protein Bundle of the Influenza A Virus." *Proc. Natl. Acad. Sci. U.S.A.* **2010**, 107, 15075-15080.

[12] Y. Tang, F. Zaitseva, R. A. Lamb and L. H. Pinto. "The Gate of the Influenza Virus M2 Proton Channel is Formed by a Single Tryptophan Residue." *J. Biol. Chem.* **2002**, 277, 39880-39886.

[13] A. Okada, T. Miura and H. Takeuchi. "Protonation of Histidine and Histidine-Tryptophan Interaction in the Activation of the M2 Ion Channel from Influenza A Virus." *Biochemistry* **2001**, 40, 6053-6060.

[14] M. Sharma, M. Yi, H. Dong, H. Qin, E. Peterson, D. Busath, H. X. Zhou and T. A. Cross. "Insight into the Mechanism of the Influenza A Proton Channel from a Structure in a Lipid Bilayer." *Science* **2010**, 330, 509-512.

[15] J. K. Williams, Y. Zhang, K. Schmidt-Rohr and M. Hong. "pH-Dependent Conformation, Dynamics, and Aromatic Interaction of the Gating Tryptophan Residue of the Influenza M2 Proton Channel from Solid-State NMR." *Biophys. J.* **2013**, 104, 1698-1708.

[16] A. J. Hay, A. J. Wolstenholme, J. J. Skehel and M. H. Smith. "The Molecular Basis of the Specific Anti-Influenza Action of Amantadine." *EMBO J.* **1985**, 4, 3021-3024.

[17] A. L. Stouffer, R. Acharya, D. Salom, A. S. Levine, L. Di Costanzo, C. S. Soto, V. Tereshko, V. Nanda, S. Stayrook and W. F. DeGrado. "Structural Basis for the Function and Inhibition of an Influenza Virus Proton Channel." *Nature* **2008**, 451, 596-599.

[18] S. D. Cady, K. Schmidt-Rohr, J. Wang, C. S. Soto, W. F. DeGrado and M. Hong. "Structure of the Amantadine Binding Site of Influenza M2 Proton Channels in Lipid Bilayers." *Nature* **2010**, 463, 689-692.

[19] S. D. Cady, J. Wang, Y. Wu, W. F. DeGrado and M. Hong. "Specific Binding of Adamantane Drugs and Direction of Their Polar Amines in the Pore of the Influenza M2 Transmembrane Domain in Lipid Bilayers and Dodecylphosphocholine Micelles Determined by NMR Spectroscopy." *J. Am. Chem. Soc.* **2011**, 133, 4274-4284.

[20] W. Luo and M. Hong. "Conformational Changes of an Ion Channel Detected Through Water-Protein Interactions Using Solid-State NMR Spectroscopy." *J. Am. Chem. Soc.* **2010**, 132, 2378-2384.

[21] J. Hu, F. Riqiang and T. A. Cross. "The Chemical and Dynamical Influence of the Anti-Viral Drug Amantadine on the M2 Proton Channel Transmembrane Domain." *Biophys. J.* **2007**, 93, 276-283.

[22] R. A. Bright, D. K. Shay, B. Shu, N. J. Cox and A. I. Klimov. "Adamantane Resistance Among Influenza A Viruses Isolated Early During the 2005-2006 Influenza Season in the United States." *JAMA* **2006**, 295, 891-894.

[23] A. C. Hurt, P. Selleck, N. Komadina, R. Shaw, L. Brown and I. G. Barr. "Susceptibility of Highly Pathogenic A(H5N1) Avian Influenza Viruses to the Neuraminidase Inhibitors and Adamantanes." *Antiviral Res.* **2007**, 73, 228-231.

[24] H. Zaraket, R. Saito, Y. Suzuki, Y. Suzuki, I. Caperig-Dapat, C. Dapat, I. I. Shabana, T. Baranovich and H. Suzuki. "Genomic Events Contributing to the High Prevalence of Amantadine-Resistant Influenza A/H3N2." *Antivir. Ther.* **2010**, 15, 307-319.

[25] L. Simonsen, C. Viboud, B. T. Grenfell, J. Dushoff, L. Jennings, M. Smit, C. Macken, M. Hata, J. Gog, M. A. Miller and E. C. Holmes. "The Genesis and Spread of Reassortment Human Infleunza A/H3N2 Viruses Conferring Adamantane Resistance." *Mol. Biol. Evol.* **2007**, 24, 1811-1820.

[26] R. M. Pielak, J. R. Schnell and J. J. Chou. "Mechanism of Drug Inihibition and Drug Resistance of Influenza A M2 Channel." *Proc. Natl. Acad. Sci. U.S.A.* **2009**, 106, 7379-7384.

[27] L. B. Andreas, M. T. Eddy, J. J. Chou and R. G. Griffin. Magic-Angle-Spining NMR of the Drug Resistant S31N M2 Proton Transporter from Influenza A." *J. Am. Chem. Soc.* **2012**, 134, 7215-7218.

[28] V. Balannik, V. Carnevale, G. Fiorin, B. G. Levine, R. A. Lamb, M. L. Klein, W. F. Degrado and L. H. Pinto. "Functional Studies and Modeling of Pore-Lining Residue Mutants of the Influenza A Virus M2 Ion Channel." *Biochemistry* **2010**, 49, 696-708.

[29] J. Wang, Y. Wu, C. Ma, G. Fiorin, J. Wang, L. H. Pinto, R. A. Lamb, M. L. Klein and W. F. Degrado. "Structure and Inhibition of the Drug-Resistant S31N Mutant of the M2 Ion Channel of Influenza A Virus." *Proc. Natl. Acad. Sci. U.S.A.* **2013**, 110, 1315-1320.

[30] C. Wang, K. Takeuchi, L. H. Pinto and R. A. Lamb. "Ion Channel Activity of Influenza A Virus M2 Protein: Characterization of the Amantadine Block." *J. Virol.* **1993**, 67, 5585-5594.

[31] M. Hohwy, H. J. Jakobsen, M. Eden, M. H. Levitt and N. C. Nielsen. "Broadband Dipolar Recoupling in the Nuclear Magnetic Resonance of Rotating Solids: A Compensated C7 Pulse Sequence." *J. Chem. Phys.* **1998**, 108, 2686-2694.

[32] M. Hong and R. G. Griffin. "Resonance Assignments for Solid Peptides by Dipolar-Mediated $^{13}C/^{15}N$ Correlation Solid-State NMR." *J. Am. Chem. Soc.* **1998**, 120, 7113-7114.

[33] D. P. Raleigh, M. H. Levitt and R. G. Griffin. "Rotational Resonance in Solid State NMR." *Chem. Phys. Lett.* **1988**, 146, 71-76.

[34] Y. Su, T. Doherty, A. J. Waring, P. Ruchala and M. Hong. "Roles of Arginine and Lysine Residues in the Translocatoin of a Cell-Penetrating Peptide from ^{13}C, ^{31}P, and ^{19}F Solid-State NMR." *Biochemistry* **2009**, 48, 4587-4595.

[35] K. Y. Chung, T. H. Kim, A. Manglik, R. Alvares, B. K. Kobilka and R. S. J. Prosser. "Role of Detergents in Conformational Exchange of A G Protein-Coupled Receptor." *J. Biol. Chem.* **2012**, 287, 36305-36311.

[36] C. P. Jaroniec, B. A. Tounge, J. Herzfeld and R. G. Griffin. "Frequency Selective Heteronuclear Dipolar Recoupling in Rotating Solids: Accurate ^{13}C-^{15}N Distance Measurements in Uniformly ^{13}C, ^{15}N-Labeled Peptides." *J. Am. Chem. Soc.* **2001**, 123, 3507-3519.

[37] F. Delaglio, S. Grzesiek, G. W. Vuister, G. Zhu, J. Pfeifer and A. Bax. "NMRPipe: A Multidimensional Spectral Processing System Based on UNIX Pipes." *J. Biomol. NMR* **1995**, 6, 277-293.

[38] M. P. Foster, D. S. Wuttke, K. R. Clemens, W. Jahnke, I. Radhakrishnan, L. Tennant, M. Reymond, J. Chung and P. E. Wright. "Chemical Shift as a Probe of Molecular Interfaces: NMR Studies of DNA Binding by the Three Amino-Terminal Zinc Finger Domains from Transcription Factor IIIA." *J. Biomol. NMR* **1998**, 12, 51-71.

[39] S. D. Cady, T. V. Mishanina and M. Hong. "Structure of Amantadine-Bound M2 Transmembrane Peptide of Influenza A in Lipid Bilayers from Magic-Angle-Spinning Solid-State NMR: The Role of Ser31 in Amantadine Binding." *J. Mol. Biol.* **2009**, 385, 1127-1141.

[40] M. Gustavsson, N. J. Traaseth and G. Veglia. "Probing Ground and Excited States of Phospholamban in Model and Native Lipid Membranes by Magic Angle Spinning NMR Spectroscopy." *Biochim. Biophys. Acta* **2012**, 1818, 146-153.

[41] Z. O. Shenkarev, A. S. Paramonov, E. N. Lyukmanova, L. N. Shingarova, S. A. Yakimov, M. A. Dubinnyi, V. V. Chupin, M. P. Kirpichnikov, M. J. Blommers and A. S. Arseniev. "Lipid-Protein Nanodiscs as Reference Medium in Detergent Screening for High Resolution NMR Studies of Integral Membrane Proteins." *J. Am. Chem. Soc.* **2010**, 132, 5630-5637.

[42] M. Munowitz, W. W. Bachovchin, J. Herzfeld, C. M. Dobson and R. G. Griffin. "Acid-Base and Tautomeric Equilibriums in the Solid State: ^{15}N NMR Spectroscopy of Histidine and Imidazole." *J. Am. Chem. Soc.* **1982**, 104, 1192-1196.

[43] S. Li and M. Hong. "Protonation, Tautomerization, and Rotameric Structure of Histidine: A Comprehensive Study by Magic-Angle-Spinning Solid-State NMR." *J. Am. Chem. Soc.* **2011**, 133, 1534-1544.

[44] B. Henry, P. Tekely and J. J. Delpuech. "pH and pK Determinations by High-Resolution Solid-State ^{13}C NMR: Acid-Base and Tautomeric Equilibria of Lyophilized L-Histidine." *J. Am. Chem. Soc.* **2002**, 124, 2025-2034.

[45] W. W. Bachovchin. "Contributions of NMR Spectroscopy to the Study of Hydrogen Bonds in Serine Protease Active Sites." *Magn. Reson. Chem.* **2001**, 39, S199-S213.

[46] J. A. Vila, Y. A. Arnautova, Y. Vorobjev and H. A. Scheraga. "Assessing the Fractions of Tautomeric Forms of the Imidazole Ring of Histidine in Proteins as a Function of pH." *Proc. Natl. Acad. Sci. U.S.A.* **2011**, 108, 5602-5607.

[47] F. Hu, W. Luo, S. D. Cady and M. Hong. "Conformational Plasticity of the Influenza A M2 Transmembrane Helix in Lipid Bilayers Under Varying pH, Drug Binding, and Membrane Thickness." *Biochim. Biophys. Acta* **2011**, 1808, 415-423.

[48] J. Hu, T. Asbury, S. Achuthan, C. Li, R. Bertram, J. R. Quine, R. Fu and T. A. Cross. "Backbone Structure of the Amantadine-Blocked Trans-Membrane Domain M2 Protno Channel from Influenza A Virus." *Biophys. J.* **2007**, 92, 4335-4343.

[49] T. A. Cross, M. Sharma, M. Yi and H. X. Zhou. "Influence of Solubilizing Environments on Membrane Protein Structures." *Trends Biochem. Sci.* **2010**, 36, 117-125.

[50] C. Li, H. Qin, F. P. Gao and T. A. Cross. "Solid-State NMR Characterization of Conformational Plasticity Within the Transmembrane Domain of the Influenza A M2 Proton Channel." *Biochim. Biophys. Acta* **2007**, 1768, 3162-3170.

[51] M. L. Bodner, C. M. Gabrys, J. O. Struppe and D. P. Weliky. "^{13}C-^{13}C and ^{15}N-^{13}C Correlation Spectroscopy of Membrane-Associated and Uniformly Labeled Human Immunodeficiency Virus and Influenza Fusion Peptides: Amino Acid-Type Assignments and Evidence for Multiple Conformations." *J. Chem. Phys.* **2008**, 128, 052319.

[52] H. Yao and M. Hong. "Membrane-Dependent Conformation, Dynamics, and Lipid Interactions of the Fusion Peptide of the Paramyxovirus PIV5 from Solid-State NMR." *J. Mol. Biol.* **2013**, 425, 563-576.

[53] A. L. Lai, A. E. Moorthy, Y. Li and L. K. Tamm. "Fusion Activity of HIV gp41 Fusion Domain is Related to its Secondary Structure and Depth of Membrane Insertion in a Cholesterol-Dependent Fashion." *J. Mol. Biol.* **2012**, 418, 3-15.

[54] Y. Su, R. Mani, T. Doherty, A. J. Waring, and M. Hong. "Reversible Sheet-Turn Conformational Change of a Cell-Penetrating Peptide in Lipid Bilayers Studied by Solid-State NMR." *J. Mol. Biol.* **2008**, 381, 1133-1144.

[55] C. Ader, R. Schneider, K. Seidel, M. Etzkorn, S. Becker and M. Baldus. "Structural Rearrangements of Membrane Proteins Probed by Water-Edited Solid-State NMR Spectroscopy." *J. Am. Chem. Soc.* **2009**, 131, 170-176.

[56] K. Takeuchi, H. Takahashi, S. Kawano and I. Shimada. "Identification and Characterization of the Slowly Exchanging pH-Dependent Conformational Rearrangement in KcsA." *J. Biol. Chem.* **2007**, 282 15179-15186.

[57] M. P. Bhate, B. J. Wylie, L. Tian and A. E. McDermott. "Conformational Dynamics in the Selectivity Filter of KcsA in Response to Potassium Ion Concentration." *J. Mol. Biol.* **2010**, 401, 155-166.

[58] P. M. Hwang, R. E. Bishop and L. E. Kay. "The Integral Membrane Enzyme PagP Alternates Between Two Dynamically Distinct States." *Proc. Natl. Acad. Sci. U.S.A.* **2004**, 101, 9618-9623.

[59] S. D. Cady and M. Hong. "Amantadine-Induced Conformational and Dynamical Changes of the Influenza M2 Transmembrane Proton Channel." *Proc. Natl. Acad. Sci. U.S.A.* **2008**, 105, 1483-1488.
[60] A. L. Stouffer, C. Ma, L. Cristian, Y. Ohigashi, R. A. Lamb, J. D. Lear, L. H. Pinto and W. F. DeGrado. "The Interplay of Functional Tuning, Drug Resistance, and Thermodynamic Stability in the Evolution of the M2 Proton Channel from the Influenza A Virus." *Structure* **2008**, 16, 1067-1076.
[61] J. S. Rossman, X. Jing, G. P. Leser and R. A. Lamb. "Influenza Virus M2 Protein Mediates ESCRT-Independent Membrane Scission." *Cell* **2010**, 142, 902-913.
[62] J. S. Rossman and R. A. Lamb. "Influenza Virus Assembly and Budding." *Virology* **2011**, 411, 229-236.
[63] X. J. Song and A. E. McDermott. "Proton Transfer Dynamics and N-H Bond Lengthening in N-H···N Model Systems: A Solid-State NMR Study." *Magn. Reson. Chem.* **2001**, 39, S37-S43.
[64] J. Elguero, A. R. Katritzky and O. V. Denisko. "Prototropic Tautomerism of Heterocycles: Heteroaromatic Tautomerism – General Overview and Methodology." *Adv. Heterocycl. Chem.* **2000**, 76, 1-84.
[65] V. I. Minkin, A. D. Garnovskii, J. Elguero, A. R. Katritzky and O. V. Denisko. "The Tautomerism of Heterocycles: Five-Membered Rings with Two or More Heteroatoms." *Adv. Heterocycl. Chem.* **2000**, 76, 157-323.
[66] S. D. Cady, T. Wang and M. Hong. "Membrane-Dependent Effects of a Cytoplasmic Helix on the Structure and Drug Binding of the Influenza Virus M2 Protein." *J. Am. Chem. Soc.* **2011**, 133, 11572-11579.

4.9 Supporting Information

4.9.1 Synthesis of Deuterated WJ352 Compounds

The synthesis of unlabeled **M2WJ332** and **M2WJ352** has been reported recently.[1] We describe below the modified procedure to synthesize two deuterated forms of WJ352. All chemicals were purchased from commercial vendors and used without further purification unless otherwise noted. ^{1}H and ^{13}C NMR spectra were recorded on a Bruker-300 NMR spectrometer. Chemical shifts are reported in parts per million with respect to residual solvent, CD_3OD = 3.31 ppm and CD_2Cl_2 = 5.30 ppm, or to the internal standard, tetramethylsilane = 0.00 ppm. The following abbreviations were used in reporting the NMR spectra: singlet (s), doublet (d), and triplet (t). All reactions were carried out under N_2 atmosphere unless otherwise stated. HPLC grade solvents were used for all the reactions. Flash column chromatography was performed using silica gel (230–400 mesh; Merck). Low-resolution mass spectrometry data were obtained using an

electrospray ionization (ESI) technique on a 3200 Q Trap LC tandem MS system (Applied Biosystems).

4.9.1.1 Synthesis of D5-M2WJ352

A solution of phenyl-D5-acetylene (1mmol) in THF-H_2O mixture (1:1) was cooled down to 0°C. Na_2CO_3 (12 mmol) was added in one portion. A solution of 2-chloro-2-hydroxyliminoacetic acid ethyl ester (2.5mmol) in THF was added dropwise using a dropping funnel. The solution was stirred overnight and diluted with ethyl acetate. The layers were separated and the aqueous layer was extracted with ethyl acetate. The organic layers were combined, dried over $MgSO_4$, filtered, and concentrated under reduced pressure. The resulting crude residue was purified by flash column chromatography (10% ethyl acetate/hexane) to give the isoxazole ester as a yellow solid (45% yield).

4.9.1.2 Ethyl 5-D5-phenyl-1,2-oxazole-3-carboxylate

^{1}H NMR (300 MHz, CD_2Cl_2): δ 6.96 (s, 1H), 4.45 (q, J = 7.10 Hz, 2H), 1.44 (t, J = 7.10 Hz, 3H). ^{13}CNMR (75 MHz, CD_2Cl_2): 171.58, 159.91, 157.11, 130.29 (t, J = 23.56 Hz), 128.64 (t, J = 25.58 Hz), 126.51, 125.43 (t, J = 24.32 Hz), 99.93, 62.16, 13.95. EI-MS: m/z ($M+H^+$): 223.1 (calculated), 223.3 (found).

Ethyl 5-D5-phenyl-1,2-oxazole-3-carboxylate (1 mmol) was dissolved in CH_3OH. $NaBH_4$ (2 mmol) was added portionwise to avoid solvent boiling. The resulting solution was stirred overnight at room temperature. 1N HCl was added to quench the reaction. Solvent was removed under reduced pressure and the residue was extracted with CH_2Cl_2 and H_2O. The alcohol intermediate, (5-D5-phenyl-1,2-oxazol-3-yl)methanol, was used for the next step bromination without further purification.

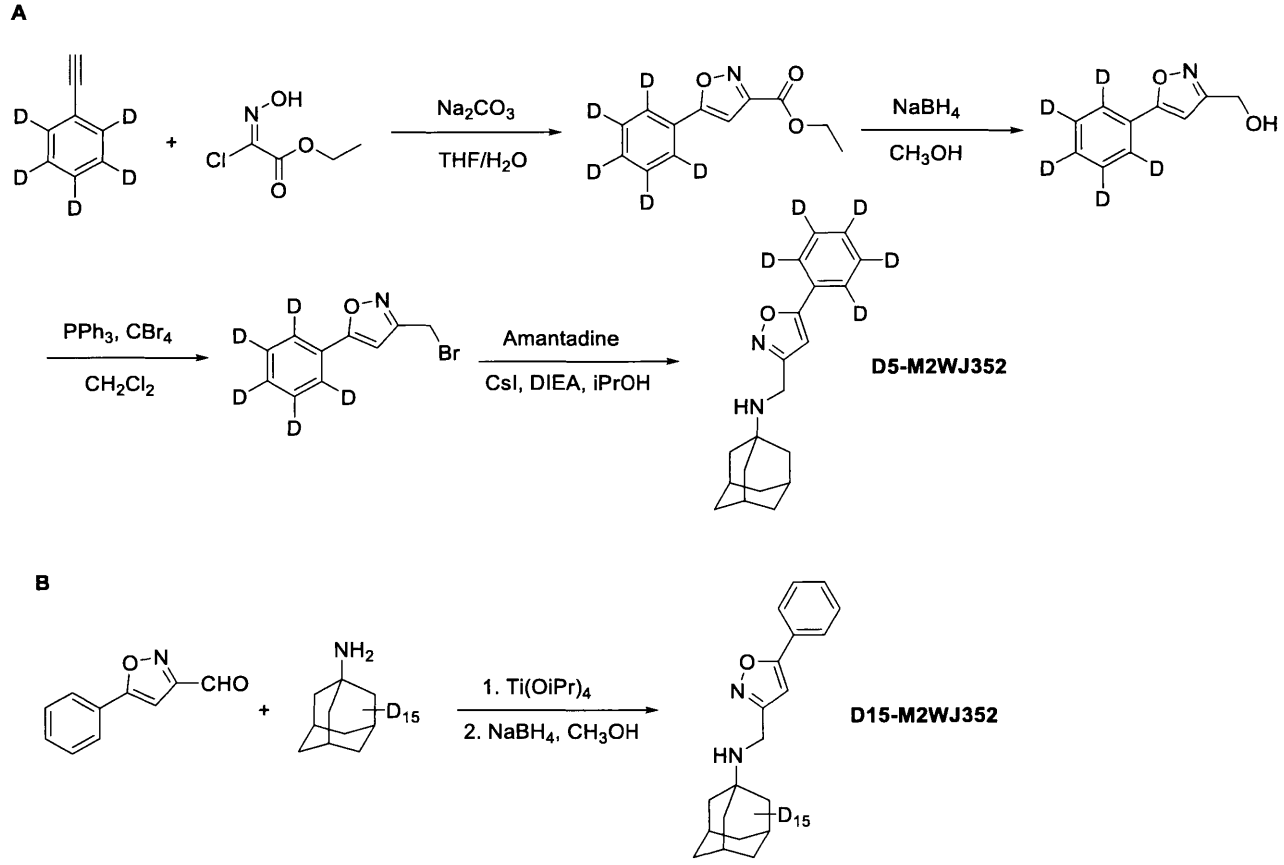

Figure 4.S1 Synthesis scheme of deuterium-labeled **M2WJ352**. (A) Synthesis of **D5-M2WJ352**. Phenyl-D_5-acetylene (Cat. # D-1086) was purchased from C.D.N isotopes Inc. (B) Synthesis of **D15-M2WJ352**. D_{15}-labeled amantadine was prepared according to the previous published procedure.[2]

4.9.1.3 N-[(5-D5-phenyl-1,2-oxazol-3-yl)methyl]adamantan-1-amine (D5-M2WJ352)

^{1}H NMR (300 MHz, CD_3OD): δ 6.83 (s, 1H), 3.88 (s, 2H), 2.10-2.08 (m, 3H), 1.77-1.70 (m, 12H). ^{13}CNMR (75 MHz, CD_3OD): 171.22, 165.38, 129.68 (t, J = 24.71 Hz), 128.55, 126.32 (t, J = 24.17 Hz), 100.45, 52.46, 42.77, 37.63, 37.16, 31.01. EI-MS: m/z ($M+H^+$): 314.2 (calculated), 314.8 (found).

(5-D5-phenyl-1,2-oxazol-3-yl)methanol (1 mmol) was dissolved in CH_2Cl_2. CBr_4 (1.5 mmol) and PPh_3 (1.5 mmol) were added sequentially. The mixture was stirred at room temperature for 3 hrs. Then solvent was removed and the mixture was extracted with CH_2Cl_2 and H_2O. The organic layer was dried over $MgSO_4$, filtered, and concentrated under reduced pressure. The

bromide (1mmol) was added to a solution of amantadine (1.5mmol) in iPrOH. Then CsI (0.2 mmol) and DIEA (1.5 eq) were added. The resulting solution was heated to reflux overnight. Solvent was removed under reduced pressure. The residue was dissolved in CH_2Cl_2 and extracted with H_2O. The organic layer was separated, dried over $MgSO_4$, filtered and concentrated under reduced pressure. The crude mixture was purified by flash column chromatography (10-15% CH_3OH/CH_2Cl_2) to give D5-M2WJ352 as a white solid (yield over three steps 21%).

4.9.1.4 Synthesis of D15-M2WJ352 (N-[(5-phenyl-1,2-oxazol-3-yl)methyl]D15-adamantan-1-amine).

Synthesis of **D15-M2WJ352** started with D15-amantadine and 5-phenyl-1,2-oxazole-3-carbaldehyde using reductive amination as reported.[3] ^{1}H NMR (300 MHz, CD_3OD): δ 7.84-7.81 (m, 2H), 7.50-7.47 (m, 3H), 6.80 (s, 1H), 4.68 (s, 2H). ^{13}CNMR (75 MHz, CD_3OD): 171.37, 166.29, 131.41, 130.19, 128.71, 126.76, 100.46, 99.71, 56.83. EI-MS: *m/z* ($M+H^+$): 324.2 (calculated), 324.6 (found).

Synthesis of selectively isotope labeled M2(19-49) S31N peptide followed the optimized solid phase synthesis protocol as reported.[4]

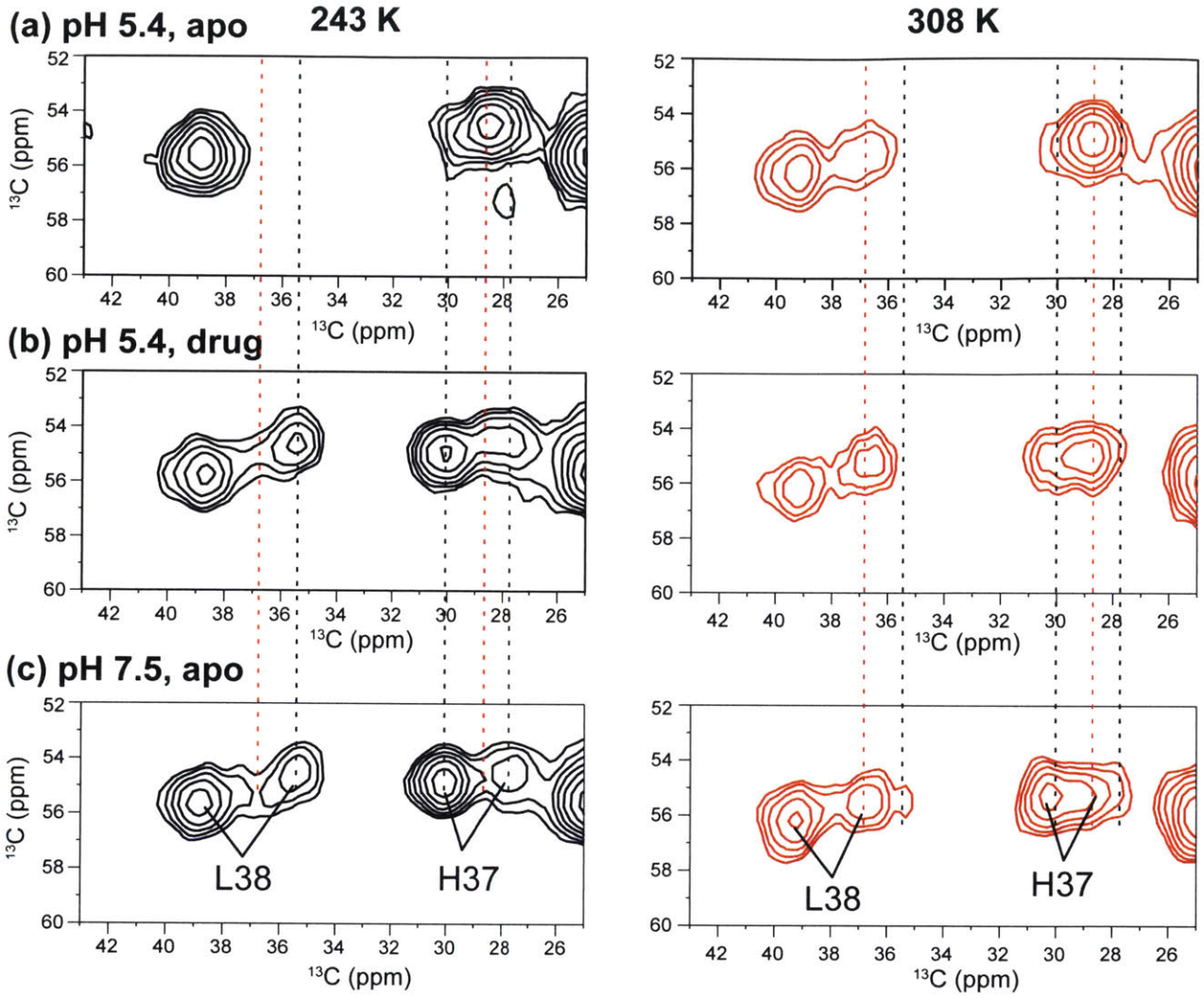

Figure 4.S2 2D ^{13}C-^{13}C correlation spectra showing the influence of pH, temperature and drug binding on the H37 and L38 chemical shifts in VGIHL-S31N-M2(19-49). (a) Apo peptide at pH 5.4. (b) Drug-bound peptide at pH 5.4. (c) Apo peptide at pH 7.5. Left column: 243 K spectra. Right column: 308 K spectra. L38 Cβ exhibits two conformations. At low temperature, the minor conformation is absent in the low-pH apo peptide but significantly present in the other two samples. At high temperature, the minor conformer is populated in the low-pH apo peptide, but the chemical shift is changed by 1.2 ppm, suggesting conformational exchange with the major conformation. H37 exhibits a similar trend.

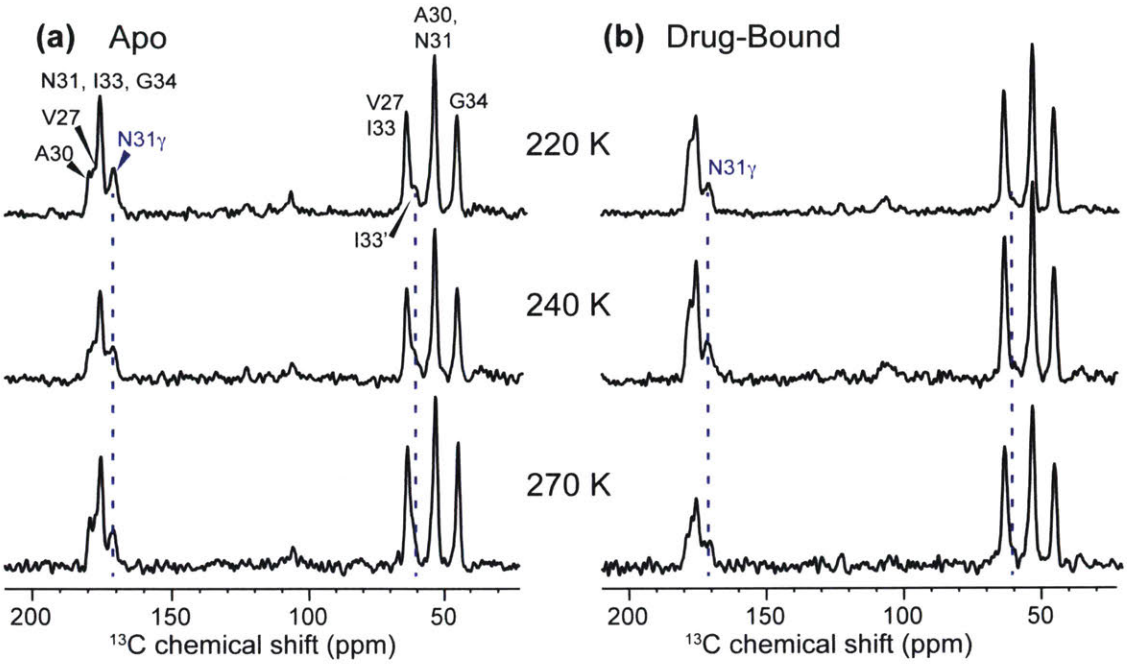

Figure 4.S3 1D ^{15}N-^{13}C dipolar filtered ^{13}C spectra of (a) apo and (b) drug-bound VANIG-S31N-M2(19-49) from 220 K to 270 K. The N31 sidechain Cγ chemical shift is unaffected by the drug.

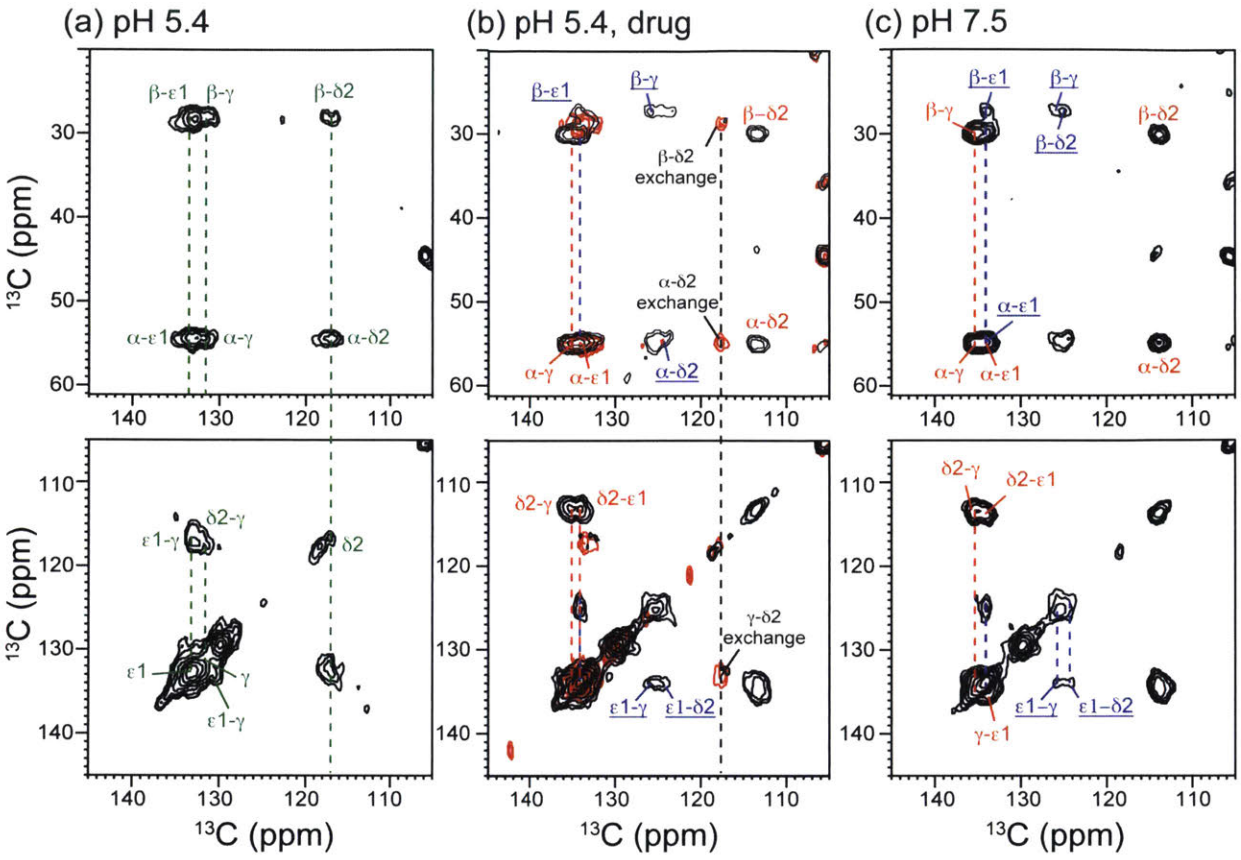

Figure 4.S4 Aromatic region of the 2D ^{13}C-^{13}C correlation spectra of His37 in VGIHL-S31N-M2(19-49). The spectra were measured at 243 K under 7 kHz MAS. (a) Apo peptide at pH 5.4. (b) Drug-bound peptide at pH 5.4. (c) Apo peptide at pH 7.5. Superimposed in red in (b) is the 308 K spectrum for the drug-bound sample, showing Cδ2 exchange peaks.

Table 4.S1 Different NMR samples used in this study.

Peptide	^{13}C, ^{15}N labeled residues	Membrane	pH	Drug:Tetramer ratio
$GIHL_{22-46}$	G34, I35, H37, L38	DMPC	7.5	Apo 1:1 d_5-WJ352 8:1 d_5-WJ352
$VANIG_{19-49}$	V27, A30, N31, I33, G34	DMPC	6.5	Apo 1:1 d_{15}-WJ352 10:1 d_{15}-WJ352
$VGIHL_{19-49}$	V28, G34, I35, H37, L38	VM+	5.4	Apo 10:1 WJ352
			7.5	Apo

Table 4.S2 ^{15}N and ^{13}C (referenced to TMS) chemical shifts of S31N-M2 in lipid membranes under various pH and drug binding conditions. Bold indicates sites with > 0.5 ppm chemical shift perturbation by the drug.

	Membrane	State	Nα	CO	Cα	Cβ	Cγ,γ1	Cγ2	Cδ,δ1	Cδ2	Cε,ε1	Nδ1,2	Nε2
V27	DMPC	Apo pH 6.5	119.8	177.3	63.7	29.4	20.7	**19.8**					
		Drug pH 6.5	120.1	177.3	63.4	29.4	20.4	**19.3**					
V28	VM+	Apo pH 5.4	**122.9**	**176.3**	65.2	29.2	**20.3**	19.5					
		Drug pH 5.4	122.6	**175.8**	65.0	28.9	**21.0**	19.3					
		Apo pH 7.5	122.0	176.0	65.2	28.9	20.7	19.3					
A30	DMPC	Apo pH 6.5	119.4	**179.5**	**53.2**	**15.5**							
		Drug pH 6.5	119.0	**177.9**	**52.7**	**16.2**							
N31	DMPC	Apo pH 6.5	117.7	**175.6** **174.8**	**53.5s** **55.1w**	**35.4s** **38.7w**	**171.3** **170.5**					106.0	
		Drug pH 6.5	117.4	**175.4**	**53.0**	**35.3**	**171.0**					106.0	
I33	DMPC	Apo pH 6.5	**119.0**	175.4	63.7s **61.4w**	35.7	28.4	**14.8**	12.0				
		Drug pH 6.5	**119.8**	175.6	63.5s **62.4w**	35.4	28.8	**15.6**	11.7				
G34	VM+	Apo pH 5.4	105.1 109.5	175.5 173.1	44.9								
		Drug pH 5.4	105.6 109.7	175.0 173.0	44.5								
		Apo pH 7.5	105.1 109.0	175.3 173.4	44.8								
	DMPC	Apo pH 6.5	**105.0**	**174.9s** **173.2w**	45.0								
		Drug pH 6.5	**106.7**	**175.1w** **173.1s**	45.4								
	DMPC	Apo pH 7.5	107.3 104.7	175.0s 173.0w	44.9								
		Drug pH 7.5	107.3	175.0s 173.2s	45.2								

I35	VM+	Apo pH 5.4	123.2 118.2	174.8	63.3	35.2	**28.6**	**15.6**	11.8				
		Drug pH 5.4	122.5 118.8	174.7 175.3	63.4	35.6	**26.6** **28.8**	**15.0** **16.4**	11.4 11.6				
		Apo pH 7.5	122.1 119.0	174.7 175.4	63.6	35.3 35.6	26.7 28.7	15.0 16.1	11.2 11.9				
	DMPC	Apo pH 7.5	122.8	175.1	63.5	35.4	28.0	15.8	11.8				
		Drug pH 7.5	122.2	175.4	63.5	35.5	27.8	15.7	11.9				
H37	VM+	Apo pH 5.4	--- 117.4 ---	--- 174.2 ---	--- 54.8 ---	--- 28.4 ---							
		Drug pH 5.4	117.2	174.2	**54.8** **54.8** **55.4**	**27.6** **28.5** **30.1**							
		Apo pH 7.5	117.6	174.3	54.8 --- 55.3	27.9 --- 30.1							
	DMPC	Apo pH 7.5	117.7	174.5	55.1	29.9	135.2			113.3	134.2	251.2τ 170.2π	159.0τ 251.2π
		Drug pH 7.5	118.0	174.5	**55.5** **58.8**	**30.0** **29.1**	135.4			113.5	134.0	165.9π 252.0τ	165.9τ 252.0π
L38	VM+	Apo pH 5.4	117.4	175.2	55.5	38.7	24.3		19.8				
		Drug pH 5.4	117.2	**175.3** **175.9**	**55.7** **54.7**	**38.6** **35.4**	24.8 24.7		**19.8** **21.3**				
		Apo pH 7.5	117.6	174.4 175.3	55.6 54.6	38.7 35.4	24.7 24.7		19.7 21.1				
	DMPC	Apo pH 7.5	117.7	175.4	55.8	38.9	24.6	**19.9**	**19.9**				
		Drug pH 7.5	118.0	175.7	55.9	39.3	24.7	**20.5**	**20.5**				

4.9.2 Supporting Information References

[1] J. Wang, Y. Wu, C. Ma, G. Fiorin, J. Wang, L. H. Pinto, R. A. Lamb, M. L. Klein and W. F. Degrado. "Structure and Inhibition of the Drug-Resistant S31N Mutant of the M2 Ion Channel of Influenza A Virus." *Proc. Natl. Acad. Sci. U.S.A.* **2013**, *110*, 1315-1320.

[2] S. D. Cady, K. Schmidt-Rohr, J. Wang, C. S. Soto, W. F. DeGrado and M. Hong. "Structure of the Amantadine Binding Site of Influenza M2 Proton Channels in Lipid Bilayers." *Nature* **2010**, *463*, 689-692.

[3] J. Wang, C. Ma, J. Wang, H. Jo, B. Canturk, G. Fiorin, L. H. Pinto, R. A. Lamb, M. L. Klein and W. F. DeGrado. "Discovery of Novel Dual Inhibitors of the Wild-Type and the Most Prevalent Drug-Resistant Mutant, S31N, of the M2 Proton Channel from Influenza A Virus." *J. Med. Chem.* **2013**, *56*, 2804-2812.

[4] S. D. Cady, J. Wang, Y. Wu, W. F. DeGrado and M. Hong. "Specific Binding of the Adamantane Drugs and Direction of Their Polar Amines in the Pore of the Influenza M2 Transmembrane Domain in Lipid Bilayers and Dodecylphosphocoline Micelles Determined by NMR Spectroscopy." *J. Am. Chem. Soc.* **2011**, *133*, 4274-4284.

5. Probing Membrane Protein Structure Using Water Polarization Transfer Solid-State NMR

Jonathan K. Williams and Mei Hong

Department of Chemistry, Iowa State University, Ames, IA

Journal of Magnetic Resonance. **2014**, vol. 247, pp. 118-127.
DOI: 10.1016/j.jmr.2014.08.007

5.1 Abstract

Water plays an essential role in the structure and function of proteins, lipid membranes and other biological macromolecules. Solid-state NMR heteronuclear-detected ^{1}H polarization transfer from water to biomolecules is a versatile approach for studying water-protein, water-membrane, and water-carbohydrate interactions in biology. We review radiofrequency pulse sequences for measuring water polarization transfer to biomolecules, the mechanisms of polarization transfer, and the application of this method to various systems. Three polarization transfer mechanisms, chemical exchange, spin diffusion and NOE, manifest themselves at different temperatures, magic-angle-spinning frequencies, and pulse irradiations. Chemical exchange is ubiquitous in all systems examined so far, and spin diffusion plays the key role in polarization transfer within the macromolecule. Tightly bound water molecules with long residence times are rare in proteins at ambient temperature. The water polarization-transfer technique has been used to study the hydration of microcrystalline proteins, lipid membranes, and plant cell wall polysaccharides, and to derive atomic-resolution details of the kinetics and mechanism of ion conduction in channels and pumps. Using this approach, we have measured the water polarization transfer to the transmembrane peptide of the influenza M2 protein to obtain information on the structure of this tetrameric proton channel. At short mixing times, the polarization transfer rates are site-specific and depend on the pH, labile protons, sidechain conformation, as well as the radial position of the residues in this four-helix bundle. Despite the multiple dependences, the initial transfer rates reflect the periodic nature of the residue positions from the water-filled pore, thus this technique provides

a way of gleaning secondary structure information, helix tilt angle, and the oligomeric structure of membrane proteins.

5.2 Introduction

Water is one of the most essential molecules for the proper structure and function of proteins and other biological macromolecules. Protein hydration, protein folding, ion channel function, and lipid self-assembly, all rely on water interactions with these molecules.[1-6] Solid-state NMR (SSNMR) spectroscopy is an excellent method to study water interactions with non-crystalline and insoluble biological macromolecules. We are particularly interested in understanding how water interacts with proteins in phospholipid membranes, and to what extent water can serve as a probe of membrane protein structure. In this perspective article, we review SSNMR pulse sequences for measuring water-biomolecule polarization transfer and recent findings of the mechanism of water interactions with proteins, lipids and other biological solids. We focus on studies that detect protein signals to obtain site-specific information about water dynamics and binding, and do not attempt to cover the large literature of direct observation of water dynamics using relaxation NMR. We then present our new study of the water interaction with the four-helix bundle formed by the influenza M2 transmembrane peptide (M2TM). The goal is to explore the extent to which secondary structure and oligomeric structure of membrane proteins can be extracted from site-specific water-protein polarization transfer rates.

5.3 Solid-State NMR Techniques for Studying Water-Protein Interactions

The main SSNMR approach for probing water-biomolecule interactions is to transfer the water ^{1}H polarization to biomolecules and detect the result of the transfer via ^{13}C, ^{15}N or other heteronuclear signals of the biomolecule. This polarization transfer technique has many pulse sequence variations. When implemented in a 1D fashion, a ^{1}H polarization gradient needs to be established first, which is usually accomplished by a ^{1}H T_2 filter. The Hahn echo retains the polarization of the dynamic water, which has long T_2, while destroying the polarization of the rigid molecules, which have much shorter T_2's. A subsequent longitudinal mixing period (t_{mix}) allows the water polarization to transfer to the biomolecule, followed by ^{1}H-X (X = ^{13}C, ^{15}N, etc.) cross-

polarization (CP) for detection (**Fig. 5.1a**). The CP step can be implemented in a spin-diffusion-free fashion by locking the ^{1}H magnetization along the magic-angle direction (LG-CP), or can include spin diffusion using the conventional Hartman-Hahn (HH) CP. In the latter case, the longitudinal mixing period may be skipped to shorten the total polarization transfer time, if one wishes to selectively examine only the nearest water protons.[7,8]

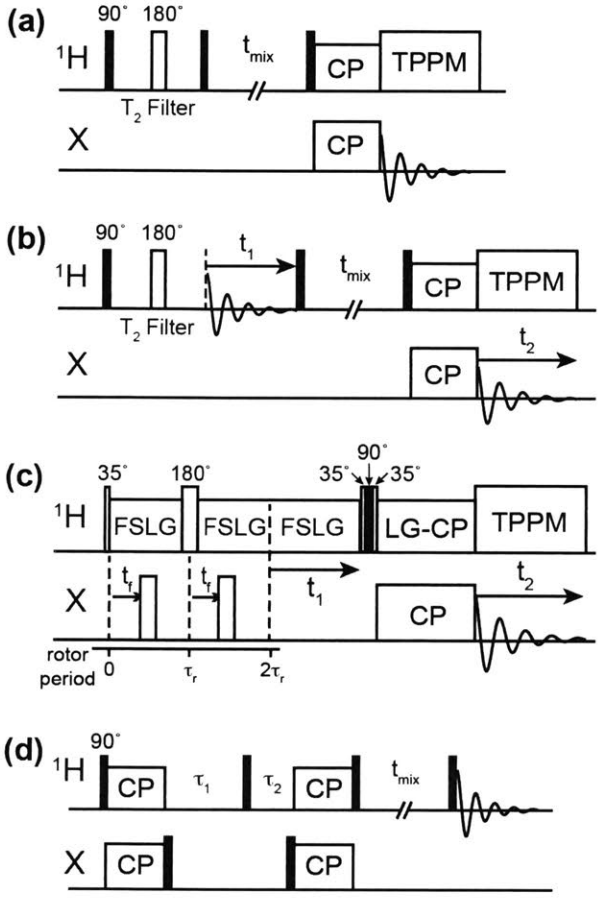

Figure 5.1 Representative pulse sequences used to measure water polarization transfer to biomolecules. (a) 1D T_2-filtered experiment. (b) 2D ^{1}H-undecoupled HETCOR experiment with spin diffusion mixing. (c) 2D dipolar-dephased MELODI-HETCOR experiment. (d) ^{1}H-detected 1D XHH experiment for sensitivity-enhanced detection of biomolecule-water polarization transfer.

This polarization transfer framework is modified from the Goldman-Shen experiment.[9,10] The heteronuclear signals reveal which sites are close to water, and the distance information can be made more quantitative by measuring the heteronuclear signals as a function of t_{mix}.

When water is not the only species that survives the ^1H T_2 filter and other dynamic species also exist, then the 1D experiment needs to be modified either by selective excitation of the water resonance[11] or by extending the experiment to 2D and encoding the ^1H chemical shift before the mixing period (**Fig. 5.1b**).[12,13] In the resulting 2D spin-diffusion heteronuclear correlation (HETCOR) experiment, ^1H homonuclear decoupling is optional during the evolution period. Without ^1H-^1H decoupling, only highly mobile molecules such as water and liquid-crystalline lipids will be detected in the indirect dimension. When homonuclear decoupling is applied, the ^1H signals of the rigid solid also become detectable, thus providing higher information content to the spectra. For the undecoupled 2D experiment, the ^1H T_2 filter is necessary for suppressing the rigid proton signals in the first t_1 slice, while for the homonuclear-decoupled experiment, the T_2 filter can be removed.

In practice, even with ^1H chemical shift encoding, some solid protons such as protein Hα can resonate near the bulk-water chemical shift of 4.8 ppm to cause ^1H resonance overlap. To address this problem, and to simplify the 2D HETCOR spectra, we developed a dipolar-filtered HETCOR experiment called MELODI (medium- and long-distance heteronuclear correlation) HETCOR, which detects only cross peaks resulting from non-bonded spin pairs (**Fig. 5.1c**).[14,15] Before the ^1H evolution period, a ^1H-X REDOR dephasing period is inserted in which an 180° X-pulse is applied every half a rotor period to recouple the ^1H-X dipolar interaction. A single ^1H 180° pulse in the center of the dephasing period refocuses the ^1H chemical shift. This REDOR filter destroys the magnetization of protons that are directly bonded to an X spin. The protons that survive this dipolar filter include water, protein protons without directly bonded ^{13}C or ^{15}N, and highly dynamic protons with weaker ^1H-X dipolar couplings. Demonstration on natural-abundance amino acids confirmed that only two-bond cross peaks such as Hα-Cβ and Hβ-Cα remained in the ^{13}C-dephased ^{13}C-^1H MELODI-HETCOR spectra.[14] For a selectively ^{13}C-labeled model protein, ubiquitin, the ^{13}C-dephased ^{13}C-^1H MELODI-HETCOR spectra contain cross peaks between labeled ^{13}C and protons without directly bonded ^{13}C, and cross peaks between labeled ^{13}C and ^{15}N-bonded protons such as backbone amides, Lys NH_3 and Arg guanidinium Hη and Hε. For a uniformly ^{13}C, ^{15}N-labeled membrane protein, colicin Ia channel domain, ^{13}C-dephased ^{13}C-^1H MELODI-HETCOR spectra exhibit ^{13}C-H^N cross peaks.

The MELODI-HETCOR technique is well suited to the study of water-protein interactions, since water is unaffected by all dephasing pulses (unless ^{17}O pulses are applied). Simultaneous irradiation of ^{13}C and ^{15}N in the dipolar dephasing period will destroy all rigid protein proton signals and leave only water ^{1}H cross peaks. Using this approach, we have investigated water interactions with arginine residues of a cationic antimicrobial peptide.[16] The data allowed the unambiguous assignment of cross peaks at a ^{1}H chemical shift at 4.9 ppm to water-Arg correlations, rather than Arg Hα-sidechain correlations. This means that water solvates membrane-inserted guanidinium ions, which provides direct evidence of the long-suspected but rarely proven phenomenon that water penetrates into the lipid membrane to lower the free energy of insertion of these cationic membrane peptides.

To enhance the sensitivity of water-protein polarization transfer experiments, we developed a ^{1}H-detected experiment called XHH, in which the ^{1}H mixing period is preceded by dual CP steps: forward ^{1}H-X CP and reverse X-^{1}H CP. In this way, only protons directly attached to the X spins are selected to undergo polarization transfer (**Fig. 5.1d**).[17] Under moderate MAS frequencies and without ^{1}H dilution by deuteration, such a CHH experiment detects only the ^{1}H magnetization of mobile water and lipids that is transferred from the ^{13}C-bonded protein protons. Between the two CP steps, the X-spin magnetization is stored along the z-axis while the initial ^{1}H magnetization is destroyed in the transverse plane. 90° ^{1}H "purge" pulses during the dephasing period can be applied to ensure clean suppression of all initial ^{1}H magnetization. The sensitivity enhancement factor of the CHH experiment depends on the ^{13}C labeling level and the number of protein protons relative to the number of mobile water and lipid protons. For ^{13}C-labeled colicin Ia channel domain, we showed that the 1D CHH experiment is faster than the 2D ^{13}C-detected ^{1}H spin diffusion experiment by a time factor of 180-350 fold and yields the same buildup curves as the 2D experiment.

A different way of transferring water polarization is via the nuclear Overhauser effect (NOE). By irradiating on the water ^{1}H resonance for several seconds before applying a 90° pulse on the X channel, one can observe NOE enhancement of the X-spin signal, which depends on the water-protein proximity. Solid-state NOEs has been observed in model compounds by Takegoshi

and Terao,[18] and application to water-protein transfer shows that enhancement factors of 50-100% can be achieved.[8]

5.4 Mechanisms of Water-Protein Polarization Transfer

As alluded to above, during the longitudinal and transverse mixing periods, three mechanisms can exist to transfer water polarization to biomolecules: chemical exchange between labile protons, spin diffusion, and the NOE (**Fig. 5.2a**). At neutral pH, chemical exchange rates range from ~100 s^{-1} for amide protons in protein backbones to ~1000 s^{-1} for amino protons of Lys, His and Arg, to ~10,000 s^{-1} for hydroxy protons of Tyr.[19,20] Exchange rates decrease with temperature and also depend on pH. Spin diffusion is dipolar-mediated relayed magnetization transfer that is described by a diffusion equation,[21,22] and is the most efficient mechanism in rigid solids. The NOE is a dipolar cross relaxation process that requires motional modulation of two spins in close proximity.[23,24]

At ambient temperature, chemical exchange has been found to be important and perhaps even necessary for water polarization transfer to biomembranes. Griffin and coworkers[7] detected the ^{15}N signals of bacteriorhodopsin using a 1D ^{1}H T_2-filtered ^{15}N CP experiment. With a T_2 filter of 1 ms, the backbone amide ^{15}N peak was completely suppressed while the Schiff-base ^{15}N peak and the free Lys NH_3 peaks survived. The ^{1}H T_2 associated with the remaining ^{15}N signals is similar to the bulk-water T_2 of ~50 ms, while the ^{1}H-^{15}N CP was equilibrated by 0.5 ms, indicating solid-like character for the protons that cross-polarize to ^{15}N. These results indicate that the Schiff base, although deeply buried in the active site of the protein, is accessible to bulk water and exchanges with it rapidly. Hong and coworkers showed that chemical exchange is necessary for water-lipid polarization transfer.[12] In 2D ^{31}P-^{1}H spin-diffusion HETCOR spectra, many lipid membranes, including POPE, POPG, POPC/cholesterol, and POPE/POPG containing membrane peptides, showed strong water ^{1}H-^{31}P cross peaks, while POPC exhibited no water cross peak even after a long mixing time of 225 ms. POPC is the only lipid without any labile protons among all the lipids examined, thus the result unambiguously shows that chemical exchange is necessary for water-lipid polarization transfer. The implication is that if labile protons are absent in the system, then

water cross peaks will not be detectable by polarization transfer experiments at ambient temperature even if the membrane surface is hydrated.

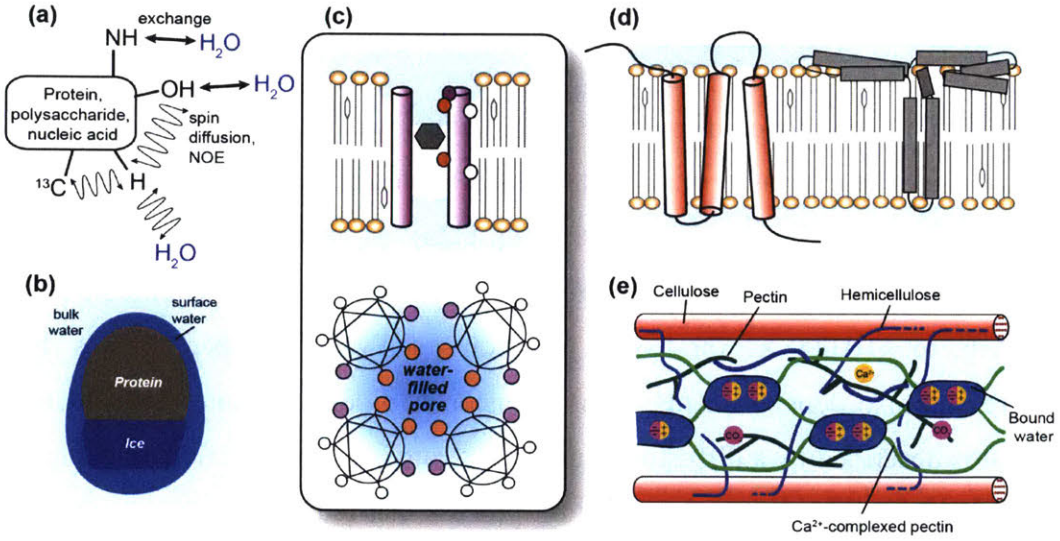

Figure 5.2 Main mechanisms of water-biomolecule polarization transfer (a) and applications of solid-state NMR to investigations of water-protein and water-polysaccharide interactions (b-e). (a) Water protons can transfer polarization to biomolecules via chemical exchange, dipolar spin diffusion, and NOE. (b) Distinguishing liquid water and ice by solid-state NMR provides structural information on ice-binding proteins. (c) Water polarization transfer to ion channels has been used to investigate ion conduction kinetics, oligomeric structure of the channel, and to identify lipid-facing versus pore-facing residues. (d) Water-edited solid-state NMR experiments have been used to determine the topology of membrane proteins in terms of surface-exposed loops (left) and helices (right) versus membrane-embedded residues. (e) Distinct water interactions with different polysaccharides of the plant cell wall have been observed provide information on the three-dimensional structure of the cell wall.

Following chemical exchange, ^1H spin diffusion is usually the dominant mechanism for polarization transfer within the rigid biomolecules. At moderate MAS frequencies, spin diffusion is readily observed, and its effect increases with decreasing temperature, which is opposite the temperature dependence of chemical exchange. Direct dipolar transfer from water to proteins is rare due to the rapid translational diffusion of water, except when water is tightly bound or confined. To investigate if there are solid-like water molecules with long residence times in proteins, Böckmann and Lesage applied a dipolar double-quantum filtered (DQF) HETCOR experiment to the microcrystalline protein, Crh.[8] Only water with residence times longer than a

few hundred microseconds can survive this DQF. They did not observe any water-protein double-quantum peaks, indicating that water molecules associated with Crh undergo translational diffusion on a much shorter timescale than microseconds. Reif and coworkers used the spin-diffusion buildup of the ^{15}N signals of the perdeuterated SH3 protein to investigate the water dynamics in this microcrystalline protein.[25] Some of the residues were found to have buildup rates that are proportional to the water-H^N dipolar couplings calculated from the crystal structure, indicating that these water molecules are sufficiently bound to the protein to give distance-dependent spin diffusion. On the other hand, surface residues, although in contact with a large number of water molecules, show slow transfer rates, indicating that the dynamic bulk water on the protein surface does not contribute significantly to spin diffusion. This finding is consistent with a Crh study in which two water pools, bulk and bound, were resolved in the ^1H spectra.[26] Removal of the bulk water did not change the water-protein polarization transfer. Water peaks with fine structures that reflect different environments are also commonly seen in membrane proteins and other hydrated biomolecules.[12,27,28]

Using Crh, Böckmann, Lesage and coworkers systematically investigated the relative importance of the three polarization transfer mechanisms and the conditions under which each mechanism dominates.[8,29] They found that chemical exchange is the primary mechanism at room temperature but slows down at low temperature, even when water is prevented from freezing by cryoprotectants. Spin diffusion is the dominant mechanism within protein protons under moderate MAS, but ultrafast MAS (> 45 kHz) suppresses this contribution, allowing the NOE mechanism to be detected. At low temperature or ultrafast MAS, these authors observed negative water-protein cross peaks in Crh,[30] which can only be assigned to rotating-frame nuclear Overhauser effects. Zilm and coworkers attributed H^N-ubiquitin cross peaks in ^1H-detected ^{15}N-^1H correlation spectra to NOE, based on the fact that the rate of the cross peak buildup with the longitudinal mixing time differs from the rate of buildup with a transverse spin-lock time.[31] The assignment of NOE cross peaks in these microcrystalline proteins suggests that a small number of water molecules are sufficiently bound to the protein sidechains to undergo correlated motion with the protein.

5.5 Water Interactions with Proteins, Lipid Membranes, and Carbohydrates

In this section we review recent applications of water polarization transfer and water-edited SSNMR experiments to different biomolecular systems (**Fig. 5.2b-e**). McDermott and coworkers investigated the water interaction of an antifreeze protein (AFP) to understand how proteins retain hydration shells and interact with ice.[32] ^{1}H spin-lattice relaxation of AFP in frozen water at -35°C showed biexponential behavior, while the non-ice-binding protein, ubiquitin, showed single-exponential relaxation. This difference indicates that two proton baths exist near AFP and undergo intermediate exchange with each other. When D_2O solution was used, the AFP relaxation became single-exponential, indicating that liquid water is responsible for the second proton bath. Cross-saturation NMR experiments provided insight into the protein-ice interaction. With a ^{1}H presaturation pulse, the ^{13}C intensities of ubiquitin decreased due to cross saturation, and the intensity reduction does not depend on the presaturation pulse length. In contrast, the ^{13}C intensities of AFP decreased over a wider ^{1}H frequency range as the presaturation pulse lengthened, indicating that there is spin diffusion between ice and AFP. Thus, without detecting the ice ^{1}H signals, which is difficult, the authors were able to show that AFP is in contact with ice. AFP also shows cross peaks with the liquid-water ^{1}H at 5 ppm in 2D ^{13}C-^{1}H HETCOR spectra, indicating that the protein retains a partial hydration shell. Taken together, these data indicate that a part of the AFP, presumably the ice-binding surface, is in contact with the ice lattice (**Fig. 5.2b**), in contrast to the non-ice-binding ubiquitin, which retains a complete hydration shell and is fully shielded from ice in the frozen solution.

The water polarization-transfer technique has been applied fruitfully to obtain structural information on membrane proteins. Baldus and coworkers showed that the intensity buildup of protein signals as a function of t_{mix} depends on the water-exposed surface area of the protein.[11] Adapting the spin diffusion theory from polymer NMR,[22] they analyzed the water-protein spin diffusion rates to extract information about structural changes of a potassium channel between high and low pH. The low-pH channel, which shows faster polarization transfer, corresponds to a 65% larger water-protein surface area. Similarly, Hong and coworkers measured the water-exposed surface area of the influenza M2 proton channel.[33] Comparison of the water-protein spin diffusion rates among three states, the low pH open state, the high pH closed state, and the high-

pH drug-bound state, revealed that the open state has the largest water-exposed protein surface area, while the drug-bound state is the least hydrated, with a 2-fold smaller water-exposed surface area (**Fig. 5.2c**). Moreover, site-specific buildup rates identified the drug-binding site to be below V27 and above G34.

The residence time of water in ion channels is a question of significant interest. Recent MD simulations suggested that long-lived water in the selectivity filter of potassium channels might explain the slow inactivation of these channels after opening. Using ultrafast MAS and ^{1}H detection experiments, Baldus and coworkers measured water cross peaks to the selectivity filter residues in KcsA.[34] They found that the conductive state of the selectivity filter has fewer water cross peaks than the inactivated state. The difference was interpreted in light of the MD prediction that buried and ordered water molecules lock the selectivity filter in the inactivated conformation, thus slowing its relaxation to the conductive state. However, the observed water-protein cross peaks appear at a ^{1}H chemical shift of 4.8 ppm, indicating that the protein-bound water is in fast exchange with bulk water, reminiscent of water contact with the Schiff base in bacteriorhodopsin. Thus, these protein-bound water molecules are unlikely to have long (microsecond) residence times. In a related context, Hong and coworkers measured the chemical shifts of protons that are dipolar-coupled to His37 imidazole nitrogens in the influenza M2 proton channel,[35] in order to distinguish between a histidine-histidine strong hydrogen-bond model[36] and a water-histidine exchange model[37] for proton conduction. At low temperature, they found H^N chemical shifts of <15 ppm for both Nε2 and Nδ1, consistent with regular N-H hydrogen bonds, while at high temperature, the Nε2 and Nδ1-correlated ^{1}H chemical shift collapsed to 4.8 ppm, indicating that His37 undergoes rapid exchange with a large number of water molecules to adopt the bulk water ^{1}H chemical shift. Thus, these data support the water-histidine exchange model for proton conduction.

Water polarization transfer can also be used in a spectral-editing fashion to selectively detect the water-exposed protein residues. This approach has been used to detect loop residues in a seven-helix transmembrane receptor,[38] cytoplasmic residues in the full-length M2 protein,[39] and to determine the topology of colicin and gramicidin channels (**Fig. 5.2d**).[10,13,40] In a complementary approach, hydrogen/deuterium (H/D) exchange has been used extensively to determine water-

exposed and water-exchanged residues in membrane proteins. The effect of H/D exchange can be manifested as attenuation of the amide ^{15}N signals after ^{1}H-^{15}N cross polarization, as amide ^{2}H spectra, and even as ^{15}N-^{2}H dipolar couplings. The exchange-induced ^{15}N signal suppression can be readily incorporated into 2D and 3D ^{15}N-^{13}C MAS correlation experiments for protein resonance assignment, and this approach has been applied to several multi-span membrane proteins to obtain topology information.[41-43] H/D exchange-edited ^{2}H NMR and ^{15}N-^{2}H dipolar coupling experiments were employed by Cross and coworkers to study the structures of gramicidin[44,45] and influenza M2 channels.[46] The exchange rates were found to be sufficiently residue-specific to give information about the structures of these membrane peptides.

Water interaction with the lipid bilayer itself has also been studied. The self-diffusion coefficient of water is known precisely to be 2.299×10^{-9} m^2/s at 25°C.[47] Deviation from this value gives information about how biomolecules interact with water to retard or speed up its translational diffusion. Han and coworkers used the Overhauser dynamic nuclear polarization technique to study water translational diffusion within 1.5 nm of the surface of a DPPC bilayer.[48,49] The self- and cross relaxations of water near a nitroxide spin label that is covalently attached to the lipid headgroup depends on the water residence time near the spin label. By observing the water signal enhancement under microwave irradiation of the spin label, these authors measured the relaxation rates to deduce the water correlation time. They found that the correlation time of the surface hydration water is 6-fold longer than that of bulk water, consistent with the expected membrane retardation of water diffusion. However, when the bulk-solution viscosity was increased 10-fold by using high osmolyte concentrations, the surface-water correlation times increased by only 2-fold. This small magnitude of change suggests that the surface topology and chemistry of the membrane, rather than bulk solvent characteristics, dominates the dynamics of the surface-hydration water. In other words, water diffusion on the membrane surface is largely decoupled from bulk-water diffusion.

In addition to proteins and lipids, the water polarization transfer technique has been applied to polysaccharides in plant cell walls by Hong and coworkers to understand the hydration of cellulose, pectins, and hemicellulose (**Fig. 5.2e**).[27] Water-pectin polarization transfer was found to be much faster than water-cellulose transfer, but chemical extraction of the cell wall exerted a

major impact on the spin diffusion rates. Removal of calcium ions and the consequent extraction of homogalacturonan dramatically slowed down water polarization transfer to all polysaccharides, while further extraction of matrix polysaccharides restored the ^{1}H spin diffusion rates. This unexpected trend indicates that calcium ions and homogalacturonan gelation in the intact cell wall increase the amount of bound water, thus speeding up polarization transfer, while calcium removal disrupts the gel and increases water dynamics, thus slowing down polarization transfer. The recovery of spin diffusion rates after more extensive extraction is attributed to increased water-exposed surface areas of the polysaccharides. The correlation between water-pectin and water-cellulose spin diffusion rates supports a single-network model of plant primary cell walls, as it indicates that a significant fraction of the cellulose microfibril surface is covered with pectins.[50]

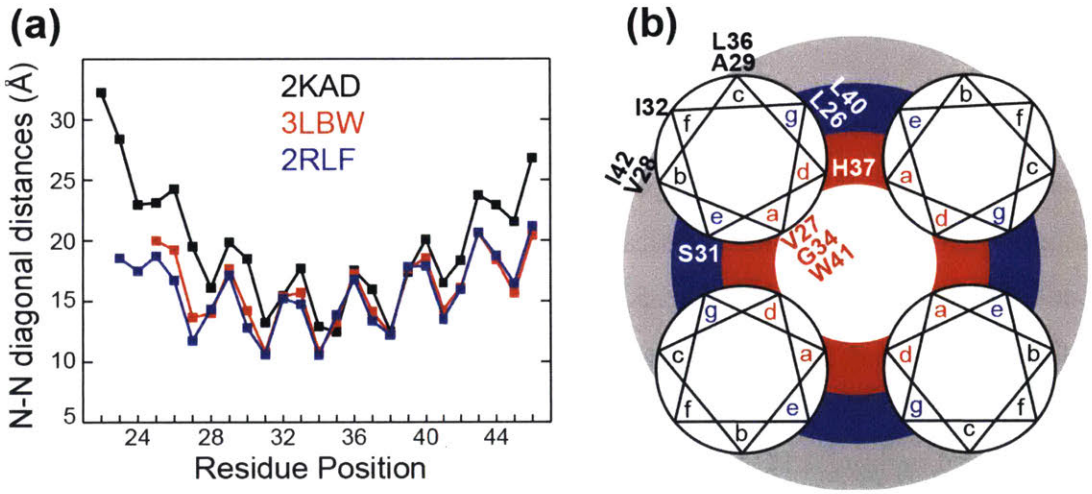

Figure 5.3 (a) Backbone N-N distances between two opposite helices in the tetrameric M2TM. The distances are extracted from three PDB structures of M2 with distinct helix tilt angles. The SSNMR structure 2KAD has a large tilt angle (~35°) that is expected for the low-pH state. The pH 6.5 crystal structure 3LBW has an intermediate tilt angle measured. The solution NMR structure 2RLF has the smallest tilt angle (~15°) and was measured at high pH. Periodic oscillation of the nitrogen distances to water, which is half the N-N distance plotted here, is seen for all structures. (b) Top view of the four-helix bundle formed by M2TM, showing the positions of the 12 labeled residues on the heptad repeat. Positions *a* and *d* (red) face the water-filled pore, *g* and *e* (blue) are interfacial, and *c*, *f*, and *b* (black) face lipids.

5.6 Water Interactions with the Influenza M2 Transmembrane Channel

We now present new results on the influenza M2 protein that illustrate one specific type of structural information that can be obtained from SSNMR measurements of water interactions with integral membrane proteins. The M2 protein of influenza viruses forms an acid-activated tetrameric proton channel in the virus envelope to conduct protons from the acidic endosome into the virion. Recent SSNMR data and other biophysical and mutagenesis results[51] showed that the transmembrane domain conducts protons by a shuttle mechanism,[52] in which a conserved histidine, H37, undergoes successive protonation and deprotonation events, accompanied by microsecond reorientations of the imidazole rings.[37,53,54] Water is important in this process because it delivers protons to H37 as well as removing protons from H37 to transfer into the virus, and water-H37 forms a mixed hydrogen-bonded chain. Thus, understanding water dynamics is integral to elucidating the structure and function of this prototypical proton channel.

In addition to its functional role, water may also provide a way to determine the structure of the four-helix bundle. The distances of successive residues from the center of the pore should exhibit a periodicity reflecting the ✔-helical pitch of 3.6 residues per turn. These distances should also depend on the helix tilt angle. **Fig. 5.3a** shows the residue-specific amide ^{15}N-^{15}N distances between the two opposing helices of the tetramer, which are twice the ^{15}N distances to the channel axis. The distances are extracted from three PDB structures of M2TM. The SSNMR structure (2KAD), measured in thin DLPC bilayers, has a 35° tilt angle and is believed to resemble the low-pH open-channel structure.[55] A 1.65 Å resolution crystal structure (3LBW), measured at pH 6.5, has an intermediate tilt angle.[56] A high-pH solution NMR structure (2RLF) has the smallest tilt angle of ~15°.[57] **Fig. 5.3a** shows that all three structures exhibit the same periodicity and "phase" in the ^{15}N-water distance oscillation as a function of residue position, while the vertical displacement and amplitude of the oscillation differ. Residues near the two termini have longer distances to the water-filled pore than residues near the crossing point of the four-helix bundle, thus the distance profile droops in the middle. This periodic water-distance pattern partly resembles the dipolar waves of oriented membrane proteins.[58] Periodic structural features are also commonly exploited in EPR spectroscopy: paramagnetic broadening by lipid- or water-soluble spin labels has long been used to measure the structure of α-helical membrane proteins.[59] We thus

ask the question whether water-protein polarization transfer rates can reveal the secondary structure and quaternary structure of ion channels. We measured the water-protein ^{1}H spin diffusion of 12 residues in the 25-residue M2TM at low and high pH, and show that indeed periodic water-protein transfer rates can be observed, even though it is mixed with other structural factors.

5.7 Experimental Methods

5.7.1 Membrane Samples

Four M2TM peptides were used in this study, each bound to cholesterol-containing virus-mimetic membranes at low and high pH, thus giving a total of eight samples that cover 12 residues of the transmembrane domain. The amino acid sequence corresponds to residues 22-46 of the Udorn strain of M2 (SSDPLVVAASIIGILHLILWILDRL). The labeled residues are: $L_{26}V_{27}A_{29}G_{34}$ (LVAG),[33] $G_{34}H_{37}I_{42}$ (GHI),[37] $V_{28}S_{31}I_{32}L_{36}$ (VSIL),[60] and $L_{40}W_{41}$ (LW).[61] LW-M2TM was bound to an unsaturated-lipid VM+ membrane consisting of POPC, POPE, sphingomyelin (SM) and cholesterol, while the other three peptides were bound to a saturated-chain virus-mimetic membrane (VM) consisting of DPPC, DPPE, SM and cholesterol.[62,63]

5.7.2 Solid-State NMR

SSNMR experiments were conducted on a Bruker DSX-400 MHz (9.4 T) and an AVANCE II 600 MHz (14.1 T) spectrometer using 4 mm MAS probes. Typical radiofrequency field strengths were 71-83 kHz for ^{1}H and 50 kHz for ^{13}C. ^{13}C chemical shifts were referenced to the CH_2 signal of adamantane at 38.48 ppm, while ^{1}H chemical shifts were referenced to the Hγ peak of phosphocholine headgroup at 3.26 ppm on the TMS scale.

2D ^{1}H-^{13}C spin-diffusion HETCOR experiments (**Fig. 5.1b**) were used to measure water-M2 cross peaks. The ^{1}H T_2 filter time was 1.9 ms or 1.2 ms. For most samples two mixing times, 4 ms and 100 ms, were used, and the samples were spun at either 7 kHz or 11 kHz. For the LVAG samples, additional spectra were measured with 1 ms and 2 ms mixing times under 10 kHz MAS to achieve more selective polarization transfer. All data were acquired at 293 K. The water ^{1}H T_1

relaxation time is about 500 ms in these samples. The water cross-peak intensity was extracted from the 2D spectra by summing over all cross sections of the water ^{1}H linewidth (~0.5 ppm). The intensity ratios between the 4 ms and 100 ms spectra, corrected for ^{1}H T_1 relaxation, are denoted as S/S_0 and compared for different residues. Error bars for S/S_0 were propagated from the signal-to-noise ratios of the peak intensities.

5.8 Results and Discussion

The 12 labeled residues measured in this work represent half of the M2TM, and populate pore-facing, lipid-facing, and interfacial positions of the heptad repeat (**Fig. 5.3b**). The pore-facing *a* and *d* positions include all functionally important residues of the channel such as V27, G34, H37 and W41. The interfacial *e* and *g* positions include the drug-interacting S31 as well as L26 and L40, whereas the lipid-facing *b*, *c*, *f* positions include bulky hydrophobic residues V28, A29, I32, L36 and I42. Our hypothesis is that the water – protein polarization transfer rates of these residues may be periodic to reflect the structure of the helix as well as the structure of the tetramer. **Fig. 5.4a,b** shows two representative 2D ^{1}H-^{13}C HETCOR spectra. With a 1.9 ms ^{1}H T_2 filter, signals of the most dynamic lipid moieties such as headgroup Hβ and chain CH_2 are not completely suppressed, thus 2D spectra are necessary to resolve only water-peptide cross peaks from the lipid-peptide cross peaks. At 100 ms, protein-lipid cross peaks at ^{1}H chemical shifts of ~1.3 ppm are observed, consistent with the membrane-spanning topology of this proton channel (**Fig. 5.4b**). Instead of measuring a full buildup curve, we chose two mixing times, 4 ms and 100 ms, and report their intensity ratio as an indicator of the initial buildup rates. **Fig. 5.4c-f** shows the water ^{1}H cross sections of three of the four peptides at 4 ms (red) and 100 ms (black) at both low and high pH. It can be seen that the 4 ms intensities are much higher at low pH than at high pH for all samples, and the low-pH GHI sample gives the highest initial intensities among all samples.

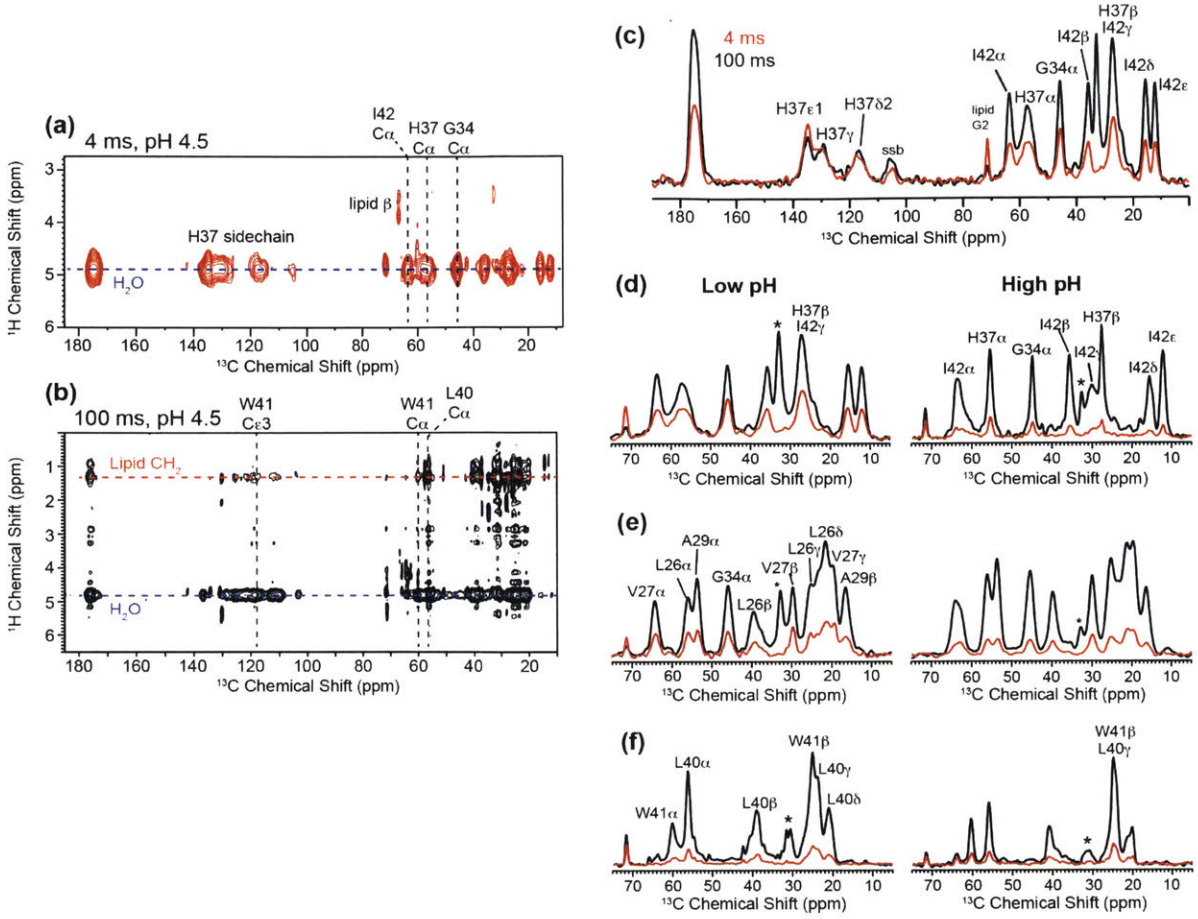

Figure 5.4 Representative water-M2TM ^{1}H spin diffusion spectra. (a) 2D spectrum of the pH 4.5 GHI sample with 4 ms mixing. (b) 2D spectrum of the pH 4.5 LW sample with 100 ms mixing. In addition to water-protein cross peaks, lipid-protein cross peaks are also observed at the ^{1}H chemical shift of 1.3 ppm, consistent with the transmembrane orientation of the channel. (c) Water ^{1}H cross sections of the low-pH GHI spectra with 4 ms (red) and 100 ms (black) mixing. (d-f) Low pH (left) and high pH (right) water ^{1}H cross sections at 4 ms and 100 ms mixing for (d) GHI, (e) LVAG, and (f) LW samples. Only the aliphatic region is shown for clarity.

Figure 5.5 plots the 4 ms versus 100 ms intensity ratios of all residues at Cα, Cβ, and Cγ. Two observations can be made. First, all residues show higher intensities at low pH than at high pH, consistent with the fact that the low-pH channel is open and better hydrated. This pH-induced S/S_0 difference is the largest for GHI, and the imidazole Cε1 has the highest S/S_0 value, about 1, among all sites (**Fig. 5.6a**). Second, the radial positions of the residues affect the initial spin diffusion rates and the pH dependence of the polarization transfer. Pore-facing residues such as V27, G34, and H37 have the largest S/S_0 values as well as the largest intensity difference between low pH (average $S/S_0 = 0.28$) and high pH (0.20). Interfacial residues at heptad repeat positions of

e and *g*, such as L26 and S31, have comparable S/S_0 values of 0.18 and 0.16 between low and high pH, whereas lipid-facing residues have S/S_0 values of 0.23 and 0.18 at low and high pH. These S/S_0 values have uncertainties of about ± 0.02; thus, the pore-facing residues' higher spin diffusion intensities compared to other radial positions are statistically significant. On the other hand, the pH-induced intensity difference for the lipid-facing residues is insignificant.

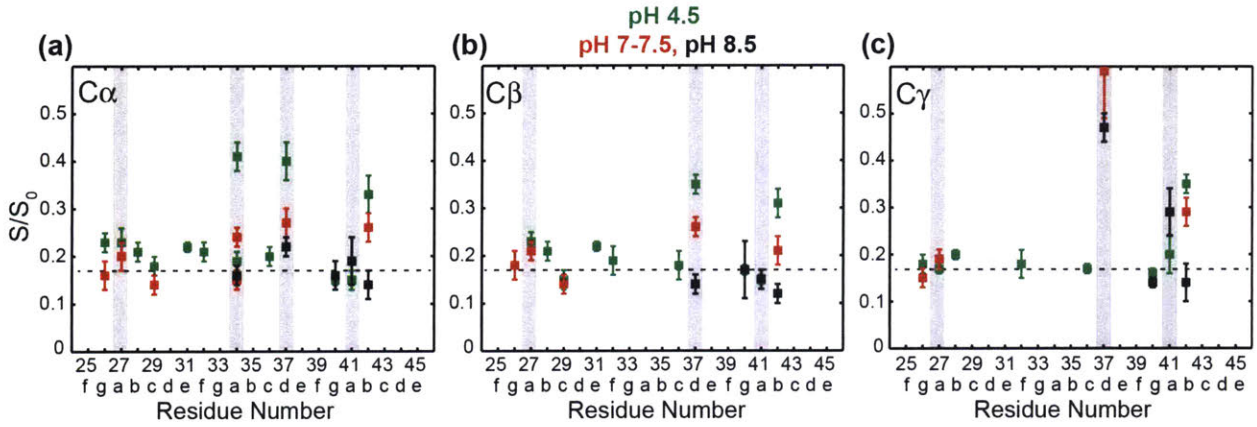

Figure 5.5 Spin diffusion intensity ratios (S/S_0) between 4 ms and 100 ms for all measured residues. (a) Cα, (b) Cβ, and (c) Cγ. Horizontal axis indicates the residue number as well as the heptad-repeat positions. Grey bars indicate residues that lie at the *a* and *d* positions. Data obtained at pH 4.5 (green), pH 7 or 7.5 (red) and pH 8.5 (black) are superimposed.

The high polarization transfer rates of the GHI sample can be partly attributed to H37, since this sidechain is known to be exposed to water and hydrogen-bond to it,[35,37] and imidazole nitrogens have one of the largest chemical exchange rates among labile protons.[19] The high G34 spin diffusion rate can also be partly attributed to the pore-facing position of this residue. However, the high S/S_0 values of the lipid-facing I42 is not expected, and suggests that sample preparation uncertainties such as lower actual pH than reported here may make these GHI-M2TM samples more efficient in receiving water magnetization. The G34 S/S_0 value in the GHI sample is higher than the G34 intensity in the LVAG sample by ~0.2 at low pH and 0.1 at high pH, suggesting that these are the approximate correction factors to account for sample preparation variations.

To investigate how the atomic position in the sidechain affects spin-diffusion intensities, we plotted the S/S_0 intensity ratios of different carbons within each residue (**Fig. 5.6**). Several trends emerge from this comparison. First, H37 and W41 are the only two residues where the

backbone Cα intensities are lower than many sidechain intensities. This is consistent with the pore-facing positions of these two residues in the heptad repeat, and confirms that both residues directly contact water to carry out the essential functions of proton conduction and gating. The pH-induced intensity differences in the Trp41 indole are smaller than the intensity differences of the His37 imidazole. This is consistent with the experimentally determined rotameric structures of these two residues, which indicate that the Trp41 sidechain is less exposed to the channel pore than the H37 sidechain. ^{19}F-^{19}F and ^{13}C-^{19}F distance measurements constrained the Trp41 rotamer to be *trans* for χ_1 and +90° for χ_2, which points the six-membered benzene ring towards the helix-helix interface while leaving the five-membered pyrrole ring in the pore.[61,64] In comparison, the His37 rotamer (*trans-trans*) points the imidazole ring straight into the pore.[37] Second, hydrophobic residues that face the lipids or the helix interface, such as I42, L26, A29 and L40, have either a flat or a decreasing intensity profile from the backbone to the sidechain tail, consistent with the fact that these sidechains point away from the water-filled pore. For the low-pH LVAG sample, both the interfacial L26 and the pore-facing V27 have higher S/S_0 values than the pore-facing G34 (**Fig. 5.6b**). This trend does not correlate with the radial positions of these two residues but reflects the fact that L26 and V27 lie close to the membrane surface and thus interact with inter-bilayer water.

These analyses indicate that in addition to the radial position of the residues, the chemical exchange rates of labile protons, the sidechain conformation, and the vertical displacement from the membrane surface, all affect the polarization-transfer rates from water. To assess the extent to which the ^{13}C-detected ^{1}H polarization transfer rates can reveal the radial position of the residues and hence the helical secondary structure, we carried out a constrained fit of the Cα and Cβ S/S_0 values (**Fig. 5.7**). We assume an ideal helical pitch of 3.6 residues per turn, and constrain the phase of the sinusoidal oscillation to be identical between Cα and Cβ and between low and high pH. The latter amounts to assuming that the rotation angle of the helix is unchanged by pH. The oscillation amplitude is allowed to vary since this parameter depends on the helix tilt angle and the intrinsic difference in the atomic positions of Cα and Cβ from the water-filled pore (**Fig. 5.7a**). Since the GHI samples show systematically higher S/S_0 values due to sample-preparation variations, we do not consider their intensities in this global fit. **Figure 5.7b** shows that a periodic pattern does exist, and reproduces the spin diffusion intensities of the N-terminal half of the helix relatively well. However, towards the C-terminal end, increasing discrepancy is seen between the experimental

data and the sinusoidal wave. This is particularly pronounced for W41: the simulated wave predicts a high S/S_0 value for W41, but the opposite was measured at low pH. In comparison, the high-pH data of W41 is better fit to the sine wave (**Fig. 5.7c**). Since the LW peptide was the only one incorporated into the unsaturated VM+ membrane while all other peptides were reconstituted into the saturated VM membrane, these intensity deviations may reflect sample preparation differences. On the other hand, we cannot exclude the possibility that the C-terminal deviation from the simulated wave may reflect deviations of the peptide from an ideal helical structure. For example, a kink could occur between the N- and C-terminal regions to change the phase of the sinusoidal oscillation. Such helix kinks have often been observed in ^{15}N-^{1}H dipolar waves and are diagnostic of the boundaries between two helices. The low-pH data could also be well fit by a significantly slower oscillation of 4 residues per turn (grey dashed lines in **Fig. 5.7b**). However, this periodicity departs significantly from an ideal α-helix structure, and predicts H37 intensities near the minimum of the wave, thus we exclude this alternative fit as unphysical.

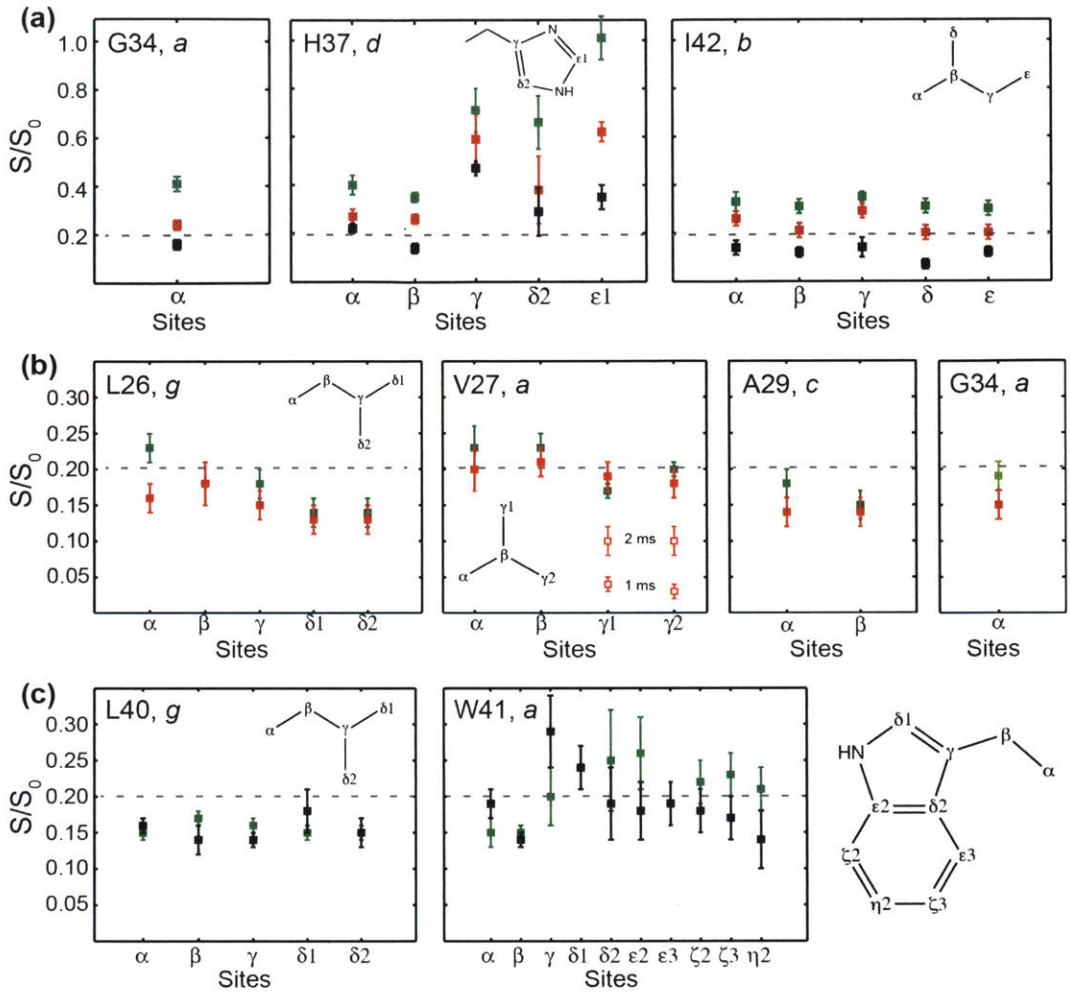

Figure 5.6 Backbone to sidechain trends in the water polarization-transfer intensity, S/S_0. (a) GHI sample. (b) LVAG sample. Open symbols in the V27 panel were data measured with shorter mixing times of 1 ms and 2 ms. (c) LW sample. Data measured at pH 4.5 are shown in green, at pH 7.0 and 7.5 in red, and at pH 8.5 in black. The residue's heptad positions are indicated.

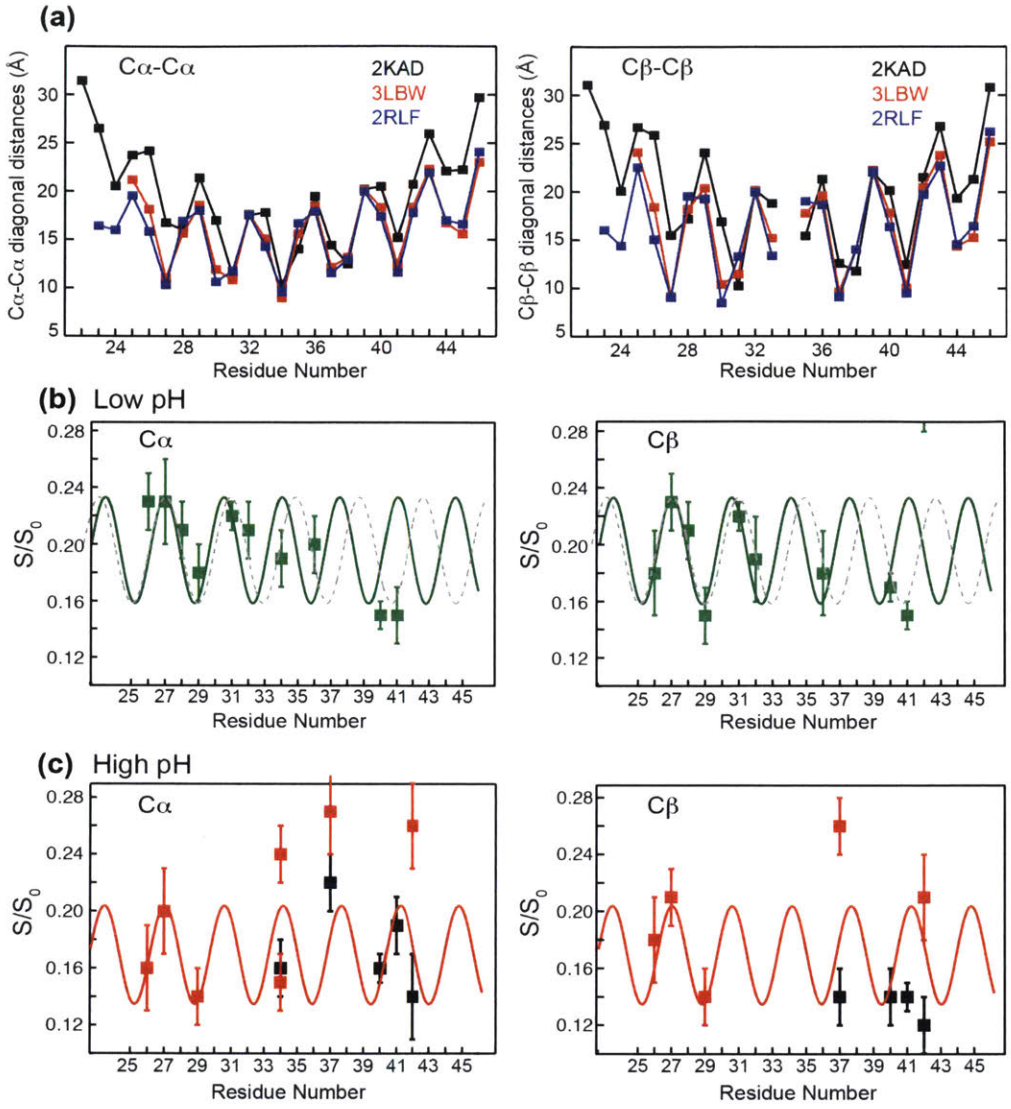

Figure 5.7 Residue-specific periodicity in the water polarization transfer to Cα and Cβ sites. (a) Extracted Cα-Cα and Cβ-Cβ diagonal distances in the M2TM tetramer, which correspond to twice the distances of these atoms to the center of the water-filled pore. Distances are extracted from three PDB structures with distinct helix tilt angles. (b) Low-pH S/S_0 values of Cα and Cβ. Solid lines are empirical fits constrained by the ideal helical structure of 3.6 residues per turn, while grey dashed lines give an alternative fit with 4 residues per turn. (c) High-pH S/S_0 values. Solid lines are empirical fits following the ideal helical structure. The GHI data are not considered in these fits.

5.9 Conclusions

The initial polarization transfer rates from water to M2TM show site-specificity that depends on pH, chemical exchange rates, sidechain conformation, as well as the secondary structure of the helix backbone. Even with this confluence of factors, oscillatory patterns in the water-protein polarization transfer can be seen and reveal the underlying helical structure of the peptide. Pore-facing residues are identified both by their high initial buildup rates and their increasing transfer rates from the backbone to the sidechain carbons. These features are distinguishable from the characteristics of lipid-facing and interfacial residues. For the same samples and residues, intensity differences between low and high pH are not susceptible to sample-preparation differences and reliably report the pH-induced changes in the protein structure.

These water ^{1}H polarization transfer experiments can be further optimized to increase the resolution of the structural information about membrane proteins. Using a single protein sample at each pH will yield more consistent residue-specific differences in the water contact. Conducting the experiments at moderate low temperatures where water remains liquid but chemical-exchange rates slow down will better emphasize distance-dependent spin diffusion as the polarization transfer mechanism. Use of shorter mixing times, as long as permitted by sensitivity, will also increase the contrast between pore-facing and lipid-facing residues. Experiments on the LVAG sample using 2 ms and 1 ms mixing times showed that the pore-facing V27 is the only residue with detectable intensities, whereas all other residues' signals are suppressed (**Fig. 5.6b**). Thus, short polarization transfer times can better discriminate between the water proximities of different residues. Finally, ^{15}N detection should provide independent and complementary information of the membrane protein structure.

5.10 Acknowledgements

This work is supported by National Institutes of Health grant GM088204 to M. H. The authors would like to thank Tuo Wang and Dr. Paul White for insightful discussions.

5.11 References

[1] B. Halle. "Protein Hydration Dynamics in Solution: A Critical Survey." *Phil. Trans. R. Soc. Lond. B* **2004**, 359, 1207-1224.

[2] E. Meyer. "Internal Water Molecules and H-Bonding in Biological Macromolecules: A Review of Structural Features with Functional Implications." *Protein Sci.* **1992**, 1, 1543-1562.

[3] R. P. Rand. "Probing the Role of Water in Protein Conformation and Function." *Phil. Trans. R. Soc. Lond. B* **2004**, 359, 1227-1285.

[4] J. M. J. Swanson, C. M. Maupin, H. Chen, M. K. Petersen, J. Xu, Y. Wu and G. A. Voth. "Proton Solvation and Transport in Aqueous and Biomolecular Systems: Insights from Computer Simulations." *J. Phys. Chem. B* **2007**, 111, 4300-4314.

[5] G. Otting, E. Liepinsh and K. Wüthrich. "Protein Hydration in Aqueous Solution." *Science* **1991**, 254, 974-980.

[6] J. A. Ernst, R. T. Clubb, H. X. Zhou, A. M. Gronenborn and G. M. Clore. "Demonstration of Positionally Disordered Water within a Protein Hydrophobic Cavity by NMR." *Science* **1995**, 267, 1813-1817.

[7] G. S. Harbison, J. E. Roberts, J. Herzfeld and R. G. Griffin. "Solid-State NMR Detection of Proton Exchange Between the Bacteriorhodopsin Schiff Base and Bulk Water." *J. Am. Chem. Soc.* **1988**, 110, 7221-7223.

[8] A. Lesage, L. Emsley, F. Penin and A. Böckmann. "Investigation of Dipolar-Mediated Water-Protein Interactions in Microcrystalline Crh by Solid-State NMR Spectroscopy." *J. Am. Chem. Soc.* **2006**, 128, 8246-8255.

[9] M. Goldman and L. Shen. "Spin-Spin Relaxation in LaF_3." *Phys. Rev.* **1966**, 144, 321-331.

[10] K. K. Kumashiro, K. Schmidt-Rohr, O. J. Murphy, K. L. Ouellette, W. A. Cramer and L. K. Thompson. "A Novel Tool for Probing Membrane Protein Structure: Solid-State NMR with Proton Spin Diffusion and X-Nucleus Detection." *J. Am. Chem. Soc.* **1998**, 120, 5043-5051.

[11] C. Ader, R. Schneider, K. Seidel, M. Etzkorn, S. Becker and M. Baldus. "Structural Rearrangements of Membrane Proteins Probed by Water-Edited Solid-State NMR Spectroscopy." *J. Am. Chem. Soc.* **2009**, 131, 170-176.

[12] T. Doherty and M. Hong. "2D ^{1}H–^{31}P Solid-State NMR Studies of the Dependence of Inter-Bilayer Water Dynamics on Lipid Headgroup Structure and Membrane Peptides." *J. Magn. Reson.* **2009**, 196, 39-47.

[13] D. Huster, X. Yao and M. Hong. "Membrane Protein Topology Probed by ^{1}H Spin Diffusion from Lipids Using Solid-State NMR Spectroscopy." *J. Am. Chem. Soc.* **2002**, 124, 874-883.

[14] X. L. Yao and M. Hong. "Dipolar Filtered ^{1}H-^{13}C Heteronuclear Correlation Spectroscopy for Resonance Assignment of Proteins." *J. Biomol. NMR* **2001**, 20, 263-274.

[15] X. L. Yao, K. Schmidt-Rohr and M. Hong. "Medium- and Long-Distance ^{1}H–^{13}C Heteronuclear Correlation NMR in Solids." *J. Magn. Reson.* **2001**, 149, 139-143.

[16] S. Li, Y. Su, W. Luo and M. Hong "Water-Protein Interactions of an Arginine-Rich Membrane Peptide in Lipid Bilayers Investigated by Solid-State Nuclear Magnetic Resonance Spectroscopy." *J. Phys. Chem. B* **2010**, 114, 4063-4069.

[17] W. Luo and M. Hong. "A 1D Sensitivity-Enhanced ^{1}H Spin Diffusion Experiment for Determining Membrane Protein Topology." *Solid State Nucl. Magn. Reson.* **2006**, 29, 163-169.

[18] K. Takegoshi and T. Terao. "^{13}C Nuclear Overhauser Polarization Nuclear Magnetic Resonance in Rotating Solids: Replacement of Cross Polarization in Uniformly ^{13}C Labeled Molecules with Methyl Groups." *J. Chem. Phys.* **2002**, 117, 1700-1707.

[19] E. Liepinsh and G. Otting. "Proton Exchange Rates from Amino Acid Side Chains-Implications for Image Contrast." *Magn. Reson. Med.* **1996**, 35, 30-42.

[20] Z. Luz and S. Meiboom. "Kinetics of Proton Exchange in Aqueous Solutions of Acetate Buffer." *J. Am. Chem. Soc.* **1963**, 85, 3923-3925.

[21] N. Bloembergen. "On the Interaction of Nuclear Spins in a Crystalline Lattice." *Physica* **1949**, 15, 386-426.

[22] K. Schmidt-Rohr and H.W. Spiess. "Multidimensional Solid-State NMR and Polymers." Academic Press, San Diego, **1994**.

[23] J. H. Noggle and R. E. Shirmer. "The Nuclear Overhauser Effect: Chemical Applications." Academic Press, New York, **1971**.

[24] I. Solomon. "Relaxation Processes in a System of Two Spins." *Phys. Rev.* **1955**, 99, 559-565.

[25] V. Chevelkov, K. Faelber, A. Diehl, U. Heinemann, H. Oschkinat and B. Reif. "Detection of Dynamic Water Molecules in a Microcrystalline Sample of the SH3 Domain of α-Spectrin by MAS Solid-State NMR." *J. Biomol. NMR* **2005**, 31, 295-310.

[26] A. Böckmann, C. Gardiennet, R. Verel, A. Hunkeler, A. Loquet, G. Pintacuda, L. Emsley, B.H. Meier and A. Lesage. "Characterization of Different Water Pools in Solid-State NMR Protein Samples." *J. Biomol. NMR* **2009**, 45, 319-327.

[27] P. B. White, T. Wang, Y. B. Park, D. J. Cosgrove and M. Hong. "Water–Polysaccharide Interactions in the Primary Cell Wall of Arabidopsis Thaliana from Polarization Transfer Solid-State NMR." *J. Am. Chem. Soc.* **2014**, 136, 10399-10409.

[28] H. Yao and M. Hong. "Conformation and Lipid Interaction of the Fusion Peptide of the Paramyxovirus PIV5 in Anionic and Negative-Curvature Membranes from Solid-State NMR." *J. Am. Chem. Soc.* **2014**, 136, 2611-2624.

[29] A. Lesage and A. Böckmann. "Water-Protein Interactions in Microcrystalline Crh Measured by ^{1}H-^{13}C Solid-State NMR Spectroscopy." *J. Am. Chem. Soc.* **2003**, 125, 13336-13337.

[30] A. Lesage, C. Gardiennet, A. Loquet, R. Verel, G. Pintacuda, L. Emsley, B. H. Meier and A. Böckmann. "Polarization Transfer Over the Water-Protein Interface in Solids." *Angew. Chem. Int. Ed. Engl.* **2008**, 47, 5851-5854.

[31] E. K. Paulson, C. R. Morcombe, V. Gaponenko, B. Dancheck, R. A. Byrd and K. W. Zilm. "High-Sensitivity Observation of Dipolar Exchange and NOEs Between Exchangeable Protons in Proteins by 3D Solid-State NMR Spectroscopy." *J. Am. Chem. Soc.* **2003**, 125, 14222-14223.

[32] A. B. Siemer, K.-Y. Huang and A. E. McDermott. "Protein–Ice Interaction of an Antifreeze Protein Observed with Solid-State NMR." *Proc. Natl. Acad. Sci. U.S.A.* **2010**, 107, 17580-17585.

[33] W. Luo and M. Hong. "Conformational Changes of an Ion Channel Detected Through Water-Protein Interactions Using Solid-State NMR Spectroscopy." *J. Am. Chem. Soc.* **2010**, 132, 2378-2384.

[34] M. Weingarth, E. A. W. van der Cruijsen, J. Ostmeyer, S. Lievestro, B. Roux and M. Baldus. "Quantitative Analysis of the Water Occupancy Around the Selectivity Filter of a K^+ Channel in Different Gating Modes." *J. Am. Chem. Soc.* **2014**, 136, 2000-2007.

[35] M. Hong, K. J. Fritzsching and J. K. Williams. "Hydrogen-Bonding Partner of the Proton-Conducting Histidine in the Influenza M2 Proton Channel Revealed from ^{1}H Chemical Shifts." *J. Am. Chem. Soc.* **2012**, 134, 14753-14755.

[36] M. Sharma, M. Yi, H. Dong, H. Qin, E. Peterson, D. Busath, H.X. Zhou and T.A. Cross. "Insight Into the Mechanism of the Influenza A Proton Channel from a Structure in a Lipid Bilayer." *Science* **2010**, 330, 509-512.

[37] F. Hu, W. Luo and M. Hong. "Mechanisms of Proton Conduction and Gating in Influenza M2 Proton Channels from Solid-State NMR." *Science* **2010**, 330, 505-508.

[38] M. Etzkorn, S. Martell, O. C. Andronesi, K. Seidel, M. Engelhard and M. Baldus. "Secondary Structure, Dynamics, and Topology of a Seven-Helix Receptor in Native Membranes, Studied by Solid-State NMR Spectroscopy." *Angew. Chem. Int. Ed. Engl.* **2007**, 46, 459-462.

[39] S. Y. Liao, K. J. Fritzsching and M. Hong. "Conformational Analysis of the Full-Length M2 Protein of the Influenza A Virus Using Solid-State NMR." *Protein Sci.* **2013**, 22, 1623-1638.

[40] Y. Chen, Z. Zhang, X. Tang, J. Li, C. Glaubitz and J. Yang. "Conformation and Topology of Diacylglycerol Kinase in E.coli Membranes Revealed by Solid-State NMR Spectroscopy." *Angew. Chem. Int. Ed.* **2014**, 53, 5624-5628.

[41] L. Shi, I. Kawamura, K. -H. Jung, L. S. Brown and V. Ladizhansky. "Conformation of a Seven-Helical Transmembrane Photosensor in the Lipid Environment." *Angew. Chem. Int. Ed.* **2011**, 50, 1302-1305.

[42] S. Wang, L. Shi, I. Kawamura, L. S. Brown and V. Ladizhansky. "Site-Specific Solid-State NMR Detection of Hydrogen-Deuterium Exchange Reveals Conformational Changes in a 7-Helical Transmembrane Protein." *Biophys. J.* **2011**, 101, L23-L25.

[43] S. Huo, S. Arumugam and T. A. Cross. "Hydrogen Exchange in the Lipid Bilayer-Bound Gramicidin Channel." *Solid State Nucl. Magn. Reson.* **1996**, 7, 177-183.

[44] M. Cotten, R. Fu and T. A. Cross. "Solid-State NMR and Hydrogen-Deuterium Exchange in a Bilayer-Solubilized Peptide: Structural and Mechanistic Implications." *Biophys. J.* **1999**, 76, 1179-1189.

[45] C. Tian, P. F. Gao, L. H. Pinto, R. A. Lamb and T. A. Cross. "Initial Structural and Dynamic Characterization of the M2 Protein Transmembrane and Amphipathic Helices in Lipid Bilayers." *Protein Sci.* **2003**, 12, 2597-2605.

[46] M. Holz, S. R. Heil and A. Sacco. "Temperature-Dependent Self-Diffusion Coefficients of Water and Six Selected Molecular Liquids for Calibration in Accurate ^{1}H NMR PFG Measurements." *Phys. Chem. Chem. Phys.* **2000**, 2, 4740-4742.

[47] J. M. Franck, J. A. Scott and S. Han. "Nonlinear Scaling of Surface Water Diffusion with Bulk Water Viscosity of Crowded Solutions." *J. Am. Chem. Soc.* **2013**, 135, 4175-4178.

[48] B. D. Armstrong and S. Han. "Overhauser Dynamic Nuclear Polarization to Study Local Water Dynamics." *J. Am. Chem. Soc.* **2009**, 131, 4641-4647.

[49] M. Dick-Pérez, Y. Zhang, J. Hayes, A. Salazar, O. A. Zabotina and M. Hong. "Structure and Interactions of Plant Cell-Wall Polysaccharides by Two- and Three-Dimensional Magic-Angle-Spinning Solid-State NMR." *Biochemistry* **2011**, 50, 989-1000.

[50] M. Hong and W. F. DeGrado. "Structural Basis for Proton Conduction and Inhibition by the Influenza M2 Protein." *Protein Sci.* **2012**, 21, 1620-1633.

[51] L. H. Pinto, G. R. Dieckmann, C. S. Gandhi, C. G. Papworth, J. Braman, M. A. Shaughnessy, J. D. Lear, R. A. Lamb and W. F. DeGrado. "A Functionally Defined Model for the M2 Proton Channel of Influenza A Virus Suggests a Mechanism for its Ion Selectivity." *Proc. Natl. Acad. Sci. U.S.A.* **1997**, 94, 11301-11306.

[52] F. Hu, K. Schmidt-Rohr and M. Hong. "NMR Detection of pH-Dependent Histidine-Water Proton Exchange Reveals the Conduction Mechanism of a Transmembrane Proton Channel." *J. Am. Chem. Soc.* **2012**, 134, 3703-3713.

[53] J. K. Williams, D. Tietze, J. Wang, Y. Wu, W. F. DeGrado and M. Hong. "Drug-Induced Conformational and Dynamical Changes of the S31N Mutant of the Influenza M2 Proton Channel Investigated by Solid-State NMR." *J. Am. Chem. Soc.* **2013**, 135, 9885-9897.

[54] S. D. Cady, T. V. Mishanina and M. Hong. "Structure of Amantadine-Bound M2 Transmembrane Peptide of Influenza A in Lipid Bilayers from Magic-Angle-Spinning Solid-State NMR: The Role of Ser31 in Amantadine Binding." *J. Mol. Biol.* **2009**, 385, 1127-1141.

[55] A. Acharya, V. Carnevale, G. Fiorin, B. G. Levine, A. Polishchuk, V. Balannick, I. Samish, R. A. Lamb, L. H. Pinto, W. F. DeGrado and M. L. Klein. "Structural Mechanism of Proton Transport Through the Influenza A M2 Protein." *Proc. Natl. Acad. Sci. U.S.A.* **2010**, 107, 15075-15080.

[56] J. R. Schnell and J. J. Chou. "Structure and Mechanism of the M2 Proton Channel of Influenza A Virus." *Nature* **2008**, 451, 591-595.

[57] J. Hu, T. Asbury, S. Achuthan, C. Li, R. Bertram, J. R. Quine, R. Fu and T. A. Cross. "Backbone Structure of the Amantadine-Blocked Trans-Membrane Domain M2 Proton Channel from Influenza A Virus." *Biophys. J.* **2007**, 92, 4335-4343.

[58] L. G. Cuello, D. M. Cortes and E. Perozo. "Molecular Architecture of the KvAP Voltage-Dependent K^+ Channel in a Lipid Bilayer." *Science* **2004**, 306, 491-495.

[59] Y. Su, F. Hu and M. Hong. "Paramagnetic Cu(II) for Probing Membrane Protein Structure and Function: Inhibition Mechanism of the Influenza M2 Proton Channel." *J. Am. Chem. Soc.* **2012**, 134, 8693-8702.

[60] J. K. Williams, Y. Zhang, K. Schmidt-Rohr and M. Hong. "pH-Dependent Conformation, Dynamics, and Aromatic Interaction of the Gating Tryptophan Residue of the Influenza M2 Proton Channel from Solid-State NMR." *Biophys. J.* **2013**, 104, 1698-1708.

[61] W. Luo, S. D. Cady and M. Hong. "Immobilization of the Influenza A M2 Transmembrane Peptide in Virus Envelope-Mimetic Lipid Membranes: A Solid-State NMR Investigation." *Biochemistry* **2009**, 48, 6361-6368.

[62] S. Cady, T. Wang and M. Hong. "Membrane-Dependent Effects of a Cytoplasmic Helix on the Structure and Drug Binding of the Influenza Virus M2 Protein." *J. Am. Chem. Soc.* **2011**, 133, 11572-11579.

[63] W. Luo, R. Mani and M. Hong. "Sidechain Conformation and Gating of the M2 Transmembrane Peptide Proton Channel of Influenza A Virus from Solid-State NMR." *J. Phys. Chem.* **2007**, 111, 10825-10832.

6. Relaxation-Compensated Difference Spin Diffusion NMR for Detecting ^{13}C-^{13}C Long-Range Correlations in Proteins and Polysaccharides

Tuo Wang[1*], Jonathan K. Williams[1*], Klaus Schmidt-Rohr[2], Mei Hong[1]
[*]*equal contribution*

[1]Department of Chemistry, Massachusetts Institute of Technology, Cambridge, MA
[2]Department of Chemistry, Brandeis University, Waltham, MA

Journal of Biomolecular NMR. **2015**, vol. 61, pp. 97-107.
DOI: 10.1007/s10858-014-9889-0

6.1 Abstract

The measurement of long-range distances remains a challenge in solid-state NMR structure determination of biological macromolecules. In 2D and 3D correlation spectra of uniformly ^{13}C-labeled biomolecules, inter-residue, inter-segmental, and intermolecular ^{13}C-^{13}C cross peaks that provide important long-range distance constraints for three-dimensional structures often overlap with short-range cross peaks that only reflect the covalent structure of the molecule. It is therefore desirable to develop new approaches to obtain spectra containing only long-range cross peaks. Here we show that a relaxation-compensated modification of the commonly used 2D ^{1}H-driven spin diffusion (PDSD) experiment allows the clean detection of such long-range cross peaks. By adding a z-filter to keep the total z-period of the experiment constant, we compensate for ^{13}C T_1 relaxation. As a result, the difference spectrum between a long- and a scaled short-mixing time spectrum show only long-range correlation signals. We show that one- and two-bond cross peaks equalize within a few tens of milliseconds. Within ~200 ms, the intensity equilibrates within an amino acid residue and a monosaccharide to a value that reflects the number of spins in the local network. With T_1 relaxation compensation, at longer mixing times, inter-residue and inter-segmental cross peaks increase in intensity whereas intra-segmental cross-peak intensities remain unchanged relative to each other and can all be subtracted out. Without relaxation compensation, the difference 2D spectra exhibit both negative and positive intensities due to heterogeneous T_1 relaxation in most biomolecules, which can cause peak cancellation. We demonstrate this relaxation-compensated difference PDSD approach on amino acids, monosaccharides, a

crystalline model peptide, a membrane-bound peptide and a plant cell wall sample. The resulting difference spectra yield clean multi-bond, inter-residue and intermolecular correlation peaks, which are often difficult to resolve in the parent PDSD spectra.

6.2 Introduction

One of the most important elements in biomolecular structure determination using solid-state NMR spectroscopy is the measurement of long-range distances, which define the three-dimensional fold of proteins, sidechain packing, relative orientations between two domains in a macromolecule, and intermolecular interfaces.[1,2] To date, the measurement of such long-range distances, operationally defined as distances longer than about 5 Å, has been mostly conducted using through-space ^{13}C correlation experiments, which give cross peaks whose intensities qualitatively reflect internuclear distances. The most commonly used correlation experiment is the ^{1}H-driven spin diffusion (PDSD) experiment, which can be conducted in 2D or 3D, with one or two mixing times.[3-5] In these spectra, both one-bond and two-bond correlations, which are useful for resonance assignment but not distance extraction, and long-range correlations with high structural content, are present. The former usually have much higher intensities than the latter, thus making it difficult to assign and extract the structurally informative long-range distances.[6]

This problem is partly alleviated by the PAR experiment developed by Griffin and coworkers,[7,8] which increases the intensities of long-range cross peaks relative to the short-range ones by attenuating the dipolar truncation mechanism through trilinear coherence terms between ^{13}C and ^{1}H spins. It is also reduced by selective isotopic labeling,[9-13] which reduces the number of directly bonded ^{13}C-^{13}C spin pairs in the protein. However, no experiment so far exists to completely remove the short-range cross peaks in the spectra of uniformly ^{13}C-labeled biomolecules.

In this work, we introduce a simple T_1-relaxation-compensated difference PDSD experiment that allows the clean detection of long-range cross peaks without overlap from short-range cross peaks for ^{13}C-labeled proteins, polysaccharides and other biomolecules. The term "short range" here includes two scenarios: one- and two-bond cross peaks on the one hand, and

intra-residue, mostly multi-bond, cross peaks on the other. The one- and two-bond cross peaks can be suppressed by subtracting a spectrum measured with mixing times on the order of ~30 ms from spectra measured with mixing times on the order of a few hundred milliseconds, while suppression of all intra-residue cross peaks requires, as we show below, subtraction of a spectrum measured with intermediate mixing times of ~100 ms from spectra measured with very long mixing times of ~1 s. Since the shortest ^{13}C T_1 relaxation times of methyl-containing biomolecules are on the order of a few hundred milliseconds, the difference spectra obtained from the second scenario are subject to significant and differential T_1 relaxation effects, giving positive difference peaks for the slow-relaxing species, which are desirable, and negative difference peaks for the fast-relaxing moieties, which are undesirable because they reflect mostly short-range correlations. We address this problem by adding a z-filter before the ^{13}C chemical shift evolution period to make the total z-period constant (**Fig. 6.1**). This relaxation compensation principle was first introduced in the CODEX technique;[14,15] the current implementation differs by not involving any recoupling of anisotropic spin interactions.

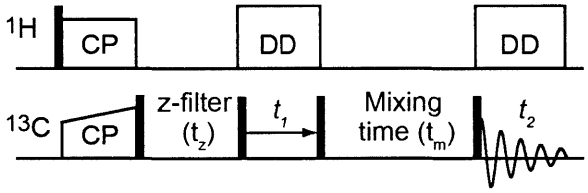

Figure 6.1 Pulse sequence for the relaxation-compensated PDSD experiment. The sum of the z-filter and mixing time is kept constant while the mixing times are varied.

In addition, we consider what pairs of mixing times will give only the desired long-range cross peaks in the difference spectrum. At very short mixing times of ~10 ms, two-bond cross peaks still rise in intensity while one-bond signals are already past their maximum. These factors cause both positive and negative cross peaks in the difference spectrum,[6] which can cause partial peak cancellations in a congested spectrum. By choosing both mixing times to be longer (≥ 30ms) than the one- and two-bond transfer rates, we ensure that the intensities of the one- and two-bond cross peaks remain unchanged relative to each other but their total intensities decrease together at the longer mixing time due to magnetization loss to longer-range correlations. Thus in a suitably scaled difference spectrum, all short-range cross peaks will be removed.

We demonstrate this relaxation-compensated difference PDSD method on several small-molecule model compounds, a membrane peptide and plant cell walls, and show that the difference spectra give uniformly positive long-range correlation signals that are multi-bond, inter-residue, or intermolecular. For comparison, difference spectra obtained without relaxation compensation exhibit mixed negative and positive cross peaks. To identify the best mixing times for difference spectroscopy, we measured the spin diffusion buildup curves of the model compounds, which are seen to equilibrate to a value that reflects the number of spins in the local network, thus providing useful structural information.

6.3 Materials and Methods

Four uniformly ^{13}C-labeled model compounds, histidine (His), glutamine (Gln), the tripeptide formyl-Met-Leu-Phe-OH (MLF), and D-glucose, were used to examine the spin diffusion buildup of the relaxation-compensated PDSD experiment. The pH 6.0 histidine sample contains both cationic histidine and the neutral τ tautomer.[16] The tripeptide MLF[17,18] has 20 ^{13}C labels and allows us to assess the performance of the difference PDSD experiment in a large spin network analogous to uniformly ^{13}C, ^{15}N-labeled proteins. A site-specifically labeled influenza M2 transmembrane peptide (M2TM) sample was used to investigate the determination of long-range distances in membrane proteins. The peptide contains ^{13}C, ^{15}N-labeled residues at G34, H37, and I42,[19] and is bound to a virus-mimetic lipid membrane[20] at pH 4.5, which corresponds to the open state of this proton channel. We also applied the relaxation-compensated PDSD experiment to uniformly ^{13}C-labeled *Arabidopsis thaliana* primary cell wall,[21,22] which contains a mixture of polysaccharides and glycoproteins. The plant was ^{13}C-labeled by growth in the dark in liquid culture containing ^{13}C-labeled glucose as the only carbon source. The seedlings were harvested, and soluble molecules, lipids, intracellular proteins, and starch were removed by treatments with chloroform/ethanol (1:1) solution, pH 5.2 sodium acetate buffer containing SDS and sodium metabisulfite, and α-amylase, respectively. The remaining alcohol-insoluble material is the cell wall.

6.3.1 Solid-State NMR Experiments

Histidine, glutamine, MLF, and M2TM spectra were measured on a Bruker 400 MHz spectrometer, while glucose and plant cell wall spectra were measured on a Bruker 600 MHz NMR spectrometer. Typical radiofrequency field strengths were ~70 kHz for ^{1}H decoupling and 50 kHz for ^{13}C pulses. All ^{13}C chemical shifts were externally referenced to the adamantane CH_2 peak at 38.48 ppm on the TMS scale.

The pulse sequence for the relaxation-compensated PDSD experiment (**Fig. 6.1**) contains a z-filter before the evolution period, and the sum of the z-filter (t_z) and mixing time (t_m) is kept constant to compensate for T_1 relaxation. Glutamine, histidine and MLF spectra were measured at room temperature using constant z-periods of 0.505 s, 1.005 s, and 1.505 s, respectively, and the MAS frequencies ranged from 7 to 10 kHz (**Table 6.S1**). The M2TM spectra were measured with a constant z-period of 1.505 s at 273 K under 9 kHz MAS. The glucose and plant cell wall samples were measured using a constant z-period of 1.005 s under 8 kHz MAS. The temperature was 273 K for glucose and 253 K for the plant cell wall.

The difference spectra were obtained by subtracting a short mixing-time spectrum from a long mixing-time spectrum, with an adjustable scaling factor for the former. For the histidine difference spectrum, no scaling was applied. For glucose, the difference spectrum between 1.0 s and 0.2 s involved scaling the latter by 0.95 to give null intensities, while the difference spectrum between 200 ms and 20 ms involved scaling the 20 ms spectrum by 0.78 to remove the one-bond cross peaks. For MLF, a difference spectrum between 300 ms and 30 ms used a scaling factor of 0.35 to remove one-bond cross peaks. For influenza M2TM, a scaling factor of 0.70 was applied to the 100 ms spectrum before subtraction from the 1.5 s spectrum. For the plant cell wall sample, the relaxation-compensated difference between 1.0 s and 0.2 s spectra used a scaling factor of 0.78 for the latter, while a regular PDSD difference spectrum used a scaling factor of 0.69 for the 0.2 s spectrum.

6.4 Results and Discussion

6.4.1 Small-Molecule Model Compounds

We first demonstrate the T_1-compensated PDSD experiment on model compounds containing a small number of ^{13}C spins. We monitor the spin diffusion buildup behavior of cross peaks to identify the magnetization equilibration times. To make the cross-peak intensity values meaningful, we divide the integrated area of a peak by the sum of all peak areas in the same ω_1 cross section:

$$y(\omega_a, \omega_b; t_m) = A(\omega_a, \omega_b; t_m) / \sum_{i=1}^{n} A(\omega_a, \omega_i; t_m) \qquad (6.1)$$

When spin diffusion in a local network of n spins is complete, the cross-peak intensity should equilibrate to $1/n$. This normalization procedure is advantageous over a previous method that involves double normalization by comparison with a short-mixing spectrum.[22,23] As shown for glutamine (**Fig. 6.S1**), Eq. (6.1) yields an equilibrium intensity of 0.20 for all carbons in this five-carbon molecule, while the double-normalization method gives rise to an arbitrary equilibrium value of 0.43.

Figure 6.2 shows the relaxation-compensated PDSD buildup curves of histidine. Using a total z-period of 1.005 s and mixing times from 5 ms to 1.0 s, we obtained an equilibrium intensity of ~17% for all Cα cross peaks, consistent with the presence of six carbons in this molecule. The exponential time constants for the initial buildup range from 2 ms for one-bond cross peaks to about 50 ms for the longest-range cross peak between the backbone Cα and imidazole Cε1. The time constants increase with the number of intervening bonds and the results are similar between cationic and neutral histidine, as expected. Importantly, once equilibrated, the ^{13}C magnetization does not decay further with mixing time, confirming that T_1 relaxation effects have been compensated for. The one-bond Cα-CO cross peak has a slower initial buildup time constant (4.8 ms) than the one-bond Cα-Cβ peak (2 ms), but the two peaks have the same decay constants (**Fig. 6.S2**). As a result, the Cα-CO intensity overshoots while the Cα-Cβ intensity does not. We

attribute the slower buildup of the Cα-CO cross peak to the lack of a proton on CO, which slows down ^{1}H-driven ^{13}C spin diffusion compared to the protonated Cβ.

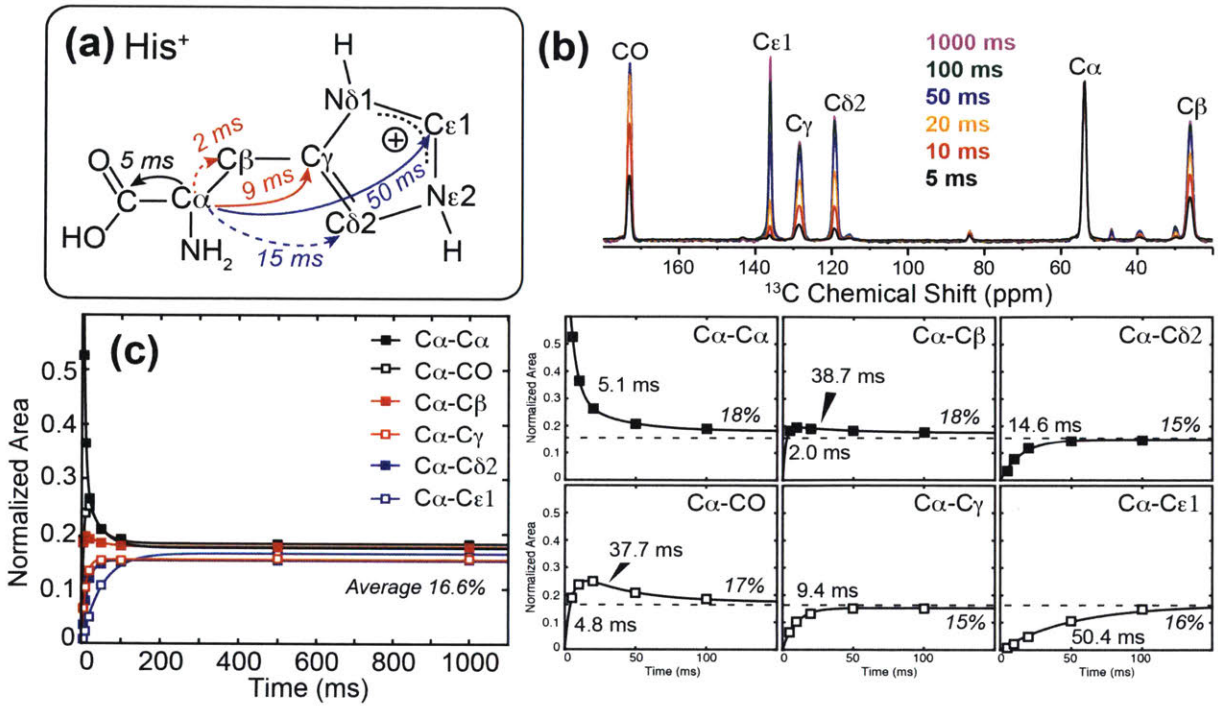

Figure 6.2 Relaxation-compensated PDSD buildup of histidine, measured with a total z-period of 1.005 s. Only the cationic histidine data is shown, but neutral histidine shows the same behavior. (a) Buildup time constants from Cα to other carbons. (b) ω_2 cross sections of cationic histidine Cα at 54 ppm, scaled to the Cα peak intensity. (c) Spin diffusion buildup curves. The peaks equilibrate to a value of 1/6, consistent with the presence of six carbons in the molecule. The buildup time constants increase with the number of bonds separating the two carbons.

Based on these buildup curves, we obtained a histidine difference 2D spectrum by subtracting the 100 ms spectrum from the 1.0 s spectrum. Since intermolecular contacts between cationic and neutral histidines are much longer than the molecular length scale, no cross peaks are expected between the different molecules and all intramolecular cross peaks should be null in the difference spectrum. This is confirmed in **Fig. 6.3**, which shows suppression of most peaks except for weak residual intensities for the Cε1-Cα and Cε1-CO peaks, which have not fully equilibrated by 100 ms due to the long distances between these carbons. No scaling factor was applied to the 100 ms spectrum, verifying that relaxation compensation and the choice of two mixing times longer than the magnetization equilibration time permit clean difference spectroscopy.

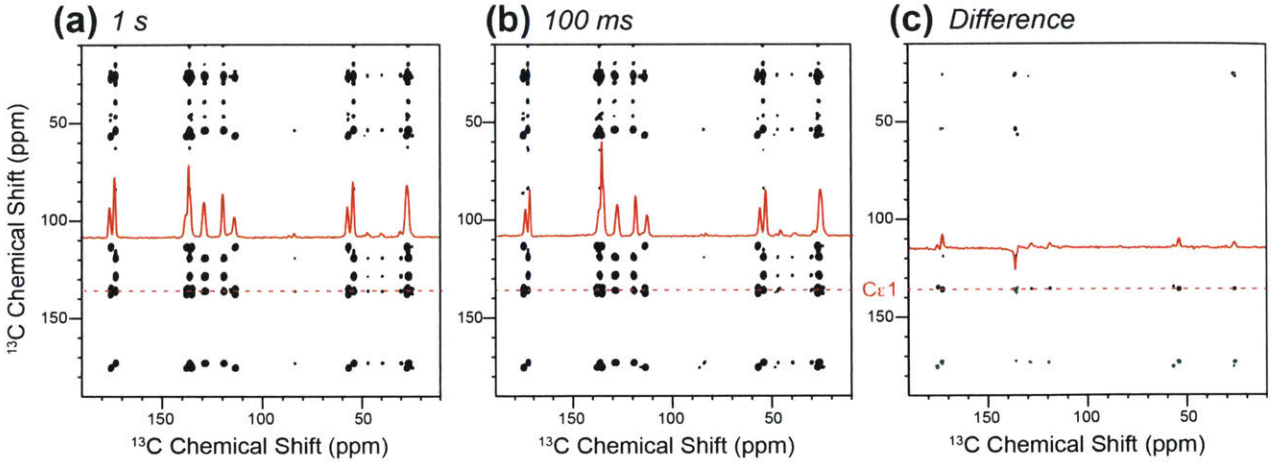

Figure 6.3 Relaxation-compensated 2D PDSD spectra of histidine, measured with a total z-period of 1.005 s. (a) 1 s mixing. (b) 100 ms mixing. (c) Difference spectrum, obtained without scaling the 100 ms spectrum. Negative intensities are plotted in *green*. Most intra-residue cross peaks are suppressed, except for weak Cε1-Cα and Cε1-CO peaks in the 136-ppm cross section due to the long-range nature of these cross peaks.

Because of its central role in carbohydrate chemistry, glucose is examined as a model compound for the relaxation-compensated PDSD experiment. In the 6-carbon pyranose ring, the magnetization is expected to equilibrate to 1/6. Indeed, all resolved ^{13}C signals reach an equilibrium intensity of 17% (**Fig. 6.4**), while the overlapped C3/C4 peak gave twofold higher equilibrium intensity (32%). The buildup constants range from 2.4 ms for one-bond correlations to ~30 ms for the C1-C6 correlation. Based on these buildup curves, we obtained a difference spectrum between 1.0 s and 200 ms, using a scaling factor of 0.95 for the latter. The difference spectrum is clean, showing no cross peaks (**Fig. 6.5a**), indicating that all intramolecular contacts have equilibrated by 200 ms and T_1 relaxation effects are corrected for. To remove one-bond cross peaks and detect only multi-bond cross peaks, we obtained a difference spectrum between the 200 ms and 20 ms spectra using a scaling factor of 0.78 for the latter (**Fig. 6.5b,c**). After 20 ms, the C1-C2 cross peak intensity still decays due to magnetization transfer to other carbons (**Fig. 6.4c**). Thus, the 20 ms C1-C2 intensity is higher than the equilibrium intensity, which accounts for the scaling factor.

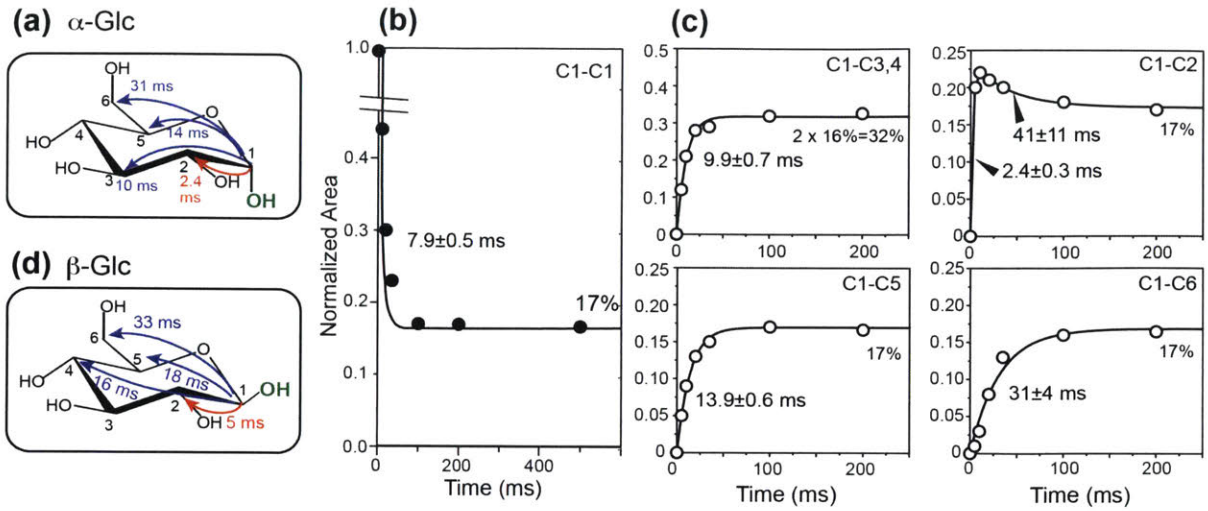

Figure 6.4 Relaxation-compensated PDSD data and buildup curves of D-glucose, measured with a total z-period of 1.005 s. (a) Buildup time constants of α-D-glucose. (b) The C1-C1 diagonal peak equilibrates to 17%. (c) Buildup curves of C1-Cx cross peaks, with equilibrium intensities of 17% for the resolved peaks and 32% for the doubly overlapped C1-C3,4 peak. (d) Buildup time constants of β-D-glucose.

6.4.2 Uniformly ^{13}C-labeled Polysaccharides and Site-Specifically Labeled Membrane Peptides

Since ^{13}C magnetization within a monosaccharide equilibrates by 200 ms (**Fig. 6.4**), longer-range correlations will manifest specifically at times longer than 200 ms. **Fig. 6.S3a,b** show the 2D PDSD spectra of *Arabidopsis* primary cell walls, measured with a total z-period of 1.005 s. The difference spectrum between 1.0 and 0.2 s, with a scaling factor of 0.78 for the latter, shows the suppression of most protein cross peaks, and only long-range correlation peaks remain in the difference spectrum (**Fig. 6.6a**). For example, the (89, 84 ppm) cross peak results from the spatial contacts between interior cellulose C4 (iC4) and surface cellulose (sC4) or xyloglucan backbone C4 (GC4). The scaling factor results from the fact that the iC4-iC6 cross peak decays between 200 ms and 500 ms due to magnetization loss to other carbons.

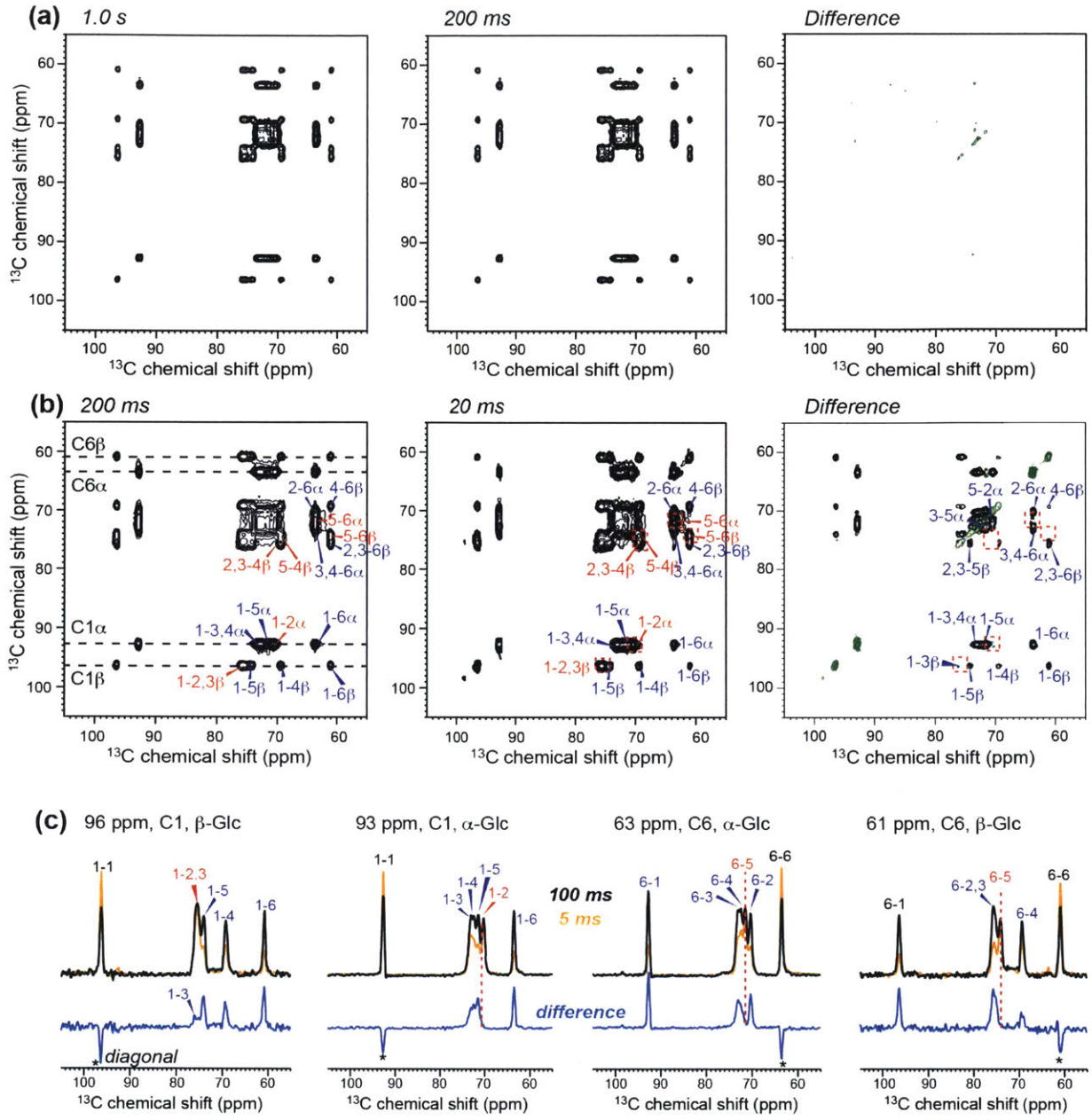

Figure 6.5 Relaxation-compensated 2D PDSD spectra of D-glucose. (a) 1.0 s spectrum, 200 ms spectrum, and difference spectrum, obtained with a scaling factor of 0.95 for the 200 ms spectrum. No cross peaks are observed in the difference spectrum, corresponding to magnetization equilibration by 200 ms. (b) 200 ms spectrum, 20 ms spectrum, and difference spectrum, obtained with a scaling factor of 0.78 for the 20 ms spectrum. All one-bond cross peaks are removed while multi-bond cross peaks remain. (c) Representative cross sections of the 200 ms, 20 ms and difference spectra. One-bond cross peaks (*red dashed lines*) have null difference intensities. The overlapped 1-2/3β peak shows residual difference intensity due to the two-bond 1-3β correlation.

T_1 relaxation compensation ensures that the difference PDSD spectrum shows only positive cross peaks. The only negative intensities appear along the diagonal, because magnetization continues to diffuse to other carbons with increasing mixing time. Having uniformly positive cross peaks is important, since in a crowded spectrum, the presence of both positive and negative intensities will cause partial peak cancellation. Without relaxation compensation, spectral subtraction fails, because functional groups with different T_1 relaxation times will exhibit different extents of intensity decay at long mixing times. **Figure 6.6b** shows the difference spectrum obtained from regular PDSD experiments. Strong negative intensities for protein and matrix polysaccharide peaks are observed due to much shorter ^{13}C T_1 relaxation times of these molecules compared to cellulose. This heterogeneous T_1 relaxation means that no single scaling factor allows the satisfactory removal of all short-range cross peaks. For the difference spectrum in **Fig. 6.6b**, we used a scaling factor that removed the cellulose intramolecular cross peaks (**Fig. 6.S3d-f**), which gave negative intensities for the fast-relaxing pectin and protein signals. Smaller scaling factors that remove the protein cross peaks will retain cellulose cross peaks in the difference spectrum. Therefore, relaxation compensation is important for detecting long-range correlations in dynamically heterogeneous samples.

The relaxation-compensated difference PDSD spectrum of the plant cell wall reveals intermolecular correlations between cellulose and pectic sugars such as galacturonic acid (GA) and rhamnose (R) (**Fig. 6.6c**), consistent with previously published 2D and 3D ^{13}C-^{13}C correlation spectra.[21,22] These cross peaks indicate that pectins contact cellulose microfibrils within ~1 nm, the distance scale probed by ^{13}C spin diffusion. The exact distances between cellulose and matrix polysaccharides are likely distributed, and this distribution is not known without high-resolution structures of the cell wall; however, we can obtain semi-quantitative information of the distances by examining the crystal structure of the I_β crystalline allomorph of cellulose,[24,25] which is the dominant form of cellulose in plant cell walls. Minimal distance separations of ~5 Å are present between surface and interior glucan chains (**Fig. 6.S4a**),[23] and the full distance distribution has significant intensities below 8 Å. Since the cellulose-matrix polysaccharide cross peaks have weaker intensities than the surface-interior cellulose cross peaks (**Fig. 6.6c**), the minimum distance separation between the cellulose surface and pectins is expected to be ~5 Å.

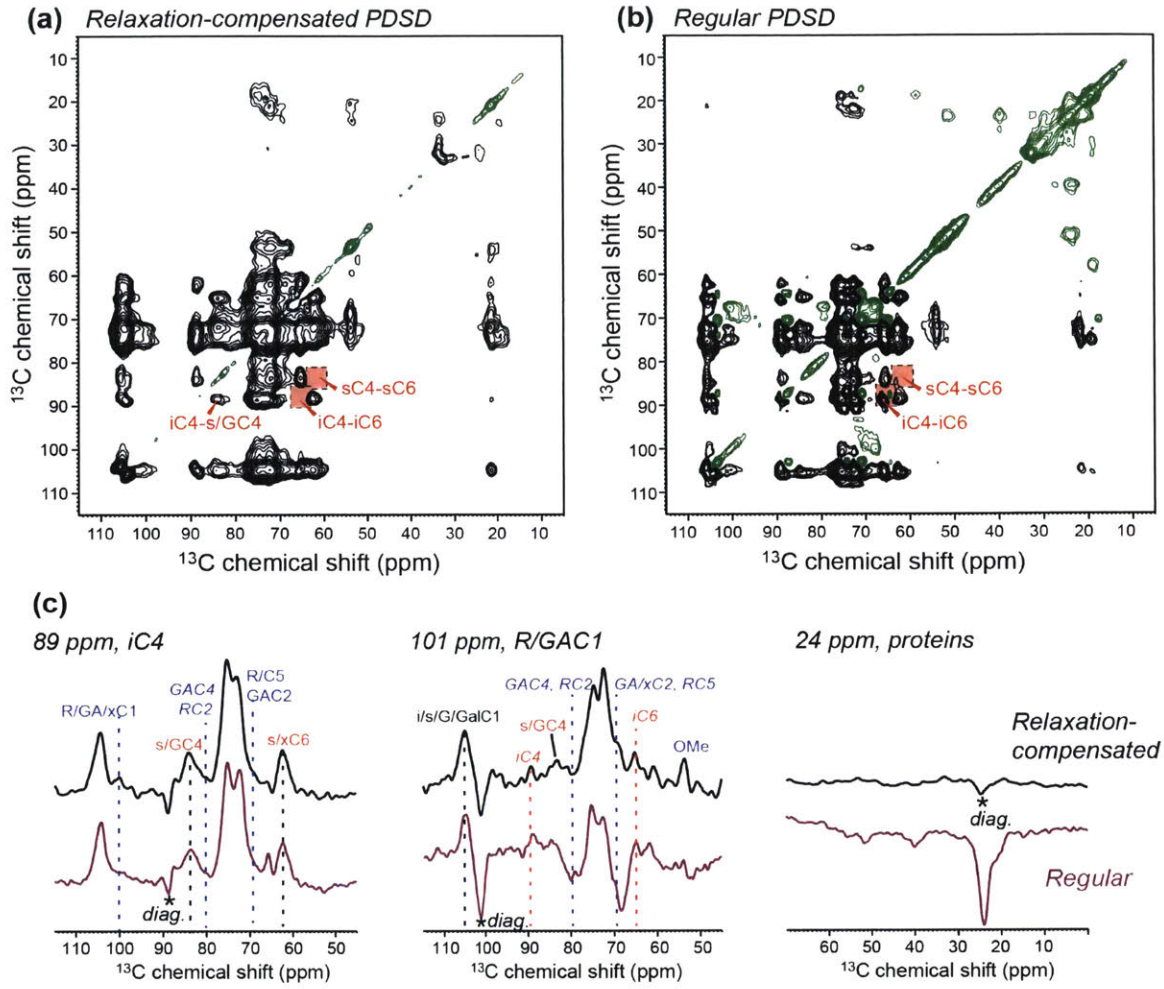

Figure 6.6 Difference 2D PDSD spectra of the *Arabidopsis* primary cell wall, obtained by subtracting the 200 ms spectrum from the 1.0 s spectrum. (a) Relaxation-compensated difference spectrum, obtained using a scaling factor of 0.78 for the 200 ms spectrum. (b) Regular PDSD difference spectrum, obtained using a scaling factor of 0.69 for the 200 ms spectrum. The relaxation-compensated difference spectrum shows only intermolecular correlations, while the regular PDSD difference spectrum has negative intramolecular protein and pectin intensities due to their fast T_1 relaxation rates. Both difference spectra are plotted using contour parameters of lev0 = 4, toplev = 100 and nlev = 16 in the Topspin software. (c) Representative 1D cross sections of cellulose, matrix polysaccharides and proteins. The relaxation-compensated difference spectra (*top row*) show positive intermolecular cross peaks between cellulose and pectins, which are difficult to resolve in the parent spectra. The regular PDSD difference spectra (*bottom row*) show a mixture of negative and positive cross peaks due to heterogeneous T_1 relaxation. Assignments are indicated in *red* for cellulose, *blue* for matrix polysaccharides, and *black* for overlapped peaks.

In non-mixture samples, significant T_1 relaxation differences can also exist, especially when ^{13}C labeling is not uniform and hence spin diffusion does not equilibrate the relaxation rates. For example, T_1 relaxation is expected to be much faster for methyl-rich protein residues such as Ile and Leu than for aromatic residues. To examine the effectiveness of relaxation-compensated difference PDSD method for site-specifically labeled samples, we measured the PDSD spectra of GHI-M2TM. A difference spectrum was obtained between 1.5 s and 100 ms mixing-time spectra, using a scaling factor of 0.70 for the latter. **Fig. 6.7** shows that all intra-residue cross peaks, including both the fast-relaxing methyl-rich I42 and the slow-relaxing aromatic moiety of H37 and the G34 backbone, are removed in the difference spectrum, while clear inter-residue cross peaks between G34 and H37 are retained. The resolution enhancement due to the difference spectroscopy is exemplified by the H37 Cα-G34 CO cross peak, which overlaps with the H37 Cα-CO cross peak in the parent spectra. High-resolution structures of the tetrameric M2TM helical bundle at both low and high pH[26,27] indicate that the shortest G34-H37 distances are intrahelical and are between 4 and 5 Å (**Fig. 6.S4b**), while interhelical G34-H37 distances are longer than 7 Å at low pH and longer than 5 Å at high pH. Thus, the observed G34-H37 cross peaks should mainly result from intrahelical contacts.

6.4.3 Uniformly ^{13}C-labeled Peptides and Proteins

To assess how well the relaxation-compensated difference PDSD method works for uniformly ^{13}C labeled peptides and proteins, we measured the spectra of MLF, which contains 20 ^{13}C spins. **Figure 6.8** shows that by ~500 ms, the ^{13}C magnetization has equilibrated between Met and Phe, which have the longest-distance contacts in the peptide. Intra-residue spin diffusion has time constants of 3 - 89 ms, comparable to those in histidine. The time constants are distinct between one-bond and multi-bond correlations. Thus, for removing one-bond cross peaks, a difference spectrum can be readily obtained by subtracting, for example, the 30 ms spectrum from a longer-mixing-time spectrum. **Figure 6.9c** shows this difference spectrum, using a scaling factor of 0.35 for the 30 ms spectrum. A few diagonal peaks remain with weak negative intensities, but all cross peaks show positive intensities and are mostly inter-residue. For example, the difference spectrum reveals long-range cross peaks from Fβ to Mα, Mβ, and Mγ (in rows and columns at 37 ppm), which are not apparent in the regular PDSD spectra due to significant overlap between the

Fβ and Mβ signals. This highlights the usefulness of our T_1-compensated difference PDSD approach.

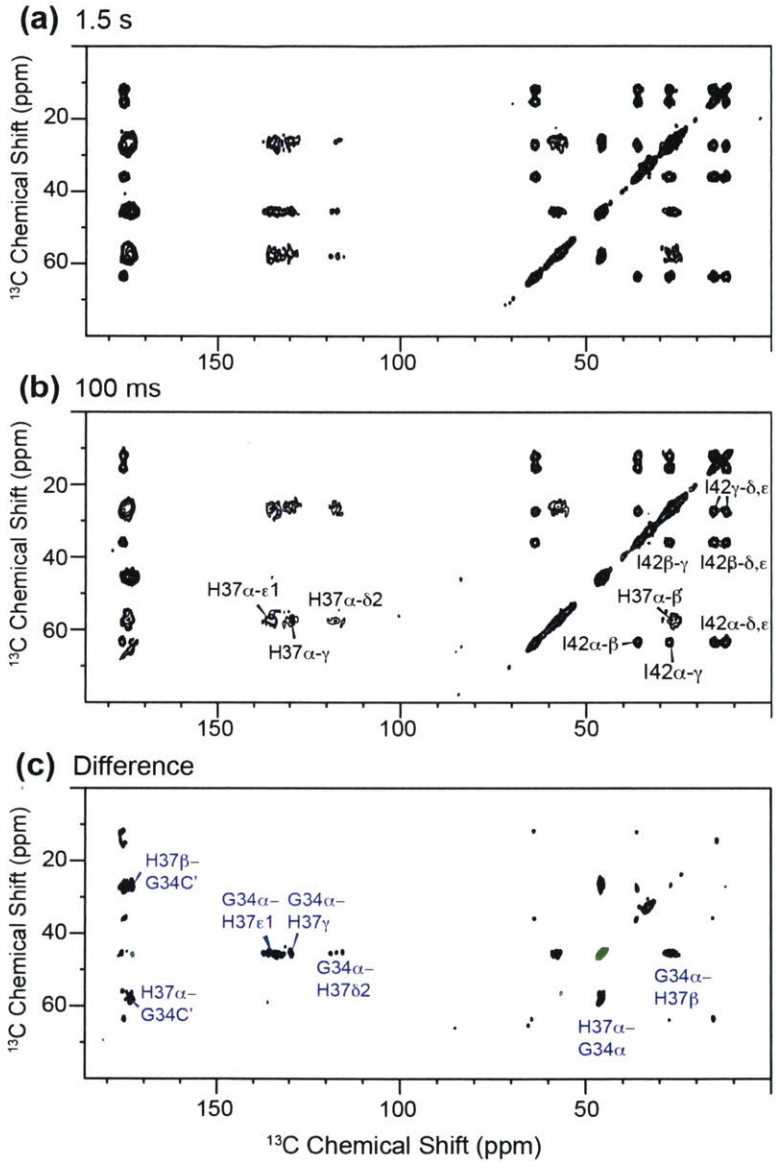

Figure 6.7 Relaxation-compensated 2D PDSD spectra of membrane-bound GHI-M2TM, using a total z period of 1.505 s. (a) 1.5 s mixing. (b) 100 ms mixing. The main intra-residue cross peaks are assigned. (c) Difference spectrum, obtained with a scaling factor of 0.70 for the 100 ms spectrum. Multiple long-range G34-H37 cross peaks are observed while intra-residue cross peaks are removed in the difference spectrum.

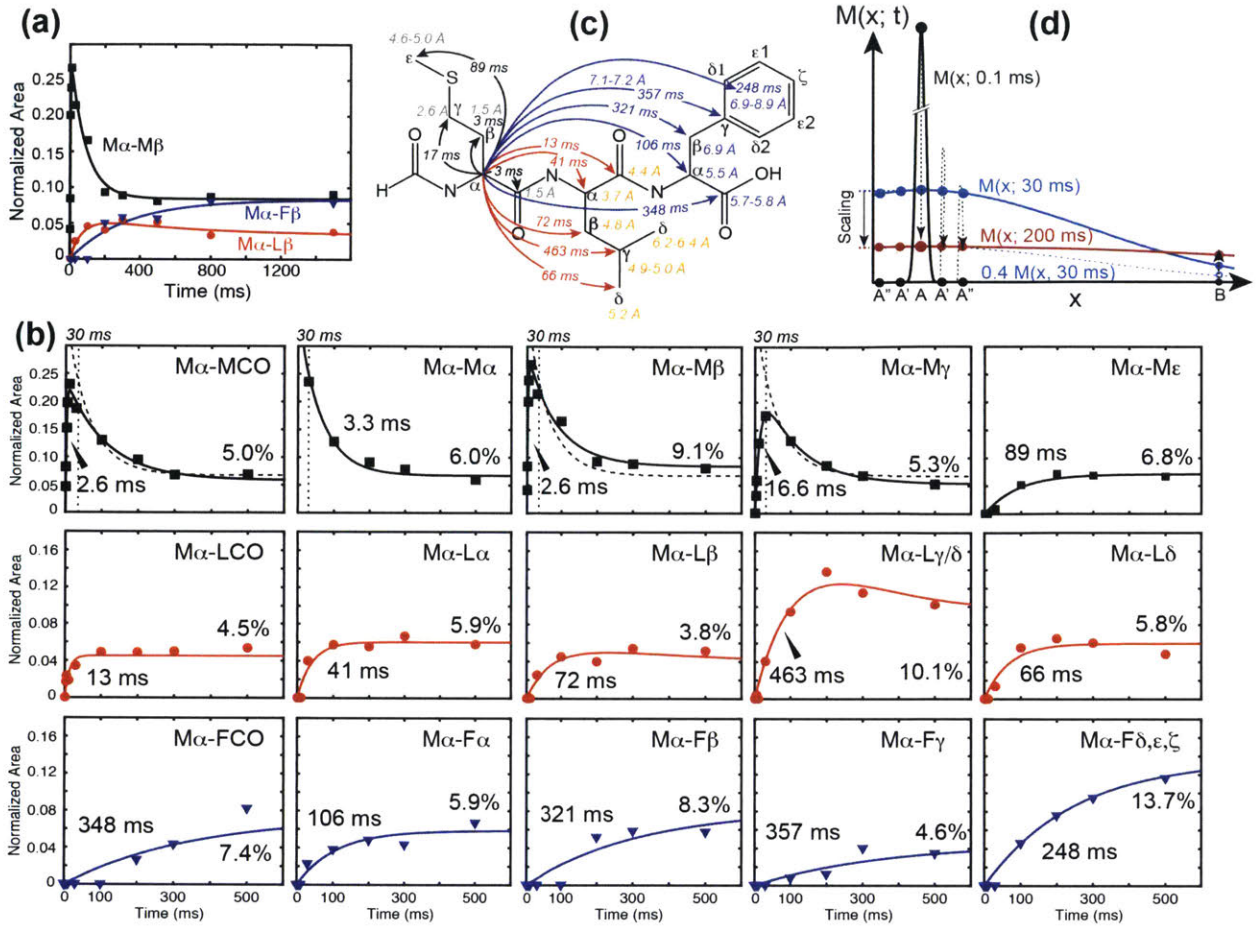

Figure 6.8 Relaxation-compensated PDSD buildup curves of MLF, obtained with a total z-period of 1.505 s. Only the Met Cα buildup curves are shown for clarity. (a) Overlay of the buildup curves of Mα-Mβ, Mα-Lβ, and Mα-Fβ for mixing times up to 1.5 s. (b) Initial trajectories up to 500 ms of individual buildup curves. *Dashed lines* in several panels in the *top row* reproduce the diagonal peak's decay curve to show that one- and two-bond decays track the diagonal peak decay. (c) Buildup time constants from Met Cα to other carbons and the corresponding internuclear distances. (d) A schematic of the magnetization transfer time course for a linear chain of spins illustrates how the cross-peak decays resemble the diagonal-peak decay increasingly closely for spins closer to the source. After a certain mixing time, the intensities of all spins within a certain distance decay similarly together and can be removed in a difference spectrum. The scaling factor in the subtraction results from the common decay of the diagonal, one- and two-bond peaks by that mixing time.

The buildup curves in **Fig. 6.8** indicate that, to detect long-range cross peaks between a segment of three residues and another domain in a protein, the mixing times needed to remove all cross peaks within the tripeptide unit is ~500 ms. For this 20-carbon peptide, each ^{13}C ideally

should reach an equilibrium intensity of 5%. The measured equilibrium intensities are quantitatively consistent with this prediction for all resolved signals. Where n peaks overlap, the final value is n times 5%. For example, the doubly overlapped Mα-Lγ/δ cross peak equilibrates to ~10% (**Fig. 6.8b**). The 5-carbon overlapped Mα-Fδ, ε, ζ cross peak equilibrates to 13.7%, which is lower than the theoretical value of 25%. We attribute this observation to the complex motion of the phenyl ring[18] and the large chemical shift anisotropies of aromatic carbons, which may slow down ^{13}C spin diffusion.

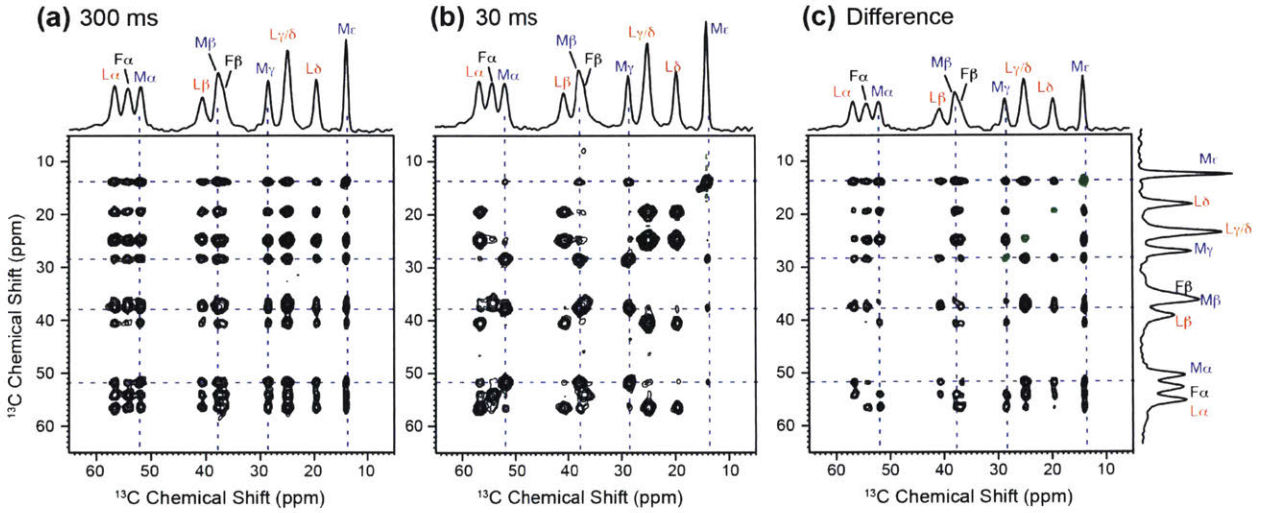

Figure 6.9 Relaxation-compensated 2D PDSD spectra of MLF measured with a total z-period of 1.505 s. (a) 300 ms mixing. (b) 30 ms mixing. (c) Difference spectrum, obtained with a scaling factor of 0.35 for the 30 ms spectrum. The cross peaks in the difference spectrum are predominantly inter-residual. *Blue dashed lines* give the positions of the Met intra-residue cross peaks, and intensities at most of these intersections have been suppressed in the difference spectrum, confirming clean subtraction due to relaxation compensation and appropriate choice of the mixing times and the scaling factor. Projections of the 2D spectra are shown at the *top* and on the *right* to facilitate cross-peak identification. All spectra are plotted using contour parameters of lev0 = 4, toplev = 100 and nlev = 16 in the Topspin software.

6.4.4 Choice of Mixing Times for Difference Spectroscopy of Relaxation-Compensated PDSD Experiments

The above examples show that the relaxation-compensated PDSD experiment works well for site-specifically labeled biomolecules and uniformly labeled biomolecular mixtures, where the

timescale of intra-segmental spin diffusion of ~ 100 ms is well separated from the inter-segmental or intermolecular spin diffusion timescale of ~ 1 s. This separation of timescale allows unambiguous detection of inter-residue and intermolecular correlations. In uniformly ^{13}C-labeled non-mixture samples, complete magnetization equilibrium in the whole protein is irrelevant, instead one- and two-bond cross peaks should be removed to detect multi-bond and inter-residue cross peaks. Since ^{13}C spin diffusion is more rapid in uniformly labeled molecules than in site-specifically labeled samples, the most suitable mixing times for difference spectroscopy should be a few tens of milliseconds and a few hundreds of milliseconds.

The difference spectra in **Figs. 6.3c**, **6.5b**, **6.6a**, **6.7c**, and **6.9c** show that removal of one-bond cross peaks always results in small, slightly negative residual diagonal peaks. This observation can be understood by a simple analysis of the spin-diffusion dynamics and is useful for determining the scaling factor without requiring a priori knowledge of which cross peaks are from one-bond couplings: if the diagonal in the difference spectrum is slightly negative (about -2% of the full diagonal intensity), then the residual one-bond cross peaks will be very small.

We consider spin A, corresponding to a diagonal peak, spin A', a one-bond neighbor of A, and spin A", a two-bond neighbor of A. These are strongly coupled, with transfer times of <10 ms (**Figs. 6.2, 6.4, 6.8**), and therefore have nearly the same magnetization level at mixing times ≥30 ms. This is confirmed experimentally by the close match between the cross-peak (solid lines) and diagonal-peak (dashed line) intensities of the Met Cα row (**Fig. 6.8b**) at mixing times ≥30 ms. During the longer mixing time of the second experiment, the magnetization from A, A', and A" is transferred to more distant spins B, B', B", etc., resulting in a loss of intensity in the A, A', A" signals. This explains why a scaling factor is necessary to eliminate the reduced-intensity peaks of A-A (diagonal), A-A' (one-bond), and A-A" (two-bond) from the difference spectrum. Due to the fast magnetization equilibration among these three spins, the intensity ratio of the three peaks does not change much with mixing time after ~30 ms and a scaling factor that eliminates the diagonal peak A-A also removes the one bond A-A' and two-bond A-A" cross peaks. A closer analysis shows that the magnetization on the initially polarized spin A is always slightly larger than that of its neighbors A' and A" (**Fig. 6.8d**). Thus, in a difference spectrum without one-bond cross peaks, the diagonal peaks will be slightly negative. This insight is useful for guiding the choice of the

scaling factor for congested spectra, in which the one-bond cross peaks may overlap with other peaks.

6.5 Conclusion

We have shown that a T_1 relaxation-compensated modification of the widely used ^{1}H-driven ^{13}C spin diffusion experiment allows structurally informative long-range correlation peaks to be detected in a difference spectrum. By adding a z-filter, we conduct the PDSD experiment with a constant total T_1 relaxation period, and avoid the appearance of negative peaks from short- and long-range correlations of short-T_1 sites in the difference spectrum. The difference between long and short mixing-time spectra, obtained using a scaling factor that makes the residual diagonal peaks slightly negative, removes all short-range cross peaks and retains only positive long-range cross peaks. The choice of the short mixing time depends on the magnetization equilibration time for the short-range correlations. For site-specifically labeled proteins, intra-residue cross peaks equilibrate by ~200 ms. Monosaccharides equilibrate their magnetization in < 100 ms, and for uniformly ^{13}C-labeled peptides and proteins, one- and two-bond cross peaks can be removed using mixing times of a few tens of milliseconds.

6.6 Acknowledgements

The amino acid and peptide component of this work was supported by NIH grant GM088204. The polysaccharide component of this work was supported by the Center for Lignocellulose Structure and Formation, an Energy Frontier Research Center funded by the U.S. Department of Energy, Office of Science, Basic Energy Sciences under Award # DE-SC0001090.

6.7 References

[1] M. Hong. "Oligomeric Structure, Dynamics, and Orientation of Membrane Proteins from Solid-State NMR." *Structure* **2006**, 14, 1731-1740.

[2] M. Hong, Y. Zhang and F. Hu. "Membrane Protein Structure and Dynamics from NMR Spectroscopy." *Annu. Rev. Phys. Chem.* **2012**, 63, 1-24.

[3] S. Li, Y. Zhang and M. Hong. "3D ^{13}C-^{13}C-^{13}C Correlation NMR for De Novo Distance Determination of Solid Proteins and Application to a Human α-Defensin." *J. Magn. Reson.* **2010**, 202, 203-210.

[4] B. H. Meier. "Polarization Transfer and Spin Diffusion in Solid-State NMR." *Adv. Magn. Opt. Reson.* **1994**, 18, 1-115.

[5] K. Takegoshi, S. Nakamura and T. Terao. "^{13}C-^{1}H Dipolar-Assisted Rotational Resonance in Magic-Angle Spinning NMR." *Chem. Phys. Lett.* **2001**, 344, 631-637.

[6] Y. Miao, T. A. Cross and R. Fu. "Identifying Inter-Residue Resonances in Crowded 2D ^{13}C-^{13}C Chemical Shift Correlation Spectra of Membrane Proteins by Solid-State MAS NMR Difference Spectroscopy." *J. Biomol. NMR* **2013**, 56, 265-273.

[7] G. De Paëpe, J. R. Lewandowski, A. Loquet, A. Böckmann and R. G. Griffin. "Proton Assisted Recoupling and Protein Structure Determination." *J. Chem. Phys.* **2008**, 129, 245101.

[8] J. R. Lewandowski, G. De Paëpe, M. T. Eddy, J. Struppe, W. Maas and R. G. Griffin. "Proton Assisted Recoupling at High Spinning Frequencies." *J. Phys. Chem. B* **2009**, 113, 9062-9069.

[9] F. Castellani, B. van Rossum, A. Diehl, M. Schubert, K. Rehbein and H. Oschkinat. "Structure of a Protein Determined by Solid-State Magic-Angle Spinning NMR Spectroscopy." *Nature* **2002**, 420, 98-102.

[10] V. A. Higman, J. Flinders, M. Hiller, S. Jehle, S. Markovic, S. Fiedler, B. -J. van Rossum and H. Oschkinat. "Assigning Large Proteins in the Solid State: A MAS NMR Resonance Assignment Strategy Using Selectively and Extensively ^{13}C-Labelled Proteins." *J. Biomol. NMR* **2009**, 44, 245-260.

[11] M. Hong. "Determination of Multiple ϕ-Torsion Angles in Proteins by Selective and Extensive ^{13}C Labeling and Two-Dimensional Solid-State NMR." *J. Magn. Reson.* **1999**, 139, 389-401.

[12] M. Hong and K. Jakes. "Selective and Extensive ^{13}C Labeling of a Membrane Protein for Solid-State NMR Investigation." *J. Biomol. NMR* **1999**, 14, 71-74.

[13] A. Loquet, G. Lv, K. Giller, S. Becker and A. Lange. "^{13}C Spin Dilution for Simplified and Complete Solid-State NMR Resonance Assignment of Insoluble Biological Assemblies." *J. Am. Chem. Soc.* **2011**, 133, 4722-4725.

[14] E. R. deAzevedo, W. G. Hu, T. J. Bonagamba and K. Schmidt-Rohr. "Principles of Centerband-Only Detection of Exchange in Solid-State Nuclear Magnetic Resonance, and Extension to Four-Time Centerband-Only Detection of Exchange." *J. Chem. Phys.* **2000**, 112, 8988-9001.

[15] K. Schmidt-Rohr, E. R. deAzevedo and T. J. Bonagamba. "Centerband-Only Detection of Exchange (CODEX): Efficient NMR Analysis of Slow Motions in Solids." *eMagRes* **2007**, 1, 1-10.

[16] S. Li and M. Hong. "Protonation, Tautomerization, and Rotameric Structure of Histidine: A Comprehensive Study by Magic-Angle-Spinning Solid-State NMR." *J. Am. Chem. Soc.* **2011**, 133, 1534-1544.

[17] C. M. Rienstra, M. Hohwy, M. Hong and R. G. Griffin. "2D and 3D ^{15}N-^{13}C-^{13}C NMR Chemical Shift Correlation Spectroscopy of Solids: Assignment of MAS Spectra of Peptides." *J. Am. Chem. Soc.* **2000**, 122, 10979-10990.

[18] C. M. Rienstra, L. Tucker-Kellogg, C. P. Jaroniec, M. Hohwy, B. Reif, M. T. McMahon, B. Tidor, T. Lozano-Pérez and R. G. Griffin. "De Novo Determination of Peptide Structure with Solid-State Magic-Angle Spinning NMR Spectroscopy." *Proc. Natl. Acad. Sci. U.S.A.* **2002**, 99, 10260-10265.

[19] F. Hu, W. Luo and M. Hong. "Mechanisms of Proton Conduction and Gating in Influenza M2 Proton Channels from Solid-State NMR." *Science* **2010**, 330, 505-508.

[20] W. Luo, S. D. Cady and M. Hong. "Immobilization of the Influenza A M2 Transmembrane Peptide in Virus Envelope-Mimetic Lipid Membranes: A Solid-State NMR Investigation." *Biochemistry* **2009**, 48, 6361-6368.

[21] M. Dick-Pérez, Y. Zhang, J. Hayes, A. Salazar, O. A. Zabotina and M. Hong. "Structure and Interactions of Plant Cell-Wall Polysaccharides by Two- and Three-Dimensional Magic-Angle-Spinning Solid-State NMR." *Biochemistry* **2011**, 50, 989-1000.

[22] T. Wang, O. Zabotina and M. Hong. "Pectin-Cellulose Interactions in the Arabidopsis Primary Cell Wall from Two-Dimensional Magic-Angle-Spinning Solid-State Nuclear Magnetic Resonance." *Biochemistry* **2012**, 51, 9846-9856.

[23] T. Wang, Y. B. Park, M. A. Caporini, M. Rosay, L. Zhong, D. J. Cosgrove and M. Hong. "Sensitivity-Enhanced Solid-State NMR Detection of Expansin's Target in Plant Cell Walls." *Proc. Nat. Acad. Sci. U.S.A.* **2013**, 110, 16444-16449.

[24] R. H. Atalla and D. L. VanderHart. "Native Cellulose: A Composite of Two Distinct Crystalline Forms." *Science* **1984**, 223, 283-285.

[25] Y. Nishiyama, P. Langan and H. Chanzy. "Crystal Structure and Hydrogen-Bonding System in Cellulose I$_\beta$ from Synchrotron X-Ray and Neutron Fiber Diffraction." *J. Am. Chem. Soc.* **2002**, 124, 9074-9082.

[26] R. Acharya, V. Carnevale, G. Fiorin, B. G. Levine, A. L. Polishchuk, V. Balannik, I. Samish, R. A. Lamb, L. H. Pinto, W. F. DeGrado and M. L. Klein. "Structure and Mechanism of Proton Transport Through the Transmembrane Tetrameric M2 Protein Bundle of the Influenza A Virus." *Proc. Nat. Acad. Sci. U.S.A.* **2010**, 107, 15075-15080.

[27] S. D. Cady, K. Schmidt-Rohr, J. Wang, C. S. Soto, W. F. DeGrado and M. Hong. "Structure of the Amantadine Binding Site of Influenza M2 Proton Channels in Lipid Bilayers." *Nature* **2010**, 463, 689-692.

6.8 Supporting Information

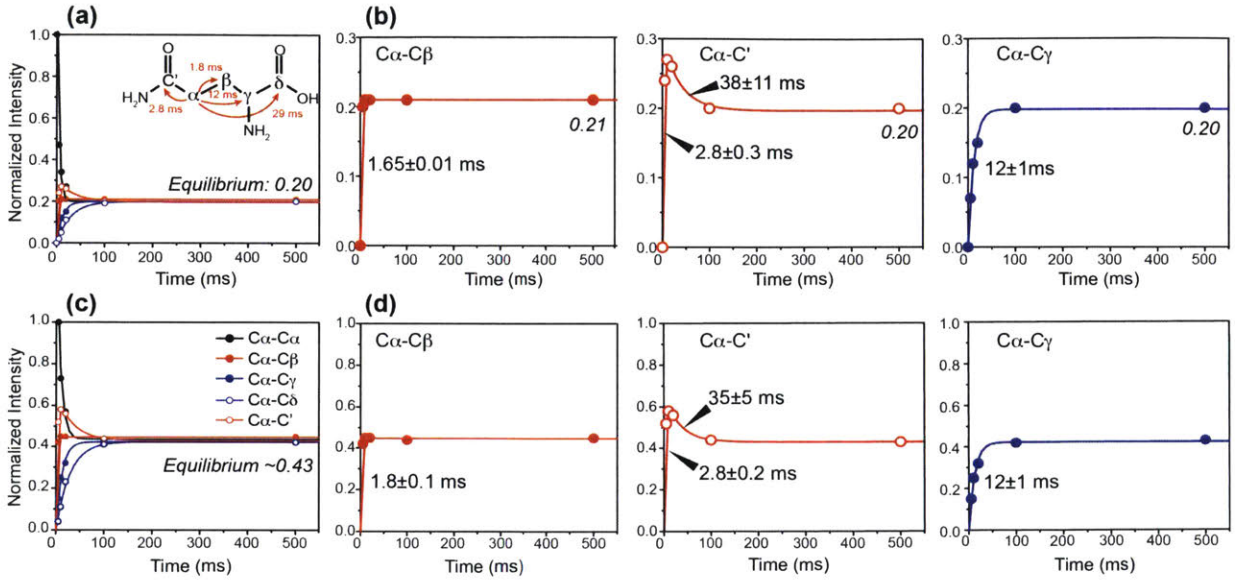

Figure 6.S1 Relaxation-compensated PDSD buildup curves of glutamine, measured with a total z-period of 505 ms. The peak intensities are analyzed in two ways. (a-b) The peak intensities are normalized as $y(\omega_a, \omega_b; t_m) = A(\omega_a, \omega_b; t_m)/\sum_{i=1}^{n} A(\omega_a, \omega_i; t_m)$, where A denotes integrated area. (a) Overlay of all C✔-Cx buildup curves, showing an equilibrium intensity of 0.20, corresponding to the inverse of the number of carbons in glutamine. (b) Representative individual buildup curves and initial time constants. (c-d) Peak intensities are normalized as $y(\omega_a, \omega_b; t_m) = \frac{H(\omega_a,\omega_b;t_m)}{\sum_{i=1}^{n} A(\omega_a,\omega_i;t_m)} \Big/ \frac{H(\omega_a,\omega_b;5\ ms)}{\sum_{i=1}^{n} A(\omega_a,\omega_i;5\ ms)}$, where H refers to height. (c) Overlay of all C✔-Cx buildup curves, showing an equilibrium intensity of 0.43, unrelated to the number of spins in the system. (d) Representative individual buildup curves. The initial time constants and the shape of the buildup curves are identical to those in (b) within experimental uncertainty, as expected.

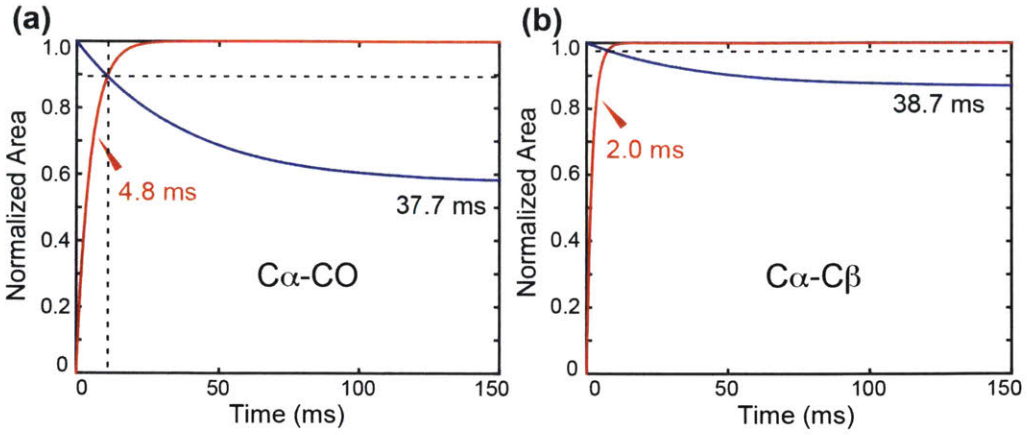

Figure 6.S2 Histidine cross-peak analysis. (a) The Cα-CO buildup curve has a buildup time constant of 4.8 ms and a decay constant of 38 ms. (b) The Cα-Cβ buildup curve has a faster buildup time constant of 2 ms and a similar decay constant of 39 ms. As a result the Cα-CO cross peak intensity overshoots, while the Cα-Cβ peak intensity does not.

Table 6.S1 Experimental conditions for the relaxation-compensated PDSD data.

Sample	z-period	Temperature	MAS frequency	^{1}H Larmor Frequency
Glutamine	0.505 s	293 K	10 kHz	400 MHz
Histidine	1.005 s	293 K	9 kHz	400 MHz
MLF	1.505 s	293 K	7 kHz	400 MHz
GHI-M2TM	1.505 s	273 K	9 kHz	400 MHz
Glucose	1.005 s	273 K	8 kHz	600 MHz
Plant Cell Wall	1.005 s	253 K	8 kHz	600 MHz

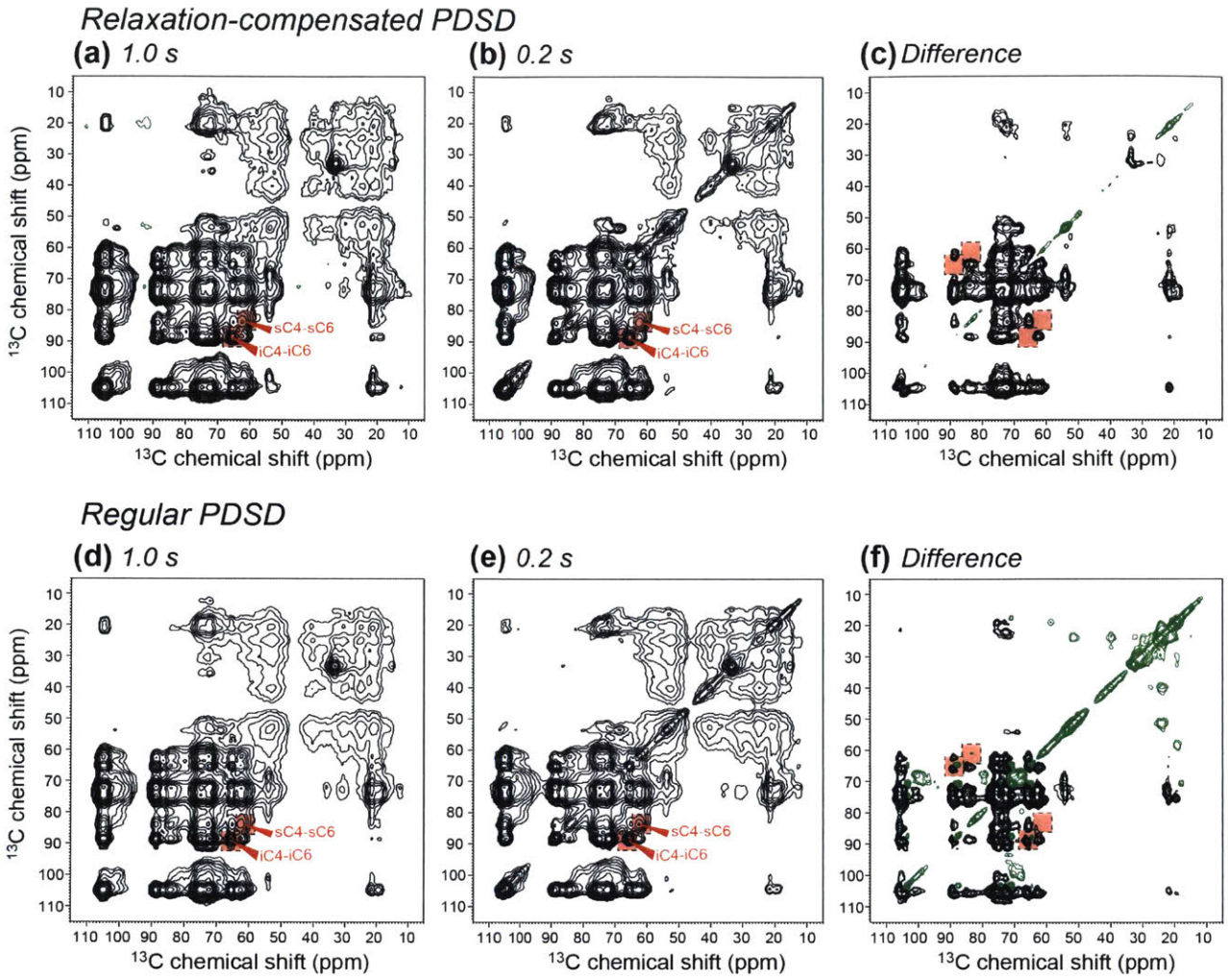

Figure 6.S3 2D PDSD spectra of *Arabidopsis thaliana* primary cell walls. (a-c) Relaxation-compensated PDSD spectra, measured with a total z-period of 1.005 s. (a) 1 s mixing. (b) 0.2 s mixing. (c) Difference spectrum, using a scaling factor of 0.78 for the 200 ms spectrum to remove intramolecular cellulose iC4-iC6 and sC4-sC6 cross peaks. Negative intensities are plotted in green. (d-f) Regular PDSD spectra. (d) 1 s mixing. (e) 0.2 s mixing. (f) Difference spectrum, where the 0.2 s spectrum is scaled by 0.69 to remove intramolecular cellulose cross peaks. The difference spectrum in (f) shows strong negative intensities for matrix polysaccharides and proteins due to their faster T_1 relaxation. All 2D spectra are plotted with the same contour parameters of lev0 = 4.0, toplev = 100 and nlev = 16 in the Bruker Topspin software.

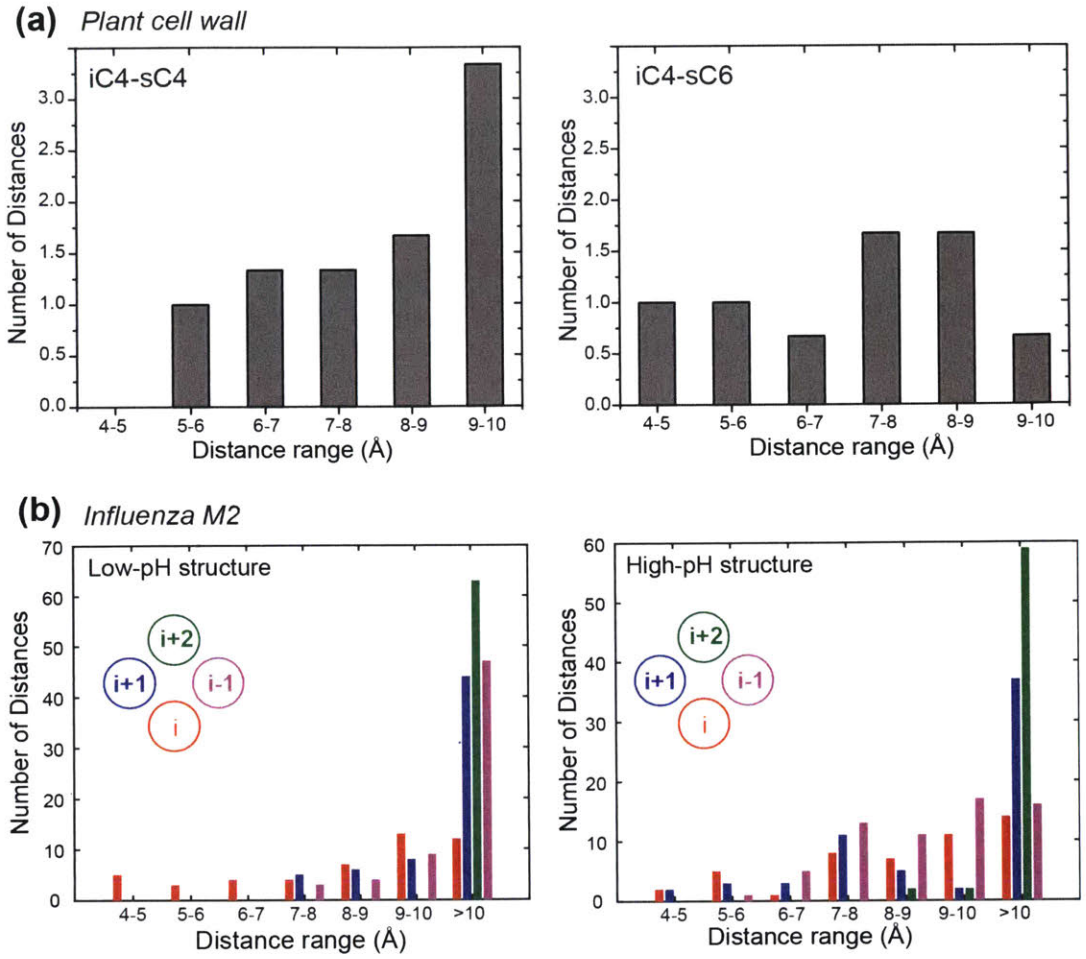

Figure 6.S4 Distance distributions in plant cell walls and the influenza M2 transmembrane peptide, which validate long-range correlation peaks detected in the difference PDSD spectra. (a) Distances between interior and surface cellulose, extracted from the I_β cellulose microfibril structural model.[1] A 1-nm radius sphere is constructed around several interior cellulose C4 carbons, and the number of surface cellulose C4 and C6 carbons within each sphere is counted and averaged. Within 6 Å of each crystalline cellulose C4, 1 and 2 surface cellulose carbons can be found. This distance range is within the detection limit of ^{13}C spin diffusion. (b) Distance distribution between G34 and H37 in M2TM, based on a low-pH crystal structure[2] and a high-pH SSNMR structure.[3] Within 6 Å, multiple G34-H37 contacts of < 6 Å are found. The nearest distances are intrahelical and are between 4.5 and 5.0 Å.

6.8.1 Supporting Information References

[1] T. Wang, Y. B. Park, M. A. Caporini, M. Rosay, L. Zhong, D. J. Cosgrove and M. Hong. "Sensitivity-Enhanced Solid-State NMR Detection of Expansin's Target in Plant Cell Walls." *Proc. Natl. Acad. Sci. U.S.A.* **2013**, 110, 16444-16449.

[2] A. Acharya, V. Carnevale, G. Fiorin, B. G. Levine, A. Polishchuk, V. Balannick, I. Samish, R. A. Lamb, L. H. Pinto, W. F. DeGrado and M. L. Klein. "Structure and Mechanism of Proton Transport Through the Transmembrane Teterameric M2 Protein Bundle of the Influenza A Virus." *Proc. Natl. Acad. Sci. U.S.A.* **2010**, 107, 15075-15080.

[3] S. D. Cady, K. Schmidt-Rohr, J. Wang, C. S. Soto, W. F. DeGrado and M. Hong. "Structure of the Amantadine Binding Site of Influenza M2 Proton Channels in Lipid Bilayers." *Nature* **2010**, 463, 689-692.

7. Aromatic Spectral Editing Techniques for Magic-Angle-Spinning Solid-State NMR Spectroscopy of Uniformly ^{13}C-Labeled Proteins

Jonathan K. Williams[1], Klaus Schmidt-Rohr[2], Mei Hong[1]

[1]Department of Chemistry, Massachusetts Institute of Technology, Cambridge, MA
[2]Department of Chemistry, Brandeis University, Waltham, MA

Solid State Nuclear Magnetic Resonance. **2015**, vol. 72, pp. 118-126.
DOI: 10.1016/j.ssnmr.2015.09.006

7.1 Abstract

The four aromatic amino acids in proteins, namely histidine, phenylalanine, tyrosine, and tryptophan, have strongly overlapping ^{13}C chemical shift ranges between 100 and 160 ppm, and have so far been largely neglected in solid-state NMR determination of protein structures. Yet aromatic residues play important roles in biology through π–π and cation-π interactions. To better resolve and assign aromatic residues' ^{13}C signals in magic-angle-spinning (MAS) solid-state NMR spectra, we introduce two spectral editing techniques. The first method uses gated ^{1}H decoupling in a proton-driven spin-diffusion (PDSD) experiment to remove all protonated ^{13}C signals and retain only non-protonated carbon signals in the aromatic region of the ^{13}C spectra. The second technique uses chemical shift filters and ^{1}H-^{13}C dipolar dephasing to selectively detect the Cα, Cβ and CO cross peaks of aromatic residues while suppressing the signals of all aliphatic residues. We demonstrate these two techniques on amino acids, a model peptide, and the microcrystalline protein GB1, and show that they significantly simplify the 2D NMR spectra and both reveal and permit the ready assignment of the aromatic residues' signals.

7.2 Introduction

Spectral overlap in solid-state NMR MAS spectra remains a challenge in structure determination of proteins and other biological macromolecules. While 2D and 3D correlation experiments are now routinely employed in structure determination,[1-7] for dynamically or statically

disordered or conformationally polymorphic proteins, the ^{13}C and ^{15}N linewidths often exceed 1 ppm,[8] which make even 3D correlation spectroscopy often insufficient for complete resolution of the signals except for the smallest proteins.[9] A number of strategies have been proposed to address this challenge. Optimized sample preparation methods can produce conformational homogeneity, although the biological relevance of the selected conformation is usually unclear. Sparse isotopic labeling[10-13] and segmental labeling based on chemical ligation[14] decrease the complexity of the NMR spectra and thus increase the reliability of the assignment, but they contain less information per spectrum. Semi-automated resonance assignment protocols have been designed to explicitly address ambiguities in resonance assignment of broad-line spectra,[15-18] but do not indicate to what extent the assignment ambiguity is due to incomplete information or due to structural polymorphism.

Spectral editing is a complementary approach to simplify and resolve protein solid-state NMR spectra without requiring the production of multiple samples. Spectral editing was first developed for natural abundance organic compounds. Opella and Frey described a modification of the 1D cross polarization (CP)-MAS experiment that selectively detects non-protonated ^{13}C signals by inserting a period without ^{1}H decoupling.[19] Zilm and coworkers distinguished between and assigned CH, CH_2 and CH_3 groups by combining CP with polarization inversion and depolarization, taking advantage of different polarization transfer rates of the differently protonated carbons.[20-22] Schmidt-Rohr and coworkers developed various spectral editing methods based on chemical shift filtering,[23-25] multiple-quantum dipolar transfer,[26,27] and dipolar dephasing[23,25] to separate and assign overlapping resonances in complex organic materials, such as soil organic matter and carbon materials.

Recently, spectral editing has also been introduced to facilitate the structure determination of uniformly ^{13}C, ^{15}N-labeled proteins. We showed how to selectively detect CH-containing Val, Leu and Ile signals using a dipolar DEPT (distortionless enhancement by polarization transfer) technique, distinguish carboxyl-containing Asp and Glu sidechains from amides by asymmetric ^{13}C-^{15}N REDOR, and selectively detect dynamic residues by gated ^{1}H decoupling.[28] In addition to spectral editing based on chemical structure and molecular motion, differences in the Cα chemical shift anisotropies (CSAs) and backbone ϕ torsion angle between β-strand and α-helical residues

have been exploited to simplify 2D correlation spectra and selectively detect helical or strand residues.[29,30] Similarly, another structural property, which is the differential water contact of protein residues, has been used to edit the spectra of membrane proteins.[8,31-33]

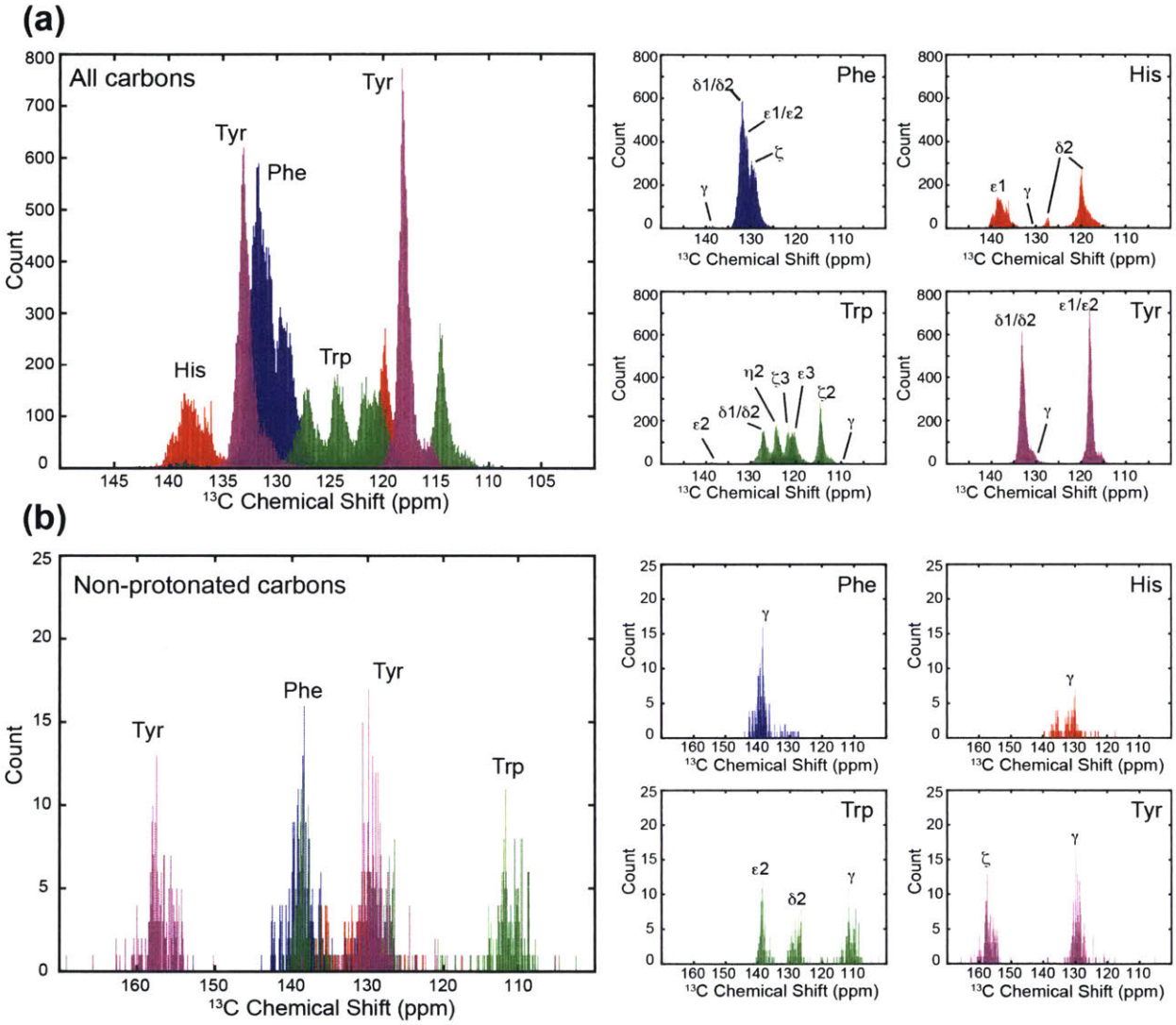

Figure 7.1 ^{13}C chemical shift distributions of the four aromatic residues in proteins from the Biological Magnetic Resonance Data Bank. A large degree of resonance overlap exists in the 110-140 ppm region. (a) All aromatic ^{13}C signals. (b) Only non-protonated aromatic ^{13}C signals. Small panels on the right show the chemical shift dispersions of the individual amino acids.

However, so far most protein spectral editing techniques target aliphatic residues, and no methods are yet available to enhance the resolution of aromatic residues. Trp, His, Tyr and Phe

and cation-π interactions among themselves and with polar residues[34-36] and by functionally relevant ring motions.[37,38] Trp is also well known to stabilize membrane protein structure and topology by acting as an anchoring residue at the membrane-water interface.[39] Aromatic carbons in these four amino acids largely resonate between 140 and 100 ppm, giving rise to a highly congested spectral region. **Fig. 7.1** shows the ^{13}C chemical shift distribution, extracted from the BMRB database,[40] of 23 aromatic carbons in proteins. For residue-type assignment, the only well resolved signals are the non-protonated Tyr Cζ peak at ~158 ppm and to some extent the Trp Cγ signal at ~110 ppm, which occupy the outer limits of the aromatic chemical shift range. The other non-protonated carbons, including Phe Cγ, Tyr Cγ, His Cγ, Trp Cδ2 and Trp Cε2, resonate between 140 and 130 ppm. For histidine, the protonation state of the sidechain significantly affects the ^{13}C chemical shifts,[41] causing the non-protonated Cγ chemical shift to vary between 128 and 138 ppm.

Two other factors that complicate the assignment of aromatic ^{13}C signals are their large CSAs and the difficulty of avoiding accidental rotational-resonance (R^2)[42] line broadening that arises when the chemical-shift difference matches the MAS frequency ν_r or $2\nu_r$ ($n = 1$ and $n = 2$ R^2 condition). The large aromatic ^{13}C CSAs give rise to spinning sidebands in the spectra that usually extend into the aliphatic region. More insidiously, the Cβ and Cγ isotropic chemical shift differences of aromatic residues are typically 80-100 ppm,[15] which fall between the $n = 1$ and $n = 2$ R^2 conditions of 120 ppm and 60 ppm for backbone Cα and CO chemical shifts, respectively. Thus, MAS frequencies are often accidentally close to some of the aromatic residues' Cβ and Cγ isotropic shift differences, broadening both peaks. **Fig. 7.2a** shows the ^{13}C CP-MAS spectra of uniformly ^{13}C, ^{15}N-labeled Trp under 4-12 kHz MAS at 1 kHz intervals. At the ^{13}C Larmor frequency of 100 MHz used to measure these spectra, these MAS frequencies correspond to 40-120 ppm. The Cγ and Cβ isotropic shift difference for Trp is 80.1 ppm, which gives an $n = 1$ R^2 condition of 8 kHz (80 ppm) MAS and an $n = 2$ R^2 condition of 4 kHz (40 ppm) MAS. Thus, the Cγ and Cβ peaks are split and broadened at 4 kHz and 8 kHz MAS, as well as within 1 kHz windows of these two frequencies (**Fig. 7.2b**). Moreover, at MAS frequencies lower than 6 kHz (or 60 ppm), significant aromatic sidebands exist that overlap with the aliphatic signals. Under 12 kHz (or 120 ppm) MAS, the CO and Cα peaks are severely split by the R^2 effect. These multiple R^2 conditions restrict the choice of MAS frequencies to 11 kHz (or 110 ppm) for Trp, which gives

the best compromise of avoiding R^2 broadening as well as minimizing spinning sidebands (**Fig. 7.2a,b**). For uniformly ^{13}C-labeled proteins with multiple aromatic residues, choosing an appropriate MAS frequency that avoids all R^2 conditions is thus crucial for minimizing mis-assignment of aromatic residues' Cβ and Cγ signals.

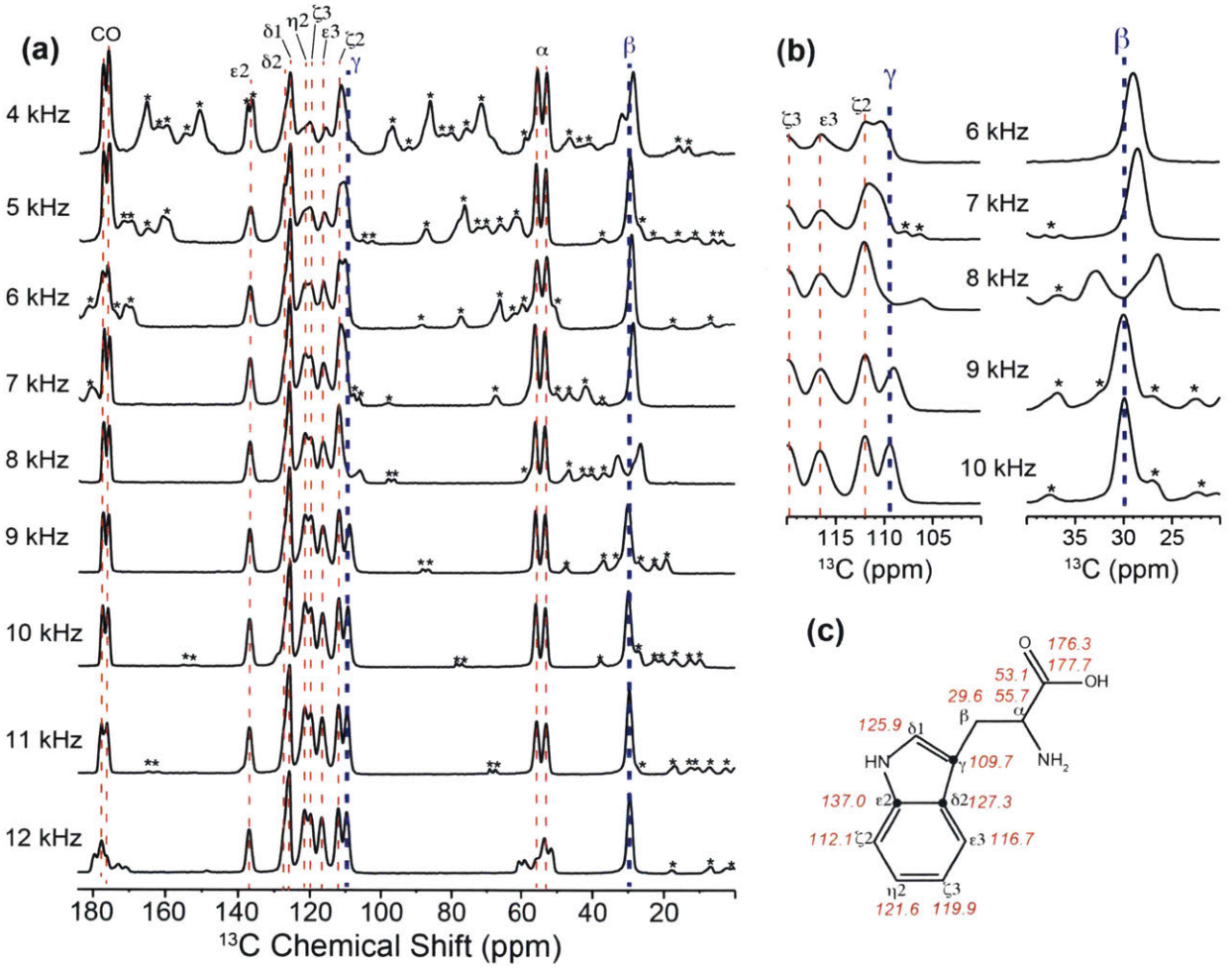

Figure 7.2 1D CP-MAS spectra of U-^{13}C,^{15}N labeled Trp as a function of MAS frequency. (a) Full 1D spectra measured in a 9.4 T magnetic field, corresponding to 100 MHz ^{13}C Larmor frequency. At 8 kHz (80 ppm) and 12 kHz (120 ppm) MAS frequencies, rotational resonance broadening is observed for the Cβ-Cγ spin pair and the Cα-CO spin pair, respectively. (b) Expanded Cγ and Cβ regions of the ^{13}C spectra, showing R^2–induced line broadening. MAS frequencies that are within 1 kHz (or 10 ppm) of the R^2 conditions are insufficient for removing line broadening. In all panels, spinning sidebands are marked with an asterisk. (c) Accurate ^{13}C isotropic shifts of Trp, obtained from the 11 kHz MAS spectrum, which is free of R^2 effects and spinning sideband overlap.

In this study, we describe two techniques for reducing spectral overlap and facilitating assignment of the ^{13}C signals of aromatic residues in proteins. The first technique is a simple modification of the 2D ^{13}C-^{13}C PDSD experiment to include a gated ^{1}H decoupling period before direct detection. The resulting 2D PDSD spectrum correlates all ^{13}C signals in the indirect dimension with only the signals of non-protonated carbons in the direct dimension. The second technique is designed to suppress all Cα-Cβ cross peaks of aliphatic residues, leaving only the Cα, Cβ and CO cross peaks of aromatic residues. The Cα and Cβ magnetization of all residues is first removed by chemical shift filters and ^{13}C-^{1}H dipolar filters, then the remaining aromatic ^{13}C magnetization is transferred to the Cα, Cβ and CO of only the aromatic residues by a short spin diffusion period. We demonstrate these two techniques on amino acids, a model peptide, and the microcrystalline model protein GB1.

7.3 Experimental Conditions

Solid-state NMR experiments were carried out on Bruker 400 MHz (9.4 T) and 800 MHz (18.8 T) spectrometers using 4 mm or 3.2 mm MAS probes. The samples were spun at frequencies between 4.0 kHz and 16.5 kHz. Typical radiofrequency field strengths were 71-83 kHz for ^{1}H and 50-71 kHz for ^{13}C. ^{13}C chemical shifts were referenced to the CH_2 peak of adamantane at 38.48 ppm on the TMS scale.[43] Four uniformly ^{13}C and ^{15}N labeled model compounds were used to test the pulse sequences: the amino acid Trp, a five-amino-acid mixture, WYIEN, the tripeptide formyl-Met-Leu-Phe (MLF),[2,44,45] and the microcrystalline protein GB1. These model systems provide increasing levels of complexity for spectral editing, culminating in GB1, which contains six aromatic residues out of a total of 56 residues.[46]

7.4 Pulse Sequences

7.4.1 ^{1}H Gated Decoupling PDSD (gPDSD) Experiment

The conventional 2D PDSD experiment gives ^{13}C-^{13}C correlation peaks within an amino acid residue at short mixing times and both short and long-range correlations at long mixing times. With a T_1-relaxation compensation scheme, difference spectra showing only long-range cross

peaks can also be obtained.[47] To detect only non-protonated aromatic ^{13}C signals in the aromatic region of PDSD spectrum, we add a ^{1}H gated decoupling period after the spin diffusion mixing time and before t_2 detection (**Fig. 7.3a**). The gate during which ^{1}H decoupling is turned off consists of a total delay of $\tau_1 + \tau_2$, which spans part of two rotor periods. They are demarcated by a ^{13}C 180° pulse on the rotor echo to refocus the ^{13}C chemical shift, and also recouple the ^{13}C-^{1}H dipolar coupling to better dephase the ^{13}C magnetization. The remaining periods during which ^{1}H decoupling is on are τ_{D1} and τ_{D2}, where $\tau_{D1} + \tau_1$ and $\tau_2 + \tau_{D2}$ equal one rotor period. τ_1 and τ_2 are in general not the same. In the current work, under 10.3 kHz MAS, we found that the optimal delays for maximal dephasing of the protonated aromatic signals are $\tau_1 = 60$ μs and $\tau_2 = 40$ μs.

7.4.2 Aromatic Selection via Spectral Editing (ASSET) Experiment

Figure 7.3b shows the pulse sequence for obtaining only aromatic Cα-Cβ cross peaks in the aliphatic region of the 2D PDSD spectra. At the beginning of the pulse sequence, the ^{13}C carrier frequency is set in the middle of the aromatic region, around 123 ppm. A ^{13}C 90° pulse together with ^{1}H-^{13}C CP allow the detection of both dynamic and rigid functional groups. A subsequent spin diffusion period, $t_{m,1}$, of ~500 ms further enhances the aromatic ^{13}C intensities by equilibrating the aliphatic and aromatic ^{13}C magnetization, since the low proton density of aromatic residues causes lower signals in a conventional ^{13}C CP spectrum.[25] After the pre-equilibration period, a 90° pulse flips all ^{13}C magnetization to the transverse plane, where chemical shift evolution with aromatic residues on or near resonance is allowed to occur for a period t_α, which alternates between 0 and a finite time that creates antiparallel magnetization vectors between Cα and aromatic carbons. For experiments at a ^{13}C Larmor frequency of 100 MHz (9.4 T), the best t_α is 0 and 83 μs. A subsequent 90° pulse with suitable phase cycling every two scans then stores the aromatic ^{13}C magnetization along +z while the Cα magnetization alternates between +z and –z. Any transverse magnetization is then dephased by ^{13}C-^{1}H dipolar coupling, which is recoupled using a ^{1}H 180° pulse every half rotor period. After this z-filter, the stored ^{13}C z-magnetization is returned to the transverse plane by another 90° pulse, and a similar chemical shift filter together with a z-filter is used to destroy the Cβ magnetization. At 100 MHz ^{13}C Larmor frequency, the optimal Cβ chemical shift filter time, t_β, is 0 and 47 μs. Due to the sufficiently high MAS frequency, t_α and t_β

need not be rotor-synchronized. The z-filter periods can also have different lengths, and were optimized to be 2 and 4 rotor periods at an MAS frequency of ~10 kHz. At this point, the remaining ^{13}C magnetization is mostly aromatic, and is allowed to re-polarize the adjacent Cβ and Cα during a t_{arom} period of 5-25 ms. The ^{13}C carrier frequency is moved to ~73 ppm at the beginning of the t_{arom} period to keep potential zero-frequency artifacts outside the relevant spectral region and avoid significant off-resonance effects. This is followed by a standard 2D PDSD module with a mixing time of $t_{m,2}$, with optional echo detection.

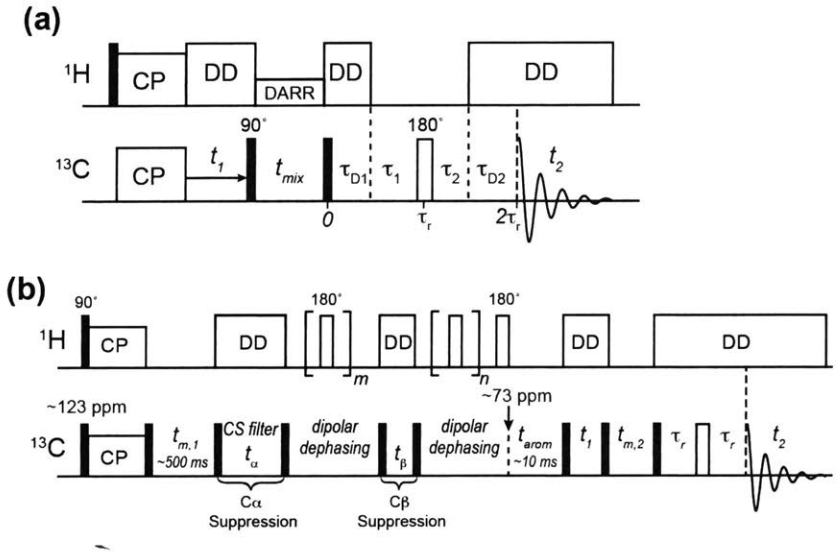

Figure 7.3 Pulse sequences developed in this work. (a) 2D PDSD with gated ^{1}H decoupling. The gated decoupling period contains $\tau_1 = 60$ μs and $\tau_2 = 40$ μs for the MAS frequencies used in this work. (b) 2D Aromatic Selection by Spectral Editing (ASSET). The initial spin diffusion period is set relatively long ($t_{m,1} = 500$ ms) to ensure polarization of aromatic side chains. This is followed by two chemical shift filters, one for Cα suppression (t_α) and one for Cβ suppression (t_β). Each chemical shift filter is followed by a ^{13}C-^{1}H dipolar recoupled z-filter period to destroy the transverse magnetization of other aliphatic carbons that are far off-resonance from the aromatic region. A spin diffusion period, t_{arom}, then transfers the remaining aromatic ^{13}C magnetization to the Cβ and Cα of the aromatic residues. 2D correlation of Cβ and Cα resonances is then conducted using a typical PDSD module with Hahn echo detection.

7.5 Results and Discussion

We demonstrate these two aromatic spectral editing techniques on several model compounds. **Fig. 7.4a,c** shows the full 2D PDSD spectra of Trp and WYIEN, where all intra-residue cross-peaks can be assigned. The gPDSD spectra show a greatly simplified aromatic region. For Trp, all protonated ^{13}C signals are removed in the direct dimension, leaving only cross-peaks of the indole Cγ, Cδ2 and Cε2 (**Fig. 7.4b**). For the amino-acid mixture, Trp Cε2, Cδ2 and Cγ and Tyr Cγ and Cζ signals are retained with efficiencies of 42-75% compared to the full spectrum while the protonated aromatic carbons are suppressed to 0-9% of the full intensity (**Fig. 7.4d**). In the aliphatic-aliphatic region of the 2D gPDSD spectrum (not shown), residual Ile Cδ and Cε methyl signals are also present due to their motionally averaged ^{13}C-^{1}H dipolar couplings, but the intensities are only ~6% of the full intensities. In the aliphatic-aromatic correlation region, the suppression of the protonated ^{13}C signals significantly simplified the assignment of the Trp and Tyr Cβ and Cα chemical shifts.

The gated-decoupling sequence similarly simplifies the aromatic region of the GB1 2D spectrum (**Fig. 7.5a,b**). Although the high resolution afforded by the 800 MHz spectrometer allowed us to resolve many aromatic ^{13}C peaks of the three Tyr residues (Y3, Y33, Y45), two Phe residues (F30, F52) and one Trp (W43),[46] resonance overlap remains among Phe Cδ and Cε and Tyr Cγ and Cδ signals, which cluster around 130 ppm. With gated ^{1}H decoupling, most of the F30 and F52 cross peaks in the 126-133 ppm region are suppressed, revealing the underlying Tyr Cγ and Cδ signals in **Fig. 7.5b**. Compared to the regular PDSD spectrum, the non-protonated ^{13}C signals are retained to an average of 86% of the full intensities while the protonated aromatic carbons' signals are suppressed to an average of 18% of the full intensities. The slightly higher residual intensities of the protonated aromatic carbons in GB1 compared to the amino acids can be attributed to two reasons. The WYIEN sample was measured on a 400 MHz spectrometer under 10.3 kHz MAS, while GB1 was measured on an 800 MHz spectrometer under 16.5 kHz MAS. The higher MAS frequency was necessary to avoid overlap between the carbonyl spinning sidebands and the aromatic signals, and the resulting shorter rotor period caused a shorter gate, thus reducing the efficiency of dipolar dephasing. The GB1 gPDSD spectrum was measured using

a total gating delay of $\tau_1 + \tau_2 = 60$ μs, while the amino acid mixture was measured with a total delay of 100 μs. The incomplete suppression under faster MAS can be remedied by extending the dipolar dephasing period. In addition, molecular motion, which may be present for the less hydrophobically embedded aromatic residues in GB1, can also reduce the efficiency of gated decoupling. For example, we observe 33% residual intensity of the Tyr Cδ and Tyr Cε peak in the gated decoupling spectrum (**Fig. 7.5b**). This can be attributed to one of the three Tyr, Y33, which is located on the surface of the protein with its sidechain pointed away from the hydrophobic pore. Indeed, Y33 was found to undergo two-site ring flips,[46] which average the ^{13}C-^{1}H dipolar couplings, thus reducing the efficiency of gated decoupling.

While gPDSD simplifies the aromatic region of 2D ^{13}C PDSD spectra, the ASSET technique selectively detects the Cβ-Cα, Cα-Cβ, Cβ-CO and Cα-CO cross peaks of aromatic residues while suppressing those of aliphatic residues. **Fig. 7.6a,d** show the full 2D spectra of the WYIEN mixture and the tripeptide MLF. All intra-residue cross peaks are observed for WYIEN with a 20 ms mixing time (**Fig. 7.6a**) while intra- and inter-residue correlations are both observed in MLF with 30 ms mixing (**Fig. 7.6d**). When the ASSET technique is applied without the transfer, i.e. $t_{arom} = 0$, the aliphatic signals are nearly completely suppressed, except for a few weak methyl signals (**Fig. 7.6b,e**) and Asn and Trp Cα-Cβ peaks, which may result from incomplete chemical shift filtering. When the aromatic transfer is turned on ($t_{arom} = 10$ ms), the Cα and Cβ signals of Trp and Tyr in the mixture are selectively enhanced, as shown by Cα-Cβ and Cβ-Cα cross peaks on both sides of the diagonal (**Fig. 7.6c,f**). These Trp and Tyr cross peaks are 20-40% of the full intensities, compared to the incompletely suppressed Ile sidechain methyl signals, which are ~3% of the full intensities. A similar result is found for MLF. Here, the Phe shows a Cβ-Cα cross peak but not the Cα-Cβ peak, indicating that the 10 ms t_{arom} is sufficiently short that polarization transfer is dominated by the Cγ-Cβ transfer while Cγ-Cα transfer is reduced. Such cross peak asymmetry can be helpful for spectral editing of larger proteins.

Figure 7.7 shows the 2D DARR and ASSET spectra of GB1 using a mixing time of 100 ms between the t_1 and t_2 dimensions. The 2D spectra were measured on an 800 MHz spectrometer under 16.5 kHz MAS, and the DARR spectrum (**Fig. 7.7a**) exhibits comparable resolution as the

published literature.[46] The ASSET sequence dramatically simplified the aliphatic and carbonyl regions of the spectrum (**Fig. 7.7b**), displaying only Cα/β-Cβ/α and Cα/β-CO cross peaks of the six aromatic residues with efficiencies of 10-20%. The Cβ-Cα cross peaks of W43, Y33, and F30 are well resolved, while the Cβ-Cα cross peaks of Y3, Y45 and F52 partially overlap. But the latter three residues are well dispersed by their carbonyl chemical shifts. The aliphatic region of the ASSET spectrum has moderate intensity asymmetry, with the Cβ-Cα cross peaks stronger than Cα-Cβ peaks, indicating that the aromatic carbon magnetization is transferred more readily to Cβ than to Cα with the t_{arom} mixing time of 25 ms used here.

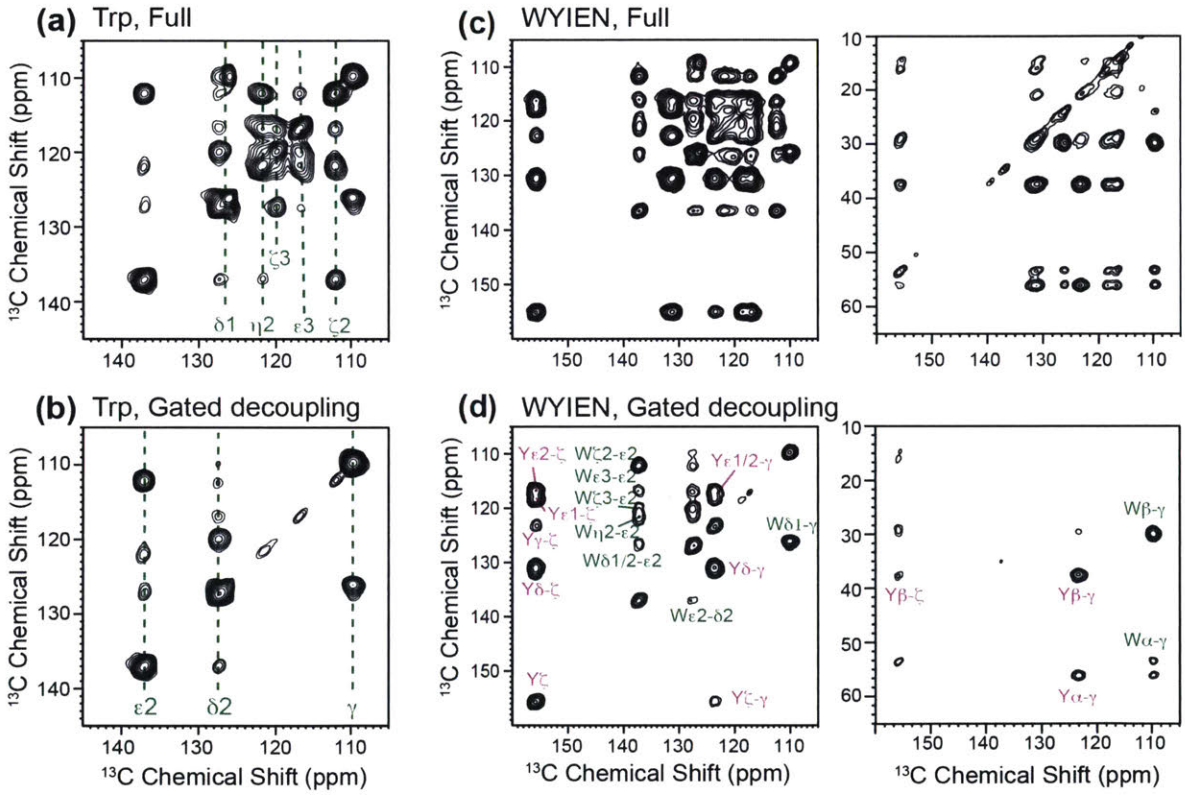

Figure 7.4 2D ^{13}C-^{13}C DARR (top) and gPDSD (bottom) spectra of U-^{13}C Trp (a, b) and the amino acid mixture WYIEN (c, d). Spectra (a) and (b) were recorded under 11 kHz MAS using a mixing time of 2 ms and ^{1}H gate times of τ_1 = 60 μs and τ_2 = 40 μs. Spectra (c) and (d) were measured under 10.3 kHz MAS using a mixing time of 10 ms and ^{1}H gate times of τ_1 = 60 μs and τ_2 = 40 μs. The aromatic region in (b) and (d) retains only the non-protonated ^{13}C signals in the direct dimension. For the amino acid mixture, the aliphatic-aromatic correlation region is also simplified after removal of the protonated aromatic ^{13}C signals, facilitating assignment of the Cβ and Cα chemical shifts of Tyr and Trp.

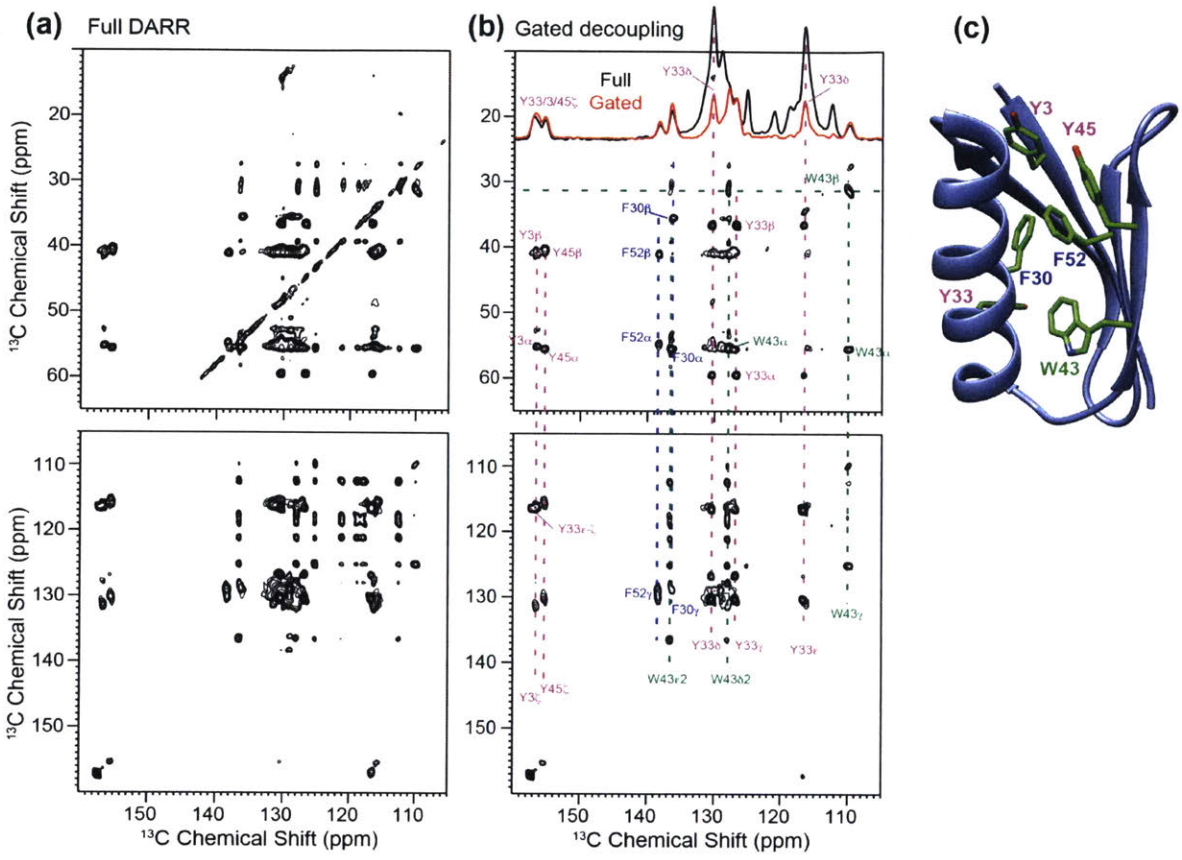

Figure 7.5 2D ^{13}C PDSD (a) and gPDSD (b) spectra of GB1 measured at 18.8 T (800 ^{1}H Larmor frequency) under 16.5 kHz MAS with a mixing time of 100 ms. ^{1}H gate times of τ_1= 36 μs and τ_2 = 24 μs were used for spectra (b). (c) GB1 structure (PDB: 2QMT) showing the positions of the six aromatic residues.

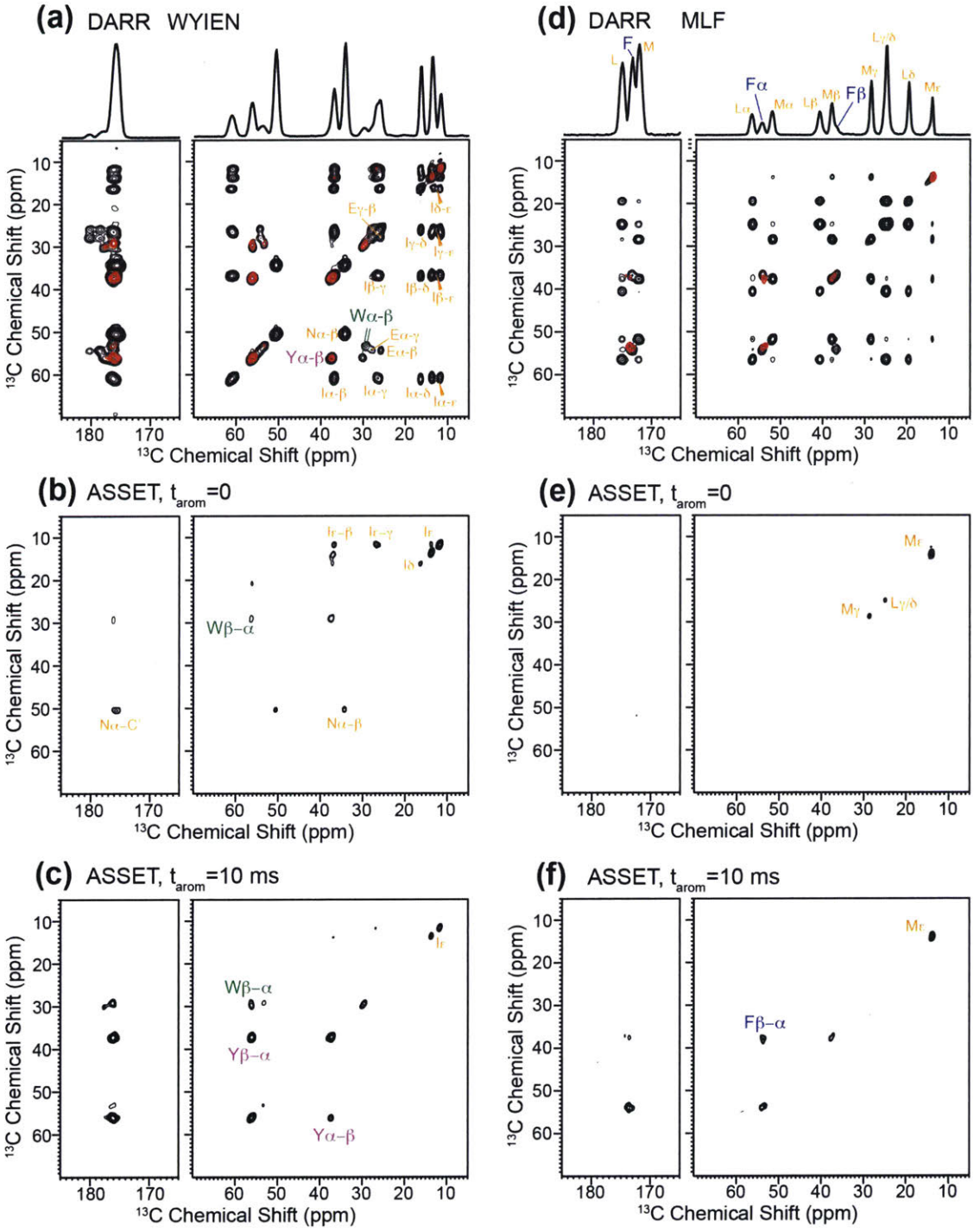

Figure 7.6 2D ^{13}C-^{13}C DARR and ASSET spectra of the amino acid mixture WYIEN (a-c) and tripeptide MLF (d-f). (a, d) Full DARR spectra showing all cross peaks. (b, e) Spectra with t_{arom} = 0, where most Cα and Cβ cross peaks are suppressed. (c, f) ASSET spectra with t_{arom} = 10 ms, which exhibit mostly aromatic Cα and Cβ cross peaks. The spectra in (c) and (f) are reproduced in red in (a) and (d) to compare with the full DARR spectra.

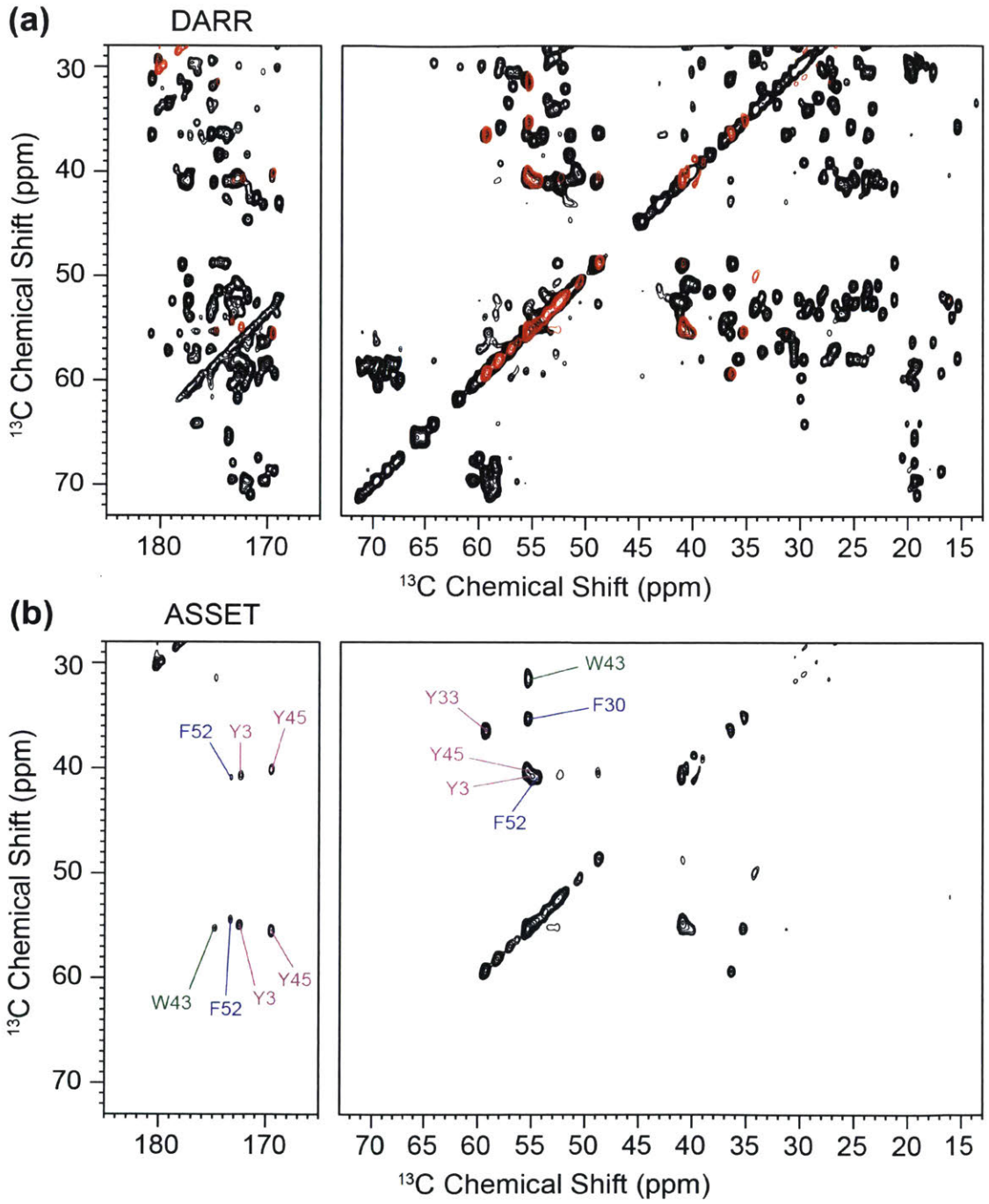

Figure 7.7 2D ^{13}C DARR (a) and ASSET (b) spectra of GB1. The ASSET spectrum was acquired with t_{arom} = 25 ms and shows only the Cα-Cβ and Cα/β-CO cross peaks of the six aromatic residues while suppressing the signals of all aliphatic residues. The ASSET spectrum is reproduced in red in (a) and superimposed on the full PDSD spectrum.

7.6 Conclusions

We have demonstrated two pulse sequences for measuring simplified and higher-resolution 2D ^{13}C-^{13}C correlation spectra of aromatic residues in proteins. The gPDSD technique results in a non-protonated aromatic ^{13}C sub-spectrum in the direct dimension, correlated with all carbons in the indirect dimension. The ASSET technique yields aromatic residues' Cβ, Cα and CO cross peaks while suppressing all aliphatic residues' cross peaks. The efficiency of the gPDSD technique for aromatic carbons is 62-86%, while the protonated ^{13}C signals are suppressed to less than 20% of the original intensities. The efficiency of the ASSET experiment is 20-40% on small molecules and 10-20% on GB1. The lower efficiency of GB1 may be due to the inherent isotropic shift dispersion, which makes the chemical shift filter imperfect. Overall, the selectivity against non-aromatic residues is excellent for both techniques, thus increasing the repertoire of spectral editing techniques for complex and disordered proteins. In principle, the aromatic-residue-only Cα-Cβ sub-spectrum can also be obtained in a 3D ^{13}C-^{13}C-^{13}C correlation experiment,[48] provided that the aromatic ^{13}C chemical shifts are reasonably well resolved, but the signal-averaging time for these 3D experiments is significantly longer than for the 2D spectrally edited ASSET experiment.

7.7 Acknowledgements

This work is supported by NIH grant GM088204 to M. H. The authors would like to thank Dr. Robert Silvers for providing the GB1 sample used in this work.

7.8 References

[1] M. Hong. "Resonance Assignment of $^{13}C/^{15}N$ Labeled Solid Proteins by Two- and Three-Dimensional Magic-Angle-Spinning NMR." *J. Biomol. NMR* **1999**, 15, 1-14.

[2] C. M. Rienstra, M. Hohwy, M. Hong and R.G. Griffin. "2D and 3D ^{15}N-^{13}C-^{13}C NMR Chemical Shift Correlation Spectroscopy of Solids: Assignment of MAS Spectra of Peptides." *J. Am. Chem. Soc.* **2000**, 122, 10979-10990.

[3] M. Baldus, A. T. Petkova, J. Herzfeld and R. G. Griffin. "Cross Polarization in the Tilted Frame: Assignment and Spectral Simplification in Heteronuclear Spin Systems." *Mol. Phys.* **1998**, 95, 1197-1207.

[4] G. Comellas and C. M. Rienstra. "Protein Structure Determination by Magic-Angle Spinning Solid-State NMR, and Insights into the Formation, Structure, and Stability of Amyloid Fibrils." *Annu. Rev. Biophys.* **2013**, 42, 515-536.

[5] A. E. McDermott. "Structure and Dynamics of Membrane Proteins by Magic Angle Spinning Solid-State NMR." *Annu. Rev. Biophys.* **2009**, 38, 385-403.

[6] S. Luca, H. Heise and M. Baldus. "High-Resolution Solid-State NMR Applied to Polypeptides and Membrane Proteins." *Acc. Chem. Res.* **2003**, 36, 858-65.

[7] M. Hong. "Solid-State NMR Studies of the Structure, Dynamics, and Assembly of β-Sheet Membrane Peptides and α-Helical Membrane Proteins with Antibiotic Activities." *Acc. Chem. Res.* **2006**, 39, 176-183.

[8] S. Y. Liao, K. J. Fritzsching and M. Hong. "Conformational Analysis of the Full-Length M2 Protein of the Influenza A Virus Using Solid-State NMR." *Protein Sci.* **2013**, 22, 1623-1638.

[9] R. Tycko. "Prospects for Resonance Assignments in Multidimensional Solid-State NMR Spectra of Uniformly Labeled Proteins." *J. Biomol. NMR* **1996**, 22, 239-251.

[10] M. Hong. "Determination of Multiple ϕ-Torsion Angles in Solid Proteins by Selective and Extensive ^{13}C Labeling and Two-Dimensional Solid-State NMR." *J. Magn. Reson.* **1999**, 139, 389-401.

[11] M. Hong and K. Jakes. "Selective and Extensive ^{13}C Labeling of a Membrane Protein for Solid-State NMR Investigations." *J. Biomol. NMR* **1999**, 14, 71-74.

[12] A. Loquet, G. Lv, K. Giller, S. Becker and A. Lange. "^{13}C Spin Dilution for Simplified and Complete Solid-State NMR Resonance Assignment of Insoluble Biological Assemblies." *J. Am. Chem. Soc.* **2011**, 133, 4722-4725.

[13] F. Castellani, B. vanRossum, A. Diehl, M. Schubert, K. Rehbein and H. Oschkinat. "Structure of a Protein Determined by Solid-State Magic-Angle Spinning NMR Spectroscopy." *Nature* **2002**, 420, 98-102.

[14] B. Kwon, D. Tietze, P.B. White, S. Y. Liao and M. Hong. "Chemical Ligation of the Influenza M2 Protein for Solid-State NMR Characterization of the Cytoplasmic Domain." *Protein Sci.* **2015**, 24, 1087-1099.

[15] K. J. Fritzsching, Y. Yang, K. Schmidt-Rohr and M. Hong. "Practical Use of Chemical Shift Databases for Protein Solid-State NMR: 2D Chemical Shift Maps and Amino-Acid Assignment with Secondary-Structure Information." *J. Biomol. NMR* **2013**, 56, 155-167.

[16] K. N. Hu, W. Qiang and R. Tycko. "A General Monte Carlo/Simulated Annealing Algorithm for Resonance Assignment in NMR of Uniformly Labeled Biopolymers." *J. Biomol. NMR* **2011**, 50, 267-276.

[17] R. Tycko and K. N. Hu. "A Monte Carlo/Simulated Annealing Algorithm for Sequential Resonance Assignment in Solid State NMR of Uniformly Labeled Proteins with Magic-Angle Spinning." *J. Magn. Reson.* **2010**, 205, 304-314.

[18] Y. Yang, K. J. Fritzsching and M. Hong. "Resonance Assignment of Disordered Proteins Using a Multi-Objective Non-Dominated Sorting Genetic Algorithm." *J. Biomol. NMR* **2013**, 57, 281-296.

[19] S. J. Opella and M. H. Frey. "Selection of Nonprotonated Carbon Resonances in Solid-State Nuclear Magnetic Resonance." *J. Am. Chem. Soc.* **1979**, 101, 5854-5856.

[20] X. Wu, S. T. Burns and K. W. Zilm. "Spectral Editing in CPMAS NMR. Generating Subspectra Based on Proton Multiplicities." *J. Magn. Reson.* **1994**, 111, 29-36.

[21] X. L. Wu and K. W. Zilm. "Complete Spectral Editing in CPMAS NMR." *J. Magn. Reson.* **1993**, 102, 205-213.

[22] X. Wu, S. Zhang and X. Wu. "Selective Polarization Inversion in Solid State High-Resolution CP MAS NMR." *J. Magn. Reson.* **1988**, 77, 343-347.

[23] J. D. Mao and K. Schmidt-Rohr. "Accurate Quantification of Aromaticity and Nonprotonated Aromatic Carbon Fraction in Natural Organic Matter by ^{13}C Solid-State Nuclear Magnetic Resonance." *Environ. Sci. Technol.* **2004**, 38, 2680-2684.

[24] J. D. Mao and K. Schmidt-Rohr. "Separation of Aromatic-Carbon ^{13}C NMR Signals from Di-Oxygenated Alkyl Bands by a Chemical-Shift-Anisotropy Filter." *Solid State Nuc. Magn. Reson.* **2004**, 26, 36-45.

[25] R. L. Johnson, J. M. Anderson, B. H. Shanks, X. Fang, M. Hong and K. Schmidt-Rohr. "Spectrally Edited 2D ^{13}C-^{13}C NMR Spectra Without Diagonal Ridge for Characterizing ^{13}C-Enriched Low-Temperature Carbon Materials." *J. Magn. Reson.* **2013**, 234, 112-124.

[26] K. Schmidt-Rohr and J. D. Mao. "Efficient CH-Group Selection and Identification in ^{13}C Solid-State NMR by Dipolar DEPT and ^{1}H Chemical-Shift Filtering." *J. Am. Chem. Soc.* **2002**, 124, 13938-13948.

[27] J. D. Mao and K. Schmidt-Rohr. "Methylene Spectral Editing in Solid-State ^{13}C NMR by Three-Spin Coherence Selection." *J. Magn. Reson.* **2005**, 176, 1-6.

[28] K. Schmidt-Rohr, K. J. Fritzsching, S. Y. Liao and M. Hong. "Spectral Editing of Two-Dimensional Magic-Angle-Spinning Solid-State NMR Spectra for Protein Resonance Assignment and Structure Determination." *J. Biomol. NMR* **2012**, 54, 343-353.

[29] M. Hong. "Solid-State NMR Determination of $^{13}C\alpha$ Chemical Shift Anisotropies for the Identification of Protein Secondary Structure." *J. Am. Chem. Soc.* **2000**, 122, 3762-3770.

[30] D. Huster, S. Yamaguchi and M. Hong. "Efficient β-sheet Identification in Proteins by Solid-State NMR Spectroscopy." *J. Am. Chem. Soc.* **2000**, 122, 11320-11327.

[31] C. Ader, R. Schneider, K. Seidel, M. Etzkorn, S. Becker and M. Baldus. "Structural Rearrangements of Membrane Proteins Probed by Water-Edited Solid-State NMR Spectroscopy." *J. Am. Chem. Soc.* **2009**, 131, 170-176.

[32] K. K. Kumashiro, K. Schmidt-Rohr, O. J. Murphy, K. L. Ouellette, W. A. Cramer and L. K. Thompson. "A Novel Tool for Probing Membrane Protein Structure: Solid-State NMR with Proton Spin Diffusion and X-Nucleus Detection." *J. Am. Chem. Soc.* **1998**, 120, 5043-5051.

[33] I. V. Sergeyev, S. Bahri, L. A. Day and A. E. McDermott. "Pf1 Bacteriophage Hydration by Magic Angle Spinning Solid-State NMR." *J. Chem. Phys.* **2014**, 141, 22D533.

[34] J. P. Gallivan and D. A. Dougherty. "Cation-π Interactions in Structural Biology." *Proc. Natl. Acad. Sci. U.S.A.* **1999**, 96, 9459-9464.

[35] S. Y. Liao, Y. Yang, D. Tietze and M. Hong. "The Influenza M2 Cytoplasmic Tail Changes the Proton-Exchange Equilibria and the Backbone Conformation of the Transmembrane Histidine Residue to Facilitate Proton Conduction." *J. Am. Chem. Soc.* **2015**, 137, 6067-6077.

[36] J. K. Williams, Y. Zhang, K. Schmidt-Rohr and M. Hong. "pH-Dependent Conformation, Dynamics, and Aromatic Interaction of the Gating Tryptophan Residue of the Influenza M2 Proton Channel from Solid-State NMR." *Biophys. J.* **2013**, 104, 1698-1708.

[37] W. Hu, N. D. Lazo and T. A. Cross. "Tryptophan Dynamics and Structural Refinement in a Lipid Bilayer Environment: Solid State NMR of the Gramicidin Channel." *Biochemistry* **1995**, 34, 14138-14146.

[38] C. M. Gall, T. A. Cross, J. A. DiVerdi and S. J. Opella. "Protein Dynamics by Solid-State NMR: Aromatic Rings of the Coat Protein in fd Bacteriophage." *Proc. Natl. Acad. Sci. U.S.A.* **1982**, 79, 101-105.

[39] M. R. R. de Planque, B. B. Bonev, J. A. A. Demmers, D. V. Greathouse, R. E. Koeppe, F. Separovic, A. Watts and J. A. Killian. "Interfacial Anchor Properties of Tryptophan Residues in Transmembrane Peptides Can Dominate Over Hydrophobic Matching Effects in Peptide-Lipid Interactions." *Biochemistry* **2003**, 42, 5341-5348.

[40] E. L. Ulrich, H. Akutsu, J. F. Doreleijers, Y. Harano, Y. E. Ioannidis, J. Lin, M. Livny, S. Mading, D. Maziuk, Z. Miller, E. Nakatani, C. F. Schulte, D. E. Tolmie, R. K. Wenger, H. Y. Yao and J. L. Markley. "BioMagResBank." *Nucleic Acids Res.* **2007**, 35, D402-D408.

[41] S. Li and M. Hong. "Protonation, Tautomerization, and Rotameric Structure of Histidine: A Comprehensive Study by Magic-Angle-Spinning Solid-State NMR." *J. Am. Chem. Soc.* **2011**, 133, 1534-1544.

[42] D. P. Raleigh, M. H. Levitt and R. G. Griffin. "Rotational Resonance in Solid State NMR." *Chem. Phys. Lett.* **1988**, 146, 71-76.

[43] C. R. Morcombe and K. W. Zilm. "Chemical Shift Referencing in MAS Solid State NMR." *J. Magn. Reson.* **2003**, 162, 479-86.

[44] M. Hong and R. G. Griffin. "Resonance Assignment for Solid Peptides by Dipolar-Mediated $^{13}C/^{15}N$ Correlation Solid-State NMR." *J. Am. Chem. Soc.* **1998**, 120, 7113-7114.

[45] C. M. Rienstra, L. Tucker-Kellogg, C. P. Jaroniec, M. Hohwy, B. Reif, M. T. McMahon, B. Tidor, T. Lozano-Perez and R. G. Griffin. "De Novo Determination of Peptide Structure with Solid-State Magic-Angle Spinning NMR Spectroscopy." *Proc. Natl. Acad. Sci. U.S.A.* **2002**, 99, 10260-10265.

[46] W. T. Franks, D. H. Zhou, B. J. Wylie, B. G. Money, D. T. Graesser, H. L. Frericks, G. Sahota and C. M. Rienstra. "Magic-Angle Spinning Solid-State NMR Spectroscopy of the β1 Immunoglobulin Binding Domain of Protein G (GB1): ^{15}N and ^{13}C Chemical Shift Assignments and Conformational Analysis." *J. Am. Chem. Soc.* **2005**, 127, 12291-12305.

[47] T. Wang, J. K. Williams, K. Schmidt-Rohr and M. Hong. "Relaxation-Compensated Difference Spin Diffusion NMR for Detecting ^{13}C-^{13}C Long-Range Correlations in Proteins and Polysaccharides." *J. Biomol. NMR* **2014**, 61, 97-107.

[48] S. Li, Y. Zhang and M. Hong. "Correlation NMR for De Novo Distance Determination of Solid Proteins and Application to a Human α-Defensin." *J. Magn. Reson.* **2010**, 202, 203-210.

8. Solid-State NMR Investigation of the Conformation, Proton Conduction, and Hydration of the Influenza B Virus M2 Transmembrane Proton Channel

Jonathan K. Williams[1], Daniel Tietze[1], Myungwoon Lee[1], Jun Wang[2], and Mei Hong[1]

[1]Department of Chemistry, Massachusetts Institute of Technology, Cambridge, MA
[2]Department of Pharmacology and Toxicology, The University of Arizona, Tucson, AZ

Journal of the American Chemical Society. **2016**, vol. 138, pp. 8143-8155.
DOI: 10.1021/jacs.6b03142

8.1 Abstract

Together with the influenza A virus, influenza B virus causes seasonal flu epidemics. The M2 protein of influenza B (BM2) forms a tetrameric proton-conducting channel that is important for the virus lifecycle. BM2 shares little sequence homology with AM2, except for a conserved HxxxW motif in the transmembrane (TM) domain. Unlike AM2, no antiviral drugs have been developed to block the BM2 channel. To elucidate the proton-conduction mechanism of BM2 and to facilitate the development of BM2 inhibitors, we have employed solid-state NMR spectroscopy to investigate the conformation, dynamics and hydration of the BM2 TM domain in lipid bilayers. BM2 adopts an α-helical conformation in lipid membranes. At physiological temperature and low pH, the proton-selective residue, His19, shows relatively narrow ^{15}N chemical exchange peaks for the imidazole nitrogens, indicating fast proton shuttling that interconverts cationic and neutral histidines. Importantly, pH-dependent ^{15}N chemical shifts indicate that His19 retains the neutral population to much lower pH than His37 in AM2, indicating larger acid-dissociation constants or lower pK_a's. We attribute these dynamical and equilibrium differences to the presence of a second titratable histidine, His27, which may increase the proton-dissociation rate of His19. Two-dimensional ^{1}H-^{13}C correlation spectra probing water ^{1}H polarization transfer to the peptide indicates that the BM2 channel becomes much more hydrated at low pH than at high pH, particularly at Ser12, indicating that the pore-facing serine residues in BM2 mediate proton relay to the proton-selective histidine.

8.2 Introduction

While influenza viruses are best known for causing devastating flu pandemics in history, they exert just as much economic and social burden by causing seasonal flu epidemics. Two types of influenza viruses, A and B, are responsible for the seasonal flu. On average influenza A infections are more common in the seasonal flu,[1] but the influenza B virus becomes dominant in the spring months, and in some seasons can account for up to 50% of infections (data available from CDC FluView, www.cdc.gov/flu/weekly/).[2]

The currently approved adamantane class of antiviral drugs works only against the influenza A virus by binding to its M2 protein (AM2) and blocking the conduction of protons into the virus, a process that is important for the virus lifecycle.[3-7] However, these drugs have no effect against the influenza B M2 protein (BM2), which also has proton-channel activity.[8] The lack of inhibition is not surprising: BM2 and AM2 share little sequence homology, with only a HxxxW motif conserved in their respective TM domains (**Fig. 8.1a**).[9] The histidine is responsible for the acid activation and proton selectivity of the channel, whereas the tryptophan is responsible for channel gating.[8,10] Sequence alignment of the two TM domains shows that the BM2 channel pore is significantly more polar than the AM2 channel, with multiple Ser residues lining the pore, suggesting the reason for the inability of the hydrophobic adamantane to inhibit BM2.[11] A high-resolution solution NMR structure of the BM2 TM domain has been determined using BM2(1-33) bound to DHPC micelles.[12] The result shows a coiled-coil tetramer with three Ser residues (S9, S12, S16) lining the pore and a bulky Phe residue (F5) lying at the N-terminal entrance. The structure of the cytoplasmic domain was also determined in the same study using a BM2(26-109) construct. Liposome assays indicate that BM2(1-33) exhibits rimantadine-insensitive proton conductance, and in *Escherichia coli* lipid extracts, the single-channel conductance of BM2(1-33) is 2-fold higher than the conductance of AM2(18-60).[12] Since AM2(18-60) has the same specific activity as full-length AM2,[13] and whole-cell voltage-clamp assays of full-length AM2 and BM2 indicate similar inward proton currents,[8] these data together indicate that BM2(1-33) encompasses the full channel activity of the intact protein. Similar to AM2, BM2's channel activity is important for virus uncoating[8,14] and for preventing hemagglutinin from prematurely adopting a low-pH conformation during transport to the cell surface.[8,15,16] The cytoplasmic domain of BM2 carries out

the separate function of incorporation of M1 and viral ribonucleoprotein complexes at the virion budding site during virus assembly.[17,18]

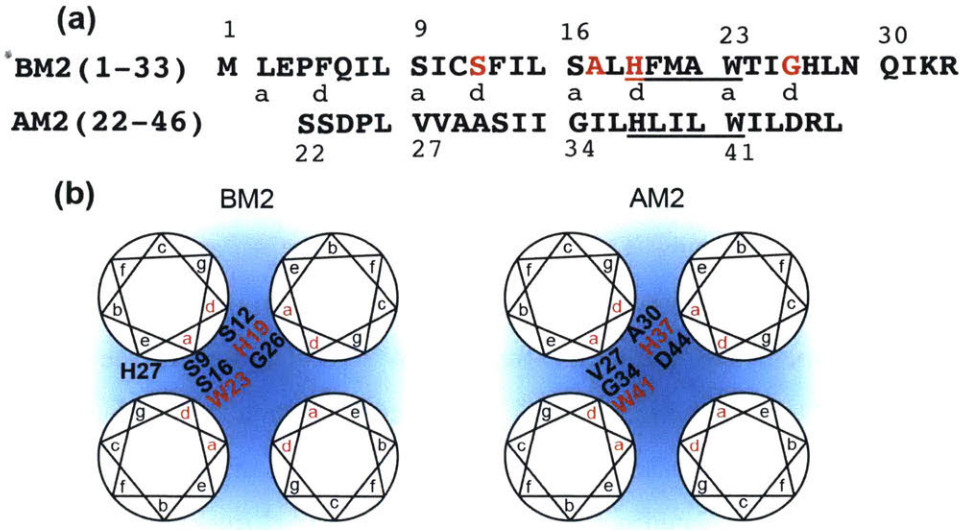

Figure 8.1 Comparison of the amino acid sequences (a) of the BM2 and AM2 transmembrane domains. Lowercase letters indicate heptad repeat, with *a* and *d* indicating pore-facing positions. The conserved HxxxW motif is underlined, and the ^{13}C,^{15}N-labeled residues are shown in red. (b) Four-helix bundle organization of the BM2 and AM2 transmembrane domains, with the pore-facing *a* and *d* residues indicated.

While AM2 and BM2 channels are functional analogs, various differences exist in their pH- and voltage-dependent proton conduction. The BM2 TM domain contains a second histidine (H27), C-terminal to the gating Trp23, whose mutation to Ala reduces the inward H^+ current by ~26%.[12] Whole-cell electrophysiological assays showed that BM2 has significant *outward* current under positive voltages, when the external pH (pH_{out}) is high and the internal pH (pH_{in}) is low, conditions under which AM2 shows negligible outward current.[8] To understand the basis for these functional differences, and to facilitate the design of antiviral drugs against influenza B infection, it is important to determine the structure of the BM2 TM domain in lipid bilayers and to investigate the mechanisms of action of the functional residues, His19 and Trp23.

A large amount of structural and dynamical information about the HxxxW motif has been obtained on the AM2 protein. The His37 residue in AM2 is now known to shuttle protons into the

virion by proton exchange with water. ^{15}N chemical exchange peaks have been observed in both TM peptide and cytoplasmic-containing constructs of AM2 and in the S31N mutant of AM2.[19-22] The line widths of the exchange peaks differ, indicating that proton-transfer rates are sensitive to protein structural differences and electrostatic effects. This proton shuttling involves ring reorientations[23] and τ-π tautomerization.[22] Measured imidazole ^{1}H chemical shifts at low and high temperatures suggest hydrogen bonding between histidine and water;[7] in addition, His-His hydrogen bonding has also been proposed.[21,24] His37-Trp41 cation-π interaction at low pH has been suggested by ^{13}C-^{19}F[25] and ^{13}C-^{15}N[26] distance experiments and UV resonance Raman experiments,[27] and has been proposed to regulate proton release from His to the C-terminal water molecules,[28,29] in agreement with the gating function of Trp.[10] Computed free-energy profiles of proton transport and 2D IR data indicate that proton conduction at low pH is facilitated by an expanded channel width and increased hydration and solvent dynamics.[30,31] The relation between channel hydration and His-mediated proton shuttling is of special interest, because the BM2 TM domain has a more polar pore-lining surface than AM2, suggesting that the histidine-mediated proton-transfer dynamics might differ from that of AM2.

Solid-state NMR spectroscopy is a powerful and versatile tool for studying the structure and dynamics of membrane proteins in lipid bilayers. Increasing evidence from studies of many membrane peptides and proteins indicates that the structures of small oligomeric membrane proteins are susceptible to changes by the membrane environment compared to large membrane protein complexes and machineries,[32-37] and some of these structural changes are functionally relevant. Solid-state NMR based structural and dynamical studies of membrane proteins in phospholipid bilayers instead of detergents are therefore essential for obtaining biologically authentic mechanistic information. In this study, we investigate the backbone conformation of BM2(1-33) using chemical shifts of site-specifically labeled peptides, and then focus on the structures and dynamics of the proton-selective His19. We also investigate channel hydration using water-protein ^{1}H-^{13}C 2D correlation experiments. We show that in cholesterol-containing eukaryotic-mimetic membranes, BM2(1-33) is stably α-helical at high and low pH, and in two different membranes examined, and His19 exhibits a number of cationic and tautomeric states that in totality resemble those seen for His37 in AM2 but that have a shifted pH dependence. ^{15}N NMR spectra of His19 yielded the four pK_a's, which are about one pH unit lower than the pK_a's of His37

in AM2. The BM2 channel hydration is both pH- and membrane-dependent: negatively charged membranes increased the pore hydration compared to neutral membranes, and the pH dependence of BM2 hydration is larger than that of AM2. These results suggest the structural reasons for some of the functional differences between these two viral proton channels, and how the amino acid sequence affects the histidine-mediated proton conduction.

8.3 Materials and Methods

8.3.1 Synthesis of Isotopically Labeled BM2(1-33)

A peptide corresponding to residues 1-33 (MLEPFQILS ICSFILSALH FMAWTIGHLN QIKR) of the B/Maryland/1/2001 strain of influenza virus was synthesized using Fmoc solid-phase peptide synthesis protocols as described previously.[22,38] Briefly, ChemMatrix Rink Amide resin was used for the peptide synthesis. For the coupling step, 5 equiv of amino acid, 5 equiv of HCTU, and 10 equiv of diisopropylamine were used, and the reaction was carried out in DMF for 5 min at 75°C. For the Fmoc deprotection step, 5% piperazine in DMF plus 0.1 M HOBt were used, and the reaction was similarly carried out in DMF for 5 min at 75°C. Final peptide cleavage from the resin was carried out in a cocktail that consists of 95% trifluoroacetic acid, 2.5% triisopropylsilane, and 2.5% H_2O for 2.5 h at room temperature. Cleaved peptide was precipitated in cold ether and purified by preparative HPLC (Vydac C4 Column). Uniformly ^{13}C,^{15}N-labeled amino acids (Sigma-Aldrich and Cambridge Isotope Laboratories) were introduced at positions S12, A17, His19 and G26.

8.3.2 Membrane Sample Preparation

The BM2(1-33) peptide was reconstituted into two lipid membranes, POPC:POPG:cholesterol (PC/PG/Chol) at molar ratios of 60%:20%:20%, and POPC:POPE:sphingomyelin:cholesterol (VM+) at equimolar concentrations.[38] Both lipid mixtures mimic eukaryotic membranes by including cholesterol, but the former contains the anionic lipid POPG, since this mixture is commonly used in M2 proton conductance assays[12] and membrane scission assays.[39] Anionic lipids are also present in the plasma membrane and the virus lipid

envelope at ~15 mol %, but usually in the form of phosphatidylserine instead of phosphatidylglycerol.[40] The neutral VM+ lipid mixture allows us to compare the structure of BM2 with that of AM2 in the same membrane.[38] The lipids were mixed together in chloroform, and then the solvent was removed by nitrogen gas. The peptide was dissolved in 1 mL of 1,1,1,3,3,3-hexafluoro-2-propanol (HFIP) or 2,2,2-trifluoroethanol (TFE), and then mixed with the lipids. The bulk solvent was removed again by nitrogen gas, then the powder was placed under vacuum at room temperature overnight followed by lyophilization for 2-3 h to fully remove fluorinated solvents. The resulting lipid-peptide mixture was suspended in buffer, vortexed, and freeze-thawed 8-10 times to create uniform vesicles. The proteoliposome solution was spun at 50,000 rpm at 4°C for 4 h to obtain homogenous membrane pellets. The pellets were allowed to dry slowly in a desiccator to 40-50% hydration by mass, then transferred into 4 mm or 3.2 mm magic-angle-spinning (MAS) rotors for solid-state NMR experiments.

Seven BM2 samples were prepared at different pH in the two membranes. For the PC/PG/Chol membrane, three samples were prepared at pH 7.5 (10 mM Tris, 1 mM EDTA, 0.1 mM NaN_3), pH 5.5 and pH 4.5 (10 mM citric acid/citrate, 1 mM EDTA, 0.1 mM NaN_3) and the peptide:lipid molar ratio was 1:15. For the VM+ membrane, four samples were prepared at pH 6.5 (20 mM Bis-Tris, 2 mM EDTA, 0.2 mM NaN_3), pH 5.5 (10 mM citric acid/citrate, 1 mM EDTA, 0.1 mM NaN_3), pH 4.5 (10 mM citric acid/citrate, 1 mM EDTA, 0.1 mM NaN_3) and pH 4.0 (20 mM citric acid/citrate, 2 mM EDTA, 0.2 mM NaN_3). The peptide:lipid molar ratio was 1:13.3. The pH of the membrane samples was measured at two time points during sample preparation: after freeze-thawing to create homogeneous vesicle solutions, and after ultracentrifugation, where the supernatant pH was measured. The measured pH was within 0.1 pH units of the desired value.

8.3.3 Membrane Samples for Dynamic Nuclear Polarization (DNP) Experiments

BM2(1-33) was reconstituted into a deuterated lipid mixture denoted d_{31}-VM+', which contains d_{31}-POPC, d_{31}-POPE, and cholesterol at a molar ratio of 40%:40%:20%.[41] The partially deuterated phospholipids were used to increase the efficiency of polarization transfer from the radical to the peptide. About 1 mg of BM2 was dissolved in TFE, and then mixed with the d_{31}-VM+' lipid mixture in chloroform at a peptide/lipid molar ratio of 1:22.5. The organic solvents

were removed under nitrogen gas, and then the mixture was lyophilized overnight. The peptide-lipid mixture was suspended in a 10 mM pH 5.5 citrate buffer and centrifuged at 40,000 rpm at 4°C overnight to obtain a homogeneous pellet, which was equilibrated to a hydration level of ~40 wt %. A small amount of a stock DNP solution, d_8-glycerol:D_2O:H_2O (60:30:10 by volume) containing 10 mM of the biradical AMUPol was titrated into the membrane pellet.[41] The pellet was vortexed to distribute the radical uniformly, and D_2O was added to reach a D_2O:H_2O volume ratio of 3:1. The sample was then allowed to equilibrate again to ~40% hydration, and then packed into a 3.2 mm sapphire rotor and sealed with a silica plug for DNP experiments at 117 K.

8.3.4 Solid-State NMR Experiments

Solid-state NMR experiments were carried out on Bruker 400 MHz (9.4 T) and 800 MHz (18.8 T) NMR spectrometers using 4 mm or 3.2 mm $^1H/^{13}C/^{15}N$ MAS probes. Typical radiofrequency (rf) field strengths were 71-83 kHz for ^1H, 62.5-71 kHz for ^{13}C, and 45-50 kHz for ^{15}N. Chemical shifts were referenced to the CH_2 signal of adamantane at 38.48 ppm on the tetramethylsilane (TMS) scale for ^{13}C, the amide signal of N-acetylvaline at 122.0 ppm on the liquid ammonia scale for ^{15}N, and the Hγ signal of the lipid phosphocholine headgroup at 3.26 ppm on the TMS scale for ^1H.

One-dimensional ^{13}C and ^{15}N cross-polarization (CP) MAS spectra were measured at 313-243 K. To extract His19 pK_a's, we measured ^{15}N CP-MAS spectra of the four VM+ bound BM2 samples at 243 K on the 400 MHz spectrometer. About 100,000 scans were averaged for each sample to obtain sufficient sensitivity. The ^1H-^{15}N CP contact time was 3 ms, and the ^1H and ^{15}N spin-lock matching condition was optimized by maximizing the 250-ppm unprotonated ^{15}N peak in a pH 8.5 histidine model compound. The ratio of the integrated intensities of the unprotonated to the protonated ^{15}N peaks in amino acid histidine ranged from 1.35 to 1.45, reflecting incomplete polarization transfer to the unprotonated nitrogen. This factor is taken into account in extracting the ratio of neutral to cationic His19 in BM2.

Two-dimensional (2D) ^{13}C-^{13}C correlation spectra were measured using a proton-driven spin-diffusion experiment with dipolar-assisted rotational resonance (DARR) mixing.[42] The 400

MHz data were acquired at 243 K with a spin-diffusion mixing time of 50 ms, while the 800 MHz data were obtained at 263 K using a mixing time of 100 ms. Two-dimensional ^{15}N-^{13}C heteronuclear correlation (HETCOR) spectra were measured at 263 K using a REDOR based pulse sequence[43] with dipolar mixing times of 0.5-0.6 ms.

A 2D ^{1}H-^{13}C HETCOR experiment with spin diffusion[44-46] was used to measure the hydration of BM2 residues. A ^{1}H T_2 filter of 1-6 ms was used before spin diffusion to suppress the peptide ^{1}H magnetization while retaining most of the water and lipid ^{1}H magnetization. Two ^{1}H spin-diffusion mixing times were measured for each sample, a short mixing time of 4 ms and a long mixing time, which was 50 ms for the pH 7.5 PC/PG/Chol sample and 100 ms for the pH 5.5 PC/PG/Chol sample and the VM+ samples. Due to the different phase transition temperatures of the two membranes, the PC/PG/Chol samples were measured at 263 K while the VM+ samples were measured at 293 K. Water ^{1}H T_1 relaxation times were measured using an inversion recovery sequence and range from ~230 to ~850 ms. The pH 7.5 PC/PG/Chol membrane showed the shortest water ^{1}H T_1 relaxation time (~230 ms); thus, we chose a long mixing time of 50 ms instead of 100 ms for this sample to obtain sufficient sensitivity. On the basis of our studies of the water interactions with a number of membrane peptides and proteins such as AM2,[46,47] antimicrobial peptides,[34,48] and bacterial toxins,[45,49] the 50 ms mixing is sufficient to equilibrate the water polarization with BM2. Water ^{1}H cross-peak intensities with peptide ^{13}C signals were extracted from the cross section of each 2D spectrum, and the intensity ratios between the short and long mixing-time spectra were corrected for ^{1}H T_1 relaxation according to $S/S_0 = S(4\ ms)e^{4\ ms/T_1}/S(100\ ms)e^{100\ ms/T_1}$ or $S/S_0 = S(4\ ms)e^{4\ ms/T_1}/S(50\ ms)e^{50\ ms/T_1}$ to give the initial spin-diffusion buildup intensity from water to the protein residue. Error bars for S/S_0 values were propagated from the signal-to-noise ratios of the peaks.

8.3.5 DNP Experiment Conditions

DNP spectra were measured on the pH 5.5 BM2 sample bound to the d_{31}-VM+' membrane on a 400 MHz/263 GHz DNP spectrometer at Bruker Biospin (Billerica, MA). The sample temperatures were ~108 K with the microwave (MW) off and ~117 K with the MW on at 130 mA. Double-quantum-filtered (DQF) 1D ^{13}C spectra were measured using 2.2 ms of SPC5 ^{13}C-^{13}C

dipolar recoupling.[50] One-dimensional and 2D ^{15}N-^{13}C dipolar filtered spectra were measured using a double CP pulse sequence with a ^{1}H-^{15}N CP contact time of 1.25 ms and a ^{15}N-^{13}C CP contact time of 9.0 ms.

8.3.6 Extraction of His19 pK_a's

His19 acid-dissociation constants (K_a's) were extracted from the ^{15}N CP-MAS spectra based on the fact that the neutral-to-cationic hisitidine concentration ratios are reflected by the relative intensities of the protonated NH peaks and the unprotonated nitrogen peak according to $[His]/[HisH^+] = 2[(I_{NH}/I_N)/\kappa - 1]^{-1}$. ^{15}N peak intensities were integrated from 258 to 240 ppm for the unprotonated imidazole nitrogen, which results exclusively from neutral histidine, and 200-150 ppm for the protonated nitrogen, which results from both neutral and cationic histidines. The κ in the equation is a correction factor for the reduced efficiency of ^{1}H-^{15}N CP for the unprotonated nitrogen compared to protonated nitrogen. The κ value is measured from the optimized CP spectrum of pH 8.5 amino acid histidine.[51] The model-compound spectrum was measured with the same CP contact time, ^{1}H and ^{15}N radiofrequency matching conditions, and MAS frequency as for the BM2 samples. For these ^{15}N CP experiments, the samples were spun at 7 kHz, and a CP contact time of 3 ms was used. Uncertainties in the neutral-to-cationic histidine concentration ratios were propagated from the signal-to-noise ratios of the spectra.

The neutral-to-cationic histidine concentration ratios at different pH were fit using the equation[19,24]

$$\frac{[His]}{[HisH^+]} = \frac{1\cdot\frac{K_{a1}}{10^{-pH}}+2\cdot\frac{K_{a1}\cdot K_{a2}}{10^{-2pH}}+3\cdot\frac{K_{a1}\cdot K_{a2}\cdot K_{a3}}{10^{-3pH}}+4\cdot\frac{K_{a1}\cdot K_{a2}\cdot K_{a3}\cdot K_{a4}}{10^{-4pH}}}{4+3\cdot\frac{K_{a1}}{10^{-pH}}+2\cdot\frac{K_{a1}\cdot K_{a2}}{10^{-2pH}}+1\cdot\frac{K_{a1}\cdot K_{a2}\cdot K_{a3}}{10^{-3pH}}} \qquad (8.1)$$

in MATLAB's Curve Fitting Toolbox. Among the four pK_a's, pK_{a4} has the highest value and is for the first protonation event, while pK_{a1} corresponds to the last protonation event and has the lowest value. Uncertainties in the determined pK_a's were estimated from the uncertainty ranges of the histidine concentration ratios.

8.4 Results

8.4.1 Backbone Conformation and Dynamics of BM2(1-33) in Lipid Membranes

We measured 1D and 2D ^{13}C spectra as a function of pH, membrane composition, and temperature (**Figs. 8.2, 8.3**) to determine the global conformation and dynamics of BM2(1-33). At low temperature (243 K), the labeled residues exhibit strong signals at α-helical chemical shifts in both PC/PG/Chol and VM+ membranes. The S12 Cα and Cβ cross peaks are close to the diagonal, characteristic of the α-helical conformation. Distinct α-helical Cα and Cβ chemical shifts are also observed for A17 and G26. Interestingly, for S12, A17, and G26, Cα and CO chemical shifts decrease at low pH compared to high pH (**Table 8.1**), suggesting that the local conformations at these residues become less ideally α-helical at acidic pH. The line widths also increase at low pH, indicative of larger conformational heterogeneity in the open state. Increasing the temperature to 303 K weakened most of the intensities of the PC/PG/Chol bound peptides while retaining the intensities of VM+ bound peptides (**Fig. 8.2a,b**). This indicates that BM2(1-33) undergoes intermediate-timescale motion[52] in PC/PG/Chol bilayers, which interferes with ^{1}H decoupling and ^{1}H-^{13}C cross-polarization, but is largely immobilized in the VM+ membrane. While the two membranes both contain POPC and cholesterol, POPE and sphingomyelin have significantly higher phase transition temperatures than POPG; thus, the VM+ membrane is more viscous than the PC/PG/Chol membrane, slowing down BM2(1-33) motion.

DNP experiments at cryogenic temperature (~117 K) enhanced the sensitivity sufficiently to allow us to resolve the BM2 signals from the lipid background signals through ^{15}N-^{13}C and ^{13}C-^{13}C dipolar filters (**Fig. 8.2c-e**). A sensitivity enhancement factor of 21-27 was achieved using a recently optimized membrane preparation protocol for DNP NMR.[41] With the removal of the natural abundance ^{13}C signals of lipids and cryoprotectants, we resolved two His19 Cβ signals at 29 and 27 ppm and the S12 Cα and Cβ signals at ~60 ppm (**Fig. 8.2d,e**).

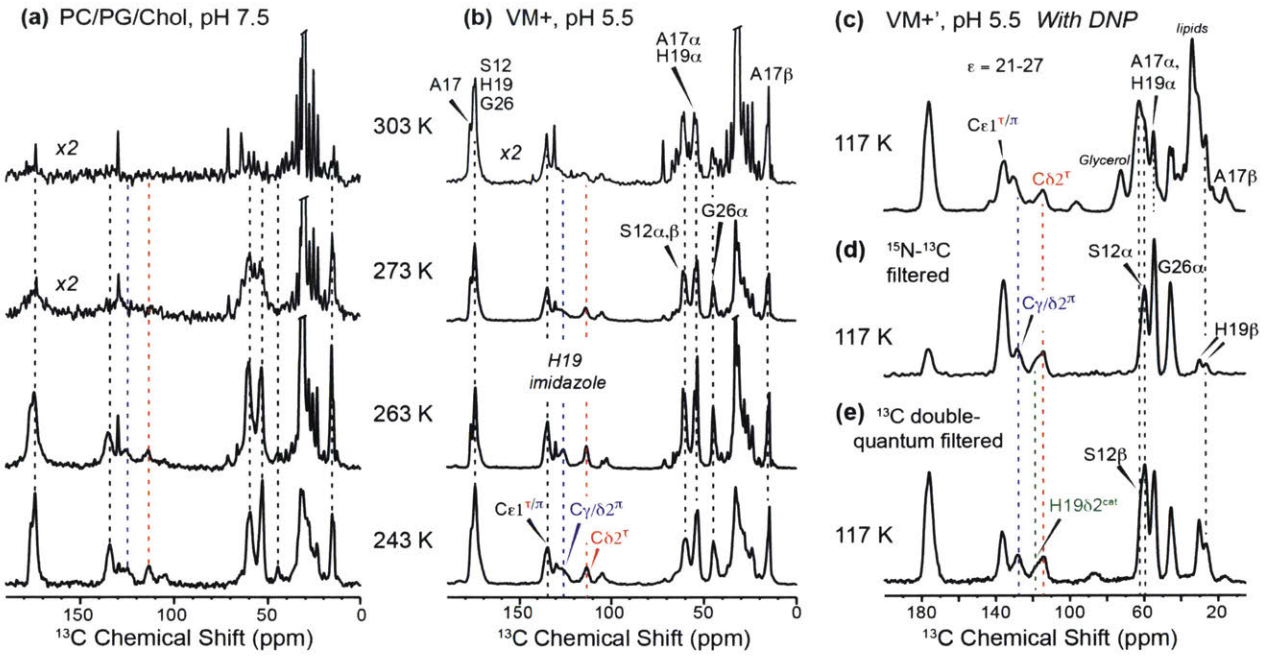

Figure 8.2 1D ^{13}C CP-MAS spectra of BM2(1-33) as a function of pH, temperature, and membrane composition. (a) BM2 in the PC/PG/Chol membrane at pH 7.5. (b) BM2 in the VM+ membrane at pH 5.5. The VM+ membrane immobilizes the peptide while the PC/PG/Chol membrane promotes peptide motion at high temperature. (c-e) DNP-enhanced ^{13}C spectra of BM2 at pH 5.5 in a partially deuterated VM+ membrane. (c) ^{13}C CP spectrum with MW on. The sensitivity is 21-27 times that of the MW-off spectrum (not shown). (d) ^{15}N-^{13}C dipolar filtered ^{13}C spectrum. (e) ^{13}C DQF spectrum.

Table 8.1 ^{13}C and ^{15}N chemicals shifts (ppm) of BM2(1-33)[a]

Residue	N	CO	Cα	Cβ	Cγ	Cδ2	Cε1	Nδ1	Nε2
S12, pH 7.5	119.1	174.6	59.4	60.9					
S12, pH 4.5	118.0	174.5	57.9	59.8					
A17, pH 7.5	123.8	176.7	53.1	15.7					
A17, pH 4.5	125.2	177.0	52.4	15.0					
H19, τ	118.9	174.7	54.8	29.7	135.6	113.6	134.3	250.9	162.6
H19, π	119.0	174.6	54.3	27.1	125.9	124.5	134.6	171.0	251.2
H19, cat1	118.8	174.4	58.0	28.9	134.4	116.4	135.9	-	171.1
H19, cat2	118.5	174.4	54.3	26.1	128.0	116.0	134.3	177.2	175.2
H19, cat3	118.5	174.4	57.2	25.3	126.4	117.3	133.2	175.7	174.8
G26, pH 7.5	106.2	174.1	45.2						
G26, pH 4.5	105.6	171.5	43.4						

[a] The chemical shifts of S12, A17, and G26 are obtained from the PC/PG/Chol sample data, while the H19 chemical are average values of the PC/PG/Chol and VM+ data. All ^{13}C chemical shifts were taken from 2D ^{13}C-^{13}C correlation experiments at low temperature, while ^{15}N chemical shifts were taken from 1D ^{15}N and 2D ^{15}N-^{13}C correlation spectra at low temperature.

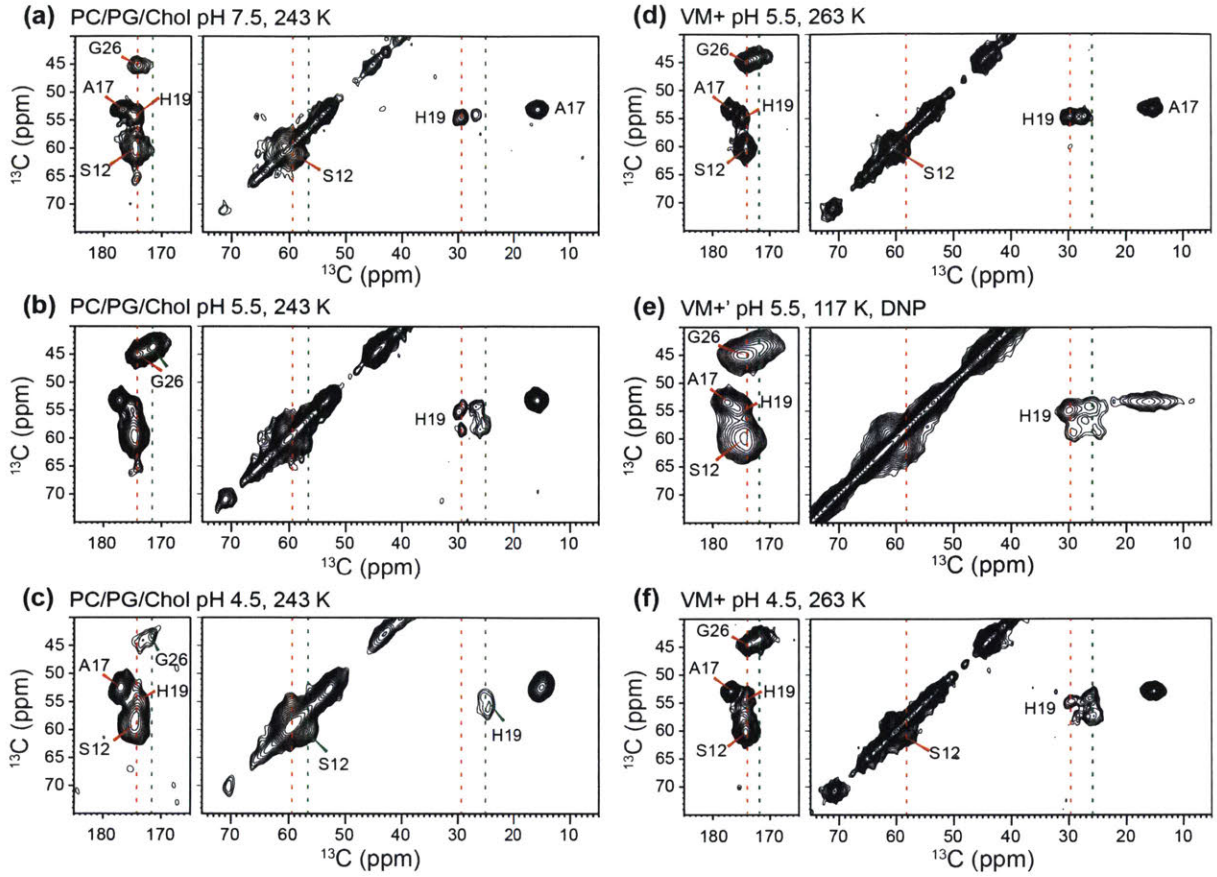

Figure 8.3 Two-dimensional ^{13}C-^{13}C correlation spectra of site-specifically labeled BM2(1-33) in different membranes and at different pH. (a) PC/PG/Chol at pH 7.5. (b) PC/PG/Chol at pH 5.5. (c) PC/PG/Chol at pH 4.5. (d) VM+ membrane at pH 5.5. (e) VM+' membrane at pH 5.5 with DNP. (f) VM+ membrane at pH 4.5.

8.4.2 pH- and Membrane-Dependent Structures of His19

One-dimensional ^{13}C spectra (**Fig. 8.2**), 2D ^{13}C-^{13}C correlation spectra (**Fig. 8.4**), and 2D ^{15}N-^{13}C correlation spectra (**Fig. 8.5**) provide detailed information on the chemical structure of the proton-selective residue, His19, under different pH and membrane compositions. In the aromatic region of the 1D spectra (**Fig. 8.2**), both the pH 7.5 PC/PG/Chol sample and the pH 5.5 VM+ sample show Cγ and Cδ2 chemical shifts of ~135 ppm and ~114 ppm, which are diagnostic of neutral histidines. The DNP-enhanced spectra show additional intensities at ~118 ppm, which can be assigned to Cδ2 of cationic histidine. Two-dimensional ^{13}C-^{13}C correlation spectra (**Fig. 8.4**) allowed unambiguous assignment of the ^{13}C signals of the various tautomeric and cationic states

of histidine. In the aliphatic region, the pH 7.5 PC/PG/Chol sample and the pH 5.5 VM+ sample both show two Cα-Cβ cross peaks, while the pH 5.5 PC/PG/Chol sample and the pH 4.5 VM+ sample exhibit four Cα-Cβ peaks. The nature of these Cα-Cβ peaks can be identified on the basis of their correlations with the side chain Cε1, Cδ2, and Cγ chemical shifts.[19,22,51] For the higher-pH spectra, the (54.8, 29.7) ppm cross peak can be assigned to the τ tautomer due to its correlation with the 113.5 ppm chemical shift of Cδ2, while the (54.3, 27.1) ppm cross peak can be assigned to the π tautomer because of its connectivity to the 124 ppm Cδ2 peak. In the lower-pH spectra, the τ tautomer Cα-Cβ peak is still present, while two cross peaks with Cβ chemical shifts of ~26 ppm can be assigned to cationic histidines, cat2 and cat3, on the basis of their correlations with Cγ and Cδ2 chemical shifts of ~127 ppm and ~117 ppm. The fourth cross peak at (58.0, 28.9) ppm is correlated with the same Cε1 and Cγ peaks as the τ tautomer, but also correlates with a 116.5-ppm Cδ2 peak, which thus reveals it to be a cationic histidine. This state is similar to the previously observed cat1 state of AM2 His37.[20] Finally, in the pH 4.5 PC/PG/Chol sample, the spectrum simplifies to only cationic histidine, with two partially overlapped Cα-Cβ cross peaks (**Fig. 8.4c**). These chemical shifts are summarized in **Table 8.1**.

These 2D ^{13}C-^{13}C correlation spectra show that the VM+ membrane produces the same set of His19 structures as the PC/PG/Chol membrane, but at 1-2 pH units lower. Thus, the negatively charged membrane facilitates proton association with His19. The τ and π tautomers that coexist in the pH 5.5 VM+ membrane have weak but clear cross peaks with each other, for example between the τ Cβ chemical shift and the π Cγ chemical shift at (30, 126) ppm and between π Cδ2 and τ Cδ2 at (125, 114) ppm (**Fig. 8.4d**). These intertautomer cross peaks indicate that both τ and π tautomers exist in the same tetramer instead of being separated into different channels.[23]

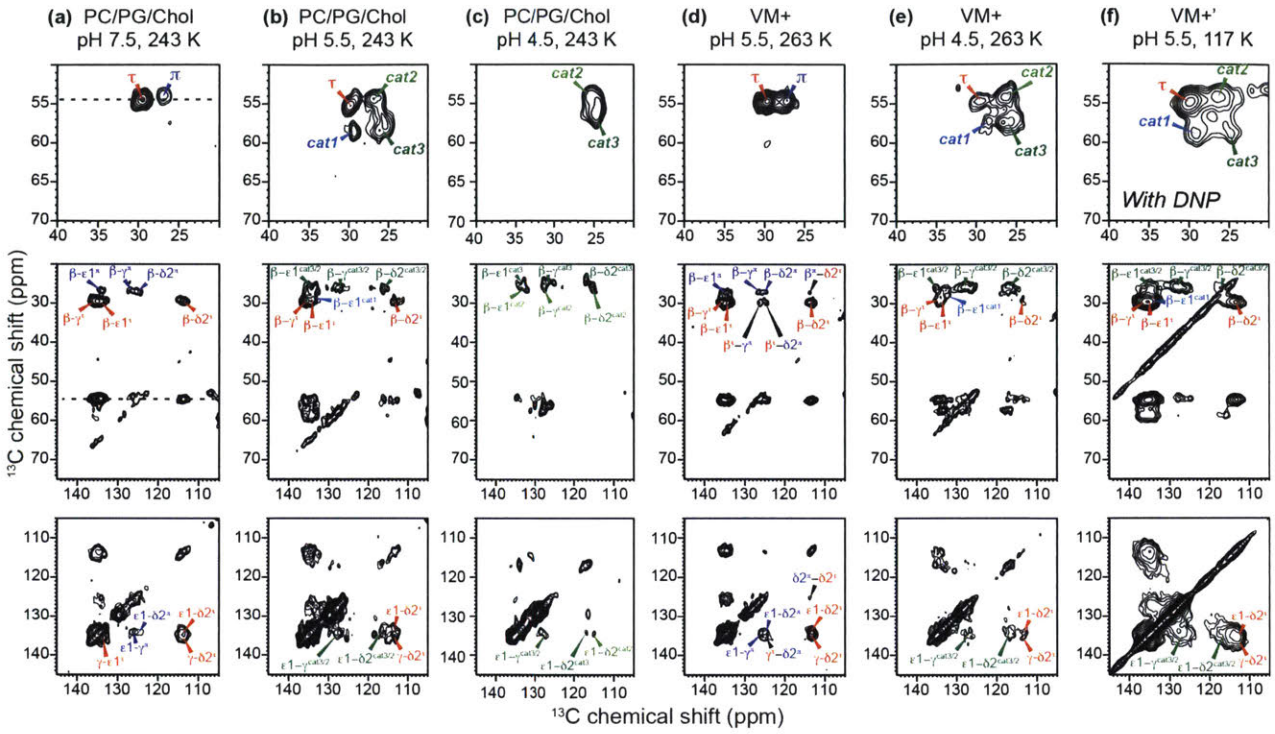

Figure 8.4 His19 regions of the 2D ^{13}C-^{13}C correlation spectra of BM2(1-33) at different pH and in different lipid membranes. The spectra in parts (a-c) were measured at 243 K on PC/PG/Chol bound peptide. (a) pH 7.5, (b) pH 5.5, (c) pH 4.5. The spectra in parts (d-e) were measured at 263 K on VM+ bound peptide at (d) pH 5.5 and (e) pH 4.5. (f) DNP-enhanced spectrum of BM2(1-33) in the d_{31}-VM+' membrane at pH 5.5. Spectra (a-c) were measured on a 400 MHz spectrometer under 7 kHz MAS, while spectra (d-e) were measured on an 800 MHz spectrometer with 14.5 kHz MAS. The DNP spectrum (f) was measured on a 400 MHz/263 GHz spectrometer at 117 K under 9 kHz MAS. The DARR mixing times were 50 or 100 ms in these spectra.

Two-dimensional ^{15}N-^{13}C HETCOR spectra (**Fig. 8.5**) provide complementary information about the pH-dependent structure distribution of His19. At pH 5.5, the backbone N-Cα cross peaks show relatively narrow linewidths of 1.5 ppm. Decreasing the pH to 4.5 increased the backbone linewidths, similar to the situation of the 2D ^{13}C-^{13}C correlation spectra. The aromatic region of the 2D spectrum is simple for the pH 5.5 sample, with two τ tautomer peaks and one π tautomer peak (**Fig. 8.5a**). But at pH 4.5 the 2D spectrum is much more complex, showing multiple cationic species (**Fig. 8.5b**). Four Nε2-Cδ2 cross peaks are resolved at ^{13}C chemical shifts of 113 - 118 ppm, and can be assigned to the τ tautomer and three cationic histidines, while two Nδ1-Cγ cross peaks are observed and can be assigned to cat2 and cat3.

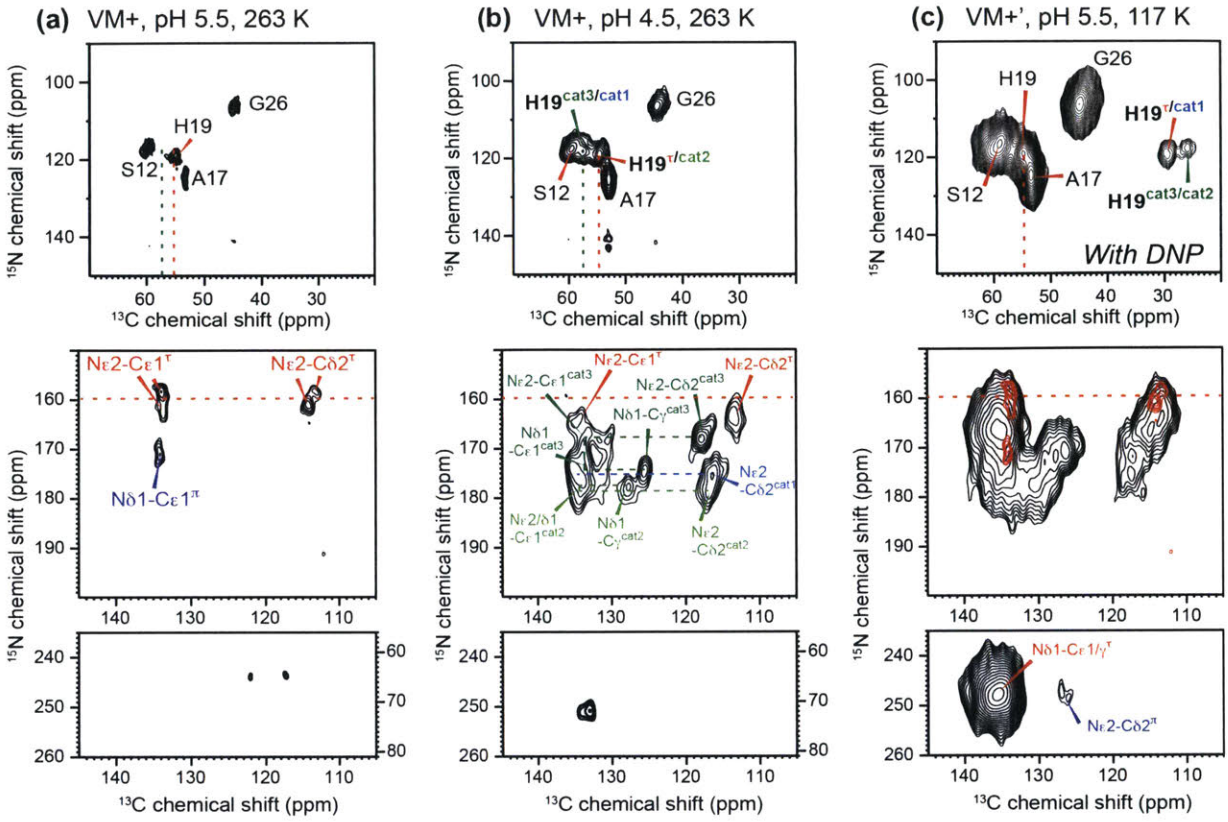

Figure 8.5 Two-dimensional ^{15}N-^{13}C correlation spectra of His19 in BM2(1-33). (a, b) BM2 in the VM+ membrane, measured on an 800 MHz spectrometer with 14.5 kHz MAS at 263 K. (a) pH 5.5. (b) pH 4.5. (c) BM2 at pH 5.5 in the d_{31}-VM+' membrane, measured on a 400 MHz/263 GHz DNP spectrometer under 9 kHz MAS at 117 K. Note the different neutral and cationic histidine distribution between high and low temperatures at pH 5.5, indicating temperature-induced pK_a shifts.

Figure 8.6 compares the pH-dependent 2D ^{13}C-^{13}C correlation spectra encoding the ^{13}C chemical shifts of His19 in BM2 and His37 in AM2. With decreasing pH, His19 progresses from a dual τ–π tautomeric mixture to a four-state neutral and cationic mixture. This change occurs from pH 7.5 to pH 5.5 in the PC/PG/Chol membrane and from pH 5.5 to pH 4.5 in the VM+ membrane. At sufficiently low pH, which is 4.5 for the PC/PG/Chol membrane and pH 4.0 for the VM+ membrane, a single cationic state is observed. The cytoplasmic-containing AM2(21-97) also resolved four cationic His37 species, cat1 to cat4 (**Fig. 8.6b**), with similar chemical shifts as those of BM2 His19; however, the four states do not occur at the same pH. These four species have been assigned to histidines in variously charged tetrads, +1 to +4, based on the pH at which they become

populated.[20] The shorter AM2 TM peptide also showed similar tautomeric chemical shifts (**Fig. 8.6c**), but fewer cationic species were found compared to the cytoplasmic-containing AM2. Importantly, the pH at which the multiple histidine states appear differs qualitatively between BM2 and AM2: BM2 concentrates a larger number of histidine species into a narrower pH range, which is around pH 4.5 for the VM+ membrane and about pH 5.5 for the PC/PG/Chol membrane. AM2(21-97) shows three cationic species at pH 5.4 while AM2(22-46) shows only two cationic states at pH 5.2. Since these AM2 and BM2 spectra were measured in the similar eukaryotic-mimetic lipid mixtures of VM+ and VM, the different pH dependences reflect real differences in the acid-dissociation equilibria of the histidines. Specifically, BM2 His19 retains neutral tautomers to lower pH than His37 in AM2, indicating lower pK_a's (*vide infra*).

8.4.3 DNP-Enhanced 2D Spectra at Cryogenic Temperature

Sensitivity enhancement by DNP allowed the observation of additional features in 2D ^{13}C-^{13}C and ^{15}N-^{13}C correlation spectra at pH 5.5 (**Fig. 8.4f, 8.5c**). Where previously only neutral τ and π tautomers were detected at 263 K, we now also observe the signals of cat1, cat2 and cat3, while the π tautomer cross peaks are below the detection limit (**Fig. 8.4f**). Spectral integration indicates that the cationic species represent 50-60% of the total intensities under the DNP experimental condition, while the higher-temperature 2D spectra at pH 5.5 do not show detectable cationic histidine intensities. Instead, the DNP spectrum at pH 5.5 is more similar to the high-temperature 2D spectrum at pH 4.5, which shows ~80% cationic intensities. This suggests that the effective pK_a's of the histidine are higher at cryogenic temperature than at high temperature. The 2D ^{15}N-^{13}C correlation spectrum (**Fig. 8.5c**) shows similar results, with the intensity pattern approaching the pH 4.5 spectrum at high temperature (**Fig. 8.5b**).

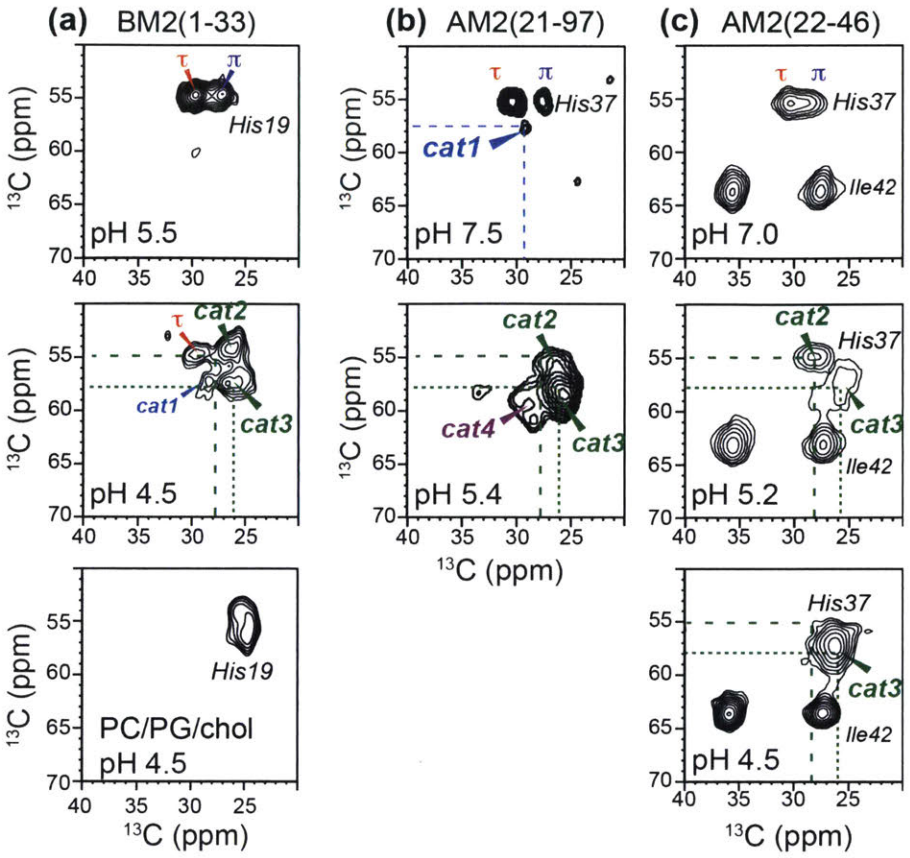

Figure 8.6 Comparison of His19 and His37 conformational distribution in BM2 and AM2 from 2D ^{13}C-^{13}C correlation spectra. All peptides and proteins were bound to eukaryotic-mimetic lipid membranes, except for the pH 4.5 spectrum of BM2, which was bound to the PC/PG/Chol membrane. Spectra were measured at moderate low temperatures (243 - 273 K) where the peptides and proteins are immobilized. (a) BM2(1-33) in VM+ membranes at pH 5.5 and pH 4.5, and BM2(1-33) in the PC/PG/Chol membrane at pH 4.5. (b) AM2(21-97) in the VM+ membrane at pH 7.5 and pH 5.4. (c) AM2 TM peptide (residues 22-46) in the VM membrane at pH 7.0, 5.2 and 4.5. BM2 His19 exhibits the largest number of coexisting species, at pH 4.5. The fact that neutral tautomers persist to lower pH in BM2 indicates that His19 protonates with lower and more clustered pK_a's. The spectrum of the pH 4.5 VM+ bound BM2 resembles the spectrum of the PC/PG/Chol bound BM2 at pH 5.5 in **Fig. 8.4b**, indicating the influence of the negatively charged lipid on the protonation equilibria.

8.4.4 His19 Proton Exchange Equilibria and Dynamics

To obtain quantitative information about the His19 protonation equilibria, we measured the 1D ^{15}N CP-MAS spectra of VM+ bound BM2 from pH 6.5 to pH 4.0. Since there are in principle four acid-dissociation constants for the tetrameric channel, the pK_a extraction requires a

minimum of four samples. The spectra were measured at 243 K where proton-transfer dynamics are suppressed. **Figure 8.7a** shows the expected progressive decrease of the 250 ppm unprotonated ^{15}N peak intensity with decreasing pH. As shown before,[19] the relative concentration of neutral and cationic histidines can be obtained from the intensity ratio I_{NH}/I_N. **Fig. 8.8b** and **Table 8.2** show that [His]/[HisH$^+$] decreases rapidly from 10.8 to 0.14 over the pH range 6.5-4.0 for the VM+ bound peptide. Fitting these values to equation (1) yielded pK_a's of $6.1 \pm 0.1, 5.7 \pm 0.1, 4.5 \pm 0.3$, and 4.2 ± 0.4. The two lowest pK_a's have the largest uncertainty, due to the fact that the unprotonated ^{15}N peak intensity is weak at pH 4.0; thus, the percentage of neutral histidines is difficult to determine with high precision. Alternative fits assuming only two distinct pK_a's can also agree with the data, and extraordinarily high precision and accuracy in the concentration ratios as well as the sample pH would be required to distinguish these different models. Nevertheless, the BM2 data differs from the recent studies of His37 in AM2(18-60) and in the cytoplasmic-containing AM2(21-97), whose ^{15}N spectra could not be adequately fit to four pK_a's.[20,53] Regardless of whether there are two or four distinct pK_a's, the observation that the two highest pK_a's cluster and the two lowest pK_a's cluster is unambiguous, and this translates to charged-tetrad population curves that have a high percentage of the +2 state over a relatively wide pH range, preceded by the persistence of the fully neutral (0 charge) and +1 tetrads above pH 6, and followed by quick onsets of the +3 and +4 channels below about pH 4.5 (**Fig. 8.8c**).

Table 8.2 BM2(1-33) His19 Imidazole ^{15}N Intensities and Neutral to Cationic Histidine Concentration Ratios

pH	I_{NH}/I_N	κ	[His]/[HisH$^+$]
4.0	21.7 ± 10.9	1.44 ± 0.04	0.14 ± 0.07
4.5	7.0 ± 0.9	1.33 ± 0.04	0.47 ± 0.06
5.5	3.1 ± 0.3	1.35 ± 0.03	1.54 ± 0.15
6.5	1.6 ± 0.2	1.35 ± 0.04	10.8 ± 1.4

Incorporating BM2(1-33) into the anionic PC/PG/Chol membrane caused a shifted pH dependence of the ^{15}N spectral intensities: the pH 7.5 PC/PG/Chol spectrum resembles the pH 5.5 VM+ spectrum while the pH 5.5 PC/PG/Chol spectrum approaches the pH 4.5 VM+ spectrum (**Fig. 8.7b**). This is consistent with the 2D spectra that indicate a shift of the His19 protonation equilibria to higher pH in the anionic membrane compared to the neutral membrane.

To investigate the proton-transfer kinetics, we measured ^{15}N CP spectra at high temperature (**Fig. 8.7c**). Since BM2 tetramers undergo intermediate-timescale motion in the PC/PG/Chol membrane, high-temperature intensities can only be observed for VM+ bound peptide. At 303-308 K, the pH 5.5 VM+ sample retained the neutral tautomer peaks at 251 ppm and 160-170 ppm, but in addition a broad band of intensities between 170 and 250 ppm emerged, suggesting chemical exchange of the imidazole nitrogens with a distribution of equilibrium constants. Most importantly, at pH 4.5, the spectrum exhibits an exchange peak at 213 ppm and additional intensities at ~185 ppm. These intermediate ^{15}N chemical shifts are identical to the values seen for His37 in AM2, and can be assigned to Nε2 and Nδ1 chemical exchange among the τ tautomer, π tautomer, and cationic histidine.[19,22] Thus, the chemical-exchange equilibria among the three histidine states are conserved between AM2 and BM2.

8.4.5 BM2 Channel Hydration from Water-Protein 2D Correlation Experiments

To investigate whether BM2 channel hydration differs from that of AM2, we measured 2D water-peptide ^{1}H-^{13}C correlation spectra as a function of the ^{1}H spin-diffusion mixing time. **Fig. 8.9a** shows a representative 2D spectrum of BM2(1-33) in the PC/PG/Chol membrane at pH 7.5, measured with a ^{1}H mixing time of 50 ms. Spectra measured at a shorter mixing time of 4 ms give information about the initial spin-diffusion rate from water to the peptide. At pH 7.5 (**Fig. 8.9b**), the intensity of the short-mixing spectrum is 20-30% of the long-mixing spectrum for the Cα and Cβ peaks, while the His19 aromatic signals have higher intensities of > 40%. At acidic pH, the 4 ms Cα and Cβ peak intensities increase compared to those for the higher pH sample, indicating faster water-protein polarization transfer. The His19 side chain intensities are the highest, showing 80-90% of the equilibrium intensities. Thus, BM2 is much more hydrated at low pH than at high pH, consistent with an open channel.

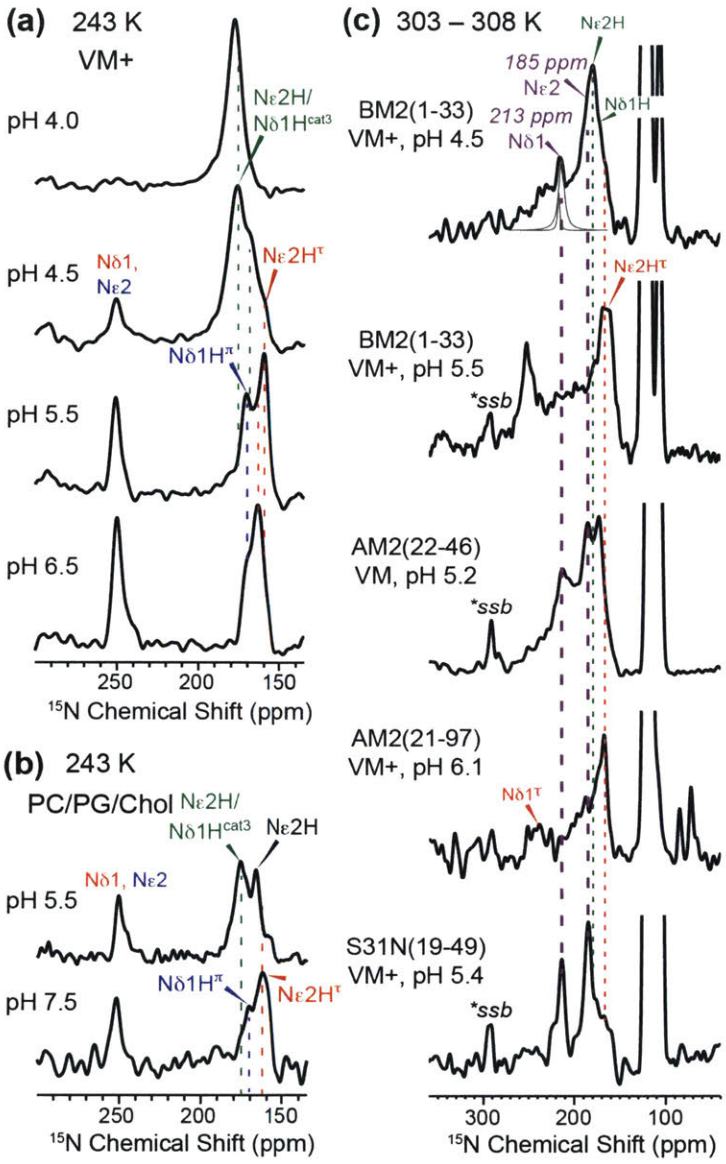

Figure 8.7 One-dimensional ^{15}N CP spectra of BM2(1-33) as a function of pH, membrane composition and temperature. (a) Spectra of the VM+ bound BM2 from pH 4.0 to pH 6.5 at 243 K. (b) Spectra of PC/PG/Chol-bound BM2 at pH 5.5 and pH 7.5 at 243 K. (c) Comparison of high-temperature (303 - 308 K) ^{15}N spectra of BM2 and AM2 at acidic pH. An ^{15}N exchange peak is detected at ~213 ppm at pH 4.5 for BM2, at pH 5.2 for AM2-TM, and at pH 5.4 in the S31N mutant of AM2-TM. The exchange-averaged chemical shifts are the same in all M2 samples, but the exchange linewidths differ. The BM2 exchange peak is fit (gray line) to give a line width of 400 ± 140 Hz.

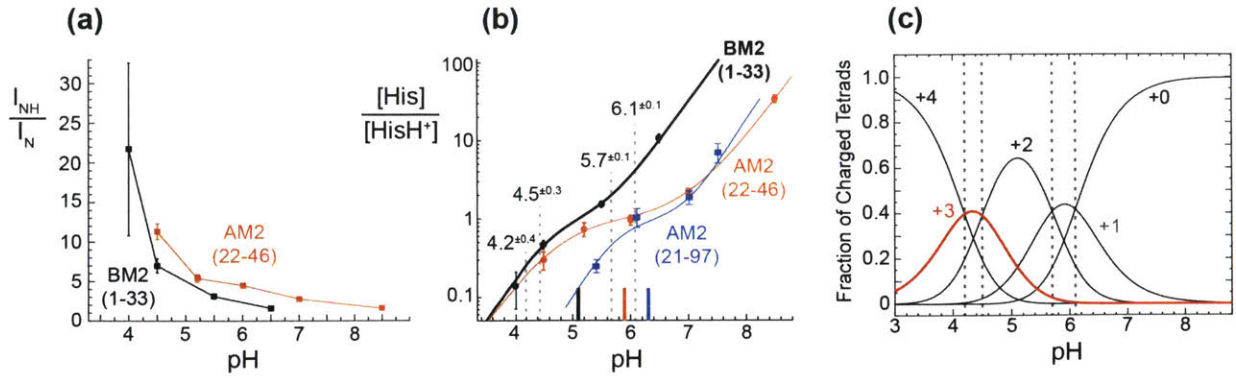

Figure 8.8 pK_a extraction of His19 in BM2(1-33). (a) NH to N intensity ratios as a function of pH. (b) Neutral-to-cationic histidine concentration ratios as a function of pH. The BM2 data (black) are compared with previously measured AM2 TM peptide data[54] (orange) and AM2(21-97) data (blue). The neutral histidine concentration in BM2 is higher than that of AM2 at similar pH . The extracted pK_a's for BM2 are 6.1, 5.7, 4.5 and 4.2, whose average is lower than that of AM2 constructs. The average pK_a's of the three M2 samples are indicated as solid lines at the bottom. (c) Populations of charged tetrads of His19 in BM2 as a function of pH. The intercepts of adjacent population curves correspond to the pK_a's.

Figure 8.9e,f summarizes the S/S_0 ratios of the resolved ^{13}C signals of BM2(1-33). For each membrane, the water cross peaks are higher at low pH than at high pH. Between the two lipid membranes, the PC/PG/Chol bound BM2 exhibits higher water cross peaks than the VM+ bound peptide at the same pH, indicating that the anionic membrane facilitates channel hydration. Thus, the viscous and neutral VM+ membrane contains less hydrated BM2 channels than the PC/PG/Chol membrane. Among the four labeled residues, the His19 side chain has the highest water cross peaks, consistent with the polar and pore-facing nature of this residue. Interestingly, S12 exhibits a large pH-dependent change in the water cross-peak intensity. In the PC/PG/Chol membrane, the S/S_0 values changed from 0.29 ± 0.04 at pH 7.5 to 0.42 ± 0.04 at pH 5.5. Decreasing the pH by 1 unit in the VM+ membrane causes the S/S_0 values to increase from 0.14 ± 0.03 to 0.38 ± 0.03. The latter change is larger than that of all other residues measured so far in AM2 and BM2, including S31 in AM2 (**Fig. 8.9h**), indicating that the pore-facing serine residues in BM2 play a prominent role in channel hydration, which should promote H^+ relay to the HxxxW motif.

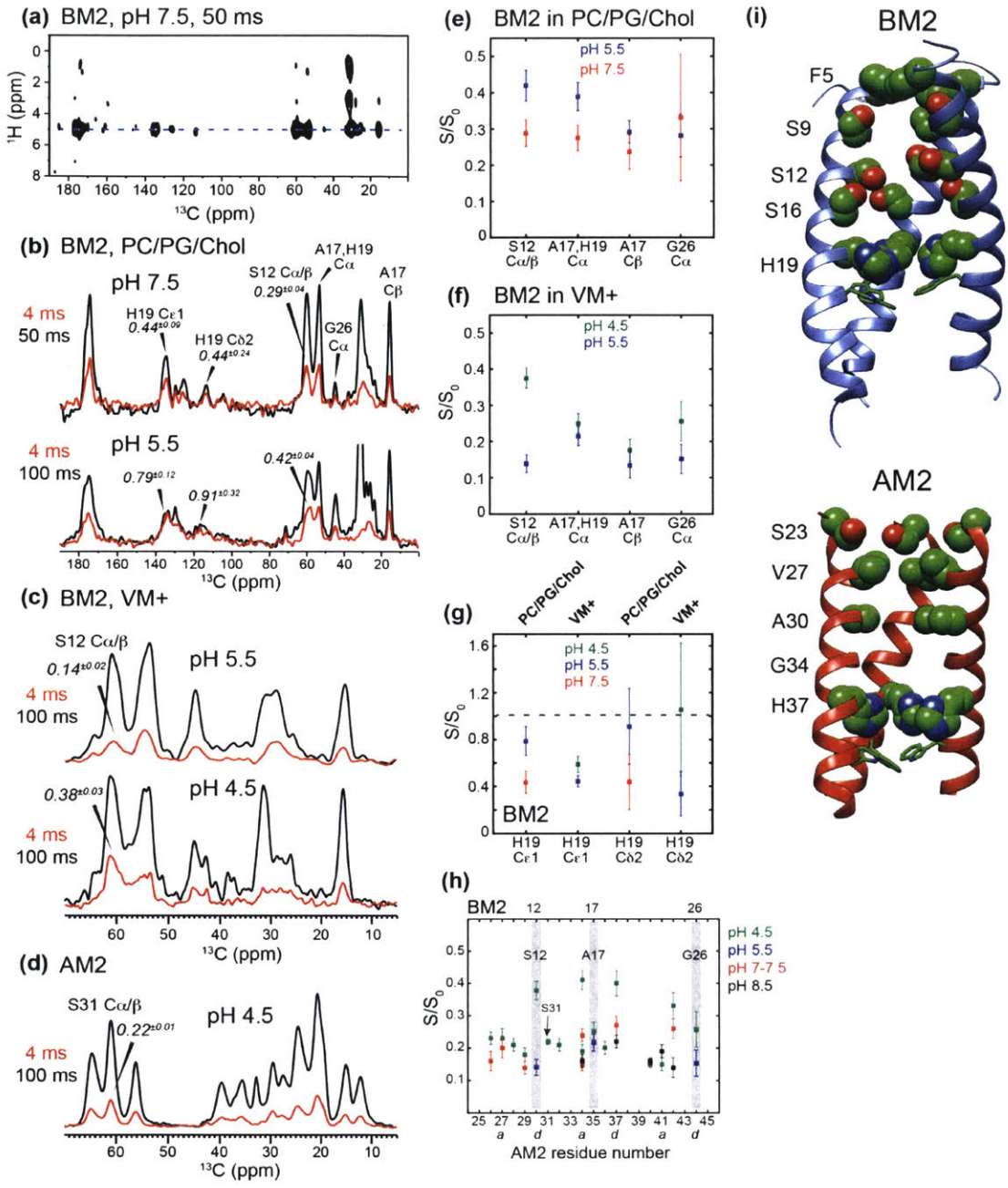

Figure 8.9 Two-dimensional ^{1}H-^{13}C HETCOR spectra of membrane-bound BM2(1-33) to probe channel hydration. (a) Representative 2D spectrum of PC/PG/Chol bound peptide at pH 7.5, measured with a ^{1}H spin diffusion mixing time of 50 ms. (b) Water cross sections of BM2(1-33) between 4 ms and 50 or 100 ms for the pH 7.5 and pH 5.5 PC/PG/Chol samples measured at 263 K. The S/S_0 values are indicated for H19 and S12. (c) Water cross sections of the aliphatic region of the VM+ bound BM2 at pH 5.5 and pH 4.5, showing the large increase of the initial buildup of the S12-water cross-peak intensity at lower pH. (d) Water cross section of the aliphatic region of VM-bound AM2 at pH 4.5, showing that the S31 S/S_0 value is lower than that of S12 in BM2. (e) Initial buildup (S/S_0 values) at

high and low pH for PC/PG/Chol-bound BM2. (f) S/S_0 values of VM+ bound BM2 at pH 5.5 and pH 4.5. (g) S/S_0 values of the His19 side chain in the two membranes. (h) S/S_0 values of the Cα sites of AM2 residues and of the BM2 residues S12, A17, and G26 (shaded bars). S12 in BM2 shows the largest low-pH induced increase of the S/S_0 value among all labeled residues of the two peptides. (i) Comparison of the solution NMR structure of BM2 (top, PDB: 2KIX) and AM2 (bottom, PDB: 2KQT) TM domains.

8.5 Discussion

The data shown here give the first detailed structural and dynamical information about the proton-conducting heart of BM2 in lipid bilayers. The chemical shifts of the four labeled residues indicate that the BM2 TM peptide is α-helical in a range of pH and in two different membranes. Although the number of labeled residues is too small to permit more detailed structural conclusions, it is nevertheless interesting that the three non-histidine residues change their chemical shifts at low pH in a direction that corresponds to less ideal α-helical conformations. This trend is opposite that of the AM2 TM peptide, which exhibits more ideal α-helical chemical shifts, and straight helices, at acidic pH.[55] The nonideal helical chemical shifts seen in BM2 may be related to the coiled coil structure found for DHPC-bound BM2, even though the solution NMR structure was solved at pH 7.5.[12]

The pH-dependent ^{15}N spectra and 2D correlation spectra indicate that His19 protonates at significantly lower pH than His37 in both the TM and cytoplasmic-containing constructs of AM2. The average pK_a of His19 in BM2-TM is 5.1 (**Table 8.3**). In comparison, the average pK_a's of His37 in AM2(22-46) and AM2(21-97) are 5.9 and 6.3, respectively, in similar virus-mimetic membranes.[19,20] The earliest measurement of His37 pK_a in AM2(22-46) was conducted in the significantly different model membrane DMPC/DMPG, and found a much higher average pK_a of ~6.9.[24] In another recent study, the intermediate construct AM2(18-60), which includes the TM helix and the amphipathic helix, was measured in the negative-curvature membrane formed by diphytanoylphosphocholine.[56,57] This study resolved two pK_a's with an average of 6.1.[53] Therefore, despite the significant variations in the protein construct lengths and membrane compositions, the His37 pK_a's in AM2 measured under all conditions so far are higher than the BM2 His19 pK_a's found here. The His19 titration curve parallels the titration curve of His37 in the cytoplasmic-

containing AM2(21-97) but is shifted by ~1.2 pH unit lower (**Fig. 8.8b**). Compared to the AM2 TM peptide, the BM2 titration curve drops more steeply at low pH. Overall, the His19 tetrads remain predominantly in low charged states of +2, +1 and 0 until about pH 5, below which the +3 and +4 tetrad populations surge (**Fig. 8.8c**). This result is found for the VM+ membrane, which is the membrane used in two of the previous four AM2 studies; thus, the pK_a decrease reflects real differences in the protonation equilibria of His19 in BM2 and His37 in AM2.

The lower pK_a's of His19 were surprising, because the BM2 channel pore is lined with polar residues such as S9, S12, and S16 (**Fig. 8.1**), which would be expected to facilitate proton relay to His19 and thus stabilize the cationic state of His19. In general, altered equilibrium constants imply altered structures; thus, the BM2 TM helix structure and structural equilibrium must differ in crucial ways from the AM2 structure to account for this pK_a decrease. The solution NMR structure of micelle-bound BM2(1-33) shows a coiled coil (**Fig. 8.9i**) while AM2 in the same micelles exhibits straighter helices. This secondary structure difference, if verified to persist in the lipid bilayer, may affect the proton-transfer equilibria at His19. Since there is yet no high-resolution bilayer-bound structure of BM2, we focus our consideration on the equality $K_a = k_{off}/k_{on}$ between the acid-dissociation constant and the ratio of the first-order proton-dissociation rate constant k_{off} and the second-order proton-association rate constant k_{on}. The lower pK_a's or larger K_a's indicate larger k_{off} and/or smaller k_{on}. Information about the proton-exchange kinetics is partly contained in the high-temperature His19 ^{15}N spectra (**Fig. 8.7c**), which show a 213 ppm exchange peak with a full width at half-maximum of 400 ± 140 Hz. In comparison, the exchange peak of His37 in the AM2 TM peptide has a larger linewidth of 640 ± 70 Hz. Since proton dissociation is the rate-limiting step in proton transfer, the narrower His19 exchange peak suggests a larger k_{off} than that of His37 in AM2. Although k_{on} may be increased by the serine triplet in the N-terminal half of the TM helix, the k_{off} may increase more, thus shifting the equilibrium towards the neutral state. This interpretation of a preferentially increased k_{off} is consistent with liposome assays that indicate a larger H^+ flux of BM2(1-33) compared to AM2(18-60).[12]

Table 8.3 Comparison of Histidine pK_a's in Influenza A and B M2 Proteins in Various Lipid Membranes

M2 constructs	Phospholipid membrane	His19 and His37 pK_a's	Average pK_a
BM2(1-33)	POPC, POPE, SM, cholesterol	6.1, 5.7, 4.5, 4.2	5.1
AM2(22-46)[54]	DPPC, DPPE, SM, cholesterol	7.6, 6.8, 4.9, 4.2	5.9
AM2(21-97)	POPC, POPE, SM, cholesterol	7.1, 5.4	6.3
AM2(22-46)	DMPC, DMPG	8.2, 8.2, 6.3, < 5.0	<6.9
AM2(18-60)	DPhPC	7.6, 4.5	6.1

What might be the structural basis for an increased proton-dissociation rate constant for His19? We propose that the second titratable histidine, His27, C-terminal to the HxxxW motif and one helical turn away from Trp23, may speed up proton release from the His19-Trp23 pair. A UV resonance Raman study showed that His27 has a higher pK_a than His19,[58] indicating that His27 is more cationic than His19 at the same pH and thus is consistent with this hypothesis. Mutation of His27 to Ala was found to decrease the H^+ conductance by ~25% compared to the wild-type, indicating that His27 plays an active role in H^+ conduction through the BM2 channel. Importantly, this second histidine is absent in the AM2 TM domain, whose equivalent position harbors an Arg45, which is constitutively charged under the full pH range of the channel. Thus, this single amino acid difference may explain the observed destabilization of the cationic state of His19 or the lowering of the pK_a's.

At high temperature, the exchange-averaged ^{15}N chemical shifts (213 ppm and ~185 ppm) of BM2 are the same as for AM2. We have previously shown that this interconversion among different histidine structures is most observable in low charged tetrads,[22] because they contain a high concentration of neutral histidine, and correspond to a concentration ratio of 2:1:1 for the interconverting τ tautomer, π tautomer, and cationic histidine. Thus, the resolvable ^{15}N chemical exchange peak does not reflect the full population distribution, and an altered histidine-water proton-transfer equilibrium at low temperature can coexist with a conserved histidine interconversion equilibrium at high temperature.

The above quantified pK_a's are obtained from BM2 bound to the neutral and relatively viscous VM+ membrane. The membrane composition also affects the relative concentrations of neutral and cationic histidines. The ^{15}N spectra of the peptide in the anionic and more fluid PC/PG/Chol membrane clearly indicate that His19 protonates at higher pH in this membrane. We

attribute this change to increased local proton concentrations and enhanced protein conformational motions necessary for proton binding and release in the negatively charged and fluid PC/PG/Chol membrane. If the former accounts for the entire extent of change in the cationic/neutral histidine ratios, then the true equilibrium constant would be unaffected because the higher local H^+ density rather than the average sample pH should be used in considering the equilibrium constant. The importance of electrostatic charges on the H^+ transfer equilibria is also observed in a recent study of the cytoplasmic-containing AM2, which shows higher pK_a's for His37 than the TM peptide. This result was attributed to the anionic nature of the cytoplasmic domain,[20] which should elevate the local proton concentrations.

The NMR observed reduction of BM2 His19 pK_a's compared to AM2 His37 differs from UV resonance Raman data, which found that AM2 His37 has an average pK_a of 5.7[27] while BM2(3-33) exhibits a midpoint of transition at pH ~6.5 for the pH-dependent quenching of W23 fluorescence emission by His19.[58] These resonance Raman data were obtained from POPE/POPS (1:1) bound peptides. Two possible reasons could explain this discrepancy. First, the negatively charged POPE/POPS membrane may affect the BM2 and AM2 protonation equilibria differently in comparison to the neutral VM+ membranes used in the solid-state NMR experiments. Second, fluorescence quenching can be caused by changes in the environmental polarity and mobility of the Trp side chain, in addition to the His-Trp cation-π interaction; thus, the interpretation of the resonance Raman spectra has inherent uncertainty. In comparison, the ^{15}N NMR chemical shifts are unambiguous indicators of the chemical structure of histidine.

The water-peptide 2D correlation spectra show increased hydration at low pH than at high pH for BM2, similar to the AM2 behavior.[46] The negatively charged PC/PG/Chol membrane at pH 7.5 gives higher water cross peaks than the VM+ membrane at pH 5.5, indicating that the VM+ membrane causes a tighter and less hydrated channel. The increased pore hydration at more acidic pH should facilitate His19 protonation by delivering protons through the water molecules rapidly to histidine. Interestingly, the VM+ bound S12 exhibits the largest pH-dependent increase of the water cross-peak intensity among all residues measured so far in both BM2 and AM2. This acid-induced hydration increase is not solely due to the pH dependence of chemical exchange between the serine hydroxyl group and water, because S31 in AM2 does not show a particularly high S/S_0

value at low pH, and S12 at pH 5.5 has similar water cross-peak intensities as the nonexchangeable A17 and G26. It is known that the chemical exchange rate of serine OH is ~900 s^{-1} at pH 7 and 35°C, which is 2-fold smaller than the proton exchange rate of imidazole NH (1700 s^{-1}).[59] Yet, here S12 Cα has higher S/S_0 than H19 Cα at pH 4.5 (**Fig. 8.9f**). Thus, S12 hydration is truly increased at low pH, suggesting that this residue is important for mediating proton relay to the HxxxW motif.

The DNP spectra at cryogenic temperature show moderate differences in the pH equilibria of His19 from the high-temperature data. For the pH 5.5 sample, the concentration of cationic histidine increased to 40-50%, while at 263 K mainly neutral histidines are observed at the same prepared pH. We attribute this increased cationic concentration at low temperature to the different temperature dependences of the buffer and the imidazole pK_a's. The citrate buffer pK_a has a linearly extracted temperature coefficient $d(pK_a)/dT$ of -0.01,[60,61] while the imidazole pK_a has a larger temperature coefficient of -0.02. Thus, as the sample temperature decreases, the citrate pK_a should increase but to a smaller extent than the imidazole pK_a. This means that, at low temperature, the imidazole sidechain will be more readily protonated by the buffer. The thermodynamic parameters for the ionization of buffer ions and imidazoles are not known to very low temperatures, and the exact freezing temperature of the channel water is also unknown. However, the relative trend that the imidazole pK_a has a more negative temperature coefficient than the citrate pK_a's is reliable, and favors protonation of His19 at low temperature. A potential acid-base equilibrium change between cryogenic temperature and ambient temperatures should thus be taken into account in DNP NMR experiments of pH-sensitive proteins and other biomolecules in buffered solution.

8.6 Conclusions

In its global conformational and dynamical behavior, BM2(1-33) is similar to the AM2 TM peptide: the tetrameric channel is α-helical and undergoes intermediate-timescale motion in low-viscosity membranes at physiological temperature. However, important differences are found at the proton-selective histidine in the HxxxW motif, and in the pore-lining residues leading to this motif. His19 in BM2 remains neutral down to lower pH than His37 AM2, and cationic His19 appears in a narrower pH range than His37 in AM2. Thus, His19 in the tetrameric BM2 channel

protonates with lower and more clustered pK_a's. Quantitative analysis of the ^{15}N spectra yielded pK_a values of 6.1, 5.7, 4.5, and 4.2, which are about 1 pH unit lower than His37 in AM2. We propose that the altered pK_a's result from the presence of a second titratable histidine, C-terminal to His19, in BM2. This second histidine is absent in AM2 and likely increases the proton-dissociation rate constant of His19. This model is consistent with the narrower His19 chemical exchange peak compared to AM2 His37 and with H^+ flux and mutagenesis data. Similar to AM2, BM2 channels are more hydrated at acidic pH than at high pH, but compared to AM2, S12 in BM2 exhibits the largest acid-induced increase in the water cross-peak intensity, consistent with the model that the Ser triplet lining the BM2 pore facilitates proton relay to His19 by increasing pore hydration. We found that the lipid membrane also plays a significant role in proton-transfer dynamics and channel hydration: anionic membranes facilitate His19 protonation at high pH and increase the channel hydration compared to neutral membranes. These results give rich insights into how the amino acid sequence and the membrane environment affect the functional structure and dynamics of this family of viral proton channels.

8.7 Acknowledgements

This work is supported by NIH grant GM088204 to M.H. The authors would like to thank Dr. Ivan Sergeyev (Bruker Biospin) for help with measuring the DNP NMR spectra.

8.8 References

[1] L. Brammer, K. Kniss, S. Epperson, L. Blanton, D. Mustaquim, C. Steffens, T. D'Mello, A. Perez, R. Dhara, S. S. Chaves, A. A. Elal, L. Gubareva, T. Wallis, X. Xu, J. Villanueva, J. Bresee, N. Cox, L. Finelli and F. Havers. "Influenza Activity — United States, 2012–13 Season and Composition of the 2013–14 Influenza Vaccine." *Morbidity and Mortality Weekly Report, Centers for Disease Control and Prevention* **2013**.

[2] M. Koutsakos, T. Nguyen, W. Barclay and K. Kedzierska. "Knowns and Unknowns of Influenza B Viruses." *Future Microbiol.* **2016**, 11, 119-135.

[3] S. D. Cady, K. Schmidt-Rohr, J. Wang, C. S. Soto, W. F. DeGrado and M. Hong. "Structure of the Amantadine Binding Site of Influenza M2 Proton Channels in Lipid Bilayers." *Nature* **2010**, 463, 689-692.

[4] S. D. Cady and M. Hong. "Amantadine-Induced Conformational and Dynamical Changes of the Influenza M2 Transmembrane Proton Channel." *Proc. Nat. Acad. Sci. U.S.A.* **2008**, 105, 1483-1488.

[5] A. L. Stouffer, R. Acharya, D. Salom, A. S. Levine, L. Di Costanzo, C. S. Soto, V. Tereshko, V. Nanda, S. Stayrook and W. F. DeGrado. "Structural Basis for the Function and Inhibition of an Influenza Virus Proton Channel." *Nature* **2008**, 451, 596-599.

[6] L. H. Pinto, G. R. Dieckmann, C. S. Gandhi, C. G. Papworth, J. Braman, M. A. Shaughnessy, J. D. Lear, R. A. Lamb and W. F. DeGrado. "A Functionally Defined Model for the M2 Proton Channel of Influenza A Virus Suggests a Mechanism for its Ion Selectivity." *Proc. Natl. Acad. Sci. U.S.A.* **1997**, 94, 11301-11306.

[7] M. Hong, K. J. Fritzsching and J. K. Williams. "Hydrogen-Bonding Partner of the Proton-Conducting Histidine in the Influenza M2 Proton Channel Revealed from ^{1}H Chemical Shifts." *J. Am. Chem. Soc.* **2012**, 134, 14753-14755.

[8] J. A. Mould, R. G. Paterson, M. Takeda, Y. Ohigashi, P. Venkataraman, R. A. Lamb and L. H. Pinto. "Influenza B Virus BM2 Protein has Ion Channel Activity that Conducts Protons Across Membranes." *Dev. Cell* **2003**, 5, 175-184.

[9] L. H. Pinto and R. A. Lamb. "The M2 Proton Channels of Influenza A and B Viruses." *J. Biol. Chem.* **2006**, 281, 8997-9000.

[10] Y. Tang, F. Zaitseva, R. A. Lamb and L. H. Pinto. "The Gate of the Influenza Virus M2 Proton Channel is Formed by a Single Tryptophan Residue." *J. Biol. Chem.* **2002**, 277, 39880-39886.

[11] C. Ma, C. S. Soto, Y. Ohigashi, A. Taylor, V. Bournas, B. Glawe, M. K. Udo, W. F. DeGrado, R. A. Lamb and L. H. Pinto. "Identification of the Pore-Lining Residues of the BM2 Ion Channel Protein of Influenza B Virus." *J. Biol. Chem.* **2008**, 283, 15921-15931.

[12] J. Wang, R. M. Pielak, M. A. McClintock and J. J. Chou. "Solution Structure and Functional Analysis of the Influenza B Proton Channel." *Nat. Struct. Mol. Biol.* **2009**, 16, 1267-1271.

[13] C. Ma, A. L. Polishchuk, Y. Ohigashi, A. L. Stouffer, A. Schön, E. Magavern, X. Jing, J. D. Lear, E. Freire, R. A. Lamb, W. F. DeGrado and L. H. Pinto. "Identification of the Functional Core of the Influenza A Virus A/M2 Proton-Selective Ion Channel." *Proc. Natl. Acad. Sci. U.S.A.* **2009**, 106, 12283-12288.

[14] M. Hatta, H. Goto and Y. Kawaoka. "Influenza B Virus Requires BM2 Protein for Replication." *J. Virol.* **2004**, 78, 5576-5583.

[15] T. Betakova and E. Kollerova. "pH Modulation Activity of Ion Channels of Influenza A, B, and C Viruses." *Acta Virologica* **2006**, 50, 187-193.

[16] T. Betakova and A. J. Hay. "Comparison of the Activities of BM2 Protein and its H19 and W23 Mutants of Influenza B Virus with Activities of M2 Protein and its H37 and W41 Mutants of Influenza A Virus." *Arch. Virol.* **2009**, 154, 1619-1624.

[17] M. Imai, S. Watanabe, A. Ninomiya, M. Obuchi and T. Odagiri. "Influenza B Virus BM2 Protein is a Crucial Component for Incorporation of Viral Ribonucleoprotein Complex into Virions During Virus Assembly." *J. Virol.* **2004**, 78, 11007-11015.

[18] M. Imai, K. Kawasaki and T. Odagiri. "Cytoplasmic Domain of Influenza B Virus BM2 Protein Plays Critical Roles in Production of Infectious Virus." *J. Virol.* **2008**, 82, 728-739.

[19] F. Hu, K. Schmidt-Rohr and M. Hong. "NMR Detection of pH-Dependent Histidine-Water Proton Exchange Reveals the Conduction Mechanism of a Transmembrane Proton Channel." *J. Am. Chem. Soc.* **2012**, 134, 3703-3713.

[20] S. Y. Liao, Y. Yang, D. Tietze and M. Hong. "The Influenza M2 Cytoplasmic Tail Changes the Proton-Exchange Equilibria and the Backbone Conformation of the Transmembrane Histidine Residue to Facilitate Proton Conduction." *J. Am. Chem. Soc.* **2015**, 137, 6067-6077.

[21] Y. Miao, R. Fu, H. X. Zhou and T. A. Cross. "Dynamic Short Hydrogen Bonds in Histidine Tetrad of Full-Length M2 Proton Channel Reveal Tetrameric Structural Heterogeneity and Functional Mechanism." *Structure* **2015**, 23, 1-9.

[22] J. K. Williams, D. Tietze, J. Wang, Y. Wu, W. F. DeGrado and M. Hong. "Drug-Induced Conformational and Dynamical Changes of the S31N Mutant of the Influenza M2 Proton Channel Investigated by Solid-State NMR." *J. Am. Chem. Soc.* **2013**, 135, 9885-9897.

[23] F. Hu, W. Luo and M. Hong. "Mechanisms of Proton Conduction and Gating in Influenza M2 Proton Channels from Solid-State NMR." *Science* **2010**, 330, 505-508.

[24] J. Hu, R. Fu, K. Nishimura, L. Zhang, H. X. Zhou, D. D. Busath, V. Vijayvergiya and T. A. Cross. "Histidines, Heart of the Hydrogen Ion Channel from Influenza A Virus: Toward an Understanding of Conductance and Proton Selectivity." *Proc. Natl. Acad. Sci. U.S.A.* **2006**, 103, 6865-6870.

[25] J. K. Williams, Y. Zhang, K. Schmidt-Rohr and M. Hong. "pH-Dependent Conformation, Dynamics, and Aromatic Interaction of the Gating Tryptophan Residue of the Influenza M2 Proton Channel from Solid-State NMR." *Biophys. J.* **2013**, 104, 1698-1708.

[26] K. Nishimura, S. Kim, L. Zhang and T. A. Cross. "The Closed State of a H^+ Channel Helical Bundle Combining Precise Orientational and Distance Restraints from Solid State NMR." *Biochemistry* **2002**, 41, 13170-13177.

[27] A. Okada, T. Miura and H. Takeuchi. "Protonation of Histidine and Histidine-Tryptophan Interaction in the Activation of the M2 Ion Channel from Influenza A Virus." *Biochemistry* **2001**, 40, 6053-6060.

[28] M. Sharma, M. Yi, H. Dong, H. Qin, E. Peterson, D. D. Busath, H. X. Zhou and T. A. Cross. "Insight into the Mechanism of the Influenza A Proton Channel from a Structure in a Lipid Bilayer." *Science* **2010**, 330, 509-512.

[29] H. Dong, M. Yi, T. A. Cross and H. X. Zhou. "Ab Initio Calculations and Validation of the pH-Dependent Structures of the His37-Trp41 Quartet, The Heart of Acid Activation and Proton Conductance in the M2 Protein of Influenza A Virus." *Chem. Sci.* **2013**, 4, 2776-2787.

[30] A. Ghosh, J. Qiu, W. F. DeGrado and R. M. Hochstrasser. "Tidal Surge in the M2 Proton Channel, Sensed by 2D IR Spectroscopy." *Proc. Natl. Acad. Sci. U.S.A.* **2011**, 108, 6115-6120.

[31] R. Liang, H. Li, J. M. Swanson and G. A. Voth. "Multiscale Simulation Reveals a Multifaceted Mechanism of Proton Permeation Through the Influenza A M2 Proton Channel." *Proc. Natl. Acad. Sci. U.S.A.* **2014**, 111, 9396-9401.

[32] T. A. Cross, M. Sharma, M. Yi and H. X. Zhou. "Influence of Solubilizing Environments on Membrane Protein Structures." *Trends Biochem. Sci.* **2011**, 36, 117-125.

[33] H. Yao, M. W. Lee, A. J. Waring, G. C. Wong and M. Hong. "Viral Fusion Protein Transmembrane Domain Adopts β-strand Structure to Facilitate Membrane Topological Changes for Virus-Cell Fusion." *Proc. Natl. Acad. Sci. U.S.A.* **2015**, 112, 10926-10931.

[34] R. Mani, S. D. Cady, M. Tang, A. J. Waring, R. I. Lehrer and M. Hong. "Membrane-Dependent Oligomeric Structure and Pore Formation of a β-Hairpin Antimicrobial Peptide in Lipid Bilayers from Solid-State NMR." *Proc. Natl. Acad. Sci. U.S.A.* **2006**, 103, 16242-16247.

[35] S. D. Cady, T. Wang and M. Hong. "Membrane-Dependent Effects of a Cytoplasmic Helix on the Structure and Drug Binding of the Influenza Virus M2 Protein." *J. Am. Chem. Soc.* **2011**, 133, 11572-11579.

[36] M. Hong and W. F. DeGrado. "Structural Basis for Proton Conduction and Inhibition by the Influenza M2 Protein." *Protein Sci.* **2012**, 21, 1620-1633.

[37] H. X. Zhou and T. A. Cross. "Influences of Membrane Mimetic Environments on Membrane Protein Structures." *Annu. Rev. Biophys.* **2013**, 42, 361-392.

[38] S. D. Cady, J. Wang, Y. Wu, W. F. DeGrado and M. Hong. "Specific Binding of Adamantane Drugs and Direction of their Polar Amines in the Pore of the Influenza M2 Transmembrane Domain in Lipid Bilayers and Dodecylphosphcholine Micelles Determined by NMR Spectroscopy." *J. Am. Chem. Soc.* **2011**, 133, 4274-4284.

[39] J. S. Rossman, X. Jing, G. P. Leser and R. A. Lamb. "Influenza Virus M2 Protein Mediates ESCRT-Independent Membrane Scission." *Cell* **2010**, 142, 902-913.

[40] M. J. Gerl, J. L. Sampaio, S. Urban, L. Kalvodova, J. M. Verbavatz, B. Binnington, D. Lindemann, C. A. Lingwood, A. Shevchenko, C. Schroeder and K. Simons. "Quantitative Analysis of the Lipidomes of the Influenza Virus Envelope and MDCK Cell Apical Membrane." *J. Cell Biol.* **2012**, 196, 213-221.

[41] S. Y. Liao, M. Lee, T. Wang, I. V. Sergeyev and M. Hong. "Efficient DNP NMR of Membrane Proteins: Sample Preparation Protocols, Sensitivity, and Radical Location." *J. Biomol. NMR* **2016**, 64, 223-237.

[42] K. Takegoshi, S. Nakamura and T. Terao. "^{13}C-^{1}H Dipolar-Assisted Rotational Resonance in Magic-Angle Spinning NMR." *Chem. Phys. Lett.* **2001**, 344, 631-637.

[43] M. Hong and R. G. Griffin. "Resonance Assignments for Solid Peptides by Dipolar-Mediated $^{13}C/^{15}N$ Correlation Solid-State NMR." *J. Am. Chem. Soc.* **1998**, 120, 7113-7114.

[44] T. Doherty and M. Hong. "2D ^{1}H-^{31}P Solid-State NMR Studies of the Dependence of Inter-Bilayer Water Dynamics on Lipid Headgroup Structure and Membrane Peptides." *J. Magn. Reson.* **2009**, 196, 39-47.

[45] D. Huster, X. Yao and M. Hong. "Membrane Protein Topology Probed by ^{1}H Spin Diffusion from Lipids Using Solid-State NMR Spectroscopy." *J. Am. Chem. Soc.* **2002**, 124, 874-883.

[46] J. K. Williams and M. Hong. "Probing membrane Protein Structure Using Water Polarization Transfer Solid-State NMR." *J. Magn. Reson.* **2014**, 247, 118-127.

[47] W. Luo and M. Hong. "Conformational Changes of an Ion Channel Detected Through Water-Protein Interactions Using Solid-State NMR Spectroscopy." *J. Am. Chem. Soc.* **2010**, 132, 2378-2384.

[48] M. Hong and Y. Su. "Structure and Dynamics of Cationic Membrane Peptides and Proteins: Insights from Solid-State NMR." *Protein Sci.* **2011**, 20, 641-655.

[49] K. K. Kumashiro, K. Schmidt-Rohr, O. J. Murphy, K. L. Ouellette, W. A. Cramer and L. K. Thompson. "A Novel Tool for Probing Membrane Protein Structure: Solid-State NMR with Proton Spin Diffusion and X-Nucleus Detection." *J. Am. Chem. Soc.* **1998**, 120, 5043-5051.

[50] M. Hohwy, C. M. Rienstra, C. P. Jaroniec and R. G. Griffin. "Fivefold Symmetric Homonuclear Dipolar Recoupling in Rotating Solids: Application to Double Quantum Spectroscopy." *J. Chem. Phys.* **1999**, 110, 7983-7992.

[51] S. Li and M. Hong. "Protonation, Tautomerization, and Rotameric Structure of Histidine: A Comprehensive Study by Magic-Angle-Spinning Solid-State NMR." *J. Am. Chem. Soc.* **2011**, 133, 1534-1544.

[52] S. D. Cady, C. Goodman, C. D. Tatko, W. F. DeGrado and M. Hong. "Determining the Orientation of Uniaxially Rotating Membrane Proteins Using Unoriented Samples: A ^{2}H, ^{13}C, and ^{15}N Solid-State NMR Investigation of the Dynamics and Orientation of a Transmembrane Helical Bundle." *J. Am. Chem. Soc.* **2007**, 129, 5719-5729.

[53] M. T. Colvin, L. B. Andreas, J. J. Chou and R. G. Griffin. "Proton Association Constants of His 37 in the Influenza-A $M2_{18-60}$ Dimer-of-Dimers." *Biochemistry* **2014**, 53, 5987-5994.

[54] F. Hu, K. Schmidt-Rohr and M. Hong. "NMR Detection of pH-Dependent Histidine-Water Proton Exchange Reveals the Conduction Mechanism of a Transmembrane Proton Channel." *J. Am. Chem. Soc.* **2012**, 134, 3703-3713.

[55] F. Hu, W. Luo, S. D. Cady and M. Hong. "Conformational Plasticity of the Influenza A M2 Transmembrane Helix in Lipid Bilayers Under Varying pH, Drug Binding, and Membrane Thickness." *Biochim. Biophys. Acta* **2011**, 1808, 415-423.

[56] W. C. Hung, F. Y. Chen and H. W. Huang. "Order-Disorder Transition in Bilayers of Diphytanoyl Phosphotidylcholine." *Biochim. Biophys. Acta* **2000**, 1467, 198-206.

[57] S. Tristram-Nagle, D. J. Kim, N. Akhunzada, N. Kucerka, J. C. Mathai, J. Katsaras, M. Zeidel and J. F. Nagle. "Structure and Water Permeability of Fully Hydrated DiphytanoylPC." *Chem. Phys. Lipids* **2010**, 163, 630-637.

[58] K. Otomo, A. Toyama, T. Miura and H. Takeuchi. "Interactions Between Histidine and Tryptophan Residues in the BM2 Proton Channel from Influenza B Virus." *J. Biochem.* **2009**, 145, 543-554.

[59] E. Liepinsh and G. Otting. "Proton Exchange Rates from Amino Acid Side Chains – Implications for Image Contrast." *Magn. Reson. Med.* **1996**, 35, 30-42.

[60] E. C. W. Clarke and D. N. Glew. "Evaluation of Thermodynamic Functions from Equilibrium Constants." *Trans. Faraday Soc.* **1966**, 62, 539-547.

[61] R. N. Goldberg, N. Kishore and R. M. Lennen. "Thermodynamic Quantities for the Ionization Reactions of Buffers." *J. Phys. Chem. Ref. Data* **2002**, 31, 231-370.